Designing sensors with tensioned Silicon Nitride micromechanical resonators

by

Christopher Reetz

B.S., University of California at Santa Barbara, 2017

A thesis submitted to the

Faculty of the Graduate School of the

University of Colorado in partial fulfillment

of the requirements for the degree of

Doctor of Philosophy

Department of Physics

2023

Committee Members:

Cindy Regal, Chair

John Teufel

Konrad Lehnert

Shuo Sun

Massimo Ruzzene

Reetz, Christopher (Ph.D., Physics)

Designing sensors with tensioned Silicon Nitride micromechanical resonators

Thesis directed by Prof. Cindy Regal

Mechanical resonators based on stressed silicon nitride have both exemplary optical and mechanical properties. Tensioning the silicon nitride enhances the mechanical properties of these devices owing to the phenomenon of dissipation dilution. The effects of dissipation dilution can be further enhanced through geometric engineering of the device, which has yielded devices that are capable of quantum operation in ambient conditions. At the same time, interferometric detection allows for a quantum-limited readout of the mechanical motion of such devices. The mechanical motion of these devices can be selectively influenced by external perturbations by augmentation of the mechanical resonator. In this work, we design a variety of sensors utilizing this combination of low dissipation, precise motional readout, and a near-universal coupling to an external field of interest. In this work, we study each of these elements, as well as their interplay, as they pertain to tensioned silicon nitride mechanical resonators. We study the ramifications of functionalization for force sensors, with a specific focus on developing probes for external magnetism, acceleration, and gravity. Such sensors could enable high-resolution spin imaging or inertial navigation, and motivate geometries and probes for fundamental physics in the context of larger-scale masses. My work presents the development of specific design criteria pertaining to force sensors based on phononic crystal membrane resonators. A deeper study of these resonators leads to a generalized formalism to understand the effects of a general, spatially varying, thermal environment on the sensing performance of such devices. This formalism is verified by direct measurement of an engineered micromechanical resonator exposed to a spatially varying thermal bath. The work concludes by considering the development of a micromechanical bolometer based on frequency-shift detection in engineered tensioned silicon nitride resonators.

Acknowledgements

Over the past 6-plus years, I have had the pleasure of interacting with and working with a wide variety of people throughout CU Boulder and JILA. My PhD journey, like all PhD journeys, could not have been successful without the support of countless individuals. That being said, it would be impossible to adequately acknowledge the contributions of everybody in these few words here, but I would like to extend a general thank you to everybody who has helped in this journey.

To begin, I would like to thank the members of my committee, Konrad Lehnert, Massimo Ruzzene, and Shuo Sun for taking time out of their schedules to provide input on my research. A special thanks to John Teufel for agreeing to serve as the reader for this document.

I would like to thank all of my colleagues on the spin-mechanics / mechanics team throughout the years. To Dylan McNally and Gabriel Theilacker Assumpcao, thank you for creating a welcoming and fun lab environment when I first joined. I would like to thank Ran Fischer for providing guidance and support during my first year in the lab. To Sanjay Kumar Keshava, I can safely say that it was a joy to watch you grow as a young student and that I appreciated the energy you brought every time you were in the lab. To Sofia Brown and Ruomu Zhang, it has been a pleasure to work with you over the past year, and I look forward to where you will take our work. Last but not least, I must acknowledge Ravid Shaniv. Working with Ravid was an emotional roller coaster (his words, not mine) in the best of ways. No two days in the lab are the same with Ravid due to the sheer breadth of interesting ideas and creativity he brings with his presence.

I would be remiss to not mention other members of the Regal lab who have been a help. A big thank you Max Urmey for walking me through the early growing pains of cavity alignment. To

Luca Talamo, thank you for taking the time to review parts of this document. I would also like to extend a thanks to Pete Burns, Sarang Mittal, and David Carlson for performing fabrication runs in the NIST cleanroom. I literally could not have done this work without those contributions.

A special thanks to my general support system, including all of my family, my partner Jenny, and all of my friends who have been there every step of the way. Also I must thank Braxton for his creative input on this document.

Finally, I must acknowledge Cindy Regal for serving as my advisor during all of these years. Cindy has provided constant support and advice through all the ups and downs of my doctoral studies, as well as providing me the basis and freedom to grow as a scientist. For this I will be ever grateful.

Contents

Tables

Table

Figures

Figure

Introduction

Over the past ten years, quantum optomechanics as a field has greatly expanded its capabilities and scope. We have witnessed large leaps in capabilities in regard to operating mechanical oscillators in the quantum regime, fueled by improvements in both the design and readout of mechanical resonators. These experiments consist of a wide range of both mechanical resonators and readout mechanisms [6–31]. First studied in 2008, it was found that tensioned silicon nitride mechanical resonators were great candidates for optomechanical experiments, owing both to their exemplary mechanical and optical properties [32, 33]. This opened the way to a new class of optomechanical experiments, the membrane in the middle optical cavity, which has served as the basis for many breakthrough experiments ever since [34–46]. The mechanical property enabling these experiments is called dissipation-dilution, a concept first discovered in the 1990s in regard to tensioned mirror suspensions [47]. The re-emergence of dissipation dilution in tensioned membrane devices has led to a myriad of works seeking to reduce mechanical dissipation. These works carried out prior to and during this work, typically exploit a modification of the membrane geometry in order to modify the dissipation profile of target mechanical modes [1, 48–59]. These efforts have resulted in a vast variety of mechanical resonators based on the same material platform. Much of the focus of this work will to be explore how these emerging geometries can be utilized. Notably, we will utilize and develop new strategies that seek to maximize the applicability of these tensioned silicon nitride devices to a wide range of sensing applications.

Developing sensors from low-dissipation mechanical resonators is attractive given the relative ease at which we can change the sensing target of a single mechanical resonator. Mechanical sensing, shortly put, is achieved by coupling an external perturbation to the state of motion of a mechanical resonator. Practically, this is achieved by the addition of a functionalizing agent to the resonator, be it depositing a magnet for magnetic sensing, or metalizing the surface to couple to electric fields. Studying the effects of functionalization will be a central theme of this work. Namely, we study the ramifications that functionalization has on the dissipative, spectral, geometric, and thermal properties of micromechanical resonators and their normal modes. Another key aspect of designing micromechanical sensors is achieving low-noise mechanical readout. This work considers the implementation of a Michelson interferometer, an increasingly attractive choice as modern micromechanical resonators become lower mass and lower dissipation.

In our discussion of micromechanical sensing, we seek to be broad in our formalism while also focusing on a few sensing targets of interest. Inspired by the excellent work with cantilevers in the field of magnetic resonance force microscopy (MRFM), we consider the advantages afforded by pursuing similar experiments with tensioned silicon nitride membrane resonators. Historically for our group, this study led us to consider the previously unstudied limit of high-mass load tensionsed micromechanical resonators. This work delves into this study, identifying applications to magnetic, gravitational, and acceleration sensing. This work culminates in a new research thrust for our group, which seeks to characterize and leverage the thermal properties of our devices. First, we identify the ramifications that arise from local heating of a complex silicon nitride membrane resonator. We find that modern approaches to engineering low-dissipation modes introduce higher susceptibility to local heating effects, identifying future design goals for micromechanical resonators. Using the insight gained in this investigation, we identify a new sensing target for our micromechanical devices, namely that of thermal radiation.

Chapter 1 presents a broad overview of understanding the mechanics of solids necessary to understand tensioned mechanical sensor design. It will begin with an overview of the mechanics of thin plates, namely how to relate the stress or strain of the plane to observable quantities such as mechanical displacement. This discussion will continue with a discussion of tensioned plates, presenting the well-known physics of unpatterned membranes and strings. We will summarize the conventions used throughout this work pertaining to modeling continuous resonator modes as a simple harmonic oscillator. Finally, we will engage in an extensive overview of loss mechanisms in silicon nitride mechanical resonators. This discussion will be a review of previous works from our group, as well as updating our understanding of mechanical losses to recent conventions used in the field of optomechanics.

Chapter 2 overviews the physics of the Michelson interferometer in the context of quantum-limited measurement of the motion of a micromechanical resonator. We discuss both the fundamental and technical noise sources arising from such a system, as well as reveal experimental design considerations pertaining to the use of Michelson versus cavity-based interferometry. We also present a detailed implementation of a Michelson interferometer used throughout the rest of this work.

Chapter 3 concerns the theory of micromechanical sensing. We identify the roles of imprecision and thermal noise in the roles of force sensing as well as other measurement paradigms. We continue with a discussion of micromechanical spin sensing, including a summary of an electron spin detection experiment carried out in our lab: **Fischer, R., McNally, D. P., Reetz, C., Assumpcao, G. G., Knief, T., Lin, Y., Regal, C. A. (2019). Spin detection with a micromechanical trampoline: towards magnetic resonance microscopy harnessing cavity optomechanics. New Journal of Physics, 21(4), 043049**. We also consider the ramifications of mass loading on the sensing capabilities of tensioned micromechanical oscillators, culminating in an experimental exploration of the effects of extreme mass loading: **Shaniv, R., Keshava, S. K., Reetz, C., Regal, C. A. (2023). Understanding the Quality Factor of Mass-Loaded Tensioned Resonators. Physical Review Applied, 19(3), L031006**. We also discuss the sensing implications of the commonplace optomechanical technique of cold-damping.

Chapter 4 surveys an effort in this group to develop high-sensitivity force sensors. In particular, we will discuss the design of phononic crystal resonators arising from patterned silicon nitride membranes. We develop a theoretical understanding of these devices, revealing design principles capable of tuning the mechanical properties of these devices. These principles are tested via a survey of a variety of mechanical devices at both room temperature and cryogenic conditions. These devices were designed to be addressable with free-space optical probing while still having exemplary force-sensing capabilities. we conclude with a discussion of how to push the limits of these designs for future devices. Many of these ideas are present in our work: **Reetz, C., Fischer, R., Assumpcao, G. G., McNally, D. P., Burns, P. S., Sankey, J. C., Regal, C. A. (2019). Analysis of membrane phononic crystals with wide band gaps and low-mass defects. Physical Review Applied, 12(4), 044027**.

Chapter 5 explores thermal effects on the performance of micromechanical devices for both sensing and quantum optomechanical experiments. In particular, we investigate the effects of a spatially varying thermal bath on the thermal noise of various resonator modes. This reveals a stark contrast in the susceptibility of local heating between different modes of the same resonator, a situation germane to the field of cavity optomechanics. Through these measurements, we also develop a new method for determining material properties of silicon nitride in complex micromechanical structures. This experiment is outlined in our work: **Shaniv, R., Reetz, C., Regal, C. A. (2023). Direct Measurement of A Spatially Varying Thermal Bath Using Brownian Motion. Physical Review Research, 5(4), 043121**.

Chapter 6 introduces yet another sensing paradigm for micromechanical devices, namely the development of micromechanical bolometers based on tensioned low-dissipation silicon nitride devices. The operating principle of these sensors is the transduction of absorbed radiation to a mechanical frequency shift through the mechanism of material expansion. This requires the development of experimental protocols that track the frequency of narrow-linewidth micromechanical resonators. We discuss a few such schemes. Additionally, we will introduce a new type of micromechanical resonator, a perimeter mode device, which we modify to tailor to the application of micromechanical bolometry. This chapter culminates in a discussion of the interplay between device geometry and bolometric sensitivity.

Chapter 1

Overview of tensioned micromechanical resonators

In this chapter, we will discuss the general theory of elasticity as it pertains to the micromechanical resonators studied in this work. Namely, we will focus on the physics of elastic deformation of tensioned thin film structures, with a focus on the particular physics of thin film tensioned resonators, often constructed from silicon nitride. This discussion will outline the interplay between device geometry and the normal mode structure of these devices, which is a central theme of this work. We then will discuss how modal geometry affects modal parameters, namely mode frequency, mass, and dissipation. Following this general study of elasticity, we will also discuss dissipation dilution and its ramifications for the types of mechanical resonators studied throughout this work.

1.1 Elasticity of thin plates

The study of the elasticity of solids concerns the physics of how solid objects deform. Such a study is paramount to understanding micromechanical resonators. The theory of elasticity applies to a wide range of structures, many of which are outside the scope of this work. For this reason, we will restrict our discussion to the elastic equations concerning the deformation of thin plates, or thin films, which will describe most of the elastic physics in this work.

The kinematics of a deforming solid can be described via the strain tensor which describes the changes in the displacement field u_i of the object in space. The strain tensor $\epsilon_{i,j}$ can be defined as follows:

$$\epsilon_{i,j} = \frac{1}{2}\left(\frac{\partial u_i}{\partial x_j} + \frac{\partial u_j}{\partial x_i} + \frac{\partial u_k}{\partial x_i}\frac{\partial u_k}{\partial x_j}\right) \tag{1.1}$$

where x_i denotes the Cartesian coordinate in the i direction. Here, and throughout this work, the repeated indices k denote an implied summation over k from $k = 1$ to $k = 3$. We are concerned with the limit of a thin plate undergoing relatively small oscillations. In this limit, the description of the strain tensor can be greatly simplified under the Kirchhoff hypothesis, which posits straight lines through the mid-surface prior to deformation remain straight upon deformation, and that the plate thickness does not change [60]. Under these assumptions, we write the deformation field in a simplified form:

$$u_1 = v_1 - z\frac{\partial w}{\partial x} \tag{1.2}$$

$$u_2 = v_2 - z\frac{\partial w}{\partial y} \tag{1.3}$$

$$u_3 = w \tag{1.4}$$

where v_i describes a pure in-plane displacement in the i direction. Here we see that the out-of-plane displacement w also adds to the in-plane displacement.

Evaluating the strain tensor under these kinematic assumptions still results in a rather complicated expression for the strain as a function of these displacement fields, and thus will not be shown here. However, the resulting expansion contains many higher-order terms which can be neglected under the assumption that the deflections of the plate are small compared to the film thickness. Neglecting these higher order terms, a simplified expression referred to as the von Kármán strains can be calculated:

$$\begin{aligned} \epsilon_{11} &= \frac{\partial v_1}{\partial x} + \frac{1}{2}\left(\frac{\partial w}{\partial x}\right)^2 - z\frac{\partial^2 w}{\partial x^2} \\ \epsilon_{12} &= \frac{1}{2}\left(\frac{\partial v_1}{\partial y} + \frac{\partial v_2}{\partial x}\right) + \frac{1}{2}\frac{\partial w}{\partial x}\frac{\partial w}{\partial y} - z\frac{\partial^2 w}{\partial x \partial y} \\ \epsilon_{22} &= \frac{\partial v_2}{\partial y} + \frac{1}{2}\left(\frac{\partial w}{\partial y}\right)^2 - z\frac{\partial^2 w}{\partial y^2}. \end{aligned} \tag{1.5}$$

Note that since the plate thickness cannot change, $\epsilon_{3i} = \epsilon_{i3} = 0$ for all values of i. All further entries of the stress tensor can be calculated via the symmetry of the stress tensor. In this work, we will typically analyze mechanical modes that are primarily out-of-plane, and thus we will assume that $v_1 = v_2 = 0$ for the remainder of this discussion. With this assumption, we arrive at the form of the elastic strain that will hold for the majority of the systems studied in this work:

$$\begin{aligned}
\epsilon_{11} &= \frac{1}{2}\left(\frac{\partial w}{\partial x}\right)^2 - z\frac{\partial^2 w}{\partial x^2} \\
\epsilon_{12} &= \frac{1}{2}\frac{\partial w}{\partial x}\frac{\partial w}{\partial y} - z\frac{\partial^2 w}{\partial x \partial y} \\
\epsilon_{22} &= \underbrace{\frac{1}{2}\left(\frac{\partial w}{\partial y}\right)^2}_{\text{elongation}} - \underbrace{z\frac{\partial^2 w}{\partial y^2}}_{\text{bending}} .
\end{aligned} \tag{1.6}$$

Here we have described the two terms that appear in each non-trivial element of the strain tensor as either elongation or bending. The word elongation is meant to describe the effects of this element of the strain tensor when applied to a beam system, where this strain describes the lengthening or shortening of the beam. However, this generalizes to the case of a plate as well. Bending describes terms that contain second derivatives of the out-of-plane displacement, corresponding to the geometric curvature of the plate.

Under these assumptions of the kinematics of the thin plate, one can then derive elastic equations of motion to describe the dynamics of the plate. In this work, we will refer to the elastic equation derived in [61], where an elastic equation of motion was calculated by evaluating Newton's second law at each infinitesimal volume element. The resulting equation for a thin plate can be described as follows:

$$D_{x,x}\frac{\partial^4 w}{\partial x^4} + 2D_{x,y}\frac{\partial^4 w}{\partial x^2 \partial y^2} + D_{y,y}\frac{\partial^4 w}{\partial y^4} + h\rho\frac{\partial^2 w}{\partial t^2} = 0. \tag{1.7}$$

The equation describes the motion of a thin plate situated in the xy plane. w quantifies the out-of-plane displacement — displacement in the z direction — as a function of location on the plate. $D_{i,j}$ are the flexural rigidities calculated to be:

$$D_{i,j} = \left\{ \begin{array}{ll} \frac{E_i h^3}{12(1-\nu_{i,j}\nu_{j,i})}, & \text{if } i = j \\ \frac{E_i h^3}{12(1-\nu_{i,j}\nu_{j,i})}\nu_{j,i} + \frac{Gh^3}{6}, & \text{if } i \neq j \end{array} \right\} \tag{1.8}$$

where E_i is the Young's modulus of the material in direction i, h is the plate thickness, ν_i is the Poisson ratio associated with the deformation in the i direction arising from a stress in the j direction, and G is the shear modulus of the material. Since we are focusing our discussion on amorphous silicon nitride membranes, we can assume that the material is isotropic. This implies that $E_i = E$ and $\nu_{i,j} = \nu$. In this limit, the shear modulus can be related to the Young's modulus as $E = 2G(1 + \nu)$, which leads to a much-simplified form of the elastic deformation equation:

$$D\left(\frac{\partial^4 w}{\partial x^4} + 2\frac{\partial^4 w}{\partial x^2 \partial y^2} + \frac{\partial^4 w}{\partial y^4}\right) + h\rho\frac{\partial^2 w}{\partial t^2} = 0 \tag{1.9}$$

where $D = Eh^3/(12(1 - \nu^2))$. Now that we have the elastic deformation equation for a thin plate, we can also add a term that corresponds to an isotropic tensile stress σ:

$$D\left(\frac{\partial^4 w}{\partial x^4} + 2\frac{\partial^4 w}{\partial x^2 \partial y^2} + \frac{\partial^4 w}{\partial y^4}\right) - \sigma h\left(\frac{\partial^2 w}{\partial x^2} + \frac{\partial^2 w}{\partial y^2}\right) + h\rho\frac{\partial^2 w}{\partial t^2} = 0. \tag{1.10}$$

Above is the full elastic deformation equation for a tensioned membrane resonator. For a membrane, material properties such as σ and ρ can be considered to be uniform. However, this work often studies patterned resonators, where holes are etched into a membrane in order to engineer the geometry. This modifies the above equation. Firstly, we identify holes in the material with a spatially dependent density. In this case, $\rho(x, y)$ can be thought of as a function that is 0 in the holes and ρ_{SiN} where there is remaining silicon nitride. Secondly, $\sigma(x, y)$ will also have spatial dependence due to this patterning. This is attributed to the fact the stationary configuration of the membrane will need to change upon patterning, which consequentially creates a modulated stress distribution. A more detailed description of the effects of this redistribution will be discussed later in this work. However for the time being consider a tensioned string that changes width at some point along its length. Newton's second law states that the tension in the string is constant for the stationary state of the string. The tension is related to the stress by $T = \sigma A$ where A is the cross-sectional area of the string. Changing the width of the string changes A, but T must remain constant. This forces a change in σ. This intuition for the string holds in more complex 2D structures as well.

Despite these added complications that arise from patterned structures, an outline of how to solve Eq. 1.10 can still be described. As with many partial differential equations, it is often useful to pursue the strategy of separation of variables. Furthermore, we are looking for normal-mode solutions to the problem, and thus expect the time part of the solution to be harmonic. Therefore, we assume that $w(x,t) = w(x)e^{-i\Omega t}$. For the remainder of this work, we will refer to w as $w(x)$, and time dependence will be written explicitly when needed. Under this form of the solution, Eq. 1.10 becomes:

$$\frac{D}{h\rho}\left(\frac{\partial^4 w}{\partial x^4} + 2\frac{\partial^4 w}{\partial x^2 \partial y^2} + \frac{\partial^4 w}{\partial y^4}\right) \underbrace{-\frac{1}{c^2}\left(\frac{\partial^2 w}{\partial x^2} + \frac{\partial^2 w}{\partial y^2}\right) - \Omega^2 w}_{\text{wave equation}} = 0. \tag{1.11}$$

Here we have introduced the stress-defined speed of sound $c = \sqrt{\sigma/\rho}$ and divided the whole equation by h. We note that in general, owing to the spatial dependence of σ and ρ, the speed of sound also has spatial dependence for structures studied in this work. As indicated above, the last three terms of the equation correspond to the classical wave equation in 2 dimensions. In the limit of high tension and short wavelength, these two terms dominate the mode shape, creating roughly sinusoidal mode shapes for tensioned membranes and strings. However, it is well known that the first three terms have a large role to play when considering the boundary conditions of the problem. For micromechanical resonators, the device is secured to a substrate along its edges. For a membrane device, this will be a square along the perimeter, while for a string this will be two lines at either end. In either case, we can refer to these regions as the supports of the device and will state the boundary conditions as:

$$\begin{aligned} w(x,y)|_{\text{supports}} &= 0 \\ (\hat{n}\cdot\nabla)w|_{\text{supports}} &= 0 \end{aligned} \tag{1.12}$$

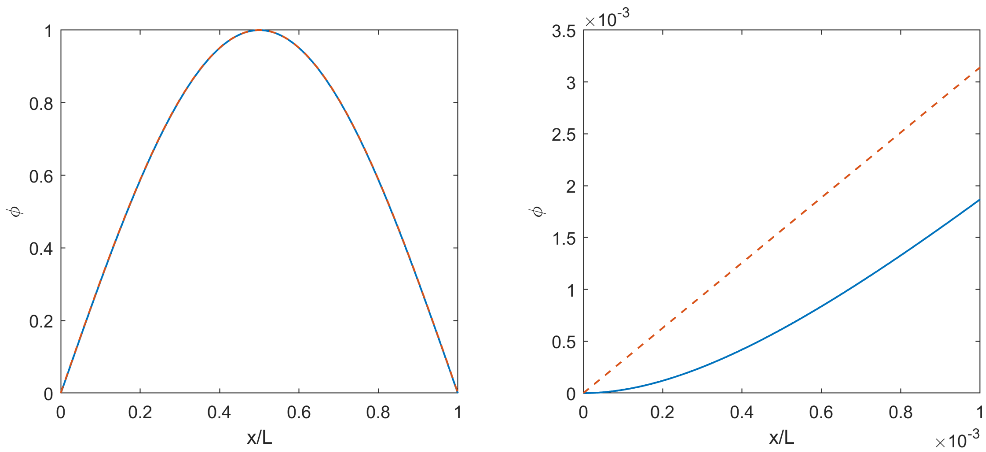

Figure 1.1: Theoretical mode shape for a tensioned string resonator. (Left) mode shape over the entire device extent. (Right) mode shape near the clamping point. The dotted line corresponds to the pure wave equation solution.

where $\hat{n}$ is a unit vector normal to the interface between the device and the supports. There boundary conditions are referred to as clamped boundary conditions. Enforcing such a boundary condition has ramifications on the solutions to Eq. 1.11. Notably, if one were to solve a wave equation with these boundary conditions — neglecting the first three terms — the only viable solution would be the trivial one of $w(x, y) = 0$. Therefore, the non wave-equation terms define the deformation close to the supports, even for a highly tensioned membrane. A full solution to this problem can be seen in [62, 63], which display such results:

$$\phi(x) = \left\{ \begin{array}{ll} \phi_l(x), & \text{if } x < L/2 \\ (-1)^{n+1}\phi_l(L - x), & x > L/2 \end{array} \right\} \tag{1.13}$$

where

$$\phi_l(x) = \sin(\beta_\sigma x) - \frac{\beta_\sigma}{\beta_E}(\cos(\beta_\sigma x) - e^{-\beta_E x}), n \tag{1.14}$$

L is the length of the string. $\beta_\sigma = n\pi/L$ and $\beta_E = \sqrt{12\sigma/h^2 E}$ are the wavenumbers associated with vibrations dictated by either tensioned or bulk properties of the material.

It is illustrative to examine the relative scales of these two wavenumbers for the case of a string with relatively generic parameters of $L = 500\ \mu$m, $\sigma =$ 1 GPa and $h =$ 100 nm. In this limit, $\beta_\sigma^{-1} \sim 200\ \mu$m while $\beta_E^{-1} = 400$ nm. This means that the exponential correction to the wave equation solution is small and that the length scale of the exponent is a small fraction of the device size. Although this analysis was carried out for the 1D case of a string, the same principles hold for a 2D membrane resonator. In general, this is a generic feature of mechanical modes on structures with these boundary conditions. Mechanical modes that extend to the supports will necessarily need to have regions where the mode shape mirrors closely that of the string discussed above. As will be discussed later, the precise mode shape ties directly to the dissipative properties of the mode, and therefore an understanding of the effects of the clamped boundary condition is useful intuition for future discussions.

1.2 Normal mode equivalence to a simple harmonic oscillator

It can be intuitively understood that the normal modes of a micromechanical resonator can be mapped to that of a simple harmonic oscillator.

$$M^{-1}Ku = \omega^2 u. \tag{1.15}$$

Solving for the eigenvalues and eigenmodes of the matrix $M^{-1}K$ results in the normal mode frequencies and normal modes of the system of particles. Each one of these normal modes can be thought of as a simple harmonic oscillator, each with its own effective resonator parameters, namely the effective mass of the mode $m_{\mathrm{eff},n}$ and the spring constant of the mode $k_{\mathrm{eff},n}$. These combine to determine the frequency of oscillation given by $\omega_n = \sqrt{k_{\mathrm{eff},n}/m_{\mathrm{eff},n}}$. Intuitively, we expect that the $m_{\mathrm{eff},n}$ should correspond roughly to the amount of mass that moves throughout the extent of the mode, while the $k_{\mathrm{eff},n}$ should correspond to roughly how stressed the resonator becomes when it undergoes a harmonic cycle of motion. However, it is apparent that the geometry of the mode also plays a deep role in how the effective parameters should be determined.

Here, we will present a method for determining these parameters that are outlined in [63].

This derivation assumes a convention for the mode shape in question relating to its normalization. Throughout this work, unless specified otherwise, we will describe the mode shape $w(x, y, t)$ as $q(t)\phi(x, y)$, where $\phi(x, y)$ has the property that it has a value of 1 at points of maximal out of plane displacement. We note here that this is not a unique way to normalize a mechanical mode and care must be taken to ascertain the normalization convention of the calculation at hand. Throughout this work, we will adopt the convention presented above.

Under this assumption, we can now derive the effective resonator parameters by multiplying Eq. 1.10 by $\phi_n(x, y)$ and integrate the result over the planar extent of the device:

$$\begin{gathered}\int_{\text{device}} \sum_m \phi_n \Big(D q_m(t) \nabla^4 \phi_m - \sigma h q_m(t) \nabla^2 \phi_m \Big) dxdy + \int_{\text{device}} h\rho \sum_m \phi_n \ddot{q}_m(t) \phi_m dxdy = \\ \int_{\text{device}} p(t)(x, y, t) \phi_n dxdy.\end{gathered} \tag{1.16}$$

Here we have introduced the biharmonic operator $\nabla^4 = \nabla^2\nabla^2$, and we have also included a pressure term in order to capture the more general case that includes an external force acting on the mode. In the above expression, the general solution for $w(x, y, t)$ has been replaced with a sum of the normal modes of the system. Under typical conditions, we assumed that $q_m(t)$ is spectrally confined to a small bandwidth around each ω_m. This is true in the limit that each normal mode is relatively low dissipation. This expression can be further simplified by the fact that the eigenmode solutions should be orthogonal:

$$\int_{\text{device}} h\rho(x, y) \phi_n \phi_m dxdy = \xi_{n,m} \delta_{n,m} \tag{1.17}$$

where $\delta_{n,m}$ is the Kronecker delta symbol and $\xi_{n,m}$ is the result of the integral when $n = m$. We emphasize here the presence of the $\rho(x, y)$ inside the integral. This is a necessary condition on the inner product such that modes will be orthogonal for nonuniform mass systems. Note that this inner product is also only correct in systems with small rotations of the object, such as those that are studied in this work.

With this in mind, we can rewrite Eq. 1.16 as follows:

$$\begin{aligned} q_n(t) \int_{\text{device}} \phi_n \Big(D\nabla^4 \phi_n - \sigma h \nabla^2 \phi_n \Big) dxdy + \ddot{q}_n(t) \int_{\text{device}} h\rho \phi_n^2 dxdy = \\ \int_{\text{device}} p(x,y,t) \phi_n dxdy - \int_{\text{device}} \sum_{m \neq n} q_m(t) \phi_n \Big(D\nabla^4 \phi_m - \sigma h \nabla^2 \phi_m \Big) dxdy. \end{aligned} \tag{1.18}$$

Here we have applied the orthogonality condition where possible and arranged all terms that contain the degree of freedom $q_n(t)$ on the first line. The second line involves all other degrees of freedom as well as the applied force. It can be shown that the integral containing all other degrees of freedom vanishes for relatively simple geometries like uniform membranes and beams [63], but it is not obvious that this expression vanishes in generality for more complex structures. For the sake of this work, we will treat this term as a perturbative term. We justify this by inspecting the spectral content of this term, which will most likely be centered around a narrow band of frequencies defined by each ω_m where $m \neq n$. This would be true in the limit of low-dissipation mechanical modes. Therefore, this perturbation term can be seen as a crosstalk term from the other degrees of freedom, which apply off-resonant forces to the mode in question. For the sake of understanding the intrinsic properties of a mode, we want to consider the bare effects of the mode, regardless of the excitation of the other degrees of freedom. Therefore, we will neglect this term for determining $k_{\text{eff},n}$ and $m_{\text{eff},n}$. To determine these terms, we match the expression in Eq. 1.18 with the canonical simple harmonic oscillator equation of motion:

$$\tilde{m}_{\text{eff},n} = \int_{\text{device}} h\rho \phi_n^2 dxdy \tag{1.19}$$

$$\tilde{k}_{\text{eff},n} = \int_{\text{device}} \phi_n \Big(D\nabla^4 \phi_n - \sigma h \nabla^2 \phi_n \Big) dxdy \tag{1.20}$$

$$\tilde{F}_{\text{eff},n} = \int_{\text{device}} p(x,y,t) \phi_n dxdy. \tag{1.21}$$

Here we also identify an effective force $\tilde{F}_{\text{eff},n}$ which depends on the spatial profile of the force applied and its overlap with the mechanical mode. We point out in Eq. 1.21 that the forms of these three expressions all depend on the normalization convention on ϕ_n, but will all scale equally as a function of the normalization. To emphasize this point, we have denoted each quantity with a tilde to denote that the actual values of each of these computed quantities should only be considered in proportion to one another. However, regardless of the normalization used, we can accurately predict the dynamics of the system in regard to calibrated inputs and outputs. It should be noted that there are well-established conventions of normalization in different fields that study the dynamics of mechanical systems. For instance, here we have explicitly stated the convention that the maximum values of $\phi_n = 1$. In this limit, the above parameters coincide with relatively physically intuitive values for simple structures like beams and membranes. For instance, low-order membrane modes will have $\tilde{m}_{\text{eff}} = m_{\text{membrane}}/4$ and low-order beam modes will have $\tilde{m}_{\text{eff}} = m_{\text{beam}}/2$, where m_{membrane} and m_{beam} are the physical masses of the membrane and beam in question. This aligns well with physical intuition where for these modes a decent fraction of the physical mass participates in the mode. Another commonly used convention that is present in the study of structural mechanics is to enforce that $\xi_{n,m}$ present in Eq. 1.17 be equal to one unit mass m_{unit}. Such normalization is referred to as mass matrix normalization, referring to how this normalization convention is used within finite element analysis software or any discretization of the continuous system being discussed.

To complete this discussion, we will now introduce yet another normalization convention for the mode shape ϕ_n that is commonly used in the field of cavity optomechanics. This convention can be motivated by considering the probing of the Brownian motion of an extended resonator mode. The equipartition theorem states that the potential and kinetic energy of a simple harmonic oscillator each have an average amount of energy equal to $k_B T/2$ where k_B is the Boltzmann constant and T is the temperature of the thermal bath of the resonator. We can relate that to the case of an extended mode by integrating the motion of each mass element throughout the resonator extent. Assuming the harmonic motion of the resonator, we arrive at the following equality:

$$\frac{1}{2}k_B T = \frac{1}{2}m_n \omega^2 q_{th,n}^2 = \frac{1}{2}\int_{\text{device}} \rho \omega_n^2 q_n^2 \phi_n^2 dV \tag{1.22}$$

where q_n is the motional degree of freedom of the resonator, m_n is the mass of the resonator, and

ω_n is the resonant frequency. We now enforce the condition that $q_n = q_{th,n}$. What this means physically is that if the resonator were to be probed at the maximal point of motion, we want to observe the Brownian motion that corresponds to a resonator with mass m_n and frequency ω_n. Under this constraint, we reveal the following equality:

$$m_n = \int_{\text{device}} \rho\phi_n^2 \equiv m_{\text{eff,opt},n} \tag{1.23}$$

where here we have defined the quantity $m_{\text{eff,opt},n}$ which corresponds to the observed inertia of the resonator when probed at the point of maximal mechanical motion.

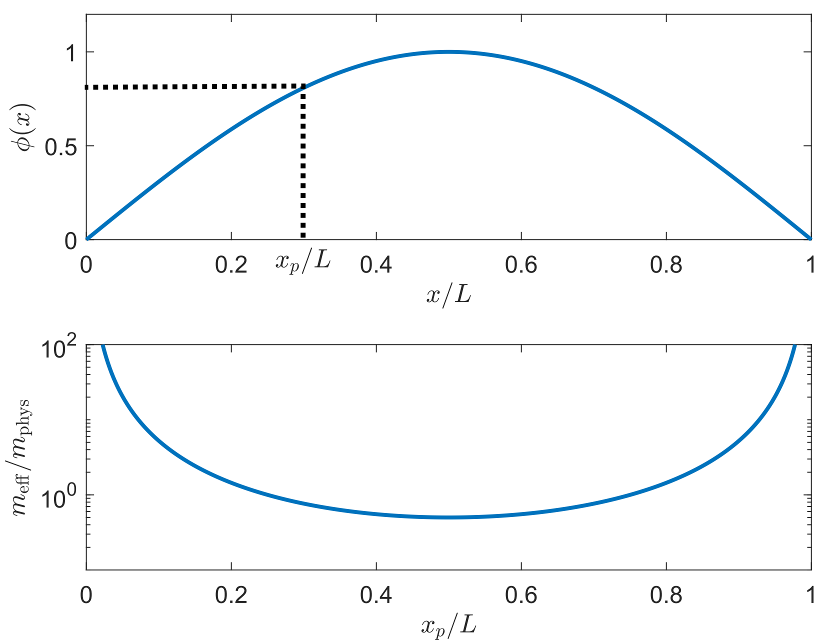

Figure 1.2: Top: Normalized mode shape ϕ_x for 1D string resonator. We have indicated with the dotted line the quantity x_p/L, which is a probe point at which the oscillator motion will be evaluated. Bottom: Ratio of the effective and physical masses of the resonator as a function of probe location. We see that while probing at the center, the effective mass is relatively low, and is on the scale of the physical resonator mass. Probing near the edges where the motion is low results in a diverging effective mass.

In general, we do not always probe at this optimal point. To correct for the probe location, we simply normalize ϕ_n by the amplitude of the point at which we probe. When probing at this non-optimal point, the motion of the resonator is less but its frequency doesn't change. As observers, we argue that we should interpret this decrease in motion as an increase in the effective mass of the resonator under the justification that we cannot ascribe this change in motion to a decrease in bath temperature or a change in mechanical frequency. Therefore, we can define this new effective mass — as a function of the probe point — as follows:

$$m_{\text{eff},n}(\vec{x}_p) = \int_{\text{device}} \rho \left(\frac{\phi_n(\vec{x})}{\phi_n(\vec{x}_p)} \right)^2 dV. \tag{1.24}$$

One can see the ramifications of the effective mass formula in Fig. 1.2. This convention for the calculation of the effective mass, along with the related normalization of the mode shape function, proves to be useful for applications where the thermal motion of the mechanical resonator is a quantity of interest. For instance, this convention readily applies to micromechanical thermometers which seek to relate an observed motional quantity to a physical temperature. This formulation is also important when considering the force-sensing performance of a resonator, where the Brownian motion is often the limiting noise in the measurement scheme. Additionally, this normalization scheme can be applied to Eq. 1.21 such that a signal force can be calibrated with respect to the observed motional response.

1.3 Mechanical response

We have now established the equivalence between a normal mode of a micromechanical resonator and a simple harmonic oscillator under the influence of an arbitrary spatial force. We complete this understanding by deriving the spectral character of the mechanical response to this force. For this discussion, we will introduce a viscous damping term to include the effects of dissipation in the response. With this damping term in mind, we can write the equation of motion as follows:

$$m_{\text{eff}}\ddot{x}(t) + \gamma m_{\text{eff}}\dot{x}(t) + k_{\text{eff}}x(t) = F_{\text{eff}}(t), \tag{1.25}$$

where $-\gamma m_{\text{eff}}\dot{x}(t)$ is the viscous damping force on the resonator. A general solution can be computed from classical linear response theory, which focuses heavily on the mechanical susceptibility χ_m. We can calculate $\chi_m(\omega)$ by solving Eq. 1.25 for the case of a harmonic drive given as $F_{\text{eff}}(\omega)e^{i\omega t}$. Under these conditions, we assume that our mechanical response is also harmonic at the same frequency: $x(\omega)e^{i\omega t}$. Here both $F_{\text{eff}}(\omega)$ and $x(\omega)$ are complex valued phasors. They are related as follows:

$$(-\omega^2 m_{\text{eff}} + i\omega\gamma m_{\text{eff}} + k_{\text{eff}})x(\omega) = F_{\text{eff}}(\omega), \tag{1.26}$$

or more concisely:

$$x(\omega) = \chi(\omega)F_{\text{eff}}(\omega) \tag{1.27}$$

$$\chi(\omega) = \frac{1}{m_{\text{eff}}(-\omega^2 + i\omega\gamma + \omega_0^2)}. \tag{1.28}$$

This is the most commonly presented form of χ for a mechanical resonator. To further parameterize the problem, we will introduce the concept of the quality factor Q:

$$Q = \frac{\omega_0}{\gamma} = 2\pi\frac{W}{\Delta W} \tag{1.29}$$

Here, we have written Q in two ways. First in terms of the frequency and linewidth of the oscillator, but also in terms of the stored energy W and the dissipated energy ΔW per oscillation cycle. Therefore, Q parameterizes the energy decay of a harmonic oscillator. Heuristically, it corresponds to the number of coherent oscillations a mechanical system undergoes prior to losing an appreciable amount of the initial energy in the system. The effects of higher values of Q — lower dissipation rates — can be seen in Fig. 1.3 where a drive near mechanical resonance generates larger mechanical responses. This is because the resonator holds energy for a longer time — around Q oscillations — and therefore reaches higher mechanical amplitudes. Far from mechanical resonance, this condition no longer holds, since the off-resonant driving begins to negatively interfere with the natural frequency response of the resonator. The phase response also changes as a function of Q. This can be understood by inspecting the form of χ far below and far above mechanical resonance. Below resonance, the resonator responds with a DC response, which is just Hooke's law $x = F_{\text{eff}}/k_{\text{eff}}$, indicating that there is no phase delay between the drive and response. Far above resonance, $\chi \sim \omega^{-2}$ which corresponds to a phase shift of $-\pi$. The transition between these two extremes happens near mechanical resonance, which is defined as a bandwidth equal to $\gamma = \omega_0/Q$. Therefore, the phase response changes more steeply for higher Q resonators.

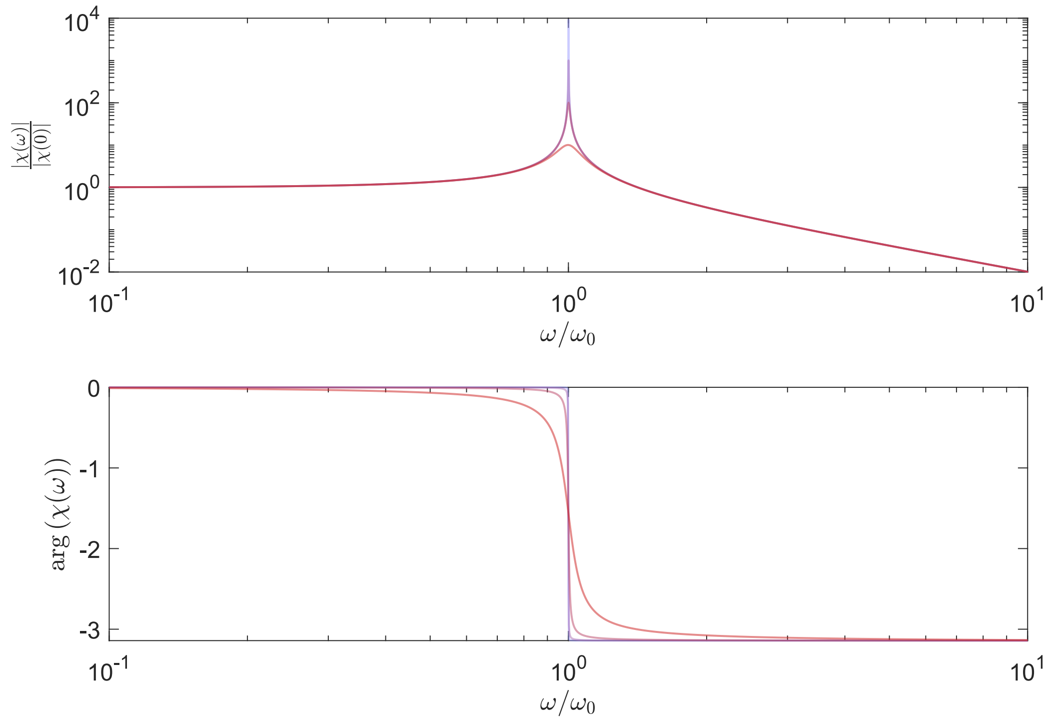

Figure 1.3: Functional form of $\chi(\omega)$ while sweeping over values of Q. Blue (red) traces correspond to values of relatively high (low) values of Q. All values of Q are much greater than unity. The top plot is the amplitude part of χ, while the bottom indicates the phase response of the resonator.

Here we will comment on our choice of how dissipation was modeled in this section, namely that it appears as a viscous damping force $-\gamma m_{\text{eff}}\dot{x}$. This in fact cannot be true in general. For instance, structural damping ($\gamma \sim \omega^{-1}$) is expected to occur in arbitrary mechanical systems and has been observed in high-stress silicon nitride micromechanical resonators [64, 65]. Such modifications to χ qualitatively affect how the system responds to thermal noise (as discussed in the next section). However, since the experiments performed in this work typically operate with high mechanical Q, and near resonance, a purely viscous damping model is sufficient for the scope of this work.

1.4 Fluctuation dissipation theorem and the thermal force

As discussed previously, we expect that micromechanical resonators will exhibit Brownian motion when exposed to a thermal bath of finite temperature. However, we did not discuss the manner in which a mechanical resonator exchanges energy with the thermal environment. The fluctuation-dissipation theorem reveals that thermal fluctuations in a physical quantity are directly proportional to the dissipation of said quantity. For the case of the mechanical resonator system in this discussion, this is quantified by the following relation [66]:

$$S_{xx}(\omega) = -\frac{4k_B T}{\omega}\mathrm{Im}\chi(\omega), \tag{1.30}$$

where S_{xx} is the single-sided power spectral density of the motional degree of freedom x, k_B is the Boltzmann constant, and T is the bath temperature. We note that in general, the fluctuation-dissipation theorem holds for any system that obeys a linear response between an observable and an external drive described by a general χ. We note here that the form of the fluctuation-dissipation theorem present in Eq. 1.30 is valid in a classical limit. In general, a full quantum mechanical treatment of the single-sided power spectral density must include vacuum fluctuations at low temperatures. The thermal energy $k_B T$ in Eq. 1.30 is the classical limit of the average energy of a bosonic mode which can be calculated by simply replacing $2k_B T/\omega \rightarrow 2\hbar/(1-\exp(-\hbar\omega/k_B T))$ [67,68]. In this work, $\hbar\omega \ll k_B T$ and therefore the classical formula will be sufficient. In this particular case, this reveals that:

$$S_{xx} = \frac{4k_B T}{m_{\mathrm{eff}}}\left((\omega_0^2 - \omega^2)^2 + \gamma^2\omega^2\right)^{-1} = 4k_B T m_{\mathrm{eff}}\gamma|\chi(\omega)|^2. \tag{1.31}$$

Eq. 1.31 describes the spectral character of the Brownian motion. We note that the final equality reveals that the thermal fluctuations match the mechanical response of the resonator for the specific use of χ that assumes viscous damping. Another interpretation of this equation is that the fluctuations of the mechanical resonator arise from a stochastic force that is uncorrelated in time. Such a force should have a white power spectral density. The relationship between force and motion indicated in Eq. 1.28 can be extended to relate their respective power spectral densities. This allows us to identify the thermal force power spectral density as:

$$S_{FF} = 4k_B T\gamma m_{\text{eff}}. \tag{1.32}$$

The presence of a white thermal force places limits on the resonator performance in many use cases, including ground state cooling, force sensing, frequency stability, and the use of a mechanical resonator has a quantum memory [49,67,69–72]. To our knowledge, there is no available strategy to remove the effects of this type of noise, owing to its white character across the measurable bandwidth of the resonator. Therefore, it is paramount to reduce the magnitude of S_{FF} when possible. This is most efficiently achieved by reducing γ or the overall dissipation, and by reducing T. The latter is typically achieved by placing the micromechanical resonator in a cryogenic environment. Throughout this work, we will revisit the effects of thermal noise for each discussed application as necessary.

1.5 Dissipation dilution

Dissipation dilution is a phenomenon first identified in the 1990s in the context of suspended pendulum systems [47]. It can be understood conceptually as arising from an increase in the stored tensile energy in mechanical systems, typically arising from tensioning of the mechanical structure. This added tension, or added strain, gives rise to a “lossless potential” into which energy can be stored. This increase in stored energy is achieved while maintaining the same amount of dissipated energy per cycle, meaning that there is no additional mechanical loss introduced by straining the underlying mechanical structure. Inspecting the energetic interpretation of Eq. 1.29 reveals that dissipation dilution increases the quality factor of mechanical resonators, even if the decay rate or linewidth of the mechanical resonance frequency stays the same. When benchmarking the performance of mechanical oscillators in quantum optomechanics experiments, the Q - f product is a useful figure of merit with which to compare oscillators of different frequencies. We readily see that systems that exhibit dissipation dilution have enhanced $Q \times f$ owing to the increase in mechanical frequency and mechanical Q, meaning that mechanical oscillators benefiting from dissipation dilution also benefit future quantum optomechanical experiments.

In the context of this work, dissipation dilution can also be applied to sensing with mechanical resonators. For thermal noise-limited mechanical modes, Eq. 1.32 depends only on γ, and therefore should not benefit from dissipation dilution. This is true to the first order. However, our cursory analysis of dissipation dilution fails to identify key ramifications of tensioning of micromechanical devices. First of all, introducing tension modifies the mode structure given the different contributions from the wave-equation terms and bulk terms in Eq. 1.11. Therefore, the mode shapes for a tensioned structure and a bulk structure will be fundamentally different. The influence of this change in geometry has been studied by others in our field, and the associated formalism will be presented in the following sections of this work [49, 51, 73, 74]. Secondly, dissipation dilution achieved via tension gives rise to relatively macroscopic mechanical resonators (on the order of 1 mm) which exhibit relatively high mechanical frequencies on the order of 1 MHz. Working at these higher frequencies escapes ubiquitous $1/f$ noise arising from a variety of technical sources including the mechanical readout and the sensing environment. When appropriate, we will discuss the benefits of working at higher mechanical frequencies throughout this work.

1.6 Dissipation channels in silicon nitride micromechanical resonators

Up to this point, we have analyzed the normal mode structures of micromechanical resonators in the absence of dissipation. We have introduced a viscous damping term in the equivalent resonator equation of motion, but have neglected to comment on its magnitude or physical origin in micromechanical membrane resonators. In reality, there are a number of dissipation channels which each contribute to the total damping of a normal mode. This can be quantified as the following two equivalent relations:

$$\gamma = \sum_i \gamma_i \tag{1.33}$$

$$\frac{1}{Q} = \sum_i \frac{1}{Q_i} \tag{1.34}$$

where γ_i and Q_i are the damping rates and quality factors of each individual channel. To date, there have been many works studying the intricacies of these loss pathways among many different classes of mechanical resonators. In general, the leading source of loss in a mechanical resonator depends on a variety of factors, including geometry, temperature, gaseous environment, material, and supports to the external environment. In this section, we will present a brief overview of relevant loss pathways for stressed silicon nitride membranes.

1.6.1 Internal losses in micromechanical resonators

In this section, we will provide an overview of the internal losses present in stressed silicon nitride micromechanical resonators. By internal loss, we are referring to loss directly associated with the motion of the micromechanical resonator, inside the volumetric extent of the resonator. To begin this discussion, it is illustrative to recall the definition of the quality factor Q in terms of the energetic properties of the resonator, as presented in Eq. 1.29. When considering the dissipation from material losses, we already can calculate W as either the average kinetic energy or average stored tensile energy of the resonator from knowledge of the mode shape, or the previously defined effective resonator parameters. One route to calculate ΔW is provided by the Zener model for anelasticity. This model modifies Hooke's law allowing for a phase lag between the stress and strain fields of a material. This mimics a viscous damping force of a simple harmonic oscillator undergoing harmonic motion $x(t) = x_0 e^{i\omega_m t}$, where the role of the "stress" is the sum of the damping force and the restoring force and the "strain" is the resonator motion:

$$F_{\text{int}} = -k_{\text{eff}}x(t) + m_{\text{eff}}\gamma\dot{x}(t) = (-k_{\text{eff}} + i\frac{k_{\text{eff}}}{Q})x_0. \tag{1.35}$$

Here we see that when considering the spectral character of motion near mechanical resonance, we can capture the effects of dissipation by introducing an imaginary part to the spring constant of the resonator. Clearly, we see that the imaginary part is much reduced from the real part by a factor of $1/Q$. Another way to arrive at this conclusion would be to solve the homogeneous equations of motion for the resonator. In the presence of damping, the eigenvalues will in general be complex-valued, reflecting this exact phenomenon we have just presented.

In the Zener model, this phase lag is captured by first identifying the most general stress-strain relationship [75]:

$$\sigma + \tau_\sigma\dot{\sigma} = E(\epsilon + \tau_\epsilon\dot{\epsilon}) \tag{1.36}$$

where τ_σ (τ_ϵ) is a time constant associated with the relaxation of the stress (strain) with respect to a changing strain (stress). In this section, it is understood that σ and ϵ are tensors. We will not explicitly write their indices unless needed. To proceed, we can again assume harmonicity of the motion, which results in the following stress-strain relation:

$$\sigma = E\left(\frac{1 + i\omega\tau_\epsilon}{1 + i\omega\tau_\sigma}\right)\epsilon \tag{1.37}$$

The above expression can thus be interpreted as the material having a complex part to its Young's modulus:

$$\sigma = E\epsilon \rightarrow \sigma = (E_1(\omega) + iE_2(\omega))\epsilon \tag{1.38}$$

where $E_1(\omega)$ and $E_2(\omega)$ are the real and imaginary parts of the Young's modulus of the material, where we have included an explicit frequency dependence that arises from the exact values of τ_σ and τ_ϵ. We also introduce the common notation of Q_{int}, often referred to as the intrinsic quality factor of the material:

$$Q_{\text{int}} = \frac{E_1}{E_2}. \tag{1.39}$$

In some situations, it is often conceptually more convenient to use Q_{int} as a metric for dissipative properties of a material.

With this expression in hand, we can calculate a general expression for ΔW in this model [49, 73]:

$$\Delta W = \int_{\text{device}} \left[\oint \sigma(t)\dot{\epsilon}(t)dt \right] dV. \tag{1.40}$$

where $\oint[\cdot]dt$ indicates integration over a single period of oscillation.

Up until this point, we have neglected the effects of a nonzero Poisson ratio on the effects of dissipation. To include the effects of the Poisson ratio, we must append Hooke's law [73]:

$$\sigma_{ij} = \frac{E}{1+\nu}(\epsilon_{ij} + \frac{\nu}{1-2\nu}\delta_{ij}\sum_l \epsilon_{ll}) \tag{1.41}$$

A generalized expression for ΔW can thus be calculated by inserting Eq. 1.41 into Eq. 1.40:

$$\Delta W = \sum_i \sum_j \int_{\text{device}} \left[\oint \frac{E_1 + iE_2}{1+\nu}(\epsilon_{ij}\dot{\epsilon}_{ij} + \frac{\nu}{1-2\nu}\delta_{ij}\dot{\epsilon}_{ij}\sum_l \epsilon_{ll})dt \right] dV. \tag{1.42}$$

Following [73], here we bring attention to the dynamic and static parts of the strain: $\epsilon_{ij}(t) = \bar{\epsilon}_{ij} + \Delta\epsilon_{ij}$. Here we argue that for calculating the energy lost per cycle, we only need to consider the dynamic part of the strain. For harmonic motion, $\dot{\epsilon}_{ij}(t) = -i\omega\Delta\epsilon_{ij}(t)$. Under this condition, $\oint[\cdot]dt$ is zero for all terms involving E_1 and is nonzero for terms involving E_2. Additionally, all terms involving the static strain also integrate to zero. Therefore:

$$\Delta W = \pi \sum_i \sum_j \int_{\text{device}} \frac{E_2}{1+\nu}(\tilde{\epsilon}_{ij}\tilde{\epsilon}_{ij} + \frac{\nu}{1-2\nu}\delta_{ij}\tilde{\epsilon}_{ij}\sum_l \tilde{\epsilon}_{ll})dV, \tag{1.43}$$

where $\tilde{\epsilon}$ is the harmonic amplitude deviation of the strain field.

Eq. 1.43 is a quite generalized expression for the energy lost per cycle for a micromechanical resonator, written in terms of the harmonic amplitude of the strain. This formulation is valid for any isotropic material, and even for multi-material micromechanical resonators. However, to focus our work to that of stressed membrane resonators, we can write insert Eq. 1.6 into Eq. 1.43. In doing so, we will neglect terms associated with the elongation of the structure, as labeled in Eq, 1.6. This is valid for small out-of-plane motional amplitudes. However, damping associated with elongation losses can manifest as amplitude-dependent damping rates [76]. In addition, we will assume that there is no out-of-plane stress of the membrane, as this would violate the symmetry of the problem. Doing so enforces that $\sigma_{33} = 0$. Plugging this into Eq. 1.41 implies that there is a connection between the in-plane strains and ϵ_{33}, namely that $(1-\nu)\epsilon_{33} = -\nu(\epsilon_{11}+\epsilon_{22})$. Performing this substitution yields:

$$\Delta W = \int_{\text{device}} \frac{\pi z^2 E_2}{1-\nu^2}\Bigg(\underbrace{(\frac{\partial^2 w}{\partial x^2}+\frac{\partial^2 w}{\partial y^2})^2}_{\text{mean curvature}} - \underbrace{2(1-\nu)(\frac{\partial^2 w}{\partial x^2}\frac{\partial^2 w}{\partial y^2}-(\frac{\partial^2 w}{\partial x \partial y})^2)}_{\text{Gaussian curvature}}\Bigg)dV. \tag{1.44}$$

Here we have split up the curvature into the mean curvature and Gaussian curvature explicitly, following the formalism established by Yu [48]. Intuitively, the mean curvature corresponds to the amount with which a surface curves at a given point, regardless of the in-plane direction of the curvature. On the other hand, the Gaussian curvature quantifies how much a surface curves in all directions at a given point. It was shown by Yu [48], that for unpatterned membranes, the Gaussian curvature integral is identically zero following an application of Green's identity. For patterned structures, this term is not necessarily zero by the same argument, given the mechanical amplitude is not defined in regions without material, meaning that the application of Green's identity requires a consideration of the mode shape along the surface of the holes as well, which doesn't necessarily yield a zero result. However, it has been found empirically that this contribution to the energy lost per cycle is a small perturbation to the overall result and therefore will be neglected when predicting quality factors in this section. However, we caution that neglecting this term when exploring novel mechanical modes, as whether or not it can be considered negligible depends heavily on the mode shape in question [77]. For instance, in Ch. 6 we will investigate mechanical modes that have large torque contributions, requiring the use of this term when predicting quality factors.

Finally, we will produce a formula for a predicted value of Q. In doing so, we can calculate W from either the kinetic energy or the stored tensile energy. Both are valid, but for conceptual clarity, we will present a formulation that utilizes the tensile energy. However, for ease of computation, often the kinetic energy is used.

The stored tensile energy is given by:

$$\int_{\text{device}} \frac{\sigma}{2}\left((\frac{\partial w}{\partial x})^2 + (\frac{\partial w}{\partial y})^2 \right) dV. \tag{1.45}$$

We note that this is only accurate in the high-stress limit for a membrane resonator. In principle, there are energetic contributions resulting from the bulk properties of the material as well. If one is concerned with these properties, a complete general treatment is also presented in the work by Fedorov [73]. A key observation about the stored tensile energy is that it scales with the stress of the membrane structure. To first order, the exact details of the mode shape stay the same regardless of stress, meaning that as stress increases, ΔW stays constant. Therefore, one sees that the predicted quality factor $Q \sim W/\Delta W \sim \sigma$. This is an example of dissipation dilution, which we referred to more coneptully earlier in this chapter. With this established formalism, we can introduce the of the dilution factor D_Q has been introduced, which quantifies the strength of this dilution [73]:

$$D_Q = \frac{Q}{Q_{\text{int}}}. \tag{1.46}$$

For mechanical modes without dissipation dilution, $D_Q = 1$. This is the case for resonators without prestress, where the bulk properties of the material dominate.

1.7 Origins of internal loss

Up to this point, we have provided a generalized model for the internal losses in a mechanical resonator in a manner that is agnostic to the fundamental sources of this loss. Here we will provide a brief overview of the known internal loss mechanisms in silicon nitride micromechanical resonators.

If the reader wishes for a very extensive and modern overview of this area, we encourage reading the thesis of Tsaturyan [78]. The first loss we will discuss is thermoelastic damping (TED). TED relates to how the material expands and contracts during motion. Any material with a finite coefficient of material expansion α_{th} changes its shape in response to a change in temperature. The converse is also true, changes in the shape of an object induce gradients of temperature in the object. These gradients of temperature mean that the motion of the resonator brings the system out of equilibrium, generating heat, and in turn leads to dissipation. This phenomenon has been modeled and studied heavily in the context of resonators originating from silicon nitride membranes [78, 79]. In the regime of resonators studied in this work, TED is not the leading source of loss and can be ignored. TED may become important to consider in the limit of thicker membrane films, as well as higher frequency mechanical resonators with resonant frequencies exceeding 10 MHz.

The main source of intrinsic losses in silicon nitride membrane resonators is surface losses. This has been established by many works, as tabulated in the overview article by Villanueva and Schmid, where quality factors dependence of devices with varied surface-to-volume ratios were studied [80]. They found that devices with larger surface-to-volume ratios exhibited higher loss, indicating that surface losses dominated most of the devices studied. To date, the origin of these surface losses is still unknown, although surface roughness and chemical impurities are promising candidates to explain the observed increase in loss at the surface of the silicon nitride membrane. Chemical treatments of the surface have been performed to improve the loss, but to our knowledge, all either leave the loss unaffected or increase the effect [81].

To account for the effects of surface loss, a phenomenological Q_{int} can be introduced that depends on the material thickness [80]:

$$Q_{\text{int}}^{-1}(h) = Q_{surf}^{-1} + Q_{vol}^{-1} = (\beta h)^{-1} + Q_{vol}^{-1} \tag{1.47}$$

with Q_{vol}= 28000 ± 2000 and $\beta = 6 \times 10^{10} \pm 4 \times 10^{10}$ m^{-1}. Here we bring to light a technical note concerning the use of Q_{int} in all formulas and calculations in this work, rather than using the more physical imaginary part of the Young's modulus E_2. In principle, it would be possible to use E_2, but in the case of surface loss this would require introducing a spatially dependent E_2 that is much higher near the surface of the nitride as opposed to the bulk.

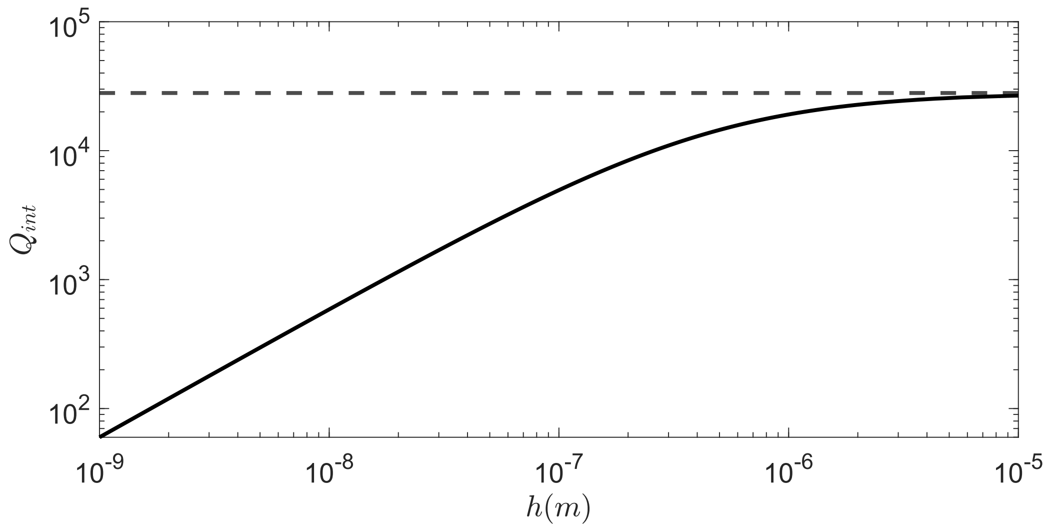

Figure 1.4: Functional form of Q_{int} as a function of membrane thickness. Dashed line indicates the bulk limit of Q_{vol}

Fig. 1.4 plots the functional form of this phenomenological Q_{int}. We see that for most typical membrane thicknesses used for silicon nitride ($h < 400$ nm) surface losses dominate the intrinsic dissipation and that overall silicon nitride is effectively more lossy for thinner membranes. Counter-intuitively, this actually doesn't mean that thinner silicon nitride membranes have higher dissipation overall. This can be seen in the form of Eq. 1.44, where we see that there is more loss associated with thicker nitride given the explicit z dependence on the bending. In fact, for a membrane, we can see this in an analytical result for the quality factor [48]:

$$Q_{mem} = \frac{1}{\lambda} Q_{\text{int}} \left(\underbrace{1}_{\text{clamp}} + \underbrace{\lambda \frac{(n^2 + m^2)\pi^2}{4}}_{\text{sinusoidal}} \right)^{-1} \tag{1.48}$$

where $\lambda = h\sqrt{E/3(1-\nu^2)\sigma l^2}$, n and m are the mode indices for (n,m) membrane modes and l is the membrane side length. Here, the contributions from integrating over the clamping region near the boundary, and the interior sinusoidal region of the membrane mode are explicitly labeled. For high aspect ratio, high-stress membranes, $\lambda \ll 1$ so $Q_{mem} \approx Q_{\text{int}}/\lambda$. This means that silicon nitride membrane modes (for low values of n and m) have their dissipation dominated by the bending at the edge of the membrane near the clamped boundary. For surface loss dominated $Q_{\text{int}} \sim h$, which means that Q_{mem} has no dependence on thickness. On the other hand, if (n and m) are large, then the sinusoidal term dominates. Notably, in this limit, $Q \sim h^{-1}$, meaning that the higher order modes of thinner membranes should have higher quality factors. This scaling is favorable for applications where low effective mass resonators are also desired since the mass also decreases linearly with the thickness.

1.8 Gas damping of micromechanical resonators

A ubiquitous source of loss of any mechanical resonator is due to interactions between the resonator and its gaseous environment. At atmospheric pressure and low vacuum, the damping arises from purely viscous forces between the resonator and the surrounding air [82]. In this work, we operate all experiments at some level of high vacuum. At these pressures, the gas does not act as a fluid and therefore doesn't exhibit viscosity. In this regime — the molecular regime — the gas transfers energy to and from the mechanical resonator through singular collisions. This model of the gas is valid as long as the mean free path of gas molecules is longer than the length scale of the mechanical structure [82]. For a 1 mm membrane, this would be around 10^{-3} mbar. In this regime, an estimate for the gas-damped quality factor Q_{gas} is given as [82]:

$$Q_{gas} = \sqrt{\frac{\pi}{32}} \frac{\rho \omega_m}{p} \frac{k_B T}{m_{gas}} \tag{1.49}$$

where m_{gas} is the mass of a single gas molecule and p is the pressure. Fig. 1.5 shows the dependence on Q_{gas} on pressure p. We note that in principle, the effects of gas damping can depend heavily on device geometry, and this calculation is meant to give a sense of scale for a proper vacuum in which to perform experiments with low intrinsic dissipation mechanical devices. For instance, to our knowledge the highest Q micromechanical resonator operated at room temperatures have Q

exceeding 10^9 [1], meaning that pressures less than 10^{-7} mbar are required for the operation of the state of the art resonators. These constraints are relaxed for higher dissipation mechanical modes. In principle, the effects of gas damping can be verified by measuring the dissipative properties of each mode as a function of vacuum pressure and then operating the experiment in a regime where gas damping is relatively negligible.

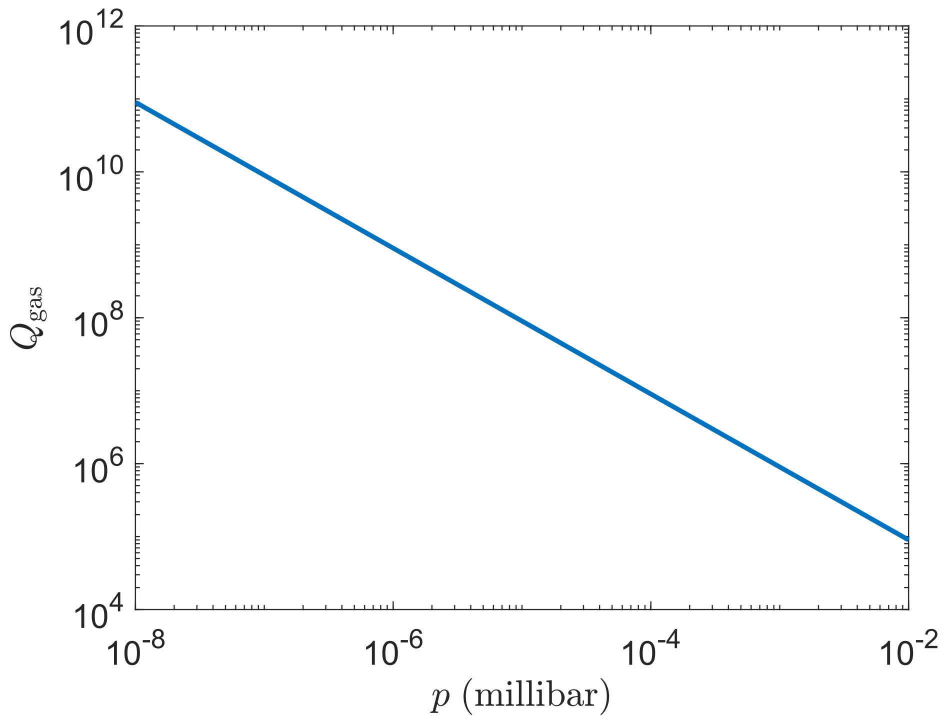

Figure 1.5: Q_{gas} for a device with $h = 100$ nm, $\omega_m = 2\pi \times$ 1MHz, and $m_{gas} = 30$ atomic mass units.

1.9 Radiation losses

Another loss channel for micromechanical resonators relates to the coupling between a mechanical mode and the support structure housing the mode. Up to this point, we have implicitly neglected this form of loss by only examining a mechanical mode shape within a simple membrane structure while imposing strict boundary conditions at the edge of the space we wish to analyze. In reality, the mechanical mode shape exists outside of this region, making this assumption of a clamped boundary condition invalid, albeit accurate enough for most situations. This is because there is typically a large impedance mismatch at the interface between a high aspect ratio membrane and the supporting substrate, which mimics a strict clamped boundary condition. However, there is a finite impedance within the substrate, so in general, the mode shape does have a small motion beyond the membrane. The effects of the mechanical mode in question coupling to the surrounding support structure or substrate is often called radiation loss or phonon tunneling loss [55].

Predicting the effects of radiation loss on overall dissipation is a complicated endeavor. The naive, brute-force way of tackling the problem would be to simply expand the analysis or simulation space to include more of the support structure for the mechanical device. By including more of the true mechanical mode shape in the analysis space, one can predict the losses that arise from participation in the support structure by the methods described previously for calculating material losses, given that the necessary material properties are known. This method is impractical for a few reasons. Firstly, it is either computationally expensive if one wishes to simulate the problem, or is analytically complicated if one wants to solve from first principles. Secondly, it would require precise knowledge of the mounting structure of a mechanical device within the apparatus, knowledge that is not readily available.

Simulation of the entire device including its support structure can be thought of as working in the true normal mode basis of a coupled system of resonators. We can relax the analysis by working in the original basis, where there are modes of the device that are coupled to modes of the support structure. This is more attractive in that it allows for a more generic analysis, where precise knowledge of the support structure is not needed. Here, we are concerned about both spectral and spatial overlap between the device modes and the support structure modes [83]. However, this picture still requires previous knowledge or some assumptions about the mode structure of the supports. This analysis can also be avoided for structures with highly localized mechanical modes, such as those found in the phononic crystal resonators discussed in Ch. 4. In this case, the lack of energetic participation at the membrane edge obviates the need to analyze the substrate in detail.

Another approach is to assume that there exists a layer of perfectly absorbing material called a perfectly matched layer (PML) at some location in the support structure [52]. Conceptually, this mimics coupling to an infinite acoustic waveguide, which would introduce dissipation since coupling to the infinite waveguide corresponds to energy leaking out of the mechanical mode. The introduction of the PML is an accurate model of radiation loss in the limit that the substrate is much larger than the acoustic wavelength, as this mimics mechanical radiation into an infinite medium. Often for normal substrate sizes (on the order of 1 cm), the substrate modes around 1 MHz or so contain reflections off of the substrate surfaces, and therefore a PML does not necessarily quantitatively predict the effects of radiation loss. Another generic model of radiation losses without introducing large levels of computational complexity is to model the support structure with an array of lossy springs [55]. This does not require an expansion of the simulation or analysis space.

Overall, the effects of radiation loss are quite complicated but cannot be ignored. This often manifests as a mounting-dependent quality factor, where the highest Q (lowest radiation loss) results are obtained when the mounting is the most "weak", or when the amount of contact area between the mechanical substrate and the rest of the apparatus is minimized. This weak mounting condition is often not attractive for other reasons, including mechanical and temperature stability. This, along with the desire for higher Q mechanical modes has brought forth a wealth of approaches that seek to minimize the coupling between the mechanical mode of interest and the modes of the environment [49, 84–86].

Chapter 2

Mechanical readout with Michelson Interferometers

This chapter will discuss mechanical displacement detection with a Michelson interferometer. Although such an instrument was first utilized over one century ago, it is still a remarkable tool even in the modern day, forming the basis for the first observation of gravitational waves [87, 88]. Here, we will also discuss its utility for a variety of optomechanics experiments. Given our group's previous and continued use of high-finesse optical cavities in a variety of experiments, we will motivate our in-depth investigation of this alternative form of mechanical readout.

High-finesse optical cavities are championed as precision displacement detectors through a dispersive coupling between the optical cavity resonant frequency and the mechanical motion of dielectric in the optical mode of the cavity [34]. This dispersive coupling can also be interpreted as a motion-induced phase shift of a near-resonant cavity probe tone. Since this phase shift is linearly proportional to the cavity finesse, one would assume that high-finesse cavities are necessary for precision readout of mechanical motion [67]. However, in this section we will prove that a Michelson interferometer is capable of reaching the standard quantum limit (SQL) of mechanical displacement detection for modern mechanical resonators, thus making it an attractive alternative to cavity-based readout.

Michelson interferometers also provide a host of practical advantages over cavity-based interferometers. High-finesse optical cavities are resonant objects that typically require large degrees of stabilization for implementation in optomechanical experiments. This stabilization presents many technical challenges. A concrete example is the use of an optical cavity in a closed-cycle cryostat.

These systems typically have moving parts as required by the cryogenic refrigeration cycle, thus leading to vibrations of the optomechanical system affixed to the baseplate of the cryostat. If these vibrations create acceleration noise, leading to cavity-frequency fluctuations exceeding the cavity linewidth, then locking the cavity becomes exceedingly difficult or impossible. Thus much care needs to be taken in order to operate high-finesse optical cavities in these systems. There are engineering challenges associated with vibrational noise change when considering a Michelson interferometer in the same situation. Now, one is mostly concerned with the relative displacement noise of the device with a reference point on the optical table. In order for stable operation, this relative displacement noise needs to be on a scale less than the optical wavelength used in the experiment, which is a less stringent requirement than prescribed by a high-finesse cavity.

Another advantage of using a Michelson interferometer for mechanical readout is the relative ease with which one can address the mechanical resonator. To couple a Fabry-Perot cavity to a mechanical resonator, one needs to precisely reference the two cavity end mirrors and the mechanical device. This task becomes even more difficult when also requiring a fairly small optical spot size. Also, Fabry-Perot optical cavities should be constructed in as rigid a manner as possible in order to increase their stability. Practically speaking, this enforces a single probe location of the optical spot once the cavity is assembled, limiting the flexibility of the measurement. This fixed configuration can also lead to technical challenges associated with thermal expansion and contraction of the cavity assembly, where the optical spot can move when subjecting the device to cryogenic conditions, potentially leading to sub-optimal measurements of mechanical motion. None of these technical issues apply to Michelson interferometers, since the alignment can be carried out with free-space optics at room temperature. Thus, Michelson interferometers are easy to use and implement for experiments with fast device turn around, or experiments where vibrations are expected.

It is worth discussing the Michelson interferometer in the context of other optical interferometers. One technique of note is the use of an etalon made from the planar mechanical device in question and a partially reflecting mirror. When working with fixed-frequency laser sources, it is often necessary to allow for direct control of the interferometer arm lengths, or in the case of the etalon, the etalon length. Such control affords flexibility in the measurement process, as well as calibration of power fluctuations to mechanical displacement. For Michelson interferometers, the arm paths present in atmospheric pressure typically require active feedback in order to stabilize the arm lengths relative to one another. Etalons provide potential advantages since the two interfering paths exist in a vacuum, and therefore are not susceptible to disturbances arising from air currents, allowing for feedback-free operation of these interferometers. However, there are experimental difficulties associated with the operation of these etalons. In order to achieve optimal performance, the membrane and mirror surface should be nearly parallel in order to ensure the maximal visibility of the interferometer fringe. Therefore, each assembled etalon needs to be carefully constructed in order to minimize any tilt. This susceptibility to tilt becomes more problematic under cryogenic conditions due to the differential thermal expansion of materials during a cool-down. A Michelson avoids this issue of tilt since the local oscillator can always be realigned in order to ensure optimal mode matching to the reflected probe beam.

2.1 Theoretical description of the Michelson interferometer

Here we present a theoretical discussion of the operating principles of a Michelson interferometer. Such an interferometer comprises two arms over which a differential optical phase will be accumulated. For the purpose of detecting micromechanical motion, the end mirror of the signal arm will be a micromechanical membrane or any mechanical object that reflects the probe light. Therefore, the motion of the mechanical device in question will modulate the optical path length of the signal arm, thus changing the phase accumulation of light that passes through that arm of the interferometer. To read out this optical phase, this light can be compared to a reference arm, often called a local oscillator. The optical path length of this arm can be considered to be constant in time, and therefore the phase difference between the signal optical field and the local oscillator field will contain information about the motion of the mechanics. This phase difference can be transduced to a changing optical power via interference between the two fields.

For all Michelson interferometers in this work, the splitting of the signal and local oscillator

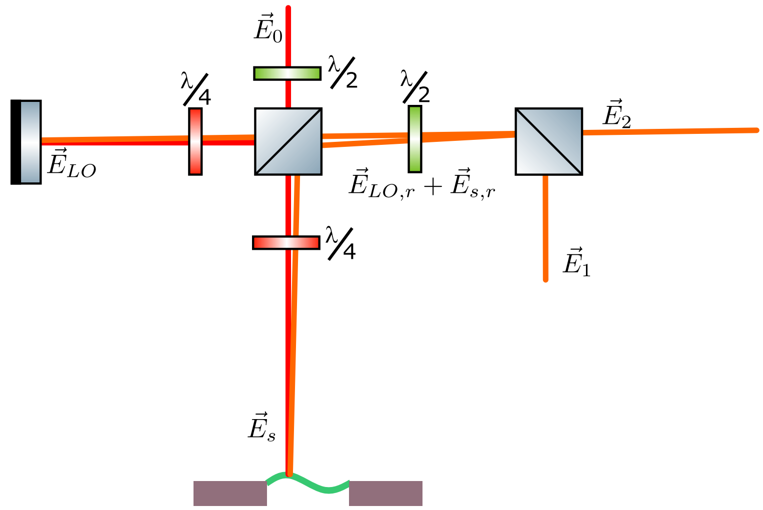

Figure 2.1: Basic diagram of a Michelson interferometer using a polarizing beamsplitter to split and combine the two arms of the interferometer. Quarter waveplates (shaded red) are placed into both the signal and local oscillator arms in order to direct the reflected light to the output port of the polarizing beam splitter. The sum of the reflected fields is then rotated and split again on an additional beam splitter in order to interfere the two beams.

fields, as well as their subsequent recombination, was performed with a polarizing beam splitter. This can in principle be accomplished with non-polarizing beam splitters with the cost of wasted optical power. A classical description of this problem begins with considering the electric field at each part of the interferometer. Fig. 2.1 outlines the electric fields of interest. The relative field amplitude of $\vec{E}_{LO}$ and $\vec{E}_s$ – the local oscillator and signal electric fields respectively – can be controlled via a rotation of a half-wave plate at the entry port of the interferometer.

The explicit fields are written as:

$$\vec{E}_0 = E_0 \hat{x} \tag{2.1}$$

$$\vec{E}_{LO} = E_0 \cos(2\theta_{\mathrm{sp}}) \hat{y} \tag{2.2}$$

$$\vec{E}_s = E_0 \sin(2\theta_{\mathrm{sp}}) \hat{x} \tag{2.3}$$

$$\vec{E}_{LO,r} = e^{i\phi_{LO}} E_0 \cos(2\theta_{\mathrm{sp}}) \hat{y} \tag{2.4}$$

$$\vec{E}_{s,r} = e^{i\phi_s} r_m E_0 \sin(2\theta_{\mathrm{sp}}) \hat{x} \tag{2.5}$$

where E_0 is the input electric field amplitude, θ_{sp} is the angle between the fast axis of the half wave plate and the plane of the optical table. $\hat{x}$ and $\hat{y}$ denote the direction of S and P polarized light respectively. ϕ_{LO} and ϕ_s are the accumulated optical phases of the electric field corresponding to the optical path lengths of the local oscillator and signal arms respectively. r_m is the reflectivity coefficient of the membrane being probed. We note that for the sake of this discussion, r_m can be considered to be real-valued.

At the output of the interferometer, the two electric fields are spatially overlapping, but have orthogonal electric fields, and thus cannot interfere. By rotating the polarization of the output field of the PBS by 45 degrees and subsequently splitting that light onto an additional PBS, one can calculate the output fields of the second PBS as:

$$\vec{E}_1 = \frac{E_0}{\sqrt{2}}\left(e^{i\phi_s} r_m \cos(2\theta_{\text{sp}}) - e^{i\phi_{LO}} \sin(2\theta_{\text{sp}})\right)\hat{y} \tag{2.6}$$

$$\vec{E}_2 = \frac{E_0}{\sqrt{2}}\left(e^{i\phi_s} r_m \cos(2\theta_{\text{sp}}) + e^{i\phi_{LO}} \sin(2\theta_{\text{sp}})\right)\hat{x}. \tag{2.7}$$

Once the fields are known, it is possible to then calculate the intensity of the beam by $I \propto |\vec{E}|^2$. Often we are concerned about the total power in the beam, which corresponds to an integral over the intensity over the plane transverse to the optical axis. Therefore, we can assume that $P_i \propto |\vec{E}_i|^2$ at all points in the optical system. In addition, the proportionality constant should be the same everywhere as long as the entire Gaussian beam profile is integrated over. Furthermore, we will now parameterize these two powers in terms of the reflected power from the membrane $P_{s,r}$ and the reflected power from the local oscillator P_{LO}. Therefore, one can then calculate the optical power exiting the second PBS:

$$P_1 = \frac{1}{2}\left(P_{LO} + P_{s,r} - 2\eta\sqrt{P_{LO}P_{s,r}}\cos(\phi_{LO} - \phi_s)\right) \tag{2.8}$$

$$P_1 = \frac{1}{2}\left(P_{LO} + P_{s,r} + 2\eta\sqrt{P_{LO}P_{s,r}}\cos(\phi_{LO} - \phi_s)\right) \tag{2.9}$$

$$. \tag{2.10}$$

Both P_1 and P_2 have a term that depends on the phase difference of the two arms, which is the mechanism through which the interferometer can transduce the motion of a mechanical oscillator to a modulation of optical power. We have added included a mode-matching efficiency parameter $\eta \in [0, 1]$ which quantifies the spatial overlap between the reflected beam from the device and the local oscillator. The translation from optical phase to motion can be understood by calculating the optical path length as a function of the membrane motion:

$$\phi_s = 2\left(\frac{2\pi L_s(t)}{\lambda}\right) = \frac{4\pi(L_0 + x(t))}{\lambda} \tag{2.11}$$

where $L_s(t)$ is the physical length of the signal arm, and λ is the wavelength of the laser light used in the interferometer. We make the time-dependent part of the arm length explicit by setting $L_s(t) = L_0 + x(t)$, where $x(t)$ is the motion that we wish to probe and L_0 is the equilibrium length of the arm. For all discussions to follow, $x(t) \ll \lambda$, and therefore allows for a small signal analysis of the system when needed. There is an overall factor of 2 in this formula since the arm is traversed twice by the laser beam on the forward and backward journeys through the system.

We can first assess the performance of the system in the simplest case where one reads out either P_1 or P_2. We note here that this would correspond to a Michelson interferometer which uses a 50:50 non-polarizing beam splitter in the same geometry as shown in Fig. 2.1, and is therefore worthy of discussion. When examining this case, we will define the sensitivity parameter ζ:

$$\zeta \equiv \left|\frac{dP}{dx}\right|\Big|_{x=0} \tag{2.12}$$

which in this case is:

$$\zeta_{\text{single}} = \left|\frac{dP}{dx}\right|\Big|_{x=0} = \frac{4\pi}{\lambda}\eta\sqrt{P_{LO}P_{s,r}} \tag{2.13}$$

where L_{LO} is the arm length of the local oscillator. In order to maximize the sensitivity, the arm lengths can be adjusted such that $L_{LO} - L_0 = n_i\lambda/8$ where $n_i \in \mathbf{Z}$. Similarly, it is apparent that θ_{sp} should be a multiple of $\pi/8$, meaning that optimal sensitivity is achieved when the input power to the interferometer is evenly split between the two arms. The matching of the arm lengths can be achieved via active control over the local oscillator length.

As will be discussed later, it is often advantageous to perform this measurement in a balanced manner. That is, one will read out a signal that corresponds to $P_2 - P_1$. This can be achieved with a balanced photodetector whose photodiodes are wired in series. When wired as indicated in Fig. 2.2, the output of the circuit will have a voltage that is proportional to the photocurrents – and in turn the optical powers – of the two photodiodes.

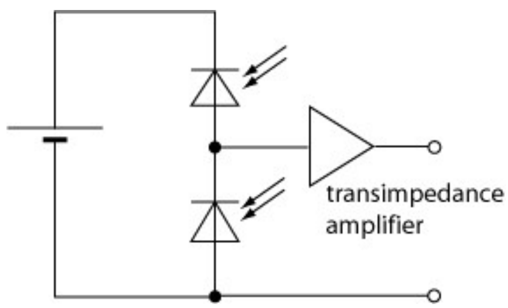

Figure 2.2: Basic schematic of a balanced photodetector taken from the RP Photonics encyclopedia [2]. As wired, the current towards the transimpedance amplifier is the difference between the photocurrents produced by the two photodiodes.

For this configuration, the sensitivity parameter becomes:

$$\zeta_{\text{bal}} = \frac{8\pi}{\lambda}\eta\sqrt{P_{LO}P_{s,r}}, \tag{2.14}$$

which is just $2\zeta_{\text{single}}$. This arises from the fact that the balanced detector uses all of the optical power in the interferometer by measuring both P_1 and P_2.

2.2 Michelson interferometer signal to noise

To this point, the current discussion has focused on the transduction of mechanical motion to an optical field with a corresponding intensity fluctuation. Any such interferometer will have some sort of noise. In the context of optomechanical systems, the fundamental noise source comes from the quantum mechanical nature of the optical fields used to read out the motion [89]. Notably, it is the random distribution of the optical field photons that gives rise to the two fundamental sources of noise. Firstly, there is the photon shot noise that occurs during the detection of the optical fields. The random arrival of the optical photons generates a random fluctuation of optical power. For interferometers, this noise is often referred to as imprecision noise, a convention that we will use in this work. Secondly, the same random occurrence of optical photons gives rise to radiation pressure shot noise (RPSN) which applies a random force to the mechanical resonator, which necessarily changes its state of motion. This noise is often referred to as the back-action noise.

Here we present a mathematical description of these two noise terms. For imprecision, one can understand the effective noise by first understanding the optical shot noise. The spectrum of shot noise is:

$$S_{PP} = 2h\nu\bar{P} = \frac{2hc}{\lambda}\bar{P}. \tag{2.15}$$

Here, h is Planck's constant, ν is the optical frequency of the light used in the measurement, c is the speed of light, and $\bar{P}$ is the average optical power in the optical field incident on the detector used in readout. The optical power fluctuations can be related to fluctuations in mechanical motion with the sensitivity parameter of the interferometer:

$$S_{xx,\mathrm{imp}} = \frac{S_{PP}}{\zeta^2}. \tag{2.16}$$

We note here that the imprecision noise floor is white in frequency due to the flat response of the interferometer to mechanical motion. This is in stark contrast to the imprecision noise floors seen in optomechanical systems involving high finesse optical cavities coupled to mechanical resonators. In that scenario, the finite linewidth of the cavity adds a frequency dependence to the imprecision noise floor.

Clearly, Eq. 2.16 depends on the interferometer sensitivity ζ, which depends on the distribution of power in the arms of the interferometer:

$$S_{xx,\text{imp}} = \frac{c\lambda\hbar}{16\pi\eta^2}\frac{P_{LO}+P_{s,r}}{P_{LO}P_{s,r}}. \tag{2.17}$$

An examination Eq. 2.17 indicates that for a fixed amount of input optical power, optimal imprecision is achieved when the reflected signal power and the local oscillator power are balanced ($P_{LO} = P_{s,r}$):

$$S_{xx,\text{imp}}^{(P_{LO}=P_{s,r})} = \frac{c\lambda\hbar}{8\pi\eta^2}\frac{1}{P_{s,r}}. \tag{2.18}$$

When this is the case, we can readily see a $1/P$ scaling in the imprecision, as is expected for shot-noise-limited measurements. Another limit to examine is the limit of high local oscillator power ($P_{LO} \gg P_{s,r}$), which is typically used for optical homodyne measurements [90]:

$$S_{xx,\text{imp}}^{(P_{LO}\to\infty)} \approx \frac{c\lambda\hbar}{16\pi\eta^2}\frac{1}{P_{s,r}}. \tag{2.19}$$

For optimal measurements of mechanical motion, the effects of measurement backaction must be accounted for. The backaction noise can be calculated first by identifying the radiation pressure force on the mechanical device. An arbitrary optical force on the membrane is given by:

$$F_{opt} = \frac{2P_{ref}+P_{abs}}{c}. \tag{2.20}$$

where P_{ref} is the power of the reflected light and P_{abs} is the power of absorbed light. The factor of 2 preceding P_{ref} arises from the presence of an incoming and reflected light field. This is equivalent to a picture where a reflected photon imprints an impulse that corresponds to twice its incoming momentum. For devices fabricated from LPCVD stoichiometric silicon nitride membranes as studied throughout this work, the optical absorption can be neglected when calculating the radiation pressure force on the membrane.

From here, one can readily derive the backaction force spectral density:

$$S_{FF,\text{BA}} = \frac{4}{c^2}S_{P_{s,r}P_{s,r}} = \frac{16\pi\hbar}{c\lambda}P_{s,r} \tag{2.21}$$

Once calculated, one can evaluate the performance of the interferometer with respect to a generalized Heisenberg uncertainty relation as defined in [67] as:

$$S_{FF,\mathrm{BA}} S_{xx,\mathrm{imp}} \geq \hbar^2. \tag{2.22}$$

Note that Eq. 2.23 this uncertainty is presented when using single-sided spectral densities. This inequality encodes a key idea in the quantum-limited measurement of mechanical systems, in that there will always be a trade-off between how precisely the system measures the motion (minimizing $S_{xx,\mathrm{imp}}$) and how strongly the system perturbs the system ($S_{FF,\mathrm{BA}}$). This is readily seen by observing the functional forms of these aforementioned spectral densities with respect to power. Notably, $S_{xx,\mathrm{imp}}$ scales as P_0^{-1}, while $S_{FF,\mathrm{BA}}$ scales as P_0.

In our case, this inequality reads:

$$S_{FF,\mathrm{BA}} S_{xx,\mathrm{imp}} = \frac{\hbar^2}{\eta^2}\left(1 + \frac{P_{s,r}}{P_{LO}}\right) \geq \hbar^2. \tag{2.23}$$

Here, we have rewritten this formula in terms of in terms of the reflected power off of the membrane $P_{s,r}$ and the local oscillator power P_{LO}. The presence of the reflected power in the signal arm denotes the fact that the transmitted power through the membrane imparts no backaction, and therefore there is no penalty associated with not collecting that energy for the final measurement. With this in mind, it is apparent that the SQL can be saturated in this system in the limit of infinite local oscillator power, and ideal efficiency $\eta = 1$. This limit of arbitrarily high local oscillator power is typically assumed in optical homodyne measurements in order to reach optimal signal-to-noise ratios [90]. Furthermore, we should remind the reader that there was an assumption of zero optical absorption in the membrane. In principle, optical absorption would prevent saturation of the SQL since absorbed light imparts backaction but provides no signal.

The SQL can be calculated by finding the minimum of the added noise in the system. As revealed above, the SQL is saturated in the limit of large local oscillator power. To calculate the total added noise. We can calculate this by thinking about our interferometer as a displacement detector with a noise floor defined as the sum of the imprecision noise and backaction motion. To find the backaction motion, one needs to calculate the response of the mechanical oscillator to the backaction force:

$$S_{xx,\mathrm{BA}} = S_{FF,\mathrm{BA}}|\chi_m(\omega)|^2 \tag{2.24}$$

where here χ_m is the mechanical susceptibility of the oscillator being probed. Therefore the total added noise in the system is:

$$S_{xx,\mathrm{add}}(\omega) = S_{xx,\mathrm{BA}}(\omega) + S_{xx,\mathrm{imp}}(\omega). \tag{2.25}$$

We have added the frequency dependence back in here to emphasize that the noise floor of the system has spectral dependence. For simplicity, we will analyze the added noise on mechanical resonance since this is germane to most discussions of mechanical detection. Given the previously examined functional dependence on optical power for each term, $S_{xx,\mathrm{add}}(\omega)0)$ is minimized when $S_{xx,\mathrm{BA}}(\omega_0) = S_{xx,\mathrm{imp}}(\omega_0)$. This condition reveals both the noise floor at the SQL as well as the optical power required to measure at the SQL:

$$S_{xx,\mathrm{add},min}(\omega_0) = \frac{1+\eta^2}{\eta}\frac{\hbar}{m\gamma\omega_0} \geq \frac{2\hbar}{m\gamma\omega_0} = S_{xx,zp}(\omega_0) \tag{2.26}$$

$$P_{SQL} = \frac{cm\gamma\lambda\omega_0}{16\pi\eta} \tag{2.27}$$

We see that the added noise depends on the efficiency of the mode matching between the two beams. In principle, other sources of loss could also lead to inefficiencies with the measurement. We see that in the limit of an ideal measurement ($\eta = 1$), the lower limit of this added noise matches that of the zero point fluctuation power spectral density $S_{xx,zp}$ as discussed in [67]. We would like to remind the reader that the expression for P_{SQL} is the amount of power reflected from the membrane required to reach the standard quantum limit. We have already assumed a limit of large local oscillator power, and therefore the total amount of laser power in the interferometer required to reach this limit will be higher.

As stated previously, it is often experimentally more convenient not to minimize the total added noise of the interferometer, but rather to operate the point of highest ζ, which corresponds with the interferometer fringe visibility. In this work, this will be the case unless otherwise stated. It should be noted that the expression for the minimum added noise in this limit is only slightly different than what is shown in Eq. 2.26:

$$S^{(\mathrm{balanced})}_{xx,\mathrm{add},min}(\omega_0) = \sqrt{2}\frac{1+\eta^2}{\eta}\frac{\hbar}{m\gamma\omega_0} = \sqrt{2}S_{xx,\mathrm{add},min}(\omega_0). \tag{2.28}$$

This is achieved at a reflected power of:

$$P^{(\mathrm{balanced})}_r = \frac{\sqrt{2}cm\gamma\lambda\omega_0}{16\pi\eta} = \sqrt{2}P_{SQL}. \tag{2.29}$$

These expressions reveal that for applications where quantum-limited measurements are not a requirement, we can reach very near SQL which is much less total laser power required to perform the measurement, since we do not need to operate in a limit of high local oscillator power.

2.3 Laser phase noise in Michelson interferometers

Up to this point, the analysis of this interferometer has been performed assuming an ideal laser source. This assumes that the optical spectrum of the light field is a delta function peaked at the optical frequency of the laser. However, any laser source will have a finite linewidth due to spontaneous emission of the gain medium used to achieve lasing, written as [91, 92]:

$$\delta\nu_{laser} = \frac{\pi h\nu_{laser}(\Delta\nu_c)^2}{P}, \tag{2.30}$$

where $\Delta\nu_c$ is the laser cavity linewidth. We bring attention to this formula, not for its specific contents, but just as a statement that laser phase noise is fundamental, even in an ideal system. Furthermore, a general laser system will not function ideally and will have additional technical noise. Common sources of this technical noise include vibrational and thermal noise, which induce variations in the resonant frequencies of the laser cavity, which in turn imprints frequency noise on the laser. We remark here that the laser frequency noise has a direct correspondence to its phase noise, owing to the relationship between phase and frequency:

$$\nu(t) = \frac{1}{2\pi}\frac{d\phi(t)}{dt}. \tag{2.31}$$

This relation implies an equivalent relationship between the power spectral densities describing the frequency and phase noise:

$$S_{\nu\nu} = f^2 S_{\phi\phi} \tag{2.32}$$

where f is the spectral Fourier frequency. With these descriptions of laser phase noise, we can analyze their effects on displacement detection in a Michelson interferometer. We will perform this analysis assuming that we are using a balanced photodetector, although identical reasoning can be extended to the unbalanced case. Additionally, we will restrict the analysis to the case where $\theta_{\mathrm{sp}} = \pi/8$. The signal on the balance photodetector will be proportional to $P_2 - P_1$ as defined in Eq. 2.10:

$$P_2 - P_1 = P_0\eta r_m \cos(\phi_{LO} - \phi s). \tag{2.33}$$

The interferometer operates such that the power output is linearly sensitive to the relative phase of the two arms, which is achieved by introducing a phase offset of $\pi/2$ to ϕ_{LO}. In the following discussion, we will encapsulate the length difference of the two arms to a time delay in order to be consistent with discussions of laser phase noise measurements in the literature. Additionally, since we only wish to calculate the effect of laser phase noise, we can neglect the motion of the mechanical oscillator. Therefore:

$$P_2 - P_1 = P_- \approx P_0\eta r_m(\phi_{in}(t) - \phi_{in}(t-\tau)), \tag{2.34}$$

where $\phi_{in}(t)$ is the phase of the light field entering the interferometer, and τ is the time delay between signals sent between the local oscillator and signal arms. We have taken the small-angle approximation, which is valid in the limit of low-phase noise on the laser. In order to calculate the power fluctuations due to phase noise on the interferometer, we first calculate the Fourier transform P_{-}:

$$\tilde{P}_{-}(\omega) = P_0 \eta r_m \tilde{\phi}_{in}(\omega)(1 - e^{-i\omega\tau}) \tag{2.35}$$

where $\tilde{}$ denotes a fourier transform. Therefore, the phase noise-induced noise spectrum is:

$$S_{PP,phase} = |P_0 \eta r_m|^2 \sin^2(\omega\tau/2) S_{\phi,\phi}. \tag{2.36}$$

Here, $S_{\phi,\phi}$ is the phase noise spectrum of the laser. This can in turn can be converted to motional noise via ζ:

$$S_{xx,phase}(\omega) = \frac{\lambda^2}{16\pi^2} \sin^2(\omega\tau/2) S_{\phi,\phi}(\omega) = \frac{\lambda^2}{16\pi^2} \sin^2(\omega \Delta L/c) S_{\phi,\phi}(\omega) \tag{2.37}$$

In the final form of Eq. 2.37, we have converted τ to the physical path length difference ΔL between the two arms. Notably, Eq. 2.37 has no dependence on the optical power used in the interferometer, meaning that it is solely a function of the quality of the laser source as well as the geometry of the interferometer. Here we see that by reducing ΔL close to zero, one can get rid of the effects of laser phase noise on the system. This can be understood since if the two arms have the same length, then the light field is just a delayed copy of the light field at the input, regardless of what arm it traversed. This effect is often used to measure the phase noise of a laser source, where the role of one of the interferometer arms is a delay line which enhances the effect of phase noise [93]. In the case of displacement detection, it is prudent to keep the length of the two interferometer arms as close as possible.

To illustrate this point, we calculate $S_{xx,phase}$ for various path length differences. The results of this calculation are shown in Fig. 2.3, where we assume that the phase noise spectrum has a power law scaling of ω^{-2}, and is -110 dBc/Hz at 1 MHz. The magnitude and functional character of phase noise has been measured for the Nd:YAG laser used throughout this work. A comparison of Fig. **??** and Fig. 2.3 indicates that at a reasonable level of optical power entering the interferometer (1 mW), the phase noise of the Nd:YAG used in this work would only be observable for arm length differences on the order of 1 meter. We emphasize that such length differences are easily avoided via the proper design of the optical system, and for this reason, phase noise was not considered heavily for motional readout in this work.

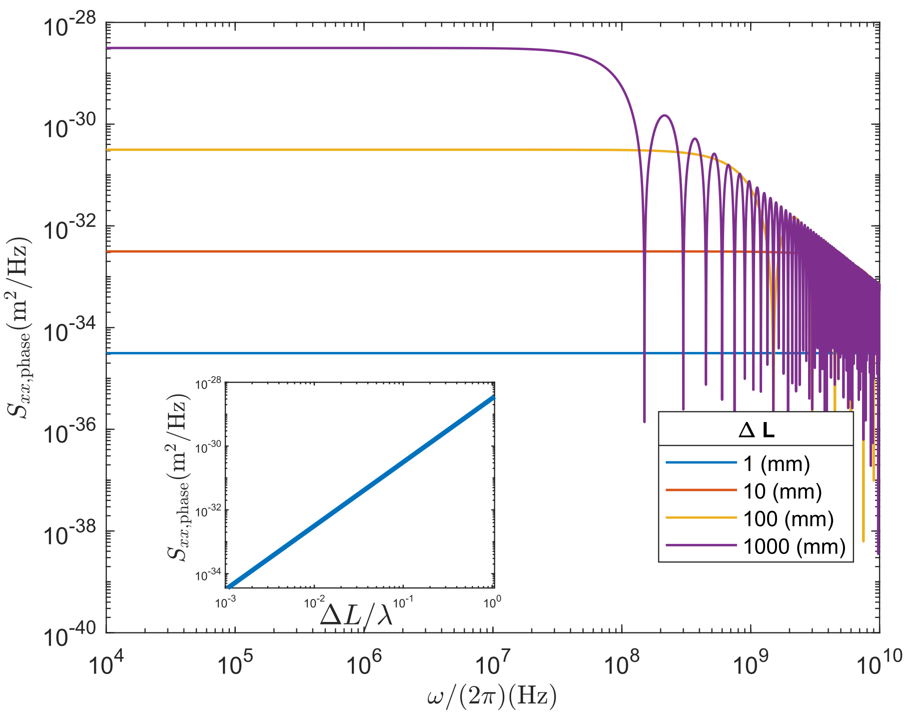

Figure 2.3: Calculated $S_{xx,phase}$ for a Michelson interferometer. (inset) DC phase noise as a function of $\Delta L/\lambda$ where we have assumed λ is 1064 nm. The low-frequency behavior of the phase noise scales as $(\Delta L)^2$.

2.4 Laser amplitude noise in Michelson interferometers

Another source of noise in a laser system is amplitude noise. We have already discussed the fundamental limit of amplitude noise, photon shot noise, which presents itself as a white noise addition to the laser power. Similarly to phase noise, technical aspects of the laser system can produce added noise above the shot noise level. For this reason, noise above the shot noise level is frequently referred to as residual intensity noise (RIN) in the literature. RIN can be described as a classical fluctuation to an otherwise constant power laser field:

$$P(t) = P_0 + \delta P(t) \tag{2.38}$$

Note that in the above equation, $\delta P(t)$ contains contributions from both (RIN) and shot noise. However, both sources are uncorrelated. Hence the amplitude noise spectrum of the laser power will be a sum of the shot noise and RIN spectra. Since RIN is a classical noise source, we consider it to scale linearly with the average power P_0 of the beam. Written directly, $P(t) = P_0(1 + \beta(t))$, for some stochastic function $\beta(t)$. For the sake of this work, $\beta_{rms} \ll 1$. This has direct implications for displacement detection. Consider a system that utilizes a single photodiode to read the optical power from the interferometer. To understand this situation, consider a simplified expression for the output of this interferometer in Eq. 2.10 under this model of noise:

$$P_1 = P_0(1 + \beta(t))(\alpha + \frac{\zeta}{P_0}x(t)) \approx P_0(\alpha + \alpha\beta(t) + \frac{\zeta}{P_0}x(t)) \tag{2.39}$$

The final equality is a good approximation when $\zeta x(t) \ll t$. Recall from Eq. 2.13 that $\zeta \sim P_0$, which means that both the noisy term and the signal term scale as the optical power, meaning that the signal to noise ratio of such a system cannot be improved by increasing the optical power in the interferometer. This contrasts the case of a shot noise-limited interferometer, which has a noise floor that scales as P_0^{-1}. In systems with appreciable RIN, the generic behavior is that at low optical powers, the system will be shot noise-limited. An increase in optical power will eventually lead to a power above which there is no further gain in signal-to-noise ratio. Ideally, one would wish to have a system that is quantum noise limited (shot noise limited). In this work, multiple strategies are employed to reach this regime. Firstly, the use of a balanced photodetector can serve as a common noise rejection of the classical amplitude noise in the system. This can be seen by considering simplified expressions for P_1 and P_2. If P_1 is of the form in Eq. 2.39, it follows that P_2 is written as:

$$P_2 = P_0(1+\beta(t))(\alpha - \frac{\zeta}{P_0}x(t)) \approx P_0(\alpha + \alpha\beta(t) - \frac{\zeta}{P_0}x(t)). \tag{2.40}$$

Therefore, a balanced photodetector which reads $P_2 - P_1 = P_-$ will read:

$$P_- = 2\zeta x(t)(1+\beta(t)) \approx 2\zeta x(t). \tag{2.41}$$

The above expression holds when the balance of power between the two beams going toward the balanced detector is perfect. Any imbalance between these two arms will lead to a leakage of RIN into the measurement. Another strategy to reduce RIN is to actively servo the intensity noise of the laser. Such a servo is commonly referred to as a noise eater for laser systems. Additionally, passing the probe light through a narrow linewidth filter cavity passively filters the RIN at frequencies higher than the linewidth of the cavity. In this work, a combination of these three strategies was employed in order to have shot noise limited displacement detection for frequencies in excess of $\approx$ 80 kHz. The details of this will be discussed in the next section.

2.5 Low imprecision Michelson interferometer

In this section, we will present a detailed overview of a low-imprecision Michelson interferometer. The design of this interferometer was originally intended for mechanical force detection experiments seeking to probe transient forces that act on short time intervals. Since the force acts over a short period of time, the amount of imprecision noise in the measurement bandwidth increases, requiring great care to be taken with the optical readout of the resonator motion. However, the basis of this optical system can be utilized for any experiment, even ones that don't require such a low imprecision noise floor. We also wish for this system to operate on a variety of mechanical devices in cryogenic conditions, making a Michelson interferometer an attractive alternative to optical-cavity-based mechanical readout.

A schematic of the optical system is displayed in Fig. 2.4. For clarity, we will describe the beamline beginning at the laser source, which is a ND:YAG laser. The beam goes through an optical isolator in order to reduce errant reflections back into the laser cavity. The beam is then split into two paths via a PBS. The transmitted path was immediately coupled into a fiber, which could route the beam to arbitrary places on the optical table for testing or optical probing. A more involved path begins with the reflected light from the PBS. The main purpose of this path will be to couple through a filter cavity. In this work, we elect to lock the laser to the filter cavity utilizing the Pound-Drever-Hall locking scheme [94]. A detailed overview of the technique is presented well in other works [95], but for this work, we will remark that a key element of PDH locking is the addition of FM sidebands to the laser. This is typically done in two ways, either by modulating the laser inside the head or by passing the beam through a resonant electro-optic modulator (EOM). In this work, we utilize the latter, as indicated in Fig. 2.4. Since the circuit is resonant, a sufficient modulation index required for the PDH locking technique can be attained via a conventional drive from a typical functional generator.

Following the EOM, the laser beam is shaped by two lenses in order to achieve mode matching with the filter cavity. This cavity is a symmetric, nearly confocal cavity that comprises two curved mirrors. Both mirrors have a radius of curvature (ROC) of 5 cm and form a cavity length of slightly less than 10 cm so as to remain in a stable configuration. The cavity itself is designed to have a linewidth of 50 kHz. The beam shaping was done to have the focus of the focusing lens preceding the cavity coincide with the midpoint of the two mirrors. However, since a confocal cavity has a diffraction-limited waist, the beam was expanded prior to focusing in order to have the smallest spot size possible. In practice, the positions of these two lenses were adjusted in order to maximize the transmission through the cavity. In this work, the maximal achieved transmission was 70 percent, although under normal conditions 50 percent transmission is typical.

Following the filter cavity, the beam is directed through a single-pass acousto-optic modulator (AOM). The beam was aligned as to maximize the deflection into the first diffraction order of the AOM. Modulation of the RF power driving the AOM allows for control of the power deflected into

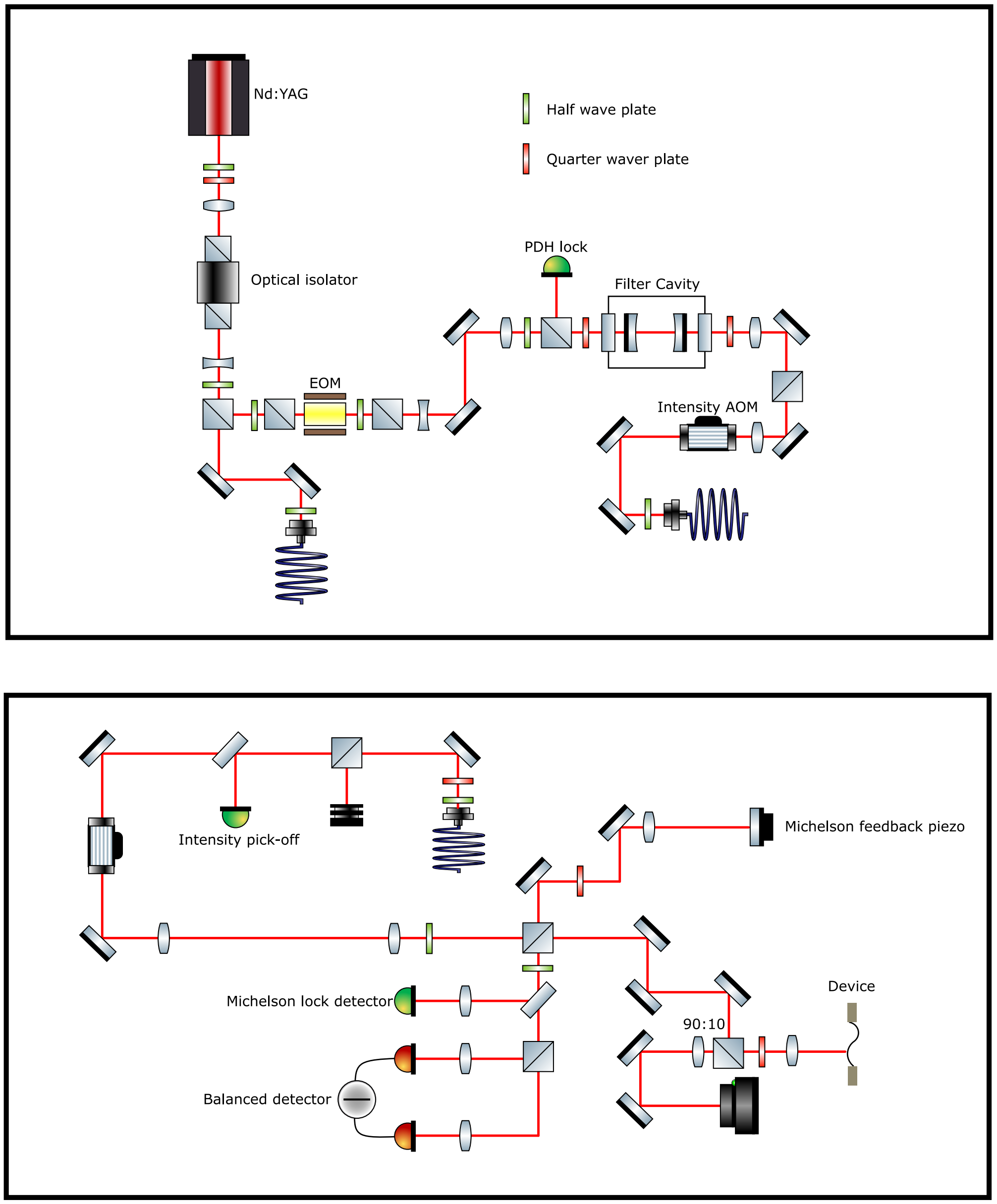

Figure 2.4: Michelson interferometer optical diagram. (Top) Pre-fiber optical apparatus. (Bottom) Optical setup on a raised breadboard that can probe a variety of different samples in both cryostats and vacuum chambers. The AOM appearing in this diagram was used as an optical switch in order to prevent damage to the device when utilizing high laser powers.

the 1st diffraction order. Throughout this work, this modulation was typically used to servo the intensity of the laser beam after it passed through more optical elements. The largest intensity noise source addressed by these servos arises from polarization drifts caused by thermal effects in optical fibers. Although all the fibers used in this work were polarization-maintaining (PM) fibers, these fibers require precise alignment to a specific polarization access in order to maintain an input polarization with high fidelity. Typically, a modest alignment to the key would result in long-term intensity drifts of around 5 percent in the downstream parts of the optical system as polarization imperfections would be transduced into intensity drifts via polarizing elements such as PBSs. The remaining intensity drifts could then be reduced via the AOM intensity servo.

A detailed diagram of an example Michelson interferometer is displayed at the bottom of Fig. 2.4. Again we will describe this setup beginning at the fiber port. This particular implementation had added functionality beyond that of a simple Michelson. Firstly, a monitor of the laser power after the fiber serves as the input signal for the aforementioned intensity servo. After the pickoff, another AOM is present to serve as an optical switch. When large amounts of circulating power are present in the interferometer, it is often prudent to turn off the laser light when not measuring so as to not damage the device in question. Although the occurrence is rather infrequent, devices can become damaged due to the presence of a high-power laser source (10 mW). Although the mechanism has not been systematically identified, we believe that the cause of this damage is most likely due to laser absorption by dust particles that fall onto the membrane device unnoticed, which leads to local heating of the membrane.

Following this optical switch, a telescope shapes the beam for optimal probing of the mechanical oscillator in question. The rest of the setup is the main interferometer as described previously. The main differences consist of an imaging path in the signal arm of the interferometer. Typically this was a simple microscope with a magnification of 4 to 5 which allowed for the location of the probe beam on the device. In order to lock the local oscillator arm-length, a RedPitaya 125-14 FPGA programmed to act as a PI servo is used. One unique aspect of this setup is the use of a separate photodetector as the error signal for this locking circuit. This choice was made in order for the system to handle optical powers up to 20 mW. At this level of power, the peak-to-peak voltage produced by the Thorlabs PDB450C balanced detector would be around 70 V, greatly exceeding the maximum output voltage of the trans-impedance amplifiers for this detector, not to mention it greatly exceeds the maximum voltages of both the RedPitaya 125-14 and the AlazarTech ATS9462 digitizer board used to read the photo signal. Under these conditions, the error signal has strong nonlinear behavior, leading to instabilities in the feedback loop. For this reason, a pickoff of 7 percent of the light was directed toward this separate locking photodetector. The relatively small amount of light on this detector allowed for a more stable lock while at the cost of a small reduction of signal.

In order for the system to be shot noise limited, the shot noise defined noise floor needs to exceed that of the electronic readout chain. In this work, most of the photodiode signals were digitized with an ATS9462 digitizer board. To characterize the noise of this board, one must first understand the noise limitations of an analog-to-digital converter (ADC). The following analysis relies heavily on the tutorial presented by Analog Devices [96].

A basic understanding of the operation of the ADC illuminates the meaning of some of these terms. An ADC maps an analog signal $V(t)$ to a digitized version. This is done with the assumption that the ADC works on a voltage range of signals, referred to as its full-scale voltage or V_{fs}. Under ideal operation, one can describe the resolution of the subsequent digitized signal as $V_{fs}/2^N$, where N is the bit depth of the ADC. One can then analyze the noise floor of the system defined solely by this quantization noise. Under this noise model, the error of each sample amounts to sampling from a uniform probability distribution between the values of $-V_{fs}/2^{N+1}$ and $V_{fs}/2^{N+1}$. One can then calculate the integrated noise power associated with this measurement as:

$$P_{quant} = \int_{-V_{fs}/2^{N+1}}^{V_{fs}/2^{N+1}} V^2 p(V) dV = \int_{-V_{fs}/2^{N+1}}^{V_{fs}/2^{N+1}} V^2 \frac{2^N}{V_{fs}} dV = \frac{1}{12}\left(\frac{V_{fs}}{2^N}\right)^2 \tag{2.42}$$

With the absolute noise power scale calculated, we calculate the associated power spectral density under the assumption that there is no time correlation between samples. This implies that the PSD is white and spread evenly across the Nyquist band of the measurement. Therefore:

$$S_{VV,quant} = \frac{1}{6 f_s}\left(\frac{V_{fs}}{2^N}\right)^2 \tag{2.43}$$

where f_s is the sample rate of the measurement. This functional form of S_{VV} reveals a dependence of f_s^{-1}, meaning that maximal performance can be achieved when using the maximum sample rate offered by the device. For the ATS9462, the maximum sample rate is 180 MS/s, corresponding to a Nyquist frequency of 90 MHz. This greatly exceeds the resonant frequency of any device used in this work, meaning that the best noise performance is obtained at the cost of oversampling the signals in question. This results in larger datasets than are required in principle. In order to alleviate issues associated with the analysis and handling of these large datasets, sub-sampling of the data can be performed. If the sub-sampling is performed by first binning the data and subsequently averaging each bin, this maintains the noise floor of the higher sample rate data while lowering the Nyquist band of the data set.

With this in mind, we can turn our attention to other noise channels associated with analog-to-digital conversion. A main channel of noise is the Johnson thermal noise that occurs within the ADC circuit itself. This can in principle be greater than the quantization noise, limiting the performance. Another source of error in an ADC is harmonic distortion, where a harmonic input signal will have added sidebands after the analog-to-digital conversion. This occurs due to any nonlinearity in the ADC components, and although well-designed ADCs will try to minimize this effect, it does limit the performance of ADCs somewhat. ADC datasheets quantify the magnitude of these two effects with the signal-to-noise and distortion ratio (SINAD). Usually, this quantity is reported in dBc, referencing the power of some input harmonic signal of interest. For the ATS9462 used in this work, the SINAD is specified to be 72.3 dB, measured using a nearly full-scale input signal. To compare this number to the quantization noise, it is often illustrative to convert this SINAD parameter into an effective number of bits (ENOB). The new noise floor can then be calculated using the ENOB instead of the raw bit depth of the ADC, taking into account distortion and other sources of input noise. ENOB and SINAD are related (assuming a fullscale input signal for the SINAD parameter) by [96]:

$$\mathrm{ENOB} = \frac{\mathrm{SINAD} - 1.76}{6.02} \tag{2.44}$$

For the ATS9642, the specified ENOB would then be 11.7. Note that in principle the actual noise floor of the board may differ from this value, and is useful to characterize the card implemented into the experimental apparatus. For instance, one can see how the noise floor of the card changes as a function of the sample rate. An example measurement is presented in Fig. 2.6. By fitting this data, one can extract that the ENOB of the card studied here is 11, slightly worse than what is specified in the datasheet.

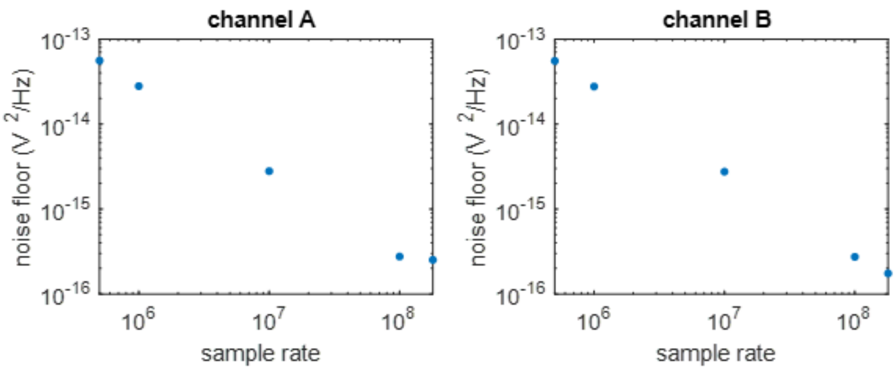

Figure 2.5: Measured electronic noise floor a ATS9462 card. This measurement was performed with the input ports 50 Ω terminated.

However, for most measurements done with this apparatus, this is sufficiently low. To illustrate the point, we can calculate the effects of this ADC noise in terms of position units. For this analysis, we can also consider the effects of detector dark noise in a typical measurement band. We note that in principle both dark noise and ADC noise are electrical in origin, and therefore are first characterized as voltage noise. The conversion of the voltage noise to position noise requires knowledge of the photodetector used to perform the question. The conversion can be calculated with knowledge of the spectral responsivity of the photodetector — the conversion of power to a photocurrent — as well as the trans-impedance gain of the current-to-voltage converter in the photodetector. Finally, this effective power noise can then be converted to position noise through the ζ parameter of the interferometer.

In this work, the PDB450C was utilized for precise measurements of the device motion and will be analyzed in Fig. 2.6. One sees that for the mW scale of input power, the system will be

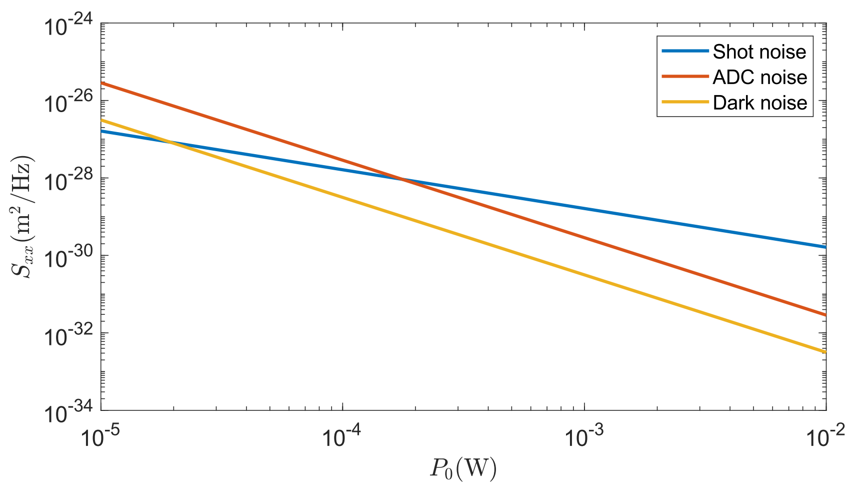

Figure 2.6: Inferred imprecision noise floor due to the various sources as a function of input laser power. This assumes the use of Thorlabs PDB450C balanced photodetector with a gain setting of 10^4. Depending on the level of the signal being probed, the gain can be adjusted accordingly so long as the bandwidth of the detector is sufficient. The level of dark noise observed on the detector used in this work is 10 dB lower than the specification sheet value and is reflected here. The ADC noise is calculated for a 180 MS/s sample rate.

shot noise limited. A technical point concerns the adjustable gain of the PDB450C. At higher gain values, the calculated effect of both ADC and dark noise decreases inversely with the gain, at the cost of the absolute bandwidth of the measurement. In principle, one should use the highest gain possible for the measurement. The ultimate limit of gain is either the required bandwidth — the bandwidth of the photodetector should exceed the mechanical frequency scale being probed — or the fullscale voltage of the ADC.

Now that we have completed the discussion of the electrical noise present in the system, it is prudent to discuss other sources of optical noise. For this system in question, the interferometer arms had roughly equal lengths, and therefore we will neglect the phase noise of the laser. RIN cannot be neglected. Rather, it is a leading source of noise for frequencies below 1 MHz for the Nd:YAG used in this work. We addressed this noise in two ways, through the use of a balanced detector and through passing the probe light through the filter cavity. The effect of the filter can be described as a low-pass filter on the RIN spectrum of the laser. This effect can be seen in Fig. 2.7, where the RIN of the input beam is reduced to the shot noise level of noise above 200 kHz. The insertion of the cavity does produce added noise below the cavity linewidth. This is most likely due to technical noise associated with the PDH locking electronics or phase-to-amplitude noise conversion of low-frequency phase noise. For the measurements performed in this work, this low-frequency sector of the spectrum was not necessary, but care should be taken for probing lower-frequency mechanical oscillators.

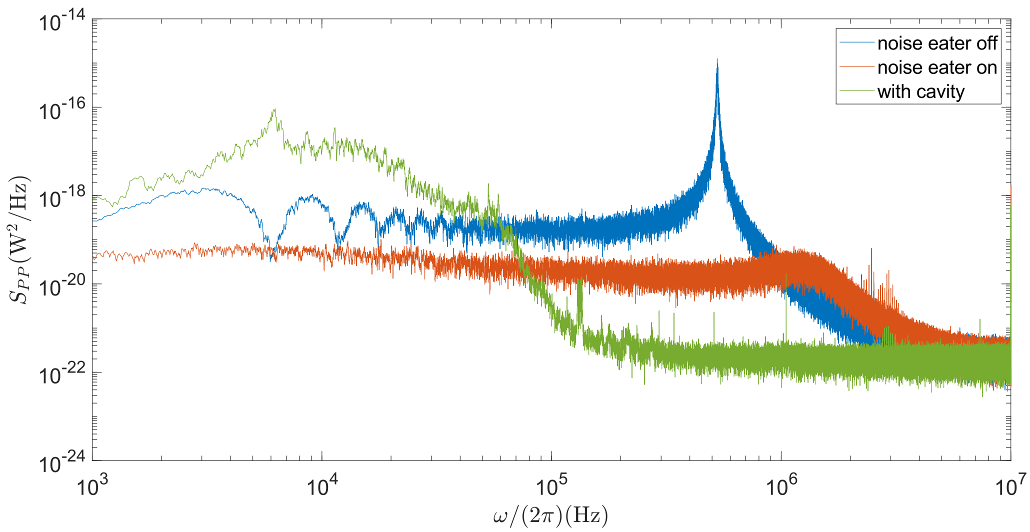

Figure 2.7: Optical spectra before the cavity (with the Nd:YAG noise eater both on and off) and after the cavity for 750 μW of power. With the noise eater off, there is a strong RIN peak around 750 kHz which is strongly suppressed by both the noise eater and the cavity. The filter cavity reduces the noise to the shot noise level for 200 kHz and above.

Fig. 2.7 shows the ability of the filter cavity to reduce RIN at low laser powers. However, at higher laser powers, there will be more RIN than measured here. A balanced detector should take care of the rest. To investigate this effect, one can adjust the relative balance between the two photodiodes. A similar effect can be achieved by changing the setpoint of the Michelson lock. This will cause the local oscillator length to induce an imbalance between the two diodes. The results of such a measurement can be seen in Fig. 2.9 over a broad spectrum. We see that a low frequencies, where there is the highest level of RIN, the absolute noise floor is very sensitive to the balance of the arms. At the highest frequencies, the noise floor is no longer dependent on the arm balance due to shot noise exceeding RIN in this frequency band. We can see that at high levels of RIN, balancing the power onto the two diodes of the balanced detector is paramount to the maximal cancellation of the extraneous noise.

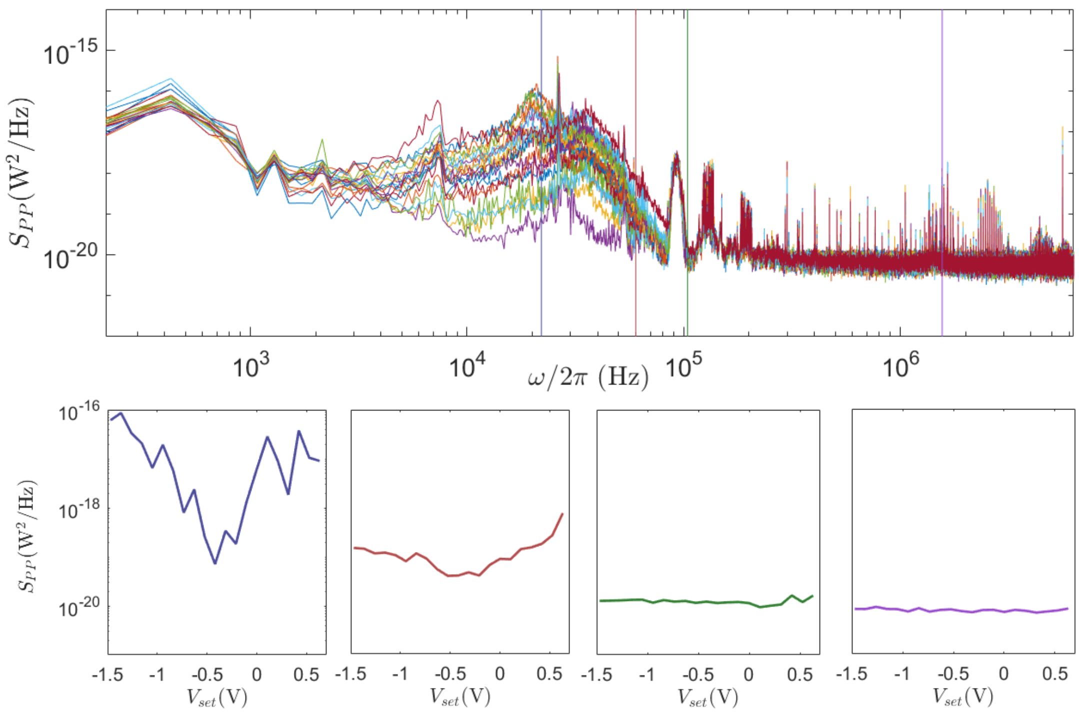

Figure 2.8: Optical power spectra measured by the balanced detector while sweeping the setpoint of the Michelson lock servo for 20 mW of incident power into the interferometer. (Top) broadband optical power noise spectrum. Spectra of higher RIN correspond to poorly selected values of the setpoint. (Bottom) These four panels correspond to the noise floor at 4 specific places in the spectrum. All panels have the same y-axis scale as indicated on the leftmost panel. The colors of the plot correspond to the frequency as indicated in the top plot of the figure. We see that at low frequency the noise floor is heavily dependent on the value of the setpoint of the Michelson.

The measurement procedure presented in Fig. 2.9 provides an avenue toward the maximal performance of the Michelson interferometer for high circulating optical powers. Finally, we can evaluate the performance of the Michelson for this optimized configuration. As seen in Fig. 2.9, the noise floor of this system reaches the level of 1 fm/$\sqrt{\mathrm{Hz}}$ for frequencies exceeding 100 kHz when operating with 20 mW of power incident on the interferometer. We note here that in principle this is not the maximal performance of the system, since this was achieved with the maximum optical power available at the time. In principle, a more precise measurement could be achieved with more incident optical power.

An illustrative analysis of this system would be to understand this performance in the context of quantum-limited measurement. Such a discussion is dependent on the parameters of the oscillator in question. For the sake of the context of this work, we will examine two such oscillators, a mass-loaded trampoline resonator and a defect mode of a membrane PnC device.

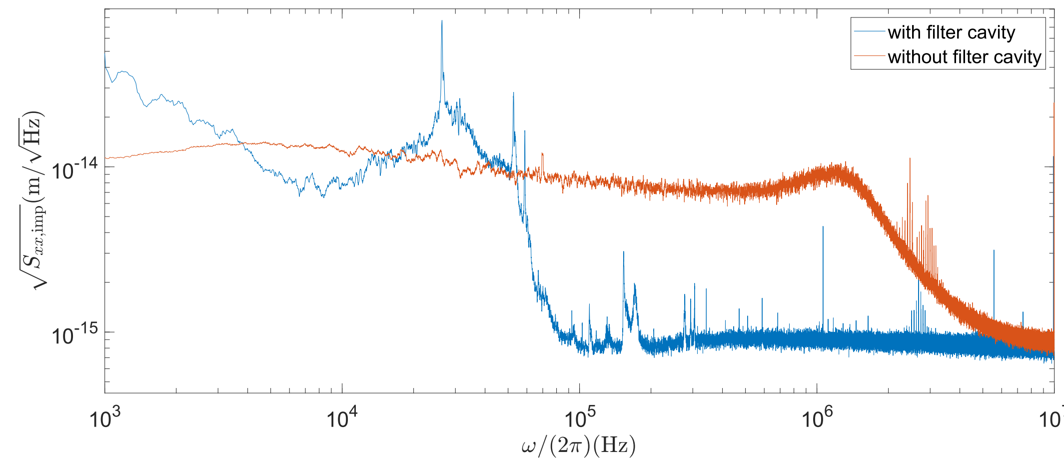

Figure 2.9: Noise floor for 20 mW of incident power incident on the Michelson, with and without the filter cavity. Above 100 kHz, the imprecision noise floor of the system is around 1 fm/$\sqrt{\mathrm{Hz}}$.

In this context, a figure of note would be the power required to operate at the standard quantum limit P_{SQL}. Powers higher than this level indicate that the backaction noise exceeds the imprecision noise on mechanical resonance. For pure position measurements of the mechanical oscillator, this is optical power to use in the interferometer. Tab. 2.1 shows a few example modes and their respective P_{SQL}. We see that the interferometer described in this section can readily achieve these power values and operate under shot noise-limited conditions, and therefore in principle, this interferometer is quantum-limited for these modes. However, for all these modes, the thermal motion will greatly exceed the quantum noise, and therefore for routine measurements, this does not truly matter.

2.6 Feedback cooling analysis of Michelson interferometer

One of the most important technical accomplishments in the field of optomechanics is the ability to ground state cool mechanical resonators. Often this is achieved in high-finesse optical cavities via the technique of sideband cooling. Another possible avenue to ground-state cooling is through feedback cooling. In such a scheme, a fast measurement bandwidth is needed to quickly learn information about the state of the oscillator. Michelson interferometers provide this bandwidth readily and thus are promising candidates to ground state cool mechanical resonators through feedback [97]. This technique has some attractive aspects, namely the absence of an optical cavity, which presents great challenges, especially when coupling to small-mode volume mechanical oscillators.

Since ground state cooling with feedback is achieved via damping of the resonator motion, a certain degree of damping is required in order to reach the ground state. Therefore, there is a limit to the amount of damping we can impose prior to the oscillator transitioning from being under-damped to over-damped. This fact amounts to the requirement that the thermal decoherence rate of the resonator must be less than the resonant angular frequency of the mode in question [97]:

$$\gamma_{th} = \frac{k_B T}{\hbar Q} < \omega_0. \tag{2.45}$$

Eq. 2.45 exhibits another reason why resonators with high $f - Q$ products are useful for quantum optomechanical experiments.

Another requirement for ground state cooling of a mechanical resonator stems from the concept that the state of the oscillator needs to be read out faster than the rate at which thermal phonons enter the resonator. This condition can be expressed mathematically as [72]:

$$\Gamma_{meas} \equiv \frac{x_{\mathrm{zp}}^2}{2S_{xx,imp}} > \frac{\Gamma_{th}}{8} \tag{2.46}$$

where $\Gamma_{th} = \gamma n_{th}$ is the thermal decoherence rate of the oscillator. One notable insight for the technique of feedback cooling is that the feedback loop can compensate for the backaction of the

Device and Mode	$\omega_0/(2\pi)$	m_{eff}	Q	P_{SQL}	$P_{gs}(T=293K)$	$P_{gs}(T=4K)$
Mass loaded trampoline	96 kHz	16 ng	800×10^3	214 μW	—	—
Bare trampoline	143 kHz	4 ng	30×10^6	11 μW	—	120 mW
device B S_1 defect mode	1.7 MHz	0.4 ng	2×10^6	3.1 mW	—	2 W
device E S_2 mode	2.4 MHz	0.4 ng	100×10^3	9.8 mW	—	61 W
Perimeter mode	350 kHz	0.1 ng	1×10^9	50 nW	16 mW	220 μW

Table 2.1: Modal parameters including P_{SQL} and P_{gs}, for a set of example modes that appear in this work, with the addition of a perimeter mode studied in [1]. Devices B and E refer to devices studied in Ch. 4 of this work. Devices that do not satisfy the inequality given in Eq. 2.45 have a blank entry for the ground state cooling power.

measurement [72]. Therefore, one should operate with the lowest imprecision possible, meaning that operating at optical powers greatly exceeding P_{SQL} is actually necessary. Eq. 2.46 implies that the necessary imprecision noise floor for ground state cooling is then:

$$S_{xx,gs} = \frac{2\hbar^2 Q}{k_B T m \omega_0}. \tag{2.47}$$

Equating this expression to that of the imprecision noise floor reveals that required reflected power from the membrane needed to ground state cool assuming ideal feedback:

$$P_{gs} = \frac{c\lambda k_B T}{16\eta^2\pi}\frac{m\omega_0}{\hbar Q} \tag{2.48}$$

We evaluate this expression for various modes studied in this work to give a scale for the level of optical power required to ground-state cool, and if ground-state cooling is possible. For a sense of scale, a state-of-the-art mechanical resonator — a perimeter mode device — is also included [1]. These devices are more difficult to optically probe, but the results of this analysis show that in principle ground state cooling is possible for such modes if great care is taken in interfacing them with both the feedback force and probe laser.

Chapter 3

Sensing with tensioned micromechanical oscillators

Up to this point, we have presented a theoretical description for modeling the mechanical properties of tensioned silicon nitride membrane resonators. In addition, we have established that the motion of these resonators can be read out interferometrically with high precision using laser interferometry. Such a system, a mechanical oscillator coupled to an electromagnetic field, broadly applies to the field of optomechanics. This apparatus is primed for an application towards sensing given that a mechanical resonator can be functionalized to couple almost ubiquitously to any external field, whether it be light, force, or even heat [49,69,98,99]. In this section of this work, we will discuss how such an optomechanical system can be utilized for sensing purposes over a wide range of sectors. Since this work mainly focuses on tensioned membrane resonators, we will discuss the roles tension plays in the design of mechanical sensors. In particular, we identify ways in which tensioning the resonator, thus raising its frequency, can be utilized to lower the effects of technical noise on an application-to-application basis.

3.1 Micromechanical sensing paradigms

The operating principle of a micromechanical resonator-based sensor is that an external perturbation affects the motion of the mechanical oscillator. The full gambit of effects can be represented via a modification to the equation of motion for a simple harmonic oscillator:

$$m(t)\ddot{x} + \gamma(t)\dot{x} + \omega^2(t)x = F(t) + F_{th}(t) \tag{3.1}$$

where we have included the thermal force on the oscillator as well. Here we see that broadly, there are two sensing paradigms: *force* and *parametric*. Force sensing is rather easy to understand: an external force drives the oscillator, usually resulting in a change in the oscillator's amplitude above its normal Brownian motion. Readout of the motion allows for a force to be inferred. Parametric sensing is much broader and also includes external forces on the oscillator. For instance, an oscillator subject to a force gradient will experience a force of the form $F_{fg} = \frac{\partial F}{\partial x}x$, which functions as a frequency shift, despite a physical force being applied to the oscillator. In this chapter, we will discuss sensing in the context of how the force appears in the equation of motion since this will dictate how to infer the strength of the perturbation on the oscillator's motion.

3.2 Direct force sensing and the role of thermal noise

In the direct force sensing paradigm, the harmonic oscillator is subject to an arbitrary force $F_{\text{eff}}(t)$, given in Eq. 1.21. The fundamental force sensitivity is defined by the random thermal force (Eq. 1.32) due to the oscillator's coupling to a thermal bath. This limit can be arrived at in two ways. The first we will call the force picture, and relies on the ability to directly infer the force acting on the oscillator. We assume that we record the motion of the oscillator $x(t)$ with perfect precision (we will discuss the effects of imprecision and backaction later in this section). With this record, we can also calculate $\dot{x}(t)$ and $\ddot{x}(t)$. Assuming that the oscillator's mass, damping, and frequency are all known, one can then insert the record of the motion into Eq. 3.1 to directly infer $F(t) + F_{th}(t)$. Therefore, we see that ideally, we can perfectly infer the total force on the oscillator, and therefore the force sensitivity can be understood to what force is required in order to reach a signal-to-noise ratio (SNR) of 1.

Another way to define the noise floor of a force sensor would be to directly compare the scale of the external force-induced motion to that of the Brownian motion. We will call this the motion picture. One can perform this comparison due to the linearity of Eq. 3.1, where we can assume that $x(t)$ is of the form $x_F(t) + x_{th}(t)$. One can then compare the spectral densities $S_{xx,F}$ and $S_{xx,th}$ to derive a signal to noise ratio:

$$\begin{aligned} S_{xx}^{\text{signal}} &= S_{FF}(\omega)|\chi_m(\omega)|^2 \\ S_{xx}^{\text{thermal}} &= S_{FF}^{\text{thermal}}|\chi_m(\omega)|^2. \end{aligned} \tag{3.2}$$

Therefore, we see that an SNR of one is obtained when $S_{FF}(\omega) = S_{FF}^{\text{thermal}}$. We would like to say a word of caution when applying this logic to a general force. Since we worked in the Fourier domain up until this point, we have assumed that the force is applied for an infinite time such that the motion is in the steady state when we calculate S_{xx}. In practice, this is equivalent to assuming that the force has acted for a time much longer than $1/\gamma$. For forces acting for times shorter than $1/\gamma$, one does not reach the steady state of motion, and therefore the signal amplitude is also lower. However, regardless of the integration time of the signal force, the oscillator is always in the steady state of the thermal force. In other words, one would expect the root-mean-square amplitude of the Brownian motion to always be $\sqrt{k_B T/m\omega_0^2}$. By comparing the now smaller signal amplitude to the unchanged noise amplitude, we might infer that we have lower SNRs for shorter measurement times. This is in direct opposition to the bound we placed in the force picture.

This apparent paradox can be resolved when considering the total contributions to the motion of the oscillator. We can consider the total motion $x(t)$ to be $x_{\text{hom}}(t) + x_F(t)$, where $x_{\text{hom}}(t)$ is a solution to the *homogenous* equations of motion for some initial condition of the system. $x_F(t)$ can thus be considered to be the deviations that arise from external forces acting on the oscillator. For short measurement times, the root-mean-square fluctuations of $x_F(t)$ will grow from zero, only arriving at the expected Brownian motion amplitude for measurement times much greater than $1/\gamma$. Therefore for short measurement times, the contributions to $x_F(t)$ from both the signal and the noise grow at the same rate, thus resolving the apparent paradox. Practically, a determination of $x_F(t)$ requires precise knowledge of the oscillator parameters, as well as the initial condition of the oscillator. Thus both the force picture and motional picture require the same knowledge of the oscillator parameters and also require low imprecision readout of the mechanical motion.

Given that both methods of inferring force from motion require precise measurements of the displacement of the oscillator, it is important to examine the effects of imprecision noise on a force measurement. In this section, we will neglect the effects of backaction on the measurement. However, this can be easily included by adding another white force term to all equations. We can readily write down the complete noise power spectral densities in both pictures by comparing the contributions of both the Brownian motion and the imprecision noise on the oscillator determined by both the detection technique and strength. For this discussion, we will assume that the imprecision noise is that of a Michelson interferometer studied in Ch. 2:

$$S_{xx}^{(\mathrm{meas})}(\omega) = 4k_B T\gamma m|\chi(\omega)|^2 + S_{xx}^{(\mathrm{imp})}(\omega) \tag{3.3}$$

$$S_{FF}^{(\mathrm{meas})}(\omega) = 4k_B T\gamma m + S_{xx}^{(\mathrm{imp})}(\omega)|\chi(\omega)|^{-2}. \tag{3.4}$$

Here we see that the labeled inferred (measured) have a symmetry between the two pictures of measurement, where the mechanical susceptibility acts as a filter to translate between the two pictures. In the force picture, one is only limited by the thermal force PSD over a narrow bandwidth that is defined by the range of frequencies in which the Brownian motion far exceeds the imprecision of the system, as indicated in Fig. 3.1a,b. This readily identifies the advantages of pushing towards better imprecision optical readout, achieved either with a high-finesse optical cavity or a Michelson interferometer as discussed in Ch. 2, since doing so improves the bandwidth over which one is limited by the fundamental force noise of the system. Fig. 3.1c,d shows the same concept but in the motional picture.

With a strong enough readout, one could in principle measure the effects of force down to DC. Measuring above resonance presents different challenges because the oscillator acts as an integrator for frequencies exceeding its natural frequency. Practically, the bandwidth will also be influenced by the multimode nature of the mechanical device, because the resonant response of the nearest mechanical modes will generically be higher than the off-resonant response of the sensing mode.

In examining the effects of imprecision, we have revealed that a force detector functions well over a finite bandwidth defined by the resonance of the oscillator as well as the vicinity of the next nearest modes of the structure. For the sake of this work, we will then discuss resonant force

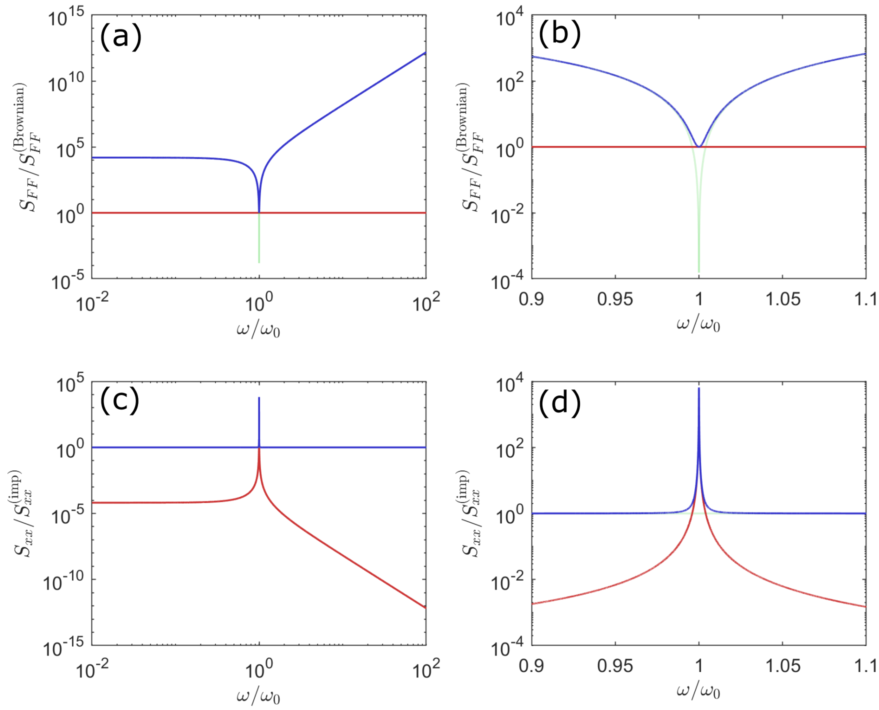

Figure 3.1: Power spectral densities indicative of the noise floor for a force sensing measurement. In all plots, red lines correspond to the thermal motion contribution to the noise, green lines indicate the contribution from imprecision, and blue lines are the total noise floor. (a) and (b) show the force noise spectral density over differing bandwidths. We see in (b) that one is limited by thermal noise over a narrow bandwidth near resonance. (c) and (d) show an equivalent message in the motional picture, where it is apparent that only near resonance the noise floor is determined from the oscillator thermal noise.

detectors.

3.3 Functionalization for direct force sensing

Up until this point, we have analyzed the raw noise performance of a micromechanical force sensor. However, we have not described the nature of a signal force. In general, introducing a signal force requires an augmentation of the micromechanical device with a coupling agent, a process called functionalization. This process can be performed in a variety of ways. As an example, the coupling of the device to external optical forces can be enhanced via either deposition of a mirror coating onto the oscillator or by patterning of a photonic crystal mirror into the resonator geometry itself [100].

Or, a mechanical device could be coupled to external electric or magnetic fields by attaching a metal or magnetic material directly onto the device. In general, an advantage of using a mechanical device as a force sensor allows for a ubiquitous coupling to an external field since almost any material can be attached to the micromechanical device.

In order for this augmentation to apply a force, there needs to be strong participation of the coupling agent with the sensing mode. This can be seen directly from Eq. 1.21, where the effective force imparted on the oscillator is calculated by an integration of the physical force against the mode shape profile. This requirement presents a challenge to the researcher when designing direct force sensors, but enables creative use of geometry to optimize device design [101]. Typically, we want to probe the oscillator at the point of maximal amplitude for the best motional sensing performance. However, such a location is also optimal for the location of the coupling agent. In general, we cannot expect a sensing mode to have two distinct locations of maximal motional amplitude, and therefore, it is often necessary to sacrifice imprecision in the readout for more coupling of the signal of interest. We note that one advantage of the low-imprecision optical detection used in this work (see Ch. 2) is that such a sacrifice can still result in a sensor with a large readout bandwidth.

Another issue with the necessity of the overlap between mechanical motion is associated with mechanical loss. For the fabrication of a micromechanical resonator, we have the freedom to select a low mechanical loss material. However, since the coupling agent needs to interact with an external field, we do not necessarily have the freedom to select a low-loss material for the coupling agent, leading to the possible introduction of additional dissipation into the resonator, hampering the susceptibility of the device to thermal noise. This presents a dilemma: the introduction of a relatively large coupling agent gives a larger signal at the cost of increased mechanical dissipation. If the mechanical loss properties of the coupling agent are known, the mode shape of the device including the coupling agent can be simulated and the added loss can be predicted, allowing for an optimization of the signal-to-noise of the designed device. Practically speaking, the mechanical loss properties are not known in general, and thus experimental verification of the added loss would need to be performed.

3.4 Spin sensing with tensioned silicon nitride mechanical resonators

Some potential sensing targets for precision force sensors are spin systems ranging from spin ensembles down to the molecular or single spin level. The coupling of the motion of a mechanical oscillator to the state of a spin system is a rather mature field at the time of writing this work. Such a system has been widely utilized for the technique of Magnetic Resonance Force Microscopy (MRFM). This technique, pioneered in the 1990s, seeks to image locations of spins in a target sample via interaction between the motion of a mechanical oscillator and a time-dependent magnetization of the spin system [98,102,103]. More concretely, the time-dependent magnetization of a spin ensemble gives rise to a time-dependent magnetic field gradient, which can apply a force to a functionalized mechanical resonator. Historically, these experiments were carried out with cantilever tips with an added micromagnet [3, 98, 104–108]. These cantilevers can then be maneuvered close to the sample of interest with techniques from atomic force microscopy (AFM), allowing for a small sample to probe distance. This small sample to probe distance, combined with single-spin force sensitivity, would enable direct imaging of single molecules [109–112].

Most MRFM protocols are performed in a relatively large quantization field of the spins, often called B_0, following the convention from the Nuclear Magnetic Resonance (NMR) field. The spins are similarly manipulated with resonant RF driving schemes, arising from a time-dependent field $B_1(t)$, usually generated from an external coil or transmission line. The goal of the external drive is to generate a time-varying magnetization $M(t)$ that has spectral components near the mechanical resonance frequency and therefore can drive the motion of the mechanical oscillator. We note here that typically driving of the spins is necessary to generate the coupling, despite the fact that the Larmor precession of the spins can generate a time-varying magnetization. However, for typical fields used in NMR and MRFM experiments, the Larmor precession frequencies greatly exceed the resonant frequencies of micromechanical cantilever resonators, and therefore additional driving is necessary to modify the dynamics of the spin system such that $M(t)$ can change the mechanical motion.

MRFM is a powerful technique due to its ability to leverage the resonant nature of both the mechanical resonator and the spin system in order to provide spatial information. A byproduct of needing a micromagnet to generate the spin-motion coupling is an appreciable dipolar field that penetrates throughout the target sample. This dipolar field changes the local magnetic field of each spin, thus spatially varying the Larmor precession frequency. Therefore, when driving the spins, only a fraction of the spins will be resonantly addressed by the driving scheme, and thus only a small slice — the resonant slice — will affect the motion of the mechanics. The precise geometry of the resonant slice dictates the spatial resolution of the MRFM technique.

The sensitivity of MRFM is demonstrated in a hallmark work of the detection of a single electron spin [3]. The apparatus used in this experiment is displayed in Fig. 3.2. Here, all the ingredients of the experiment are shown, including a rendition of the resonant slice. Since then, the absolute resolution of MRFM has been achieved for systems of both nuclear and electron spins to the scale of approximately 10 nm [105], with the current state of the art reaching the sub 1 nm regime [113]. These improvements have been performed via a reduction in the probe to sample spacing, as well as improved micromagnet designs which produce spatially narrower resonant slices.

These resolutions are on par with competing scanning probe technologies, notably those based on Nitrogen Vacancy (NV) center defects in diamonds, which makes them a suitable platform for future sensors capable of nanoscale magnetic resonance imaging (nano-MRI) [114]. Nano-MRI capable sensors not only need exceptional spatial resolution but also require exceptional noise levels in order to probe single nuclear spins. To inspect the scales of the problem, we can inspect the form of the force from a single spin:

$$\vec{F} = \nabla(\vec{\mu}_i \cdot \vec{B}) = \mu_i \nabla(\vec{S} \cdot \vec{B}) \tag{3.5}$$

where μ_i is the magnetic moment of the spin in question and $\vec{S}$ is the vector spin operator of the spin in question. For the classic case of both the quantization field and spin pointing along the z-axis, this formula simplifies to:

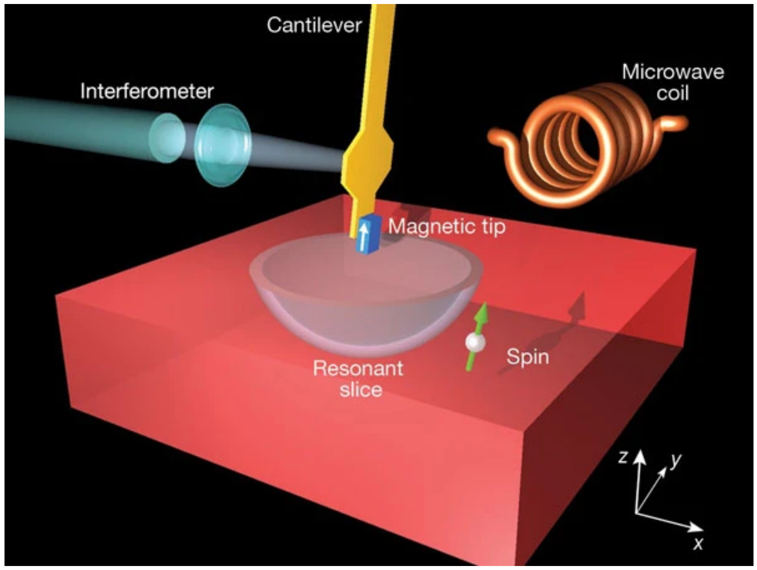

Figure 3.2: MRFM experimental schematic from the first detection of a single electron spin [3]. Figure reused with permission from Spring Nature. The semi-hemispherical shell represents the resonant slice, indicating where the probe is most sensitive to spins inside the sample. The spins are manipulated with an external RF coil while the motion is monitored with a fiber interferometer.

$$F_z = \mu_i \frac{\partial B_z}{\partial z}. \tag{3.6}$$

It is evident from the form of Eq. 3.6 that large magnetic gradients benefit not only the spatial resolution of the device but also the absolute sensitivity. We can compare the relative magnitudes of the forces for electron versus nuclear spins. Assuming a state-of-the-art value for the gradient of the magnetic field of 10^6 T/m [113], we can calculate that $F_{\text{electron}} \approx 10^{-17}$ N compared to $F_{\text{proton}} \approx 10^{-20}$ N. From the relative size of the magnetic moments, the challenge of probing a single nuclear spin is 1000 times more difficult. Given the relative difficulty of single electron spin imaging, it is no surprise that cantilever-based MRFM has not been able to do the same for a single nuclear spin.

Given that fundamentally the force sensitivity of a mechanical resonator depends on its dissipation (Eq. 3.4, it is prudent to consider the use of tensioned resonators for MRFM experiments. Notably, tensioned resonators benefit from dissipation dilution. Additionally, these resonators can be engineered to have relatively low effective masses, which makes them excellent force sensors.

The lowest observed level of thermal force on a tensioned Silicon Nitride resonator had a thermal force power spectral density of 7 $\mathrm{zN}/\sqrt{\mathrm{Hz}}$, meaning that it could detect a single nuclear spin in less than 1 second in principle [115, 116].

Tensioned membrane resonators may also afford other advantages over bulk cantilever mechanical resonators. Tensioning of the oscillator leads to an increase in resonance frequency, from the scale of 1 to 10 kHz for cantilevers to 0.1 to 1 MHz for tensioned membranes of or strings made from silicon nitride. Working at higher frequencies has been shown to lead to a decreased level of non-contact friction between the mechanical resonator and an external surface, and therefore would in principle lead to smaller sample-to-probe distances [117]. Additionally, it is ubiquitous for the surfaces of many materials to exhibit 1/f noise that is both electric and magnetic in nature [118–120]. Thus working at higher mechanical frequencies will also allow for a reduction in this added surface noise due to spectral suppression.

Attempts of MRFM experiments with tensioned silicon nitride resonators present unique challenges [4, 117, 121]. Firstly, there is the obvious geometric problem associated with the mechanical resonator being planar in nature. Positioning two planar surfaces less than 10 nm apart while allowing for scanning capabilities is technically challenging, and thus probing a large planar sample would be difficult when operating a membrane-based MRFM apparatus in the conventional MRFM paradigm. This can be alleviated by modifying the configuration presented in Fig. 3.2. Here, the membrane would house either the gradient source (or the sample), while an external tip that can be brought close to the membrane surface would hold the sample (or the gradient source). Thus the external tip would serve as the scanning implement affording the apparatus spatial information, while the readout would be achieved by a stationary membrane. The choice of what to place on the membrane — the gradient source or the sample — depends on the relative mass and dissipative properties of both the prospective samples and the micromagnet. In the case of complex single-molecule samples, which are typical targets of nano-MRI probes, we propose placing the sample on the membrane. Samples of this size, and even larger, have been shown to not affect the dissipative properties of low-dissipation membrane devices [117].

Another challenge with performing MRFM experiments with a tensioned resonator is the implementation of MRFM protocols for a MHz-scale frequency mechanical resonator. As stated previously, the frequency mismatch between the Larmor precession frequency and the mechanical resonator frequency necessitates driving the spin system to apply a resonant force. Many of the state-of-the-art MRFM protocols applied to cantilevers rely on the motion of the mechanical oscillator inducing adiabatic inversion of the spin system [3, 105, 122]. However, as resonator frequencies increase, the transit of the mechanical oscillator past the spins occurs faster than adiabatic timescales. Additionally, such schemes are reliant on larger mechanical amplitudes achievable by cantilevers, which may be difficult to achieve with stiffer tensioned mechanical devices. A few protocols have been proposed that work at higher mechanical frequencies. Work with 1 MHz nanowire-based MRFM experiments has leveraged switchable gradient sources to generate the spin-mechanical coupling [123–126]. Protocols that rely on a parametric modulation of the coupling between two membrane modes have the advantage that the modulation need only occur at the difference frequency of the two modes in question, relaxing the speed requirement of spin manipulatino [127]. Finally, operating at higher mechanical frequencies allows for a complete disregard for the frequency mismatch problem by tuning the Larmor precession frequency and mechanical frequency into resonance. Oddly enough, this was the original proposal for MRFM, but was ultimately rejected due to the technological problem of operating mechanical oscillators at high frequency [102]. Such a protocol might be fruitful for future Nano-NMR experiments because the mechanical motion couples directly to the *transverse* magnetization of the spin-system. This prospect has led to the pursuit of a resonant detection protocol between a mechanical resonator and a CaF_2 spin ensemble. However, current signal-to-noise estimates arising from simple probe-sample geometries indicate that resonant coupling would not be achievable without the implementation of specialized nano-positioning equipment.

3.5 Demonstration of electron spin detection with a trampoline resonator

In this section, we will discuss an experiment that sought to utilize a low-dissipation tensioned resonator — a trampoline resonator — in an MRFM-like experiment addressing an ensemble of electron spins [4, 121]. The main goals were to learn about the technical challenges associated with coupling a spin ensemble to the motion of a tensioned, low-mass, mechanical oscillator. For this experiment, a well-known electron spin sample of diphenylpicrylhydrazil (DPPH) was selected. DPPH is used due to its high spin concentration of $\rho_{\text{spin}} \approx 2.1 \cdot 10^{21}$ spins/cm^3 and short relaxation time, of $25 - 80$ ns. The high concentration will produce a relatively large force, and the fast decay time allows for the use of the cyclic saturation technique [108, 121, 128].

Cyclic saturation can be understood first by identifying the role of the B_1 field. For fast decaying spins, the spins rapidly align to the external magnetic field. If the B_1 field changes on a timescale much slower than the decay time of the spins, then the spin system can be considered to be in constant equilibrium with a slowly varying magnetic field. Thus the magnetization $M(t)$ follows the field, which oscillates at the mechanical frequency, thus generating a time-varying gradient that can be used to drive mechanical motion. The modulation of the field can be carried out in a number of ways. In this work, we explore both frequency and amplitude modulation of the B_1 field.

For this demonstration, two functionalized trampoline resonators were used as the force sensor. The resonators were mass-loaded with a NeFeB magnet. For this specific implementation, a relatively small magnet was used (0.1 ng) such that the mechanical quality factor of the resonators degraded minimally: the largest observed drop was from 4.5×10^6 to 2.4×10^6. The functionalized device is presented in Fig. 3.3. Later in Sec. 3.6, we will discuss the functionalization of similar trampoline devices with even higher mass loads.

To drive the spins, a microwave stripline circuit was used. The stripline tapered to a 90-degree elbow in order to concentrate the field at this point. The sample of DPPH was deposited at the elbow via the use of a glass tip and a micromanipulator. The stripline chip was electrically contacted with a PCB via a conductive epoxy. In order to specify the sample-to-probe distance,

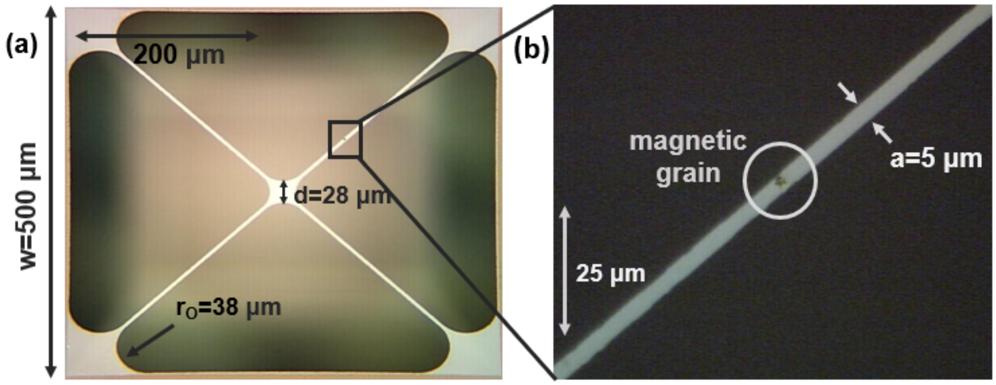

Figure 3.3: (a) SiN trampoline resonator functionalized with an NdFeB magnetic grain a few microns in diameter. (b) Zoom in to magnetic grain deposited on resonator tether.

the trampoline chip was placed inverted on top of the microwave stripline circuit in a flip-chip geometry. The flip chip was assembled by maneuvering the trampoline chip — the top chip — over the microwave stripline circuit — the bottom chip — with a vacuum chuck. The relative separation between the two chips was monitored with an optical microscope. The vacuum chuck was manipulated with a 5-axis translation-tip-tilt stage which allowed for proper alignment of the two chips. Once the two chips were aligned, the flip-chip was secured by placing Stycast epoxy at the corners. Following the curing of the epoxy, the magnet-sample distance could be determined by adjusting the focus of the optical microscope.

A schematic of the completed apparatus appears in Fig. 3.4. For this specific implementation of the experiment, the apparatus was placed in the vicinity of a strong NeFeB magnet in order to define the ≈ 900 G B_0 field for the experiment. The design of the microwave stripline is such that the B_1 field is transverse to both the B_0 field as well as the direction of mechanical motion. The mechanical motion was probed with a Michelson interferometer. The flip-chip assembly in addition to the quantization magnetic were both housed in a vacuum chamber.

The experimental protocol was performed in a sequential manner. First, the thermomechanical spectrum was measured in order to determine the resonant frequency of the sensing mode. Next, the microwave circuit was driven with a signal with carrier frequency close to 2.8 GHz, which is the expected electron Larmor precession frequency for the 900 G field used in this experiment.

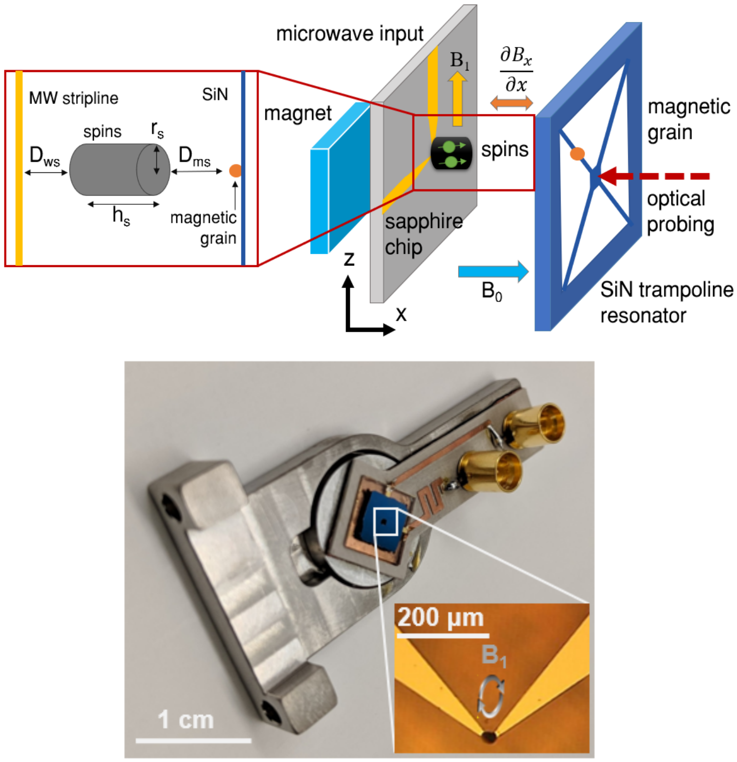

Figure 3.4: (Top) Experimental schematic for magnetic resonance force microscopy demonstration [4]. We detect electron spins in DPPH with a trampoline resonator using cyclic saturation. Readout of the trampoline resonator is through a Michelson interferometer, with the signal arm reflected from either the trampoline pad or from a gold reflector on the sapphire chip. (Bottom) completed flip-chip assembly. The inset shows the elbow of the microwave stripline. At the elbow resides the sample of DDPH.

This signal was first applied with modulation at the mechanical resonance frequency — either FM or AM — followed by an experiment where the modulation was turned off. The monitoring of the mechanical motion with and without the modulation allows for a determination of the effects of spurious forces on the mechanical oscillator due to the microwave drive. These forces arise from electrostatic interactions between the microwave stripline and trapped charges in the silicon nitride, and would therefore be present without the spins. This protocol was performed for a sweep of MW (microwave) carrier frequencies, as well as for a variable B_0 field. The B_0 field was tuned via an external shim-magnet outside of the vacuum chamber. The FM frequency deviation was 10 MHz for all experiments, while the AM modulation depth was 1 for all experiments.

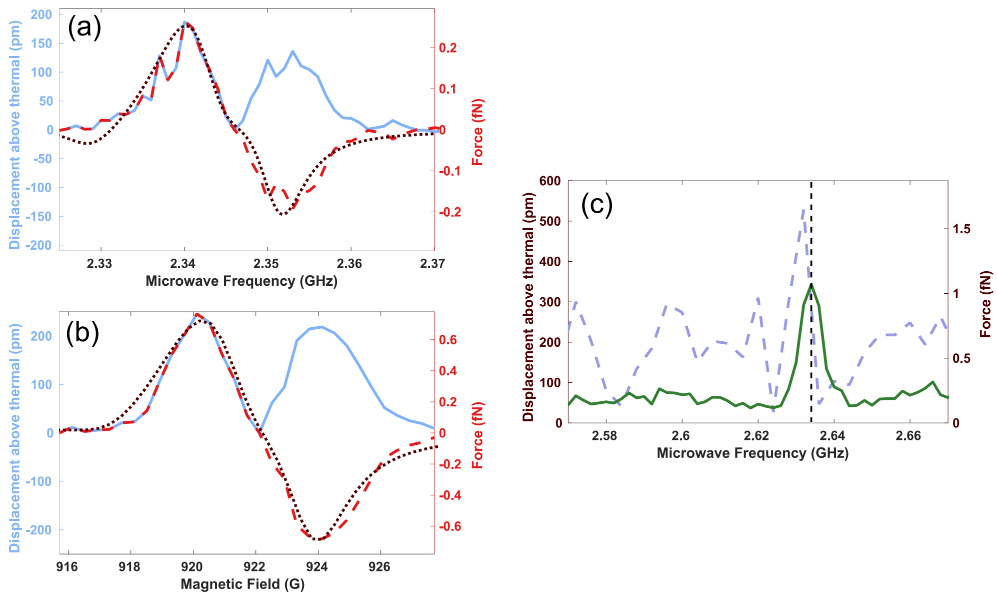

Figure 3.5: (a) MRFM resonance using an FM microwave drive. The MW frequency is swept at a fixed magnetic field. Shown are the mechanical displacement (full blue), the corresponding force signal (dashed red), and a fit of the FM signal (dotted black). (b) Same as (a), but here we sweep the magnetic field at a fixed microwave frequency of 2.564 GHz and use device B. In both (a) and (b), the input microwave drive power is -7 dBm. (c) MRFM resonance using an AM microwave drive. We show a sweep of the MW frequency at a fixed magnetic field at two different MW powers of -8 dBm (full green) and -3 dBm (dashed blue). Particularly using the AM technique, the spin-resonance signal can easily be overwhelmed by spurious electrical forces, as observed at the higher powers (dashed blue).

The results of this protocol can be seen in Fig. 3.5. Fig. 3.5a shows the FM results for a swept MW carrier frequency. Here, one sees the observed increase in mechanical amplitude (blue line), along with a simulation of the expected signal for a reasonable sample geometry (black dotted line). Of note, the modeling revealed that a cylindrical sample geometry best explained the observed signal. Despite the apparatus having no scanning capability, an adjustment of the MW carrier frequency allowed for spatial information about the sample to be determined. In order to match the absolute scale of the observed force, it was determined that there was an appreciable loss in the MW delivery circuitry. Results for AM tell a less clear story, as seen in Fig. 3.5. Here, one sees that for low MW powers (green line), there is a pronounced peak near the electron spin resonance, as expected. However, an increase in MW power gives rise to spurious forces that are larger than the MRFM signal. This is well known within the field of MRFM and was pointed out early in the history of the field [129]. It is notable that FM-based cyclic saturation is much less susceptible to these spurious forces, and thus was more useful for our investigation. For this reason, we also examine the dependence of the FM signal for a swept external magnetic field (Fig. 3.5b). The existence of a similar signal to what was observed for a MW carrier frequency sweep reveals the electron-spin-resonance origin of the force.

This demonstration exhibited the ingredients of an MRFM experiment. It used functionalized mechanical resonators that allowed for coupling to a relatively large ensemble of electron spins. To improve the spin sensitivity, there are a number of improvements to be made. Firstly, the sample-to-probe distance was in excess of 10 microns for this specific implementation. Due to the r^{-4} dependence of magnetic gradients from dipolar sources, reducing this distance could increase the coupling by many-fold. Concretely, the gradients achieved in this experiment are 6 orders of magnitude less than the state-of-the-art. We do not expect to be able to achieve sample-to-probe distances of less than 100 nm while maintaining scanning capabilities, and therefore all future implementations should be performed in a tip-membrane geometry. Additionally, the experiment could be operated in cryogenic conditions. Under these conditions, the Brownian motion of the oscillator greatly decreases, allowing for heightened force sensitivity. Also, an improved mechanical resonator design — for instance simply using thinner membranes increases Q by a factor of the inverse thickness — will also reduce the thermal force exerted on the mechanical resonator.

3.6 Mass loading of tensioned micromechanical resonators

In this section, we will study the effects of mass loading for tensioned mechanical resonators. In this work, this study was carried out for applications towards magnetic force sensing, but could equally be applied to other measurement paradigms, such as accelerometry. The details of the analysis we will present have already been presented in published work as well as in other theses of our group, so only the broad outcomes will be presented in this particular work [101, 130]. Nonetheless, the concepts will illuminate some of the complexity and open questions pertaining to the design of tensioned micromechanical sensors.

The analysis begins by considering a tensioned string resonator. In reality, the addition of a load mass should be modeled as a full three-dimensional problem. However, if one considers only the out-of-plane motion of the resonator, the system can be modeled as an Euler-Bernouli beam system under tension, with spatially dependent material parameters. The overall analysis can be further simplified by considering a somewhat constrained mass load located far from the supports of the resonator. Here, one can model the mass load as a perturbation to the local mass density for the wave equation part of the string equation [101]. In this limit, the mode shape and frequency can be calculated from the following equation:

$$\frac{Eh^2}{12\sigma}\frac{\partial^4 w}{dx^4} - \frac{\partial^2 w}{\partial x^2} - \frac{\rho(x)\omega^2}{\sigma}w \tag{3.7}$$

where $\rho(x)$ is a position dependent density. A simple analysis would be to inspect this equation in the limit that $\rho(x)$ is equal to the density of the silicon nitride everywhere, save for a small region of length a where $\rho(x) = \rho_0 + \Delta\rho$. This increase in local mass represents a deposited mass that functionalizes the device. The solutions to this problem can be studied in the low and high load mass regimes. In the low load mass regime, the added mass is much less than the physical mass of the oscillator. Here, the mode shape and mode frequency are very weakly perturbed, and the mode structure is largely unchanged.

As the load mass is increased, the mode structure begins to change appreciably from the unloaded case. In the high mass limit, the frequency of the lowest order mode of the device decreases due to the increasing load mass, while the other mode frequencies stay roughly the same. This is because all modes — except for the lowest order mode — have increasingly lower participation of the load mass. This can be understood by noting that the elastically defined speed of sound in the loaded region becomes much lower than the unloaded speed of sound, meaning that there is a large impedance mismatch for traveling waves in the device at the interface of the unloaded and loaded region. This impedance mismatch functions to prevent motion of the loaded region. A key insight is revealed here: higher order modes of a mass-loaded device have poor direct force sensing capabilities due to the low participation of the mass, and therefore any applied force, on the motion of these modes. Therefore, for sensing purposes, highly mass-loaded resonators are restricted to the use of the lowest order mode of the device.

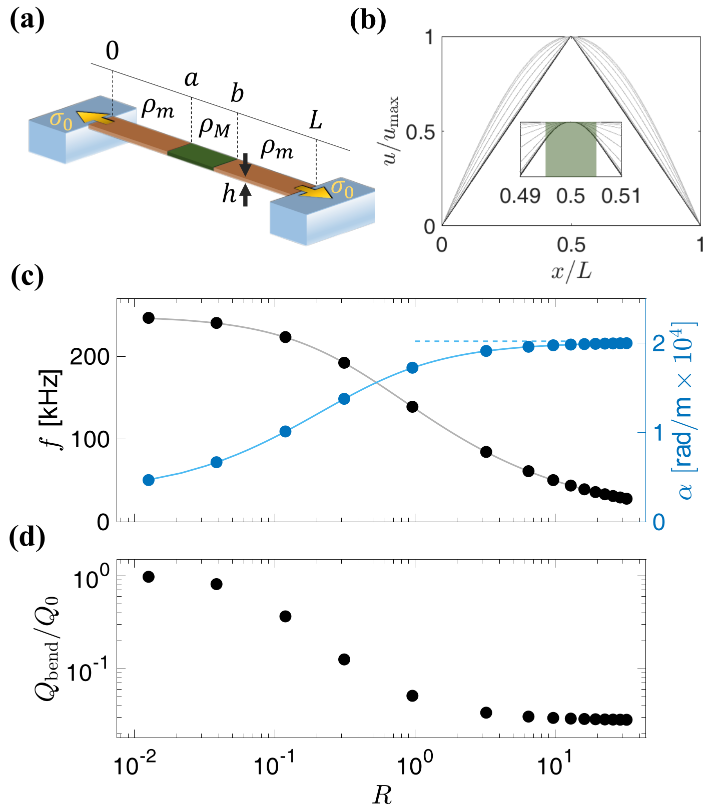

Figure 3.6: (a) Geometry of a tensioned beam under mass loading. (b) Superimposed mode shapes for increasing mass load. The sinusoidal shape is the unloaded mode shape, while the triangular shape is the saturated mode shape. (c) Frequency of the mass load as a function of mass loading ratio R (left), as well as the wavenumber α of the oscillation in the loaded region (right). One sees that the wave number saturates, giving rise to the saturation of the mode shape. (d) Calculated value of the bending loss limited Q_{bend}.

The lowest order mode has a different behavior. In the high mass limit, one expects that the mode frequency drops due to the high load mass. At a certain point, the frequency drops below a point at which the wavelength of a traveling wave in the unloaded region $\lambda \sim \omega/(2\pi)\sqrt{\rho/\sigma} \equiv 2\pi/\alpha$, where α is the wavenumber of oscillation in the unloaded region, will be much greater than the absolute size of the device. Therefore, traveling waves will not appear to be sinusoidal in the unloaded region. Rather, they will manifest as a linear displacement profile. Meanwhile, the loaded region will experience a normal sinusoidal mode shape, albeit on a much shorter length scale. This produces a triangular-shaped mode profile in the high mass limit. Another way of understanding this is that as the frequency lowers, the system approaches a quasistatic limit, where the oscillation appears as a slow oscillation of the static solution of the problem. Under this view, it is possible to readily solve for the lowest order eigenfrequency by deriving an effective spring constant of the string for a given small displacement of the load mass. The process of increasing the load mass can be seen in Fig. 3.6. We note that after a relative mass load scale, that depends on both the geometry and the density of the load, the mode shape ceases to change even while adding additional mass. We call this phenomenon mode-shape saturation. We note that even though this analysis was carried out for a one-dimensional tensioned string, it holds for a two-dimensional tensioned membrane as well.

One ramification of mode-shape saturation arises when considering the dissipative properties of the mode. As discussed in Chapter. 1, the internal losses of a mode are dictated by the geometry of the mode, in particular by its bending. However, if the mode shape saturates, then the quality factor of the mode saturates as well, a phenomenon we call Q-satuaration. This is seen in Fig. 3.6d, where when the ratio of the load mass to the resonator mass R is much greater than 1, the internal loss limited value of $Q = Q_{\text{bend}}$ saturates to a constant value, even though the mass continues to increase. We note that the predicted value of Q in this limited is diminished from the bare value of Q by over an order of magnitude. This decrease can be explained by a concentration of curvature in the mass-loaded region.

This model, although simplistic, reveals key aspects related to the act of mass-loading a tensioned resonator. However, there are aspects of real functionalization that it fails to capture. Firstly, it does not take into account the three-dimensional aspects of the load mass, which needs to be taken into consideration when wanting to model the material losses of the load mass [101]. Notably, one should consider whether or not there are mechanical modes of the load mass that could couple to the resonator. If a coupling exists, it often is associated with increased mechanical losses because the load mass will not be tensioned, and thus does not benefit from dissipation dilution [131].

With all of this in mind, it is pertinent to directly probe this theory of mass loading. Again, this discussion will be brief, and the details are already presented in [101,130]. In this work, a silicon nitride trampoline resonator was studied under mass loading. Trampoline resonators are notable for their exemplary quality factors will also exhibit reduced modal masses, making them strong candidates for force sensors [56]. Here, the trampoline resonator was mass loaded by epoxying a magnetic grain to one of its tethers. This location was selected in order to reduce mechanical losses. We note that adding mass to the central pad is sub-optimal due to higher mechanical losses, as well as interference with free-space optical probing of the motion. The addition of the magnetic grain allowed for a tunable load mass under similar mounting conditions.

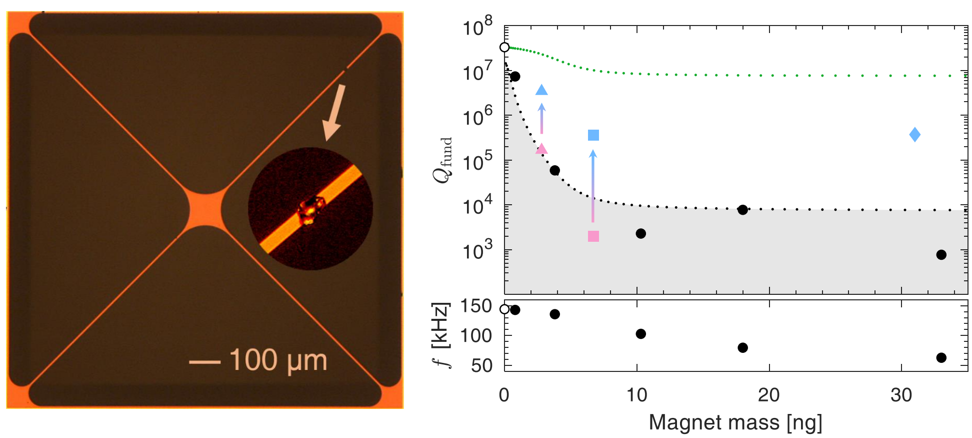

Figure 3.7: (left) Microscope image of a trampoline resonator. The inset is a zoomed-in image of the magnetic grain deposited onto the tether of the trampoline. (right) Measured quality factors and frequencies of the device as a function of load mass. The open (filled) black circles correspond to the device pictured in this figure with additional magnets added. Additional results from other devices are indicated with other markers, where pink markers correspond to room temperature results, and blue markers are the quality factors measured at 4 Kelvin. Small black dots are results from FEA simulations including the loss of the epoxy. Small green dots correspond to the same FEA simulation neglecting epoxy losses.

The results of this investigation are shown in Fig. 3.7. Here, we see that with added mass, the quality factor of the mode does not necessarily drop, but rather plateaus to some relatively low value. This increased loss is accounted for by taking into account the losses in the epoxy used to secure the load mass to the tether. We do not expect that epoxies will have low-dissipation mechanical properties owing to their material design. However, we do observe that devices measured at 4 Kelvin saw orders of magnitude increases in their quality factors, far exceeding what we would expect for the increase of Q_{int} of the silicon nitride [69]. Therefore, we conclude that the observed quality factors in this experiment were dictated by the loss of the epoxy. Mass loading without using a lossy material like epoxy would yield much better results, as indicated by predictions from FEA simulations assuming epoxy-free loading of the device (Fig. 3.7).

These results are promising for tensioned mechanical sensors with large mass loads. We point out that there have been other recent works that have investigated the limits of mass loading for tensioned mechanical devices that observe similar trends in the large mass limit [131, 132]. These developments are exciting, given the wide range of sensing targets that benefit from large load masses. These include but are not limited to, magnetic force, gravity and acceleration. All of these sensing modalities share the same property where the signal manifests itself as a force that scales as the mass. Mathematically, we can write this as the signal in general as $F(t) = \beta M$, where $F(t)$ is the signal force, M is the load mass, and β is a proportionality constant that depends on the sensing target of interest. For instance, in the case of an accelerometer, $\beta = a(t)$, the acceleration. Therefore, the force sensor we have created is actually a β sensor, and therefore we should consider the spectral density associated with noisy fluctuations of β induced by the environment. With this in mind, we can write the noise floor of the β sensor (assuming measuring close to resonance such that imprecision of the motional readout is negligible) as:

$$S_{\beta\beta}^{\mathrm{sat}} = \frac{4k_B T\omega}{MQ} = \frac{4k_B T k_{\mathrm{eff}}}{M^{3/2}Q}. \tag{3.8}$$

Here, we have assumed that the sensing mode is operating in the saturated regime. Therefore, the effective mass of the mode will be M regardless of probe location, because the load mass is much greater than the physical mass of the bare oscillator. We have also used another property of the loaded regime, where due to the quasistatic nature of the mode profile, the k_{eff} associated with the mode is constant. Therefore, we see that the sensitivity to β has a favorable $M^{-3/2}$ scaling, meaning that larger load masses can drastically increase the sensitivity of the sensor.

3.7 Effects of cold-damping for micromechanical sensors

One of the most ubiquitous effects in the field of cavity optomechanics is cold-damping, or cooling of the mechanical motion. This is commonly achieved either through passive cavity sideband cooling or through active feedback cooling schemes [35, 67, 72, 133–135]. Cooling of the mechanical motion is useful for quantum operation of the mechanical oscillator, where operating as close to the quantum ground state, or the equivalent of strong optomechanical coupling compared to dissipation, is necessary. Damping, achieved either through active feedback or passively using cavity sideband cooling, does not fundamentally improve sensitivity or bandwidth. In this section, I will discuss this concept in detail, as well as examine broader situations where increased control over mechanical motion required for some sensing protocols has been hypothesized to be mitigated by damping in the presence of technical drifts or noise [4, 116].

A classical description of micromechanical damping can be described via the addition of a damping force to the equations of motion. In addition, because the damping is achieved through a connection to a cold bath, the temperature that corresponds to the Brownian motion also decreases [67]:

$$\gamma_{\text{tot}} = \gamma + \gamma_d \tag{3.9}$$

$$T_{\text{eff}} = T_{\text{init}} \frac{\gamma}{\gamma + \gamma_d}. \tag{3.10}$$

Under these assumptions, the product $\gamma_{\text{tot}} T_{\text{eff}}$ remains constant, meaning that the force sensitivity S_{FF} stays constant. This means that cold damping does not increase the force sensitivity as dictated by the Brownian motion. This occurs, despite the lowered absolute scale of Brownian motion resulting from the cold-damping. However, one cannot damp the thermal motion of the oscillator without also damping the response to the signal force. Therefore, no improvements can be made by damping.

This analysis did not take into account the effects of imprecision in this measurement. In a similar fashion to what was expressed in Eq. 3.4, where the imprecision of the measurement manifests itself as force noise on the resonator. The only modification needed in this discussion would be for the $\chi(\omega)$ to correspond to that of a damping oscillator with a damping rate of $\gamma + \gamma_d$. This is because when performing the cold-damping, the imprecision in the measurement gets fed back to the oscillator in terms of an extra force term in the equation of motion.

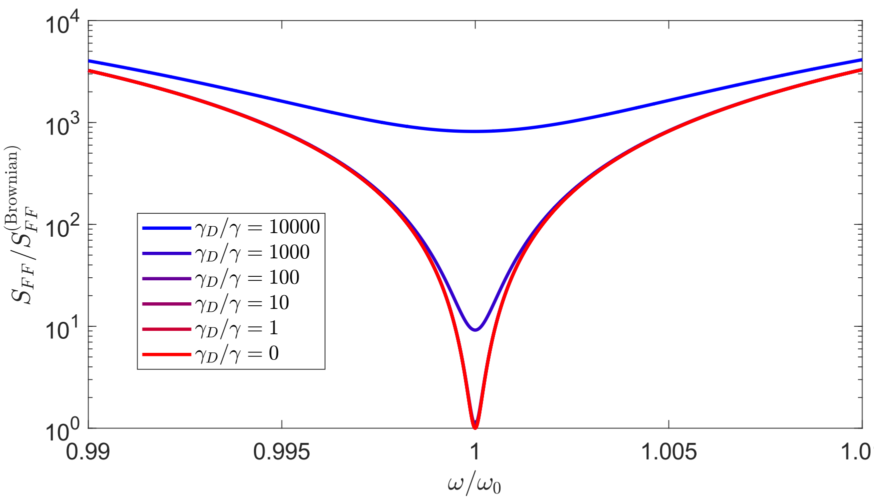

Figure 3.8: Theoretical force power spectral density for an actively damped micromechanical resonator. Here the measurement efficiency was assumed to be ideal, and the readout was shotnoise limited. Furthermore, it was assumed that the thermal occupation of the undamped resonator was much greater than unity. For low values of damping, one sees that there are no appreciable changes to the noise floor of the detector. However, for larger damping rates the imprecision noise is fed back to the resonator as a force that is larger than the thermal force, resulting in diminished performance.

One can see the ramifications of this in Fig. 3.8. Here, we see that at low damping rates, there is no discernible change to the noise floor of the resonator. However, once damping rates become larger, the added noise from the imprecision part of the damping becomes much larger than the pure thermal force, and thus the performance is diminished. One thing of note is that although damping of the resonator results in a wider resonant response bandwidth, it does not increase the sensitivity bandwidth for force detection measurements. Rather, the sensitivity bandwidth is limited — for both damped and undamped oscillators — by where the motion of the resonator is appreciably high with respect to the imprecision noise background.

This is not to say damping does not have technical advantages. As stated previously, working in the force picture and motional pictures are equivalent in terms of pure performance, but the former requires more post-processing of the motional signal in order to infer the force. Working in the motional picture presents difficulties for transient signals that act over a time shorter than the correlation time of the oscillator, but if that correlation time can be shortened — for instance by cold damping — then the interpretation of the data becomes straightforward.

Another reason to damp is for other sensing modalities that infer an external drive via a parametric change to the oscillator parameters. Typically, this parameter change results in a resonant frequency shift, and thus many of these schemes rely on frequency tracking in order to interpret the external signal. These schemes will be discussed later in this work when frequency tracking is discussed in depth. However, a cursory consideration of the problem does reveal that tracking lower dissipation (low γ) resonators presents technical difficulties owing to the narrow spectral response of the resonator. Therefore, damping may aid in applications that seek to measure frequency shifts high-Q mechanical modes for sensing purposes [5].

Chapter 4

Analysis of Membrane Phononic Crystals with Wide Band Gaps and Low-Mass Defects

This chapter will overview a thrust in the Regal group to improve the force-sensing capabilities of silicon nitride membrane resonators. The performance of resonant mechanical force sensors is maximized when both the mass and dissipation of the sensing mode are minimized. To achieve both of these design goals, we utilize a technique pioneered by Tsaturayn *et al.*, where a silicon nitride membrane is patterned with holes to create a phononic crystal (PnC) [49]. We expand upon this technique in an exploration of a wide range of geometries, identifying principles and strategies to create mechanical oscillators with excellent force-sensing capabilities that can be simultaneously probed with free space optics. This chapter will overview this project, beginning with an analytical model that brings an understanding of the structures explored in this work. We will also describe the fabrication of these devices, identifying the specific challenges associated with creating patterned silicon nitride-suspended structures. Finally, we will conclude with measurements of the dissipative properties of an array of devices. The results of these measurements will inform future design decisions when creating future membrane-based forced sensors.

A phononic crystal is an acoustic metamaterial that has discrete translational symmetry. Much like the electronic energy levels of a solid-state crystalline system, the repeated unit cell structure of a phononic crystal gives rise to a nontrivial energy spectrum that can have one or more band gaps [136–138]. Acoustic band gaps can be utilized for a variety of applications. A band gap defines a range of frequencies over which acoustic waves cannot propagate. This allows for the creation of acoustic shields, effectively decoupling an acoustic mode from the environment. This shielding leads to a reduction of radiation loss of the structure, yielding low dissipation mechanical modes in a variety of structures [86, 139–142]. For the application to tensioned mechanical resonators, the use of phononic crystals was first applied to the patterning of the substrate, which housed a simple membrane mechanical oscillator at its center [86]. However, this approach was later extended to the patterning of the membrane itself [49]. Here, the membrane was periodically patterned with a unit cell of holes, save for the center which was patterned in a unique defect structure. This central defect has mechanical modes with resonant frequencies within the acoustic bandgap. These modes oscillator throughout the defect, but upon impinging on the PnC structure, this mode evanescently decays outward. This decay effectively decouples the mechanical mode from its environment by suppressing the mechanical participation in the substrate and beyond. In addition, the evanescent decay of the mode yields improvements in the internal dissipation of the mode through a phenomenon called soft-clamping, where the effects of the clamped boundary conditions at the edge of the membrane structure are also suppressed.

4.1 1D calculation of an acoustic band gap

We will now embark on a theoretical description of PnCs that applies to tensioned membrane structures. To encapsulate many of the key concepts, we will begin by inspecting a 1D version of the problem. We remark here that the analysis directly applies to PnCs in silicon nitride string resonators [50, 51]. For a 1D tensioned string, the width of the string and 1D mass density can be spatially modulated in order to define the PnC structure. Thus the equation of motion can be stated as:

$$\frac{d^2}{dx^2}\left[I(x)E\frac{d^2w(x)}{dx^2}\right] - \mathcal{T}\frac{d^2w(x)}{dx^2} - \rho_{1\mathrm{D}}(x)\frac{d^2w(x)}{dt^2} = 0. \tag{4.1}$$

where $I(x)$ is the geometrical moment of inertial, $\mathcal{T}$ is the tension, $\rho_{1\mathrm{D}}$ is the 1D mass density, and w is the out of plane motion. We note the generality of this model towards both tensioned and non-tensioned mechanical resonators. For non-tensioned resonators, the periodicity required to produce band gaps arises from a periodically modulated moment of inertia or mass density. To accurately predict the properties of the bandgap for a highly tensioned resonator, the 4th-order term can be neglected for this analysis. Doing so reduces the equation to a wave equation with a spatially dependent speed of sound. We can reduce the equation to an eigenvalue problem additionally by also assuming harmonic time dependence:

$$c(x)^2 \frac{d^2 w(x)}{dx^2} + \omega^2 w(x) = 0. \tag{4.2}$$

In the above equation, $c(x)$ is the spatially dependent speed of sound given as $\sqrt{\mathcal{T}/\rho_{1\mathrm{D}}(x)}$. For this analysis, we will now restrict the class of structures we want to investigate. Many PnC designs are constructed a relatively massive areas which we will call pads, connected by narrow constrictions that we will call tethers. In the 1D model, the pads and tethers manifest themselves as a speed of sound that can take on two values v_p and v_t, which correspond to the local speed of sound in a pad and tether respectively. Therefore, within each region, pad, or tether, a solution to the wave equation will appear as:

$$y_k = A_k e^{ikx} + B_k e^{-ik} \tag{4.3}$$

where $k = \omega/c$. Interfaces between pads and tethers will then have reflection and transmission coefficients given as the familiar Fresnel coefficients:

$$r_{pt} = \frac{v_t - v_p}{v_t + v_p} \tag{4.4}$$

$$t_{pt} = \frac{2v_t}{v_t + v_p} \tag{4.5}$$

$$r_{tp} = \frac{v_p - v_t}{v_t + v_p} \tag{4.6}$$

$$t_{tp} = \frac{2v_p}{v_t + v_p}. \tag{4.7}$$

Here r and t correspond to reflection and transmission coefficients, while the subscripts pt and tp indicate the interface type, either going from pad to tether or tether to pad.

To continue with our analysis, we can derive the motion across as a unit cell as a transfer matrix M, which describes the transformation of the amplitude coefficients A_k and B_k across each unit cell of the PnC. The total matrix M will then just be a product of the matrices for each subsection

$$M = M_{hp} M_{tp} M_t M_{pt} M_{hp} \tag{4.8}$$

Here M_{hp} captures the accumulated phase of the plane waves across the half pads at either end of the unit cell. M_t does the same for the tether section, while M_{tp} and M_{pt} account for transmission and reflection at each interface:

$$M_{hp} = \begin{pmatrix} e^{ik_p l_p/2} & 0 \\ 0 & e^{-ik_p l_p/2} \end{pmatrix} \tag{4.9}$$

$$M_{pt} = \begin{pmatrix} t_{pt} - \frac{r_{tp} r_{pt}}{t_{tp}} & \frac{r_{tp}}{t_{tp}} \\ -\frac{r_{pt}}{t_{tp}} & \frac{1}{t_{tp}} \end{pmatrix} \tag{4.10}$$

$$M_t = \begin{pmatrix} e^{ik_t l_t} & 0 \\ 0 & e^{-ik_t l_t} \end{pmatrix} \tag{4.11}$$

$$M_{tp} = \begin{pmatrix} t_{tp} - \frac{r_{pt} r_{tp}}{t_{pt}} & \frac{r_{pt}}{t_{pt}} \\ -\frac{r_{tp}}{t_{pt}} & \frac{1}{t_{pt}} \end{pmatrix} \tag{4.12}$$

where l_p and l_t are the physical length of the pad and tether regions, and k_p and k_t are the wave numbers in the pad and tether regions.

For an infinite, periodic structure, Bloch's theorem states that translation of the solution by one unit cell length (a) gives results in a phase factor multiplication of the original solution:

$$\begin{pmatrix} A_1 \\ B_1 \end{pmatrix} = e^{iKa} \begin{pmatrix} A_0 \\ B_0 \end{pmatrix} \tag{4.13}$$

where

$$\begin{pmatrix} A_1 \\ B_1 \end{pmatrix} = M \begin{pmatrix} A_0 \\ B_0 \end{pmatrix} \tag{4.14}$$

Therefore we have the following eigenvalue problem

$$\begin{pmatrix} M_{11} & M_{12} \\ M_{21} & M_{22} \end{pmatrix} \begin{pmatrix} A_0 \\ B_0 \end{pmatrix} = e^{iKa} \begin{pmatrix} A_0 \\ B_0 \end{pmatrix} \tag{4.15}$$

We note that M is a product of unitary matrices, which places a constraint on its components:

$$M_{11}M_{22} - M_{12}M_{21} = 1 \tag{4.16}$$

Solving the eigenvalue problem gives us the implicit bandgap equation

$$\arccos S = a \tag{4.17}$$

$$S \equiv \frac{M_{11} + M_{22}}{2} \tag{4.18}$$

or written more explicitly as:

$$S = \frac{(V+1)^2}{4V} \cos\omega(t_p + t_t) - \frac{(V-1)^2}{4V} \cos\omega(t_p - t_t) \tag{4.19}$$

where $V = v_t/v_t$. We will refer to V as the contrast of the PnC, as it has direct ties to the properties of the bandgap. t_p and $_t$ are the transit times for the wave to traverse the pad and tether regions respectively. The quantity $t_p + t_t = t_{\text{tot}}$ is of interest as it is inversely proportional to the 1st bandgap center frequency.

An inspection of Eq. 4.17 reveals the condition for a bandgap as when $|S| > 1$, since it enforces an imaginary wavenumber, and thus prohibits traveling wave solutions. The form of S reveals the existence of multiple band gaps since the form of S is a sum of periodic functions in the variable ω. Fig. 4.1 shows calculated bandgaps for a variety of relative pad and tether transit times. We observe

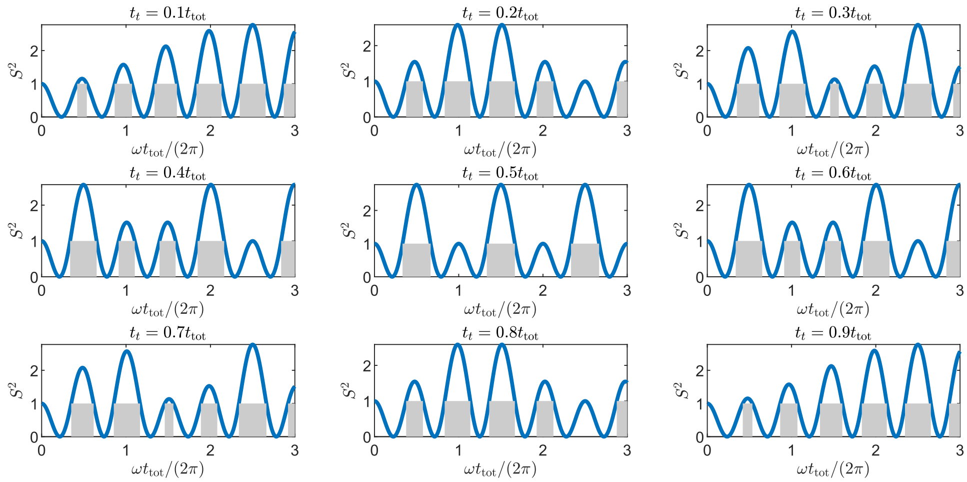

Figure 4.1: Functional form of S^2 for a variety of relative pad and tether transit time values. All plots are calculated for a contrast parameter $V = 3$. Grey-shaded regions indicate theoretical bandgaps. The title of each subplot indicates the transit time of the tether with respect to the total transit time.

that the center of the nth bandgap is located at $\omega t_{\text{tot}}/(\pi) = n$. This condition arises because of the form of the 1st term in Eq. 4.19, which has large magnitude when $\omega t_{\text{tot}}/(\pi) = n$. In the general case of $t_t \neq t_p$, there is a beating in the form of S between the two terms. This beating has the effect of widening and narrowing certain bandgap orders. In the special case of equal transit times, there is no beating effect. This has the effect of removing the even-order bandgaps while widening the odd-order bandgaps. For the purpose of this work, we will only inspect the properties of the 1st bandgap (lowest in frequency) as this bandgap is typically at the most accessible frequency scale. In order to have a large design space, it is useful to maximize this bandgap width for a given value of V. Therefore, working in the equal transit time case is ideal.

Under these conditions, we can derive an expression for the normalized bandgap width:

$$\Delta = \frac{\Delta\omega}{\omega_\pi} = \frac{2}{\pi}\arccos\left(-\frac{1-6V+V^2}{1+2V+V^2}\right) \tag{4.20}$$

Here, Δ is the gap-to-mid-gap ratio. An inspection of Eq. 4.20 reveals that wider bandgaps are produced for larger values of V.

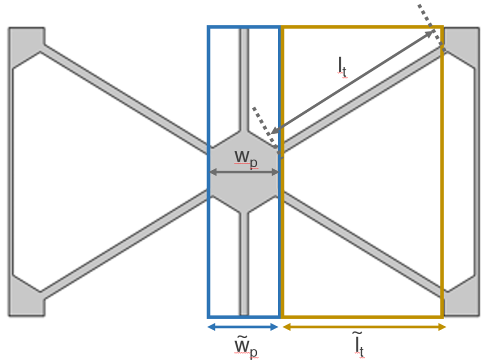

Figure 4.2: Geometry of the 2D to 1D conversion for a pad-tether unit cell. The blue box (orange box) defines the pad region (tether region) of the PnC unit cell.

4.2 Equivalence between 1D model and 2D membrane PnCs

In this section we will investigate the applicability of 1D model results to 2D structures. The approach we will take is to develop a way to map the geometry of a 2D unit cell to an effective 1D unit cell. In doing so, we imagine a traveling plane wave through the 2D structure. Our assumption is that mass that is transverse to the propagation of the wave will act to impede the progress of the wave. With this in mind, we propose the following map:

$$g_{1\mathrm{D}}(x_\mathrm{l}) = \int_G g(x_\mathrm{l}, x_\mathrm{t}) dx_\mathrm{t} \tag{4.21}$$

where x_l and x_t refer to the coordinates along the longitudinal and transverse wave directions respectively, and G refers to the domain of a single unit cell. This mapping effectively collapses the 2D geometry along a single dimension, giving rise to an effective corrugated width. Upon performing the mapping, translation to the pad-tether model presented above requires an assignment of "wide" pad regions and "narrow" tether regions. Assigning these regions is somewhat arbitrary and depends heavily on the geometry of the unit cell.

In this work, we will investigate two unit cells. The first appears in Fig. 4.2, where we have also highlighted the regions assigned to be pads and tethers. It is apparent that this design strongly reflects a pad-tether geometry, by design.

For unit cells of this type, the selection of the pad and tether regions follows naturally from the 2D geometry. Furthermore, the integration carried out in Eq. 4.21 can be carried out using geometric properties. This procedure will perform the transformation $(w_p, w_t, l_p, l_t) \to (\tilde{w}_p, \tilde{w}_t, \tilde{l}_p, \tilde{l}_t)$ of the geometric parameters.

Following this procedure, we derive the following:

$$\rho_p = \frac{\sqrt{3}}{2}\mathrm{w}_p h\rho + \frac{l_t t_w h}{\mathrm{w}_p} \tag{4.22}$$

$$\rho_t = \frac{4}{\sqrt{3}}\mathrm{w}_p h\rho \tag{4.23}$$

$$\tilde{l}_p = l_p \tag{4.24}$$

$$\tilde{l}_t = \frac{\sqrt{3}}{2}l_t \tag{4.25}$$

$$\tilde{\mathcal{T}} = \frac{4}{\sqrt{3}}\sigma t_w h \tag{4.26}$$

$$\tilde{v}_p = [\frac{3\mathrm{w}_p\rho}{8t_w\sigma} + \frac{\sqrt{3}l\rho}{4\mathrm{w}_p\sigma}]^{-\frac{1}{2}} \tag{4.27}$$

$$\tilde{v}_t = \sqrt{\frac{\sigma}{\rho}} \tag{4.28}$$

Inserting these parameters into the 1D model allows for an analytic prediction for unit cell properties without calculating the 2D band structure.

We also study other types of unit cells in this work, namely those developed by Tsaturaryan *et al* [49]. The unit cell geometry can be seen in Fig. 4.3a. Here, a honeycomb lattice is formed from circular holes patterned into the membrane. In this case, a delineation between pad and tether regions is not so well defined. In fact, it can be seen that performing the collapse procedure on this unit cell yields a rather non-trivial form of the effective 1D unit cell, as shown in Fig. 4.3b. However, here we see that there are well-defined dips in the functional form of $g_{\mathrm{1D}}(x)$, which we will elect to define as the "narrow" tether regions. We define the effective pad and tether widths as being the average of $g_{\mathrm{1D}}(x)$ over these respective intervals. A test of the use of this convention can be performed when calculating the true 2D unit cell band gap.

To calculate a 2D bandstructure, the eigenmodes of a single unit cell can be calculated by treating Eq. 1.11 as an eigenvalue problem with Floquet boundary conditions. Analytically

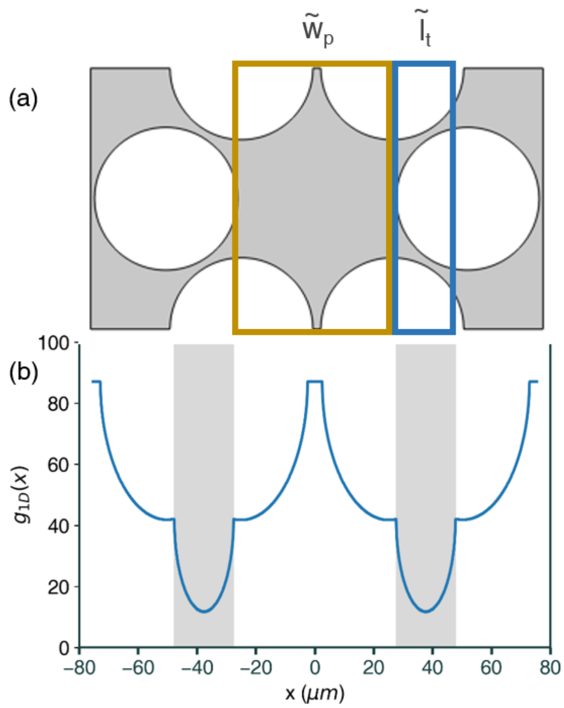

Figure 4.3: Schematic of 1D collapse for a low contrast unit cell. (a) Definition of pad and tether regions inside the low contrast unit cell. (b) Resulting 1D geometry from performing the collapse. The grey regions indicate the high-velocity tether regions used to define V for this unit cell.

speaking, this is a difficult calculation, but it can be readily performed with FEA simulations, which is the approach we will take here. Fig. 4.4 shows the results of such a calculation for a given instance of a unit cell. The left-hand side of the plot shows the physical unit cell, as well as a representation of the unit cell viewed in the reciprocal space of the lattice. Key points in reciprocal space are labeled accordingly. An inspection of the calculated band structure indicates that there is no true bandgap for this structure. Due to the high aspect ratio of this membrane structure, there is a large frequency mismatch between out-of-plane membrane modes and other polarizations. Therefore, while there may be a bandgap for the out-of-plane modes that are usually interested in, generically we observe that other polarizations can persist within this gap.

To test the validity of the 1D model in terms of predicting the properties of band gaps, we can directly compare the results of the 1D model predictions to the results of the 2D model. These

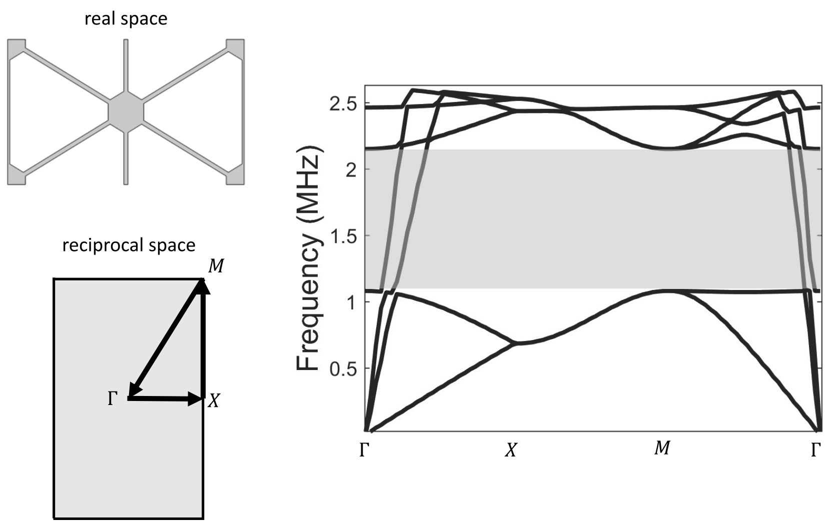

Figure 4.4: Schematic of the procedure to calculate the 2D bandgap. The left-hand side shows the physical unit cell, as well as a schematic representation of the unit cell in reciprocal space. The right-hand side shows the calculated band structure with the bandgap shaded accordingly.

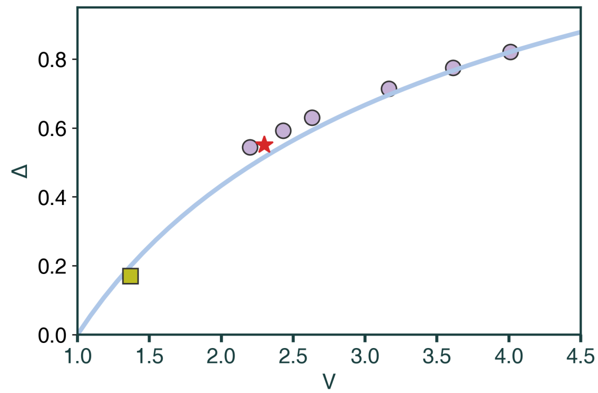

Figure 4.5: Band gap widths as a function of mass contrast as determined from the 1D model. Comparison between different models of the bandgap to mid-gap ratio (Δ) versus PnC contrast (V). Analytic prediction of the 1D model (solid blue line), finite element simulations of equivalent 2D structures (blue circle markers), experimental results of device A (red star marker) and device B (yellow square).

results are seen in Fig. 4.5. It can be seen that over a wide range of geometries, the gap-to-mid-gap ratio Δ is accurately predicted by the 1D model, over a large range of geometries. Amazingly, this is true even for the second type of unit cell, despite the lack of a clear pad-tether delineation. The overall trend presented here shows that larger values of the contrast V result in wider bandgaps. Increasing the contrast can be accomplished by increasing the ratio of pad width to tether width. One trend that is not reflected in Fig. 4.5 is that by increasing V, there is a tendency for the center bandgap frequency ω_π to decrease. This is due to the fact that by introducing wider pads, the stress within each pad must decrease, resulting in a longer net transit time over the unit cell. Therefore, it is not viable to increase the band gap width to arbitrarily high values without lowering the frequencies of all of the eigenmodes.

4.3 Effects of contrast on defect modes

In this section, we will study the effects of contrast on a general defect mode. In doing so, we will study the properties of the defect modes as a function of the contrast parameter. At the outset, we would like to examine the effects of contrast on the soft-clamping effects of defect modes. As stated previously, soft-clamping refers to how a defect mode in a membrane PnC evanescently decays into the PnC crystal bulk. Since the mechanical motion at the boundary of the membrane is largely suppressed, the clamped boundary condition at the edge has a minimal effect on the dissipative properties of the mode. However, we expect the effects of soft-clamping to be influenced by the contrast of the PnC. In the bandgap, the wavenumber of a defect mode becomes imaginary, leading to exponential decay in the surrounding structure. For higher contrast PnCs — which means wider band gaps — the corresponding decay length is expected to be shorter. A shorter decay length has the effect of concentrating the curvature of the mechanical mode over a shorter distance, which might lead to increased dissipation. However, this would mean more isolation of the mechanical mode. Not only does more isolation lead to less radiation loss, but it also might reduce residual effects from the true clamped boundary conditions at the edges. It is not apparent at the outset which effect will be stronger.

To investigate this, we will work in the 1D pad-tether model, with the addition of a 1D defect consisting of an omission of a pad at the center of a finite 1D PnC. We will sweep the contrast while scaling the pad and tether widths to keep the unit cell transit time — and thus the band gap with — constant. We do this in order to keep the defect mode frequency constant and centered in the bandgap. We will then monitor the properties of the defect mode as a function of V, notably the Q and the decay length. The results of this study are presented in Fig. 4.6. We see that as the contrast increases, the gap-to-mid-gap ratio also increases Δ. In doing so, the defect mode has a shortened decay length n_0, expressed in units of the unit cell length. At the same time, the bending loss limited quality factor Q_{bend} also decreases. This simulation takes into account the effects of clamping loss at the edges. Therefore, we can infer that the effects of the shortened decay length outweigh the effects of diminishing the true clamping losses at the edge of the membrane. This reveals a tradeoff for increasingly high-contrast PnC devices, where wider bandgaps diminish the effects of soft-clamping.

We also investigate the effects of contrast on the phononic isolation of a mode. By phononic isolation, we mean the ability for a PnC to energetically isolate a defect mode from the environment and *vice versa*. We will perform this investigation in a finite, 2D setting. The comparison will be

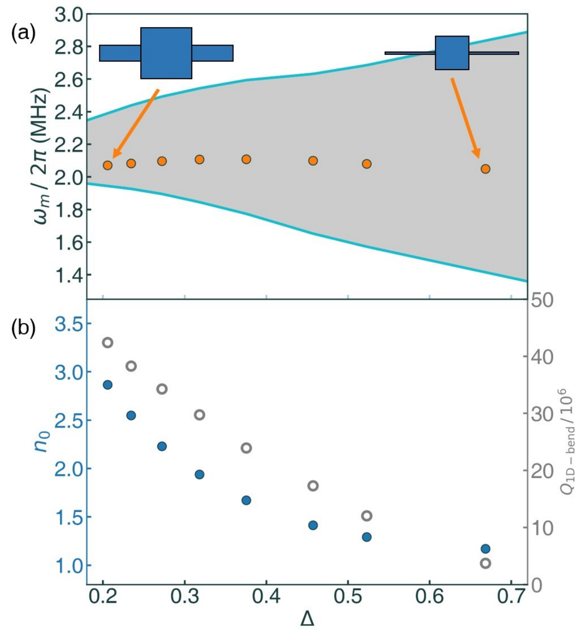

Figure 4.6: Top: Orange points correspond to defect-mode frequency as a function of Δ. The bandgap is shaded in grey. Bottom: blue points show the defect mode decay length in units of unit cell length. Open grey points show the prediction of the bending loss limited $Q = Q_{\text{bend}}$. Overall, the trend is that while the decay length decreases, the predicted bending loss limited Q also decreases.

between two devices with distinct unit cells and is mainly done to reveal conceptual trends. As a way to probe isolation, we will sweep the number of unit cells used to construct the finite structure. To quantify the isolation, we will compare the fraction of energy of the mode that is contained within 10 microns of the clamped boundary, a ratio called ΔU. Fig. 4.7 shows the results for two such devices, one with a high contrast PnC, the other with a low contrast PnC. We see a few trends, the first of which is that lower contrast PnC provides a much stronger degree of phononic isolation. In addition, the rate at which the isolation increases per unit cell added to the structure is much higher than that of the low contrast PnC. This reveals an advantage of high-contrast PnCs, namely that an appreciable amount of phononic isolation can be achieved with relatively few unit cells, meaning that the overall membrane size will be smaller. Smaller membrane sizes present technical advantages in the context of cavity optomechanics. Low-frequency membrane modes will have higher absolute Brownian motion due to the equipartition theorem. When situated in a high-finesse optical cavity, these membrane modes will be seen as a cavity length change that can destabilize the optomechanical system, often requiring active damping of these modes in order to lock the optical cavity [37]. Therefore, devices based around high-contrast PnCs have the potential to yield more stable systems overall.

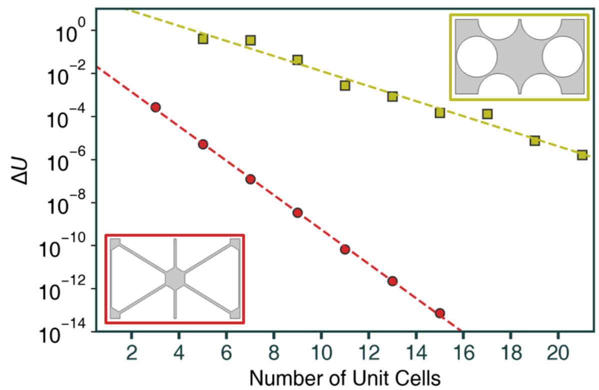

Figure 4.7: Comparison of the phononic isolation of two membrane PnC devices extracted from FEA simulations. The high (low) contrast PnC results, as well as the corresponding unit cell, are highlighted in red (yellow).

In regard to contrast, we have identified a few tradeoffs. Firstly, high-contrast PnCs afford more phononic isolation, meaning that radiative losses can be suppressed strongly with fewer unit cells. Such devices will therefore be smaller in footprint, which has a few advantages. The first is the reduction of thermal motion of the fundamental membrane modes of the structure, which will give rise to better stability in high-vibration environments. Also, the smaller device footprint will allow the PnC structure to better thermalize under local heat loads. We will discuss this topic in depth in Ch. 5. However, working with higher-contrast PnCs comes at the cost of higher internal dissipation. When considering which PnC to use for a certain application, it is therefore important to consider what the expected loss pathways will be. For room temperature applications, internal losses are expected to be higher, and thus one should use designs with are more soft-clamped, and therefore have lower contrast. In cryogenic conditions, especially at dilution refrigerator temperatures, Q_{int} can become more than 10 times higher than the room temperature values, meaning that radiative losses can become dominant [115]. Additionally, more phononic isolation can lead to the suppression of external vibrations, which are a source of technical noise in cryogenic systems. We thus identify higher contrast PnCs to have advantages at these temperatures.

4.4 Fabrication of silicon nitride membrane PnC devices

In order to test the concepts revealed in the previous section, we elected to fabricate an array of membrane PnC devices with a wide range of both PnC unit cell and defect geometries. Here we will describe the fabrication process.

Devices were fabricated on a 375 µm thick 3-inch diameter silicon wafer with 100 nm of grown stoichiometric LPCVD silicon nitride on either side. Designs were patterned using a direct write photolithography system after spinning 1 µm of SPR-660 photoresist onto either side. The top of the wafer was patterned with the PnC designs, while the back was patterned with rectangular windows aligned to each PnC. The patterning was done on both sides with $300\,\mathrm{mJ\,cm^{-2}}$ of 405 nm light. During these steps, the wafer was affixed to a sapphire carrier wafer with Crystalbond 509 in order to protect the bottom side from unwanted processing. Patterning of the silicon nitride was completed via a CF_4 reactive ion etch. The wafer was then cleaned with O_2 plasma followed by ultrasound cleaning in an acetone bath. Additional cleaning was performed with isopropyl alcohol and water.

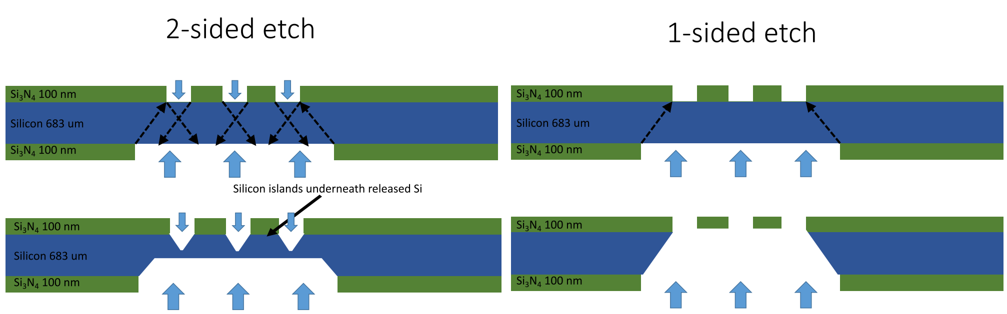

Figure 4.8: Comparison between 2-sided and 1-sided KOH etching. Displayed is a cross-section of the wafer following photolithographic patterning of the window and device side of the wafer. The top row shows the initial configuration of the wafers, as well as locations of KOH etching (blue arrows) and projected anisotropic KOH etching pathways (dashed arrows). The bottom row shows the etch part way through for the 2-sided etch, and completed for the 1-sided etch.

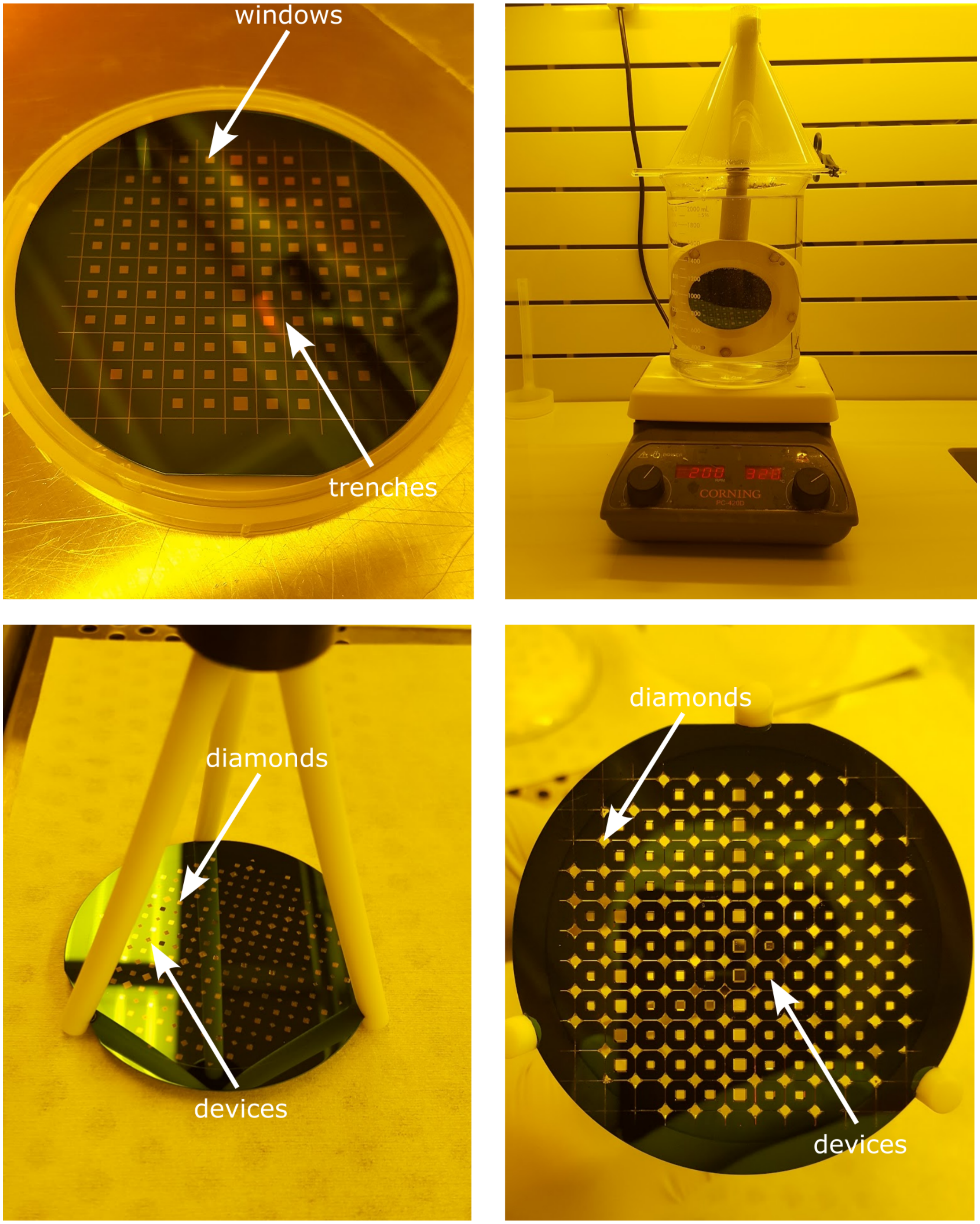

Figure 4.9: top left: window side of the wafer prior to the KOH etch. The wafer was patterned with trenches of exposed silicon nitride to be used as score lines for dicing. top right: PEEK chuck inside of KOH bath. bottom left: device side of the wafer post-KOH etch. Labeled are the “diamond” membranes that resulted from poor corner compensation of the dicing trenches. bottom right: wafer viewed from the back post etch.

To suspend the PnC structures, the window side of the wafer was etched using an 80 C KOH bath. The PnC side was protected via a PEEK wafer holder. Following wet etching, the wafer was cleaned in a Nanostrip bath, acetone, and isopropyl alcohol. We note that the KOH etch step of the process has many technical aspects that warrant discussion. Notably, we found that a one-sided KOH etch was necessary for devices to survive KOH etching. This contrasts a similar process used for trampoline resonators, where a double-sided KOH etch is sufficient. A schematic of the anisotropic etch geometry is shown in Fig. 4.8 in the two cases. For the 2-sided etch case, we see that at some point part of the way through the etch, there will be large islands of suspended silicon below the patterned device structure. We expect these islands to be unstable and provide potential failure points for the etching process. For a PnC device, there are hundreds of such failure points, meaning that the probability that a single tether breaks during the etch to occur with high probability. For a trampoline, the number of failure points is much smaller, meaning that double-sided etching is sufficient for fabricating trampolines with relatively high yield. We can circumvent this issue by doing a single-sided etch. For a single-sided etch, these islands of silicon are etched prior to the release of the PnC structure, alleviating the issue entirely.

Single-sided etching requires specialized cleanroom equipment. For this specific fabrication run, an AMMT wafer-holder single PEEK wet etching chuck was used to hold the wafer in a bath of KOH. KOH is prevented from attacking the backside of the wafer by an o-ring pressed against the front side of the wafer. Care needs to be taken when situating the wafer in the KOH bath. The chemical nature of the etch produces large amounts of H_2 bubbles to form throughout the etch. If the buoyant force on a bubble pushes it into the device, the surface tension of a single bubble has the potential to destroy an entire membrane. Thus the wafer should be situated such that the bubbles have a free pathway to the surface of the KOH bath, which amounts to angling the windows slightly upward in the KOH bath.

In order to dice the wafers post-etch, a "candy-bar" approach was utilized. On the window side of the wafer, 150-micron-wide trenches of nitride were exposed in the photolithography step. The subsequent KOH etch will cut grooves partway through the silicon wafer, defining score lines around each chip. Applying light torque to the now-scored chip along a score line will induce a separation of the wafer along said line. A repetition of this process allows for each chip to be separated from the wafer individually. This particular fabrication run had one unexpected consequence of this approach. At the intersection of two perpendicular trenches, the KOH etch will attack each of the four corners to etch a diamond pattern in the silicon wafer. With the trench dimensions used in this fabrication run, this amounted to unintended diamond membranes being etched at the corner of each intended device chip (Fig. 4.9). For future fabrication runs, the geometry of the trenches at intersection points should be changed as to avoid this effect.

4.5 Characterization of PnC membrane devices

This fabrication run of the experiment produced 7 distinct device geometries. For the interest of simplicity of analysis and narrowing the focus of the study, 5 of these devices were measured at both room temperature and 4 Kelvin. We will call these devices $A - E$ for identification. Across all devices, 2 devices have a high-contrast unit cell (devices A and E), while 3 devices have a lower-contrast unit cell (devices B, C, and D). The unit cell dimensions of each device are delineated in Fig. 4.10.

For this particular characterization, we elected to use an alternative optical interferometer to what was described in Ch. 2. Here, we construct an etalon by placing the device in question on top of a highly reflective mirror. The etalon was assembled such that there was likely a tilt between the mirror and device, meaning that the reflected light from the etalon had two beams: the prompt reflection from the device chip and the reflection from the highly reflective mirror (higher orders of the etalon can be neglected if the etalon is not well aligned). We note that if the etalon is perfectly aligned, conservation of energy prohibits a power fluctuation when probed in reflection due do the perfect reflectivity of the bottom mirror. Combining these two beams on a single photodetector generates power fluctuations of the light which correspond to the motion of the micromechanical device (see Fig. 4.11). We note that this scheme of measurement is not easily calibrated, since that requires precise knowledge of the etalon. However, this work mainly was interested in the

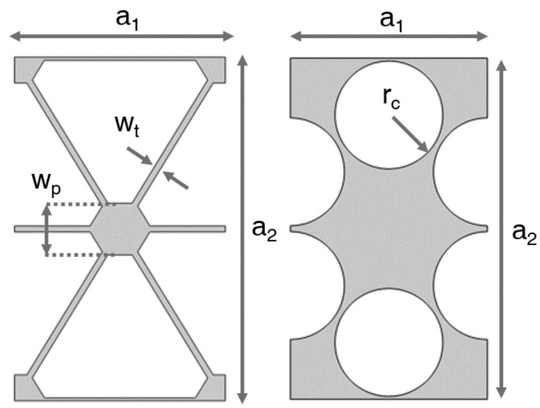

Device	a_1	a_2	n_x	n_y	w$_p$	w$_t$	r_c
A	100 µm	172 µm	12	7	30 µm	2.5 µm	–
B	87 µm	151 µm	19	11	–	–	23 µm
C	111 µm	192 µm	9	5	–	–	31 µm
D	67 µm	116 µm	15	9	–	–	18 µm
E	100 µm	172 µm	12	7	30 µm	2.5 µm	–

Figure 4.10: Critical dimensions for the unit cells of all fabricated devices. Dimensions in the table are defined above. n_x, n_y are the unit cell numbers of the PnC along the X, Y axes. Table entries are omitted where they do not apply. Fabricated devices for A and C included fillets of radii 2.5 µm at the sharp corners of the pad.

dissipative and spectral properties of the motion, and thus calibration was not necessary. We do note that this method of measurement most likely has poor imprecision properties due to a lack of control between the DC phase offset between the two beams. Practically speaking, a *ad hoc* method was developed in order to maximize the sensitivity of the measurement. The method began by performing a network analyzer measurement of the device where the drive was supplied via a piezo situated beneath the etalon. This driven measurement allows for the identification of resonances even in the case of low sensitivity. Once a mechanical mode is identified using this method, the drive is paused on resonance, while the network analyzer signal is continually recorded in a zero-span setting. In this configuration, the optics are incrementally aligned to maximize the network analyzer signal, and thus optical coupling to the mechanical mode of interest. This procedure is terminated once the sensitivity is maximized.

Example spectra for devices A and B are shown in Fig. 4.13. We see that when probing in the

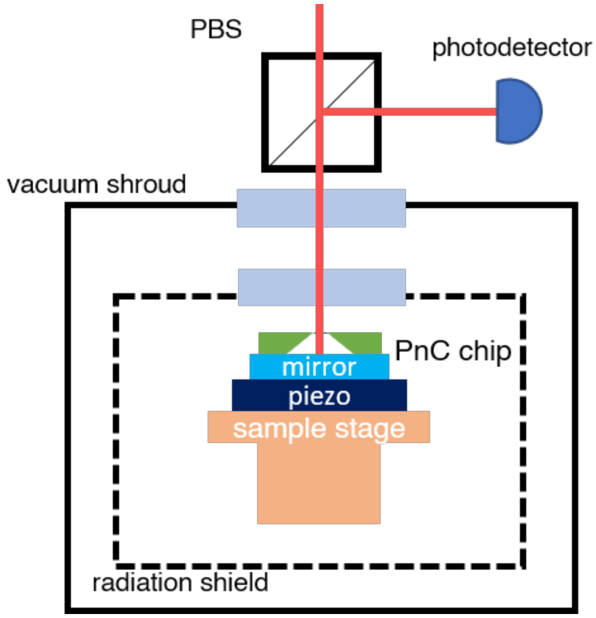

Figure 4.11: Schematic of the experimental apparatus used for measuring both mechanical spectra and ringdowns. The mechanics chip (green) is affixed atop a stack of a piezo electrical transducer (dark blue) and a highly reflective mirror (light blue). This stack is mounted onto a stage linked to the sample stage (cold stage) for room temperature (4K) measurements. The solid box represents the vacuum shroud for both the room temperature and 4K apparatus while the dashed box represents the radiation shield present for 4K measurements. The reflected light off the stack is sent to a photodiode via a polarizing beam splitter.

crystal bulk, a wide frequency band of no mechanical modes is observed, indicating the existence of a bandgap for out-of-plane modes. In order to observe the bandgap, one must probe on a tether rather than a pad. This is because modes with frequencies above the upper band edge consist of primarily the motion of tethers, while the pads stay stationary. Repeating this measurement while probing near the defect reveals extra mechanical modes inside of the bandgap, revealing the existence of in-band-gap defect modes. For the case of device A, there is one such mode, near the lower band edge, while for device B, there are many defect modes inside of the bandgap. We see that by comparing the spectra for devices A and B, the higher contrast PnC has a much wider bandgap than that of device B as expected. All devices were measured at room temperature and 4 Kelvin. This was done in order to observe a difference in the dissipative properties of silicon nitride, as well as other thermal effects. For the spectrum, measuring at 4 Kelvin had the effect of lowering the mechanical frequency of all modes. We attribute this to a differential thermal contraction between the silicon nitride membrane and the silicon substrate. Since the frequencies dropped, we believe that the stress of the silicon nitride dropped. This means that the silicon substrate contracted more than the silicon nitride membrane.

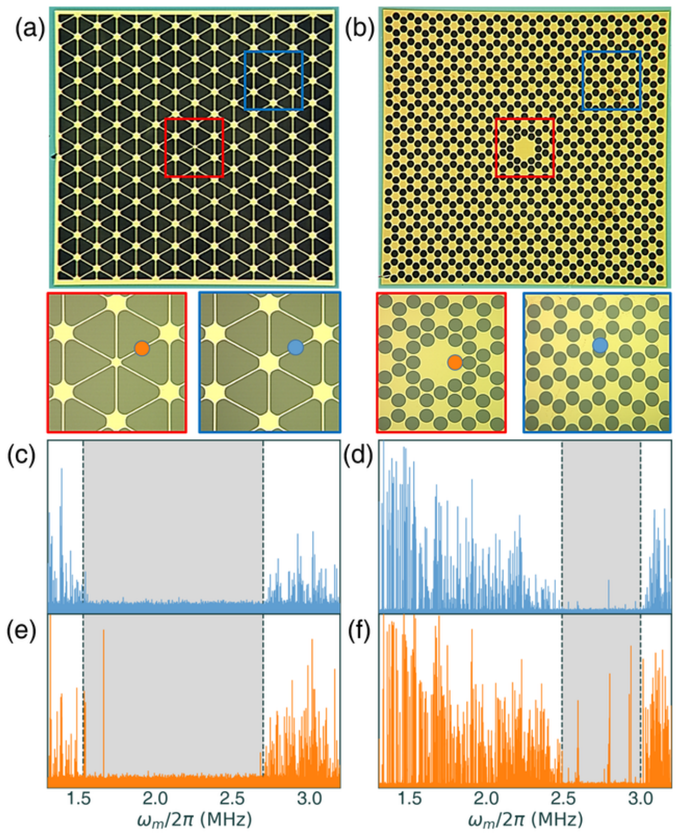

Figure 4.12: (a,b) Optical microscope image of high and low mass contrast PnC devices containing a defect respectively. The displacement of the devices was measured both in the crystal bulk (blue) and at the defect (orange). (c,e) Thermal noise spectra of the high contrast device on a logarithmic scale. The defect mode shown in (e) is the fundamental symmetric mode. (d,f) Mechanical spectra for the low contrast device on a logarithmic scale. The device was driven with sufficient white noise in order to observe all expected defect modes. The spectrum shown in (f) contains 5 separate defect modes within the bandgap, including the second symmetric mode examined in this study. Defect mode frequencies in both (e) and (f) agree with predictions from 2D FEA simulations. Mechanical modes that appear inside the bandgap in (d) have quality factors less than 100 and therefore are most likely hybridized modes between the membrane and the silicon chip or mounting assembly.

For all modes studied in this work, the dissipative properties were obtained by performing ringdown measurements. After obtaining the resonant mechanical frequency, a strong resonant drive was applied to the piezoelectric transducer situated below the mechanical device. After a sufficient drive time, the piezo signal was quickly turned off, allowing the oscillator to freely decay. In order to characterize the linear properties of the oscillator, the drive was adjusted on a mode-by-mode basis in order to avoid driving to high amplitudes (greater than 1 nm) as to not activate the Duffing nonlinearity term in the equations of motion [77]. Since these measurements were not calibrated, network analyzer measurements sweeping across resonance were performed in order to determine the onset of nonlinearity. The quality factor was then extracted from the free decay time of the mode's motion.

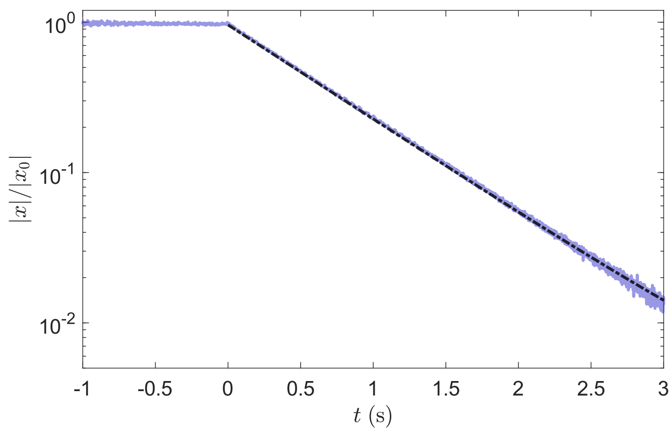

Figure 4.13: Example ringdown of the symmetric defect mode (resonant frequency of 2.55 MHz) of device B. The resonant drive was turned off at $t = 0$. The dashed line is an exponential fit to the free decay of the motion.

In general, all devices measured have multiple defect modes. This work narrowed its focus to defect modes that are symmetric, or that have the center pad of each defect moving appreciably. Such modes have relatively large pads conducive to optical probing, even in high-finesse optical cavities. This means that the effects of imprecision on the force sensitivity of these modes can be minimized, leading to larger detection bandwidths.

The defect modes and devices that we will analyze appear in Fig. 4.14. Here, we designed a series of defects of variable characteristics and performance. The top row of Fig. 4.14 shows optical microscope images in the vicinity of the geometric defect for the devices studied in this work. The

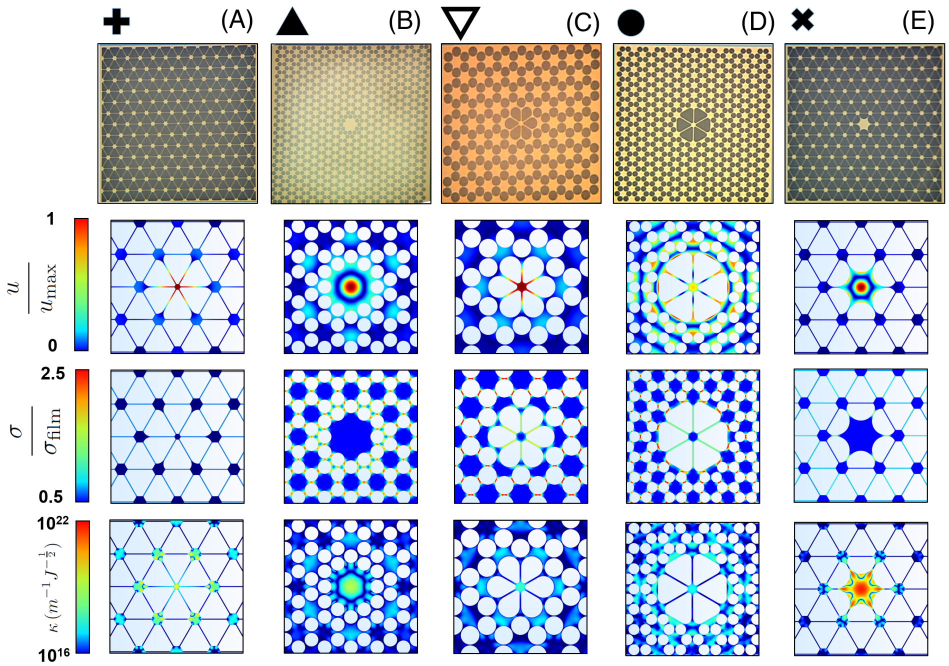

Figure 4.14: Compilation of all devices presented in this work. In the first row are optical microscope images of suspended phononic structures. Above are device labels that correspond to device properties plotted in Fig. 4.15. The second row presents FEM simulations of symmetric defect mode shapes. The third row shows FEM simulations of the static stress distribution normalized to the film stress. The fourth row displays the normalized bending loss density.

second row in Fig. 4.14 shows the displacement of each defect mode. We see that the modes have motion that is heavily confined to the vicinity of the geometric defect. The final two rows show the stress distribution and curvature map of each mode respectively. Note that the symbols at the top of Fig. 4.14 function as a legend in order to read Fig. 4.15.

Fig. 4.15a shows the observed quality factor at ambient and cryogenic temperatures for the defect modes tabulated in Fig. 4.14. These observations are plotted against a quantity L_s defined as follows:

$$\kappa = \frac{1}{U}(\partial_x^2 u(x,y) + \partial_y^2 u(x,y))^2 \tag{4.29}$$

$$L_{\mathrm{s}} = \int \kappa(x,y)dxdy \tag{4.30}$$

where U is the energy stored in the mode. We note that this is just another way to express the expected bending-loss-limited quality factor of the mode as defined in Eq. 1.44 but with less modern conventions on notation. However, it is still a valid way to predict the observed Q, and it was used in this section of the work. In Fig. 4.15a the expected Q_{bend} is plotted as dashed lines as a function of L_s. The first notable trend is the increase in quality factor for the 4 K data. This amounts to an improvement in Q_{int} by about a factor of 3 just by lowering the temperature of the device. We see that broadly, the theoretical values of L_s map well to the observed quality factors at both room temperature and 4 K. Notably, we see a spread in the dissipative properties across all modes. At room temperature, the devices housed in low-contrast PnCs tend to have the highest values of Q, as would be expected from 1D model simulations. This trend does not necessarily occur at lower temperatures, where the high-contrast structures exhibit higher increases in Q. There is a possibility that the low-contrast devices began to see effects of radiative losses for these measurements, but given the low-sample size of these measurements, we cannot necessarily claim that this was the reason for the observed effect.

For the low-contrast devices, we see a large change in Q resulting from the specific defect design. The reason for this can be seen in Fig. 4.14 in the form of the curvature map. For device E, the large central map exhibits a complex yet overall relatively large form of curvature, which should result in a lower quality factor. This curvature results from the geometry of this specific defect, where the large pad is held at only 6 points and has low stress. Since the edges of the pad are free to move, the motion of the center of the pad leads to the large curvature at the edges. Device A has the same defect archetype — a trampoline embedded in a PnC — albeit with a much smaller pad. The smaller pad size largely alleviates the curvature contribution from the pad. We note that the effect observed in device E is not solely defined by the presence of a large, stress-released pad, as evidenced by the same characteristics arising in device B. Rather, we assert that the support structure of the pad plays an important role in defining the dissipation. Device B supports the released pad with an intricate network of higher-stress tethers, which restricts the motion at the pad edges. This reduces the curvature greatly, giving rise to a large-pad device with low dissipation.

This specific study targeted the design of micromechanical membrane-based force sensors.

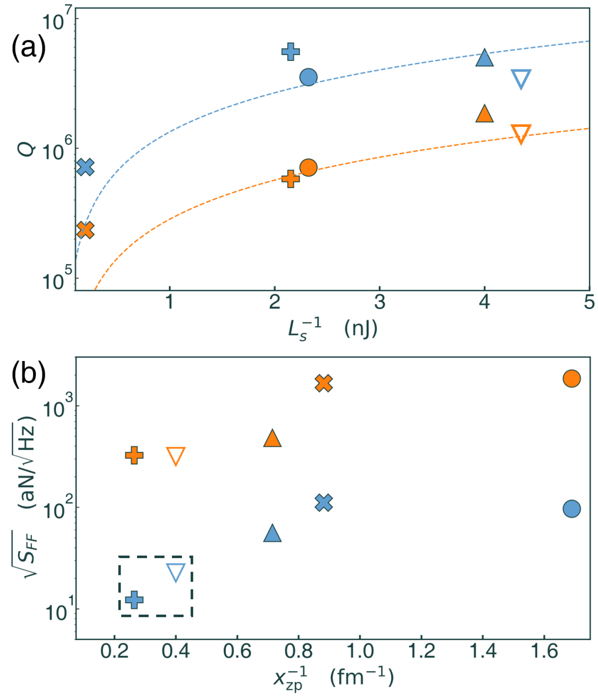

Figure 4.15: (a) Quality factor dependence on the loss factor L_s for all fabricated devices, measured at room temperature (orange), and at 4 K (blue). The symbols correspond to the key presented in Fig. 4.14. Dashed lines represent calculated Q-values determined from bending losses, with $E_2 = 80\,\mathrm{MPa}$ for the room temperature data and $E_2 = 17\,\mathrm{MPa}$ for 4 K. (b) Calculated force sensitivity at room temperature (orange) and at cryogenic conditions (blue). The box is to emphasize the similarity in defect design and performance between devices A and C.

The force sensitivity of each mode is thus plotted in Fig. 4.15 against x_{zp}^{-1} which is proportional to $m_{\mathrm{eff}}^{1/2}$ for each mode. Overall, the general trend is that the less massive modes yield the best force sensitivity. Notably, we have indicated the two best devices, devices A and C as having the same defect archetype — a small pad trampoline — but housed in the two PnC types studied in this work. The performance of these two devices is relatively self-explanatory, being that they have small physical mass while also being soft-clamped, and thus low dissipation. We note that the rather weak performance of device D, which despite having a trampoline design for its defect, has poor force sensing capabilities. This is due to the mode geometry, which has a large participation in the low-contrast PnC structure. This specific device targeted a higher-order symmetric mode of the defect, which results in an antinode of motion residing at the defect-PnC interface. This results in a larger PnC participation in the mode, and therefore high effective mass.

Device	$\omega_{\mathrm{m}}/2\pi$	$\mathrm{x_{zp}}$	Δ	ΔU	$\mathrm{w_{defect}}$	$\omega_0/2\pi$
A	1.65 MHz	3.8 fm	0.55	5.6×10^{-7}	15 µm	189 kHz
B	2.55 MHz	1.4 fm	0.17	2.3×10^{-2}	130 µm	174 kHz
C	1.70 MHz	2.2 fm	0.19	6.9×10^{-2}	30 µm	242 kHz
D	3.41 MHz	0.6 fm	0.24	3.2×10^{-2}	30 µm	246 kHz
E	2.39 MHz	1.1 fm	0.55	1.9×10^{-8}	80 µm	181 kHz

Figure 4.16: Tabulation of key parameters for each symmetric defect mode for all fabricated devices. Note the correlation between Δ and phononic isolation (ΔU).

In a discussion of the overall performance of these devices, we see that these devices reach the 10 aN/$\sqrt{\mathrm{Hz}}$ scale. This number can be improved in a myriad of ways. Firstly, reducing the thickness of the membrane results in an increase of the force sensing. It can be shown that for soft-clamped modes, $Q \sim 1/h$ and $m_{\mathrm{eff}} \sim h$. Therefore, $\sqrt{S_{FF}} \sim h$. 20 nm silicon nitride membranes are routinely used in optomechanical experiments, so we anticipate that these exact devices fabricated from 20 nm membranes would perform at the aN/$\sqrt{\mathrm{Hz}}$ scale [1, 49]. Additionally, operating at dilution refrigerator temperatures would provide 100 zN/$\sqrt{\mathrm{Hz}}$ performance from the temperature decrease alone. One should expect even better than this scale since Q_{int} of silicon nitride also improves at these temperatures. Further improvements could be made by changing the geometry of the defect modes studied. As noted in Tab 4.16, the defect pad width was maintained to be at least 15 microns in this work. This was chosen to be readily read out by free-space optical beams and to be easily interfaced with high-finesse Fabry-Perot cavities without added technical noises. If one relaxes this constraint, improvements can be made.

To see why, we will make scaling arguments of S_{FF} for 1D and 2D defects. The only parameters we need to consider are Q and m_{eff} in this discussion. It is important to delineate between 1D and 2D defects since m_{eff} will have different scaling for each. One scaling to explore would be to look at the frequency dependence of the force sensitivity for soft-clamped modes. We imagine scaling the frequency by changing the length scale of the device in question, where the frequency $f \sim 1/L$, where L is the length scale of the device. It can be shown that $Q \sim f^{-2}$ for soft-clamped modes [51]. Therefore, S_{FF} has a scaling of L^{n-3}, where n is the dimensionality of the defect. Therefore, we see that for both 1D and 2D devices, larger devices yield improved force sensitivities, with a stronger scaling for 1D devices. We should note that this scaling runs into technical difficulties rather quickly. To our knowledge, the longest silicon nitride string resonators fabricated to date are 7 mm long, and we anticipate that higher aspect ratio devices will become difficult to fabricate and cumbersome to operate [51]. Also, despite the potentially better scaling, moving towards 1D resonators makes the optical readout much more complicated, either requiring more advanced free space optics in order to produce diffraction-limited probe beams or abandoning the free space approach altogether in favor of integrated optical readout.

4.5.1 Additional defect designs

We have established the benefits of utilizing high-contrast PnCs with small-pad trampoline defects, the archetype of device A. One large drawback of this device is the location of the defect mode within the bandgap. Notably, the frequency is near the lower band edge (Fig. 4.13). This is undesirable for a host of factors. First, it is advantageous to have a clean bandwidth around the mode in question for ease of optical detection. Making the relative detunings between modes can also diminish the effects that might arise from hybridization with spectrally nearby mechanical modes. Finally, if one wants to mass-load such a mode, the placement of the mode within the bandgap will place limits on the scale of mass that can be successfully added while keeping the mechanical frequency within the bandgap. Boosting the frequency up in the bandgap is a source of difficulty, however. Notably, it cannot be achieved by shrinking the pad size down; in fact, the defect mode frequency of a string defect will be around the frequency of the defect mode in device A. This is due to a property of PnCs, where modes near the lower band edge have a wavelength roughly equal to that of a single unit cell, which is the desired geometry for the defect mode in device A. Therefore, any efforts to augment the geometry while maintaining a similar modal geometry will result in a similar relative location within the bandgap. Thus, a more complex modal geometry is necessary in order to place a defect mode closer to the center of the bandgap.

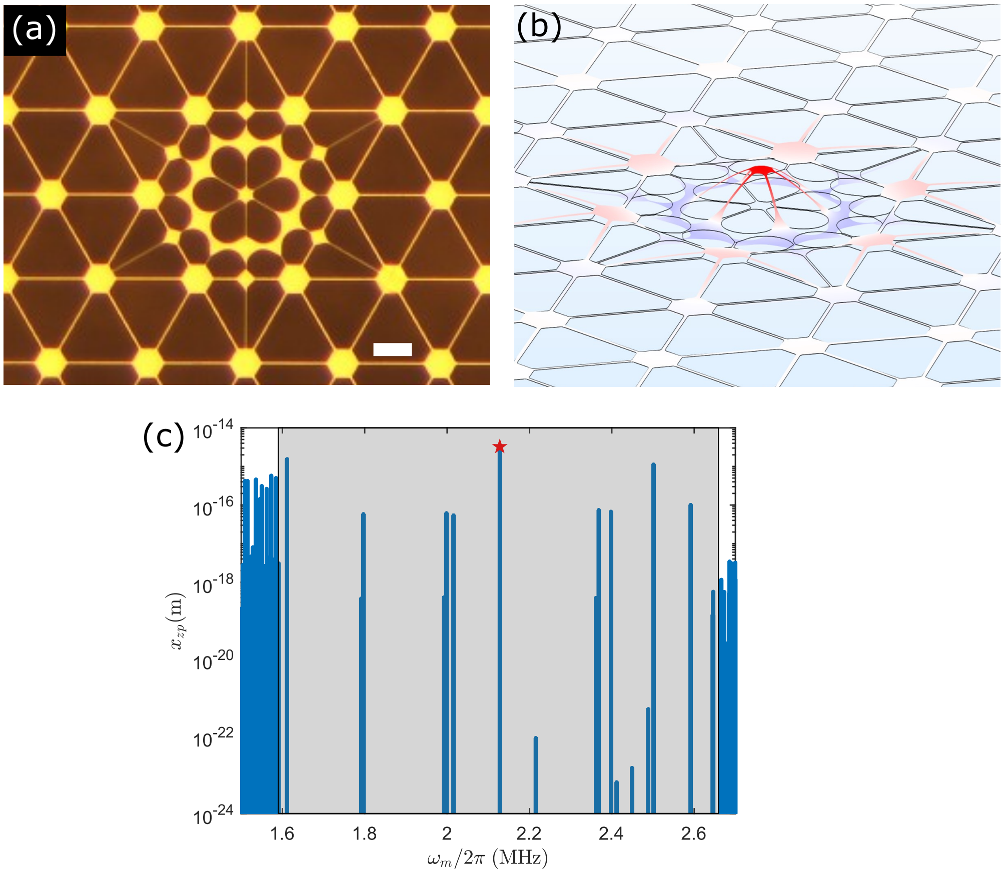

Figure 4.17: (a) Optical microscope image of the snowflake design. The scale bar is 30 microns. (b) FEA simulation of the defect mode profile. (c) Simulated mechanical mode spectra for probing at the center of the device. The bandgap is indicated by the region shaded grey. As a proxy for observed mechanical amplitude, we plot x_{zp} when probed at the center of the device, while assuming that each mode has a linewidth of 1 Hz. The red star marks the defect mode displayed in (b). We see that the defect mode lies in the center of the bandgap.

Fig. 4.17 shows a more intricate defect design that aims to put a trampoline defect mode in the center of the bandgap. The mode frequency is higher due to the addition of an inner support structure within the defect unit cell. This makes the resulting defect mode have a shorter wavelength, and thus a higher mechanical frequency. This is also achieved because the defect-trampoline tethers are rotated 30 degrees from those in device A. To maintain tension in these tethers, longer support tethers were added that connected to unit cells deeper within the PnC. Fillets were added by trial and error in order to form the desired mode. We emphasize that the exact design was achieved by sweeping over many geometric parameters, including tether widths and fillet radii. In general, this is the typical approach for designing defects for 2D PnCs. Although the device was fabricated for this work, it was never characterized. However, given the overall agreement between FEA simulation and observed mechanical properties of membrane PnC devices characterized thus far, we are confident in projections from FEA simulations of this device. With this in mind, we expect that the defect mode shown in Fig. 4.17 to have a room temperature force sensitivity of around 80 aN/$\sqrt{\text{Hz}}$, or a 4 K sensitivity of 5 aN/$\sqrt{\text{Hz}}$.

Chapter 5

Direct Measurement of A Spatially Varying Thermal Bath Using Brownian Motion

Micromechanical resonators are widely used as precision sensors and for scientific studies in classical and quantum mechanics. Their fundamental performance limit stems from the Brownian motion of each mechanical mode. A noteworthy case for non-uniform temperature is under optical detection or coupling (such as often encountered in the field of optomechanics), where localized light absorption leads to the illuminated point being significantly hotter. Under these conditions, it is pertinent to ask how the variety of modes studied in this work, from global membrane modes to localized defect modes, are differentially affected. In this chapter, we test a model that predicts the Brownian motion of a mechanical mode based on its spatial distribution of dissipation. We validate our model by studying both membrane and defect modes of a phononic crystal device in the presence of a thermal gradient. We create a large Brownian motion difference between different modes, such that on a 1 mm scale device, two modes exhibited thermal motion corresponding to temperatures of 293 K and 1700 K, simultaneously. This large modal difference enables calibration of thermal material parameters in their nano-scale values, e.g. emissivity and thermal conductivity. By identifying modes that are sensitive to the temperature at localized parts of the resonator, and even far from where they move the most, we create new design metrics for maintaining cold resonator modes in the presence of strong optomechanical coupling.

5.1 Mechanical systems in contact with nonuniform thermal baths

The common treatment for the study of Brownian motion of a single mode of a micro-mechanical oscillator is to treat each mode as a single degree of freedom of a simple harmonic oscillator. This single degree of freedom is considered to be in equilibrium with a thermal bath with a temperature T. In this case, the equipartition theorem states that the variance of the position degree of freedom of the oscillator is given as:

$$\langle x^2 \rangle = \frac{k_B T}{m\omega_i^2} \tag{5.1}$$

where k_B is the Boltzmann constant, and m and ω_i are the mass and resonant angular frequency of the oscillator respectively. There are many assumptions involved in reducing the continuous description of a mechanical mode of a micro-mechanical system to this simpler description parameterized by a few parameters. It has already been discussed in this work how the motion inferred by probing continuum mode shape at a set location can be described by an effective mass Eq. 1.21, but the treatment of T in this equation has assumed to be the trivial case that this effective single degree of freedom is coupled to a singular thermal bath. This description is insufficient in more general cases, such as when the mode in question experiences a gradient of physical temperature, or when the oscillator is subject to more than one channel of dissipation. These situations need to be treated with care, notably because they fall under the category of non-equilibrium steady states (NESS) of the system since the thermodynamic concept of equilibrium cannot occur in such systems. For the equilibrium case where the thermal bath can be considered to be at a single temperature, there is no heat exchange between the system and bath, while for a NESS, this is not the case. A simple picture is that since the system is subject to multiple baths at different temperatures (or a continuously varying bath), then heat flow must be present in the system, even if the functional form of the heat flow does not change in time [143].

In order to model this complex situation of a spatially varying local bath, we will recall the fluctuation-dissipation theorem, which codifies the link between dissipation and modal temperature:

$$S_{xx} = -\frac{4k_B T}{\omega}\mathrm{Im}(\chi). \tag{5.2}$$

χ is the linear susceptibility of the system of interest.

In Eq. 5.2, it is notable to observe the presence of both the $\mathrm{Im}(\chi)$, the dissipative part of the susceptibility, and the temperature of the thermal bath of the system. Therefore, all forms of dissipation give rise to fluctuations– or noise – in the system, with the magnitude of the fluctuations scaling with both the temperature of the thermal bath of the system, as well as the strength of the dissipation rate. With these observations in mind, there has been work to generalize the fluctuation-dissipation theorem for a NESS, or where the system of interest has multiple links to various baths at different temperatures [68, 143, 144]. Although in general, it is useful to probe the spectrum of the thermal noise of the system (S_{xx}) one can also look at the variance of the degree of freedom of interest $\langle x^2 \rangle$. In the case of a micro-mechanical oscillator $\langle x^2 \rangle$ is the Brownian motion, determined by the equipartition theorem. Notably, any calculation or measurement of the steady-state $\langle x^2 \rangle$ can determine an effective temperature T_{eff} of the degree of freedom, in this case, a mechanical normal mode. The most general determination T_{eff} assumes that the mechanical mode is defined over all of space. With this knowledge, a volumetric dissipation density α can also be inferred. α has the property that $\int_{-\infty}^{\infty} \alpha dV = \gamma$. Therefore, the effective temperature can be calculated as [143]:

$$T_{\mathrm{eff}} = \frac{\int_{-\infty}^{\infty} \alpha T dV}{\int_{-\infty}^{\infty} \alpha dV} = \frac{\int_{-\infty}^{\infty} \alpha T dV}{\gamma}. \tag{5.3}$$

An inspection of Eq. 5.3 reveals parallels to the fluctuation-dissipation theorem: the effective temperature of the normal mode–corresponding to the amount of thermal fluctuations of the motion degree of freedom – depends on both the local temperature as well as the amount of dissipation at any given point in space. We also bring attention that we define this quantity as an *effective* temperature as a matter of caution since the systems studied in this chapter will be in a NESS. However, we believe that this temperature can be thought of as a true temperature in many senses. For instance, a system with an effective temperature T_{eff} will remain unchanged if exposed to an additional thermal bath at a temperature $T = T_{\text{eff}}$. Furthermore, when assessing the noise characteristics of such a mode, the effective temperature functions exactly as a true thermodynamic temperature in formalisms typically employed to assess the performance of mechanical devices.

Although Eq. 5.3 is general for the case of mechanical modes, it is difficult to frame many channels of dissipation as having a contribution to α. A simple case would be mechanical radiation loss. In principle, correct modeling of the substrate and mounting structure of the mechanics could allow for mechanical radiation loss to be modeled as bending loss associated with the minuscule modal participation in these areas, but doing so is computationally intensive and not feasible. Gas damping of mechanical resonators also is difficult to frame in this way, since it would require knowledge of precisely how the motion of the resonator couples to pressure waves in the gas. Finally, situations like optomechanical cooling are also difficult to model in this way, since it would require modeling of the entire electromagnetic field coupled to the mechanics. Therefore is often convenient to treat each loss channel in a lumped sum model:

$$T_{\text{eff}} = \frac{\sum_i \gamma_i T_i}{\gamma} \tag{5.4}$$

where the sum over i corresponds to summing over all known loss channels. Each channel is assigned a temperature T_i. Although analogous to Eq. 5.3, Eq. 5.4 has the distinction that it can address non-local losses readily. Such a formalism is convenient when considering the effective temperature of electromagnetic degrees of freedom when coupled to a transmission line [68].

There are ramifications for mechanical resonator design when considering Eq. 5.3. For example, when operating a mechanical resonator in the quantum regime, it is imperative to minimize the rate at which thermal excitations affect the state of the resonator, quantified by the thermal decoherence rate:

$$\gamma_{th} = \gamma n_{\text{th}} = \gamma \frac{k_B T}{\hbar\omega}. \tag{5.5}$$

Here, γ_{th} is calculated assuming a uniform temperature bath at a temperature T, for a mechanical resonator with resonant frequency ω. In this case, it is evident that minimizing γ – the total dissipation of the resonator – is the correct figure of merit to optimize in order to achieve optimal performance. However, this is not generally the case. One notable example in optomechanical systems is the operation of mechanical devices coupled to optical cavities. Such operation requires high-intensity optical fields to interact strongly with the mechanical device, which can lead to heating of the device arising from optical absorption in the mechanical material. Although this effect can be mitigated through the use of high-quality, low-absorption materials to fabricate micro-mechanical resonators, quantum operation is susceptible to minute amounts of heating. Notably, in this scenario, the nature of the heat load on the device gives rise to a spatially varying map of $T(x, yz, z)$ across the device. In this scenario, many strategies for minimizing γ run into issues. Notably, soft-clamped modes of membrane resonators have the property that the mode, as well as its dissipation map α, are localized close to the location of optical probing while being far from the device edges. This localization, along with the high aspect ratio of the device, can lead to elevated temperatures at the location of large α, leading to a potential for elevated values of T_{eff} despite the majority of the device being well thermalized to the substrate temperature. For phononic crystal devices, not only does the functional form of α have a strong modal dependence, but the temperature profile T subject to a localized heat load has nontrivial geometrical dependencies. For instance, geometry-dependent coefficients of thermal conductivity k_{th} have been observed in silicon nitride nanoscale devices [99, 145]. Additionally, the effects of radiative cooling or heating of nanoscale devices with high aspect ratios are of interest when utilizing these devices for thermally sensitive sensing operations [146, 147].

Motivated by this insight, we find it important to probe this effect on a real PnC device. Such an experiment requires a few technical aspects. Firstly, a heat load needs to be applied to a device in a local manner. An absorbed laser beam can be readily shaped and directed to produce localized heating. For the stoichiometric silicon nitride membrane devices investigated in this work, the nitride has quite low optical absorption (less than 1 ppm), and therefore an addition of an optical absorber will be necessary to apply a controlled localized heat load with a reasonable amount of laser power while operating at room temperature. The addition of the absorber should be done in a minimally invasive way. That is, it should not have a considerable effect on α of the mechanical modes in question. Secondly, the device in question should support modes with various theoretical maps of α. Doing so will allow for a measure of the differential effects of the nonuniform temperature map on the observed Brownian motion of different normal modes of the system. Utilizing a silicon-nitride PnC device allows for a determination of α since we have previously established that the primary source of dissipation — for some modes — is the intrinsic dissipation associated with the material bending.

5.2 Experimental overview

For the experiment in question, we elected to a set of modes on a study device E, defined in Fig. 5.1 [148]. Device E was functionalized with an absorber by depositing Stycast 2850ft epoxy using a glass tip on one of the PnC tethers far from the defect pad as seen in Fig. 5.4a. This deposition was performed with a procedure described in depth in another thesis from our group [130]. This location was selected in order to not have large participation in a subset of modes of interest. Notably, defect modes of this device will have low participation at this point in the crystal because they are localized strongly to the defect pad region. Furthermore, membrane-like modes that have a node of motion along this tether also have reduced participation of the absorber by symmetry. The experimental concept is displayed in Fig. 5.4b. A probe beam can be directed to monitor the Brownian motion at various locations on the device (yellow beam), while a temperature profile of the material can be changed by adjusting the heating beam power (red beam). The deposition was performed in a clean room environment in a similar fashion to how magnetic grains were deposited, as discussed in Ch. 3. The epoxy used as the absorber is a two-part epoxy, comprised of a resin and a catalyst. Although the mixed epoxy appears homogeneous on a macroscopic scale, it is apparent on the microscopic scale (1 - 10 microns) that the resin is composed of micron-scale individual grains. This was apparent during the deposition process when picking up mixed epoxy with the glass tip resulting in a granular droplet attached to the tip. During deposition, it was thus imperative to ensure that absorbing material became attached to the membrane tether via a visual inspection since early attempts at deposition resulted in only resin

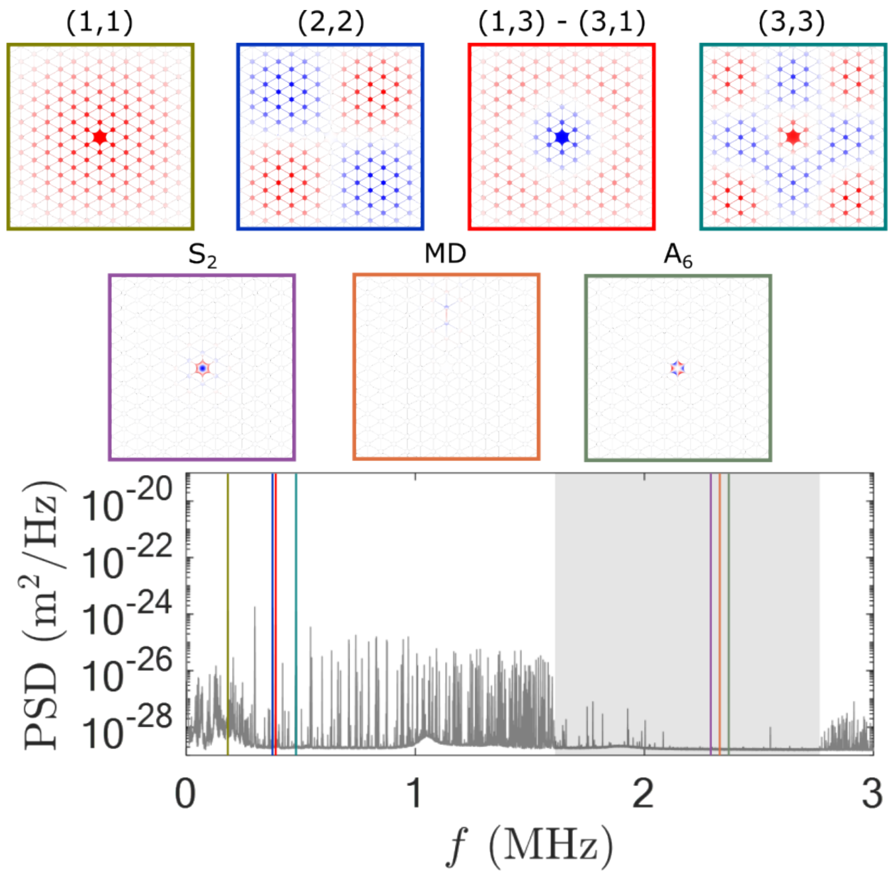

Figure 5.1: Overview of mechanical modes of device E studied in this section. The top of the figure indicates FEA simulations of the mechanical mode shapes in ascending order of frequency. The bottom shows a measured spectrum of the device while probing away from the defect. Colored vertical lines (matching the colors of the mode-shape frames) indicate the resonance frequency of each of the studied modes.

being placed on the resonator. A ramification of this is that the added mass cannot be assumed to be homogenous, and therefore does not necessarily have mechanical properties that match the macroscopically defined specified values.

Although the addition of the absorber was performed in order to be minimally invasive to the modes of the device, certain perturbations could not be avoided. Notably, the addition of a mass in the bulk of the PnC device can be interpreted as a defect in the same light as a geometric perturbation to the structure. Therefore, there is potential for defect modes associated with the addition of the mass – we will call these modes MD (mass defined) – to arise, which was the case in

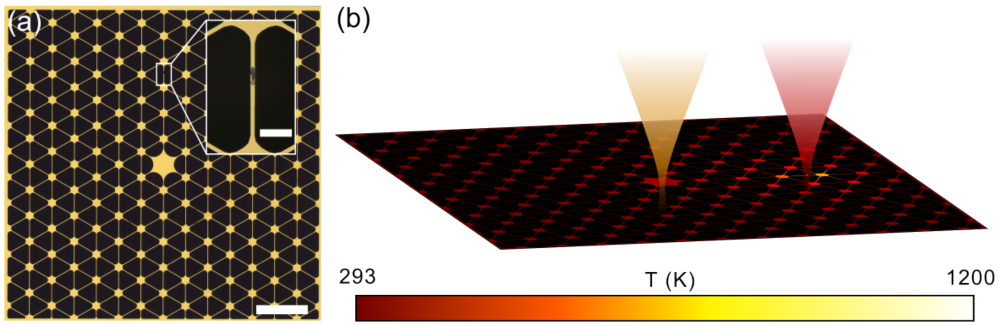

Figure 5.2: Phononic crystal membrane device and experimental scheme to probe a spatially varying thermal bath. (a) Optical microscope image of the device studied in this work (scale bar 200 microns). Inset: zoomed-in image of deposited absorber used to generate temperature gradients (scale bar 20 microns). (b) A simulated temperature map observed in this work. A localized heat load was generated by absorbed light from a heating beam (red). The Brownian motion of the device was measured interferometrically with a probe beam (yellow).

this experiment. For the mass scale of absorber deposited in this experiment, an MD mode exists in the bandgap (see Fig. 5.3). Studying the properties of this mode, notably its frequency and dissipative properties can be illuminating for understanding the effects of the absorber on other modes. This study will be presented later in this chapter.

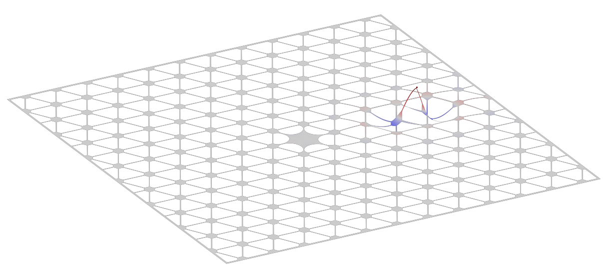

Figure 5.3: FEA simulation of the MD mode observed for device E functionalized with an optical absorber.

For this device, one would expect different responses of Brownian motion with respect to increasing heating power depending on the α distribution of the mode in question. Prior to the experiment, we could make predictions about α from FEA analysis of the modes, as well as measurements of their dissipation. It is useful to categorize modes of device E into 4 categories. (1)

radiation loss limited modes. These will have large contributions to α in the substrate or further beyond the simulation space of FEA simulations. We can identify these modes via measurements of Q that are substantially below the expected value from bending loss. (2) Membrane modes that do not experience radiation loss. These modes have α that is confined strongly to the membrane edge due to the clamped boundary condition at the interface of the membrane with the silicon substrate. These modes are differentiated from defect modes by observing that their observed quality factors match the predictions determined by bending loss alone. (3) Defect modes of the geometric defect would have modal temperatures that correspond to the overlap of their localized bending with the temperature map generated from the heating beam. Although we have not yet discussed the exact nature of the expected temperature maps in this experiment, one expects that the material temperature at the geometric defect would be elevated from the substrate temperature. (4) MD modes would have the highest temperature since they are localized to and have high relative dissipative participation of the absorber. Having access to the differential heating about these 4 categories of modes gives access to the thermal properties of the PnC device since the material temperature at the geometric pad, absorber, and frame are probed directly, while the location and nature of the heat load are known. Using this knowledge, in concert with the time-dependent nature of the heating can give access to calibrated measurements of the thermal properties of the material. This discussion will be presented later in this chapter.

Another effect to consider in this experiment is that of the material thermal expansion resulting from the spatially varying temperature map. Conceptually, thermal expansion of the silicon nitride leads to stress relaxation. This results in a lower speed of sound in these regions, resulting in frequency shifts of the mechanical normal modes of the system. Such an effect is often leveraged for micro-mechanical bolometers [99, 149]. For a device subject to a thermal gradient, it stands to reason that certain mechanical modes will experience larger shifts when compared to others. This is an additional differential effect that we can use to probe the system, as well as calibrate our measurement of the Brownian motion. Notably, the (1,1) membrane mode has the property that its Brownian motion is detectable at any probe location on the device with an appreciably high signal-to-noise ratio. Therefore, in this experiment, we can use the frequency shift of the (1,1) membrane mode of the device to cross-calibrate the absorbed heat in separate data runs.

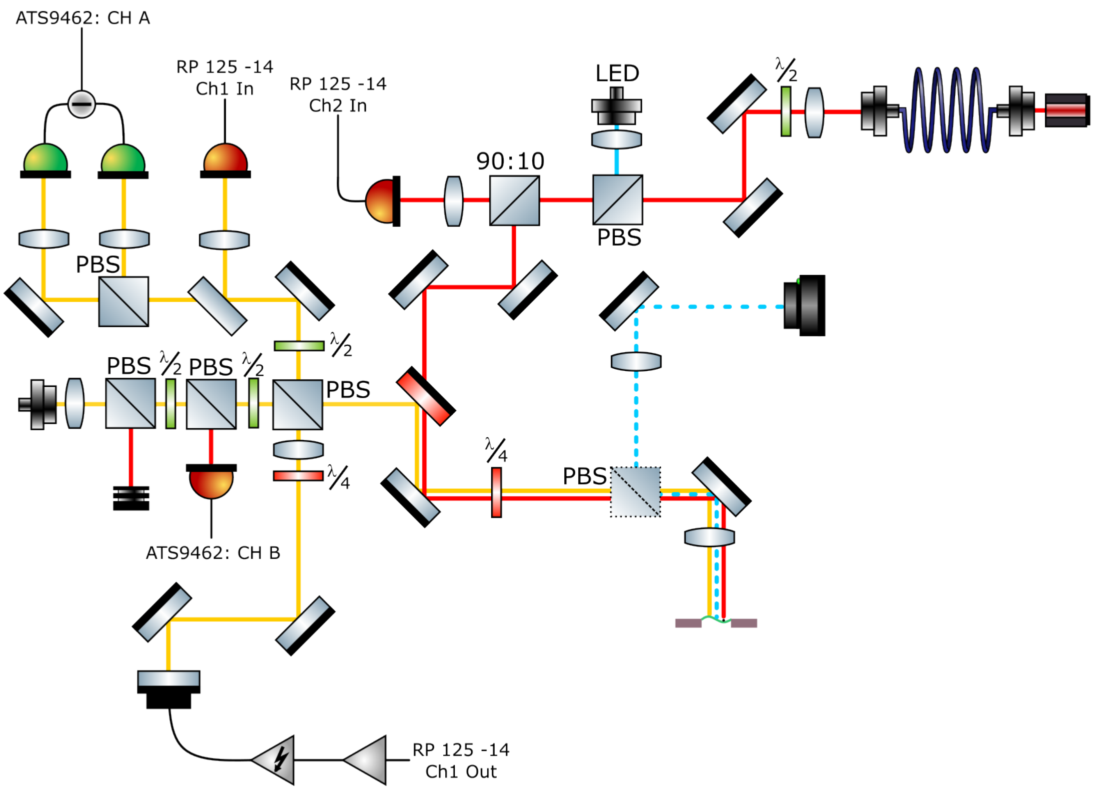

Figure 5.4: Schematic of the optical system used in this experiment. The yellow lines denote the optical path of the probe beam of the interferometer. This beam results from the Nd:YAG after the filter cavity and AOM which is used to control the intensity of the probe beam. The red beam path denotes how the 950 nm heating beam was controlled during the experiment. These beams are combined on a dichroic mirror (shaded red). In order to properly direct these two beams, a 940 nm LED was used to illuminate the device when not measuring. The forward path of this beam is omitted for visual clarity but copropagates with the heating beam upon being combined on a PBS. The return path of the scattered light is represented with a dashed blue line. A removable PBS (dashed outline) was used in order to switch between imaging and measuring modalities of the apparatus. The ATS9462 DAQ card was used to record signal traces as well as monitor beam powers in this experiment. An RP 125-14 FPGA was utilized to implement a PID to lock the Michelson interferometer as well as servo the intensity of the heating beam to a desired setpoint.

5.3 Control of the dissipation map

The added dissipation of the absorber can be measured by comparing the quality factor of each mechanical mode before and after deposition. One can then infer the added dissipation by

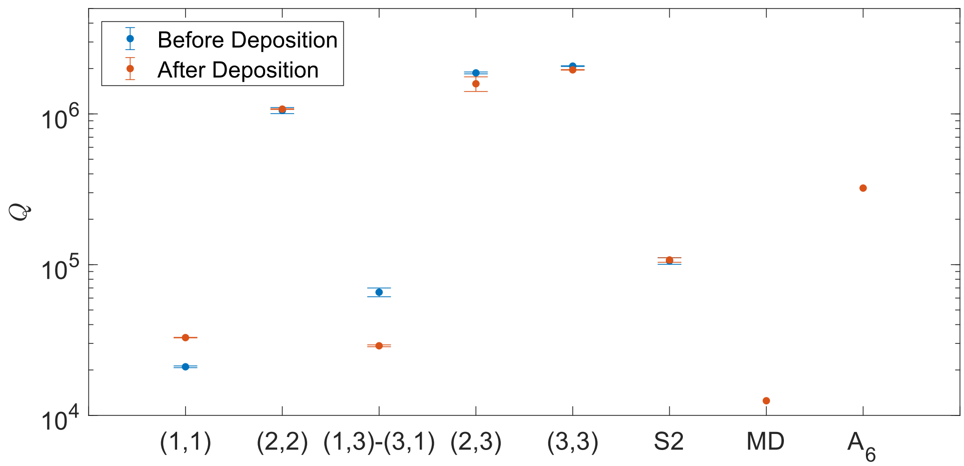

Figure 5.5: Observed quality factors of modes before and after absorber deposition. Note that the (1,1) mode was radiation loss limited, and therefore the increase in Q can be attributed to a change in the mounting environment of the chip. The A_6 Q was not measured prior to deposition.

attributing any decrease in quality factor (increase in dissipation) to the absorber via the following relation:

$$\frac{1}{Q_{\text{after}}} = \frac{1}{Q_{\text{before}}} + \frac{1}{Q_{\text{abs}}}. \tag{5.6}$$

Q_{abs} is attributed to the loss in the absorber. This relation is valid in the limit where the addition of the absorber has a negligible effect on the pre-deposition mode shape. This assumption notably fails when there are additional effects at play, such as the hybridization of modes with the MD mode. For the modes studied in this experiment, only the S_2 mode had a frequency close to that of the MD mode – differing by 40 kHz without a heat load – and therefore all other modes studied in this work should obey Eq 5.6. The effects of hybridization between the S_2 and MD modes will be extensively addressed in another discussion. Another effect to consider in this scenario is radiation loss. Notably, the device had to be removed from the vacuum chamber between measurement and deposition, and thus the mounting environment of the oscillator was not controlled to the utmost extent. Therefore, it is possible that modes that are susceptible to radiation loss – membrane modes – may have changes in Q that are not due to the absorber.

Quality factors of the modes of this device were measured in most cases by ringdown measurements. Mechanical driving was achieved via an optical force produced from a modulation of the heating beam at the mechanical resonance of the mode in question. This power modulation was achieved via a direct modulation of the laser current above threshold. As can be seen Fig. 5.5, there were some measured differences between Q_{after} and Q_{before} for certain modes. Notably, the (1,1) and (1,3)-(3,1) modes exhibited a noticeable change in Q. However, since these are all membrane modes, we cannot directly attribute this change to that of the absorber. Notably, the (1,1) mode experienced an increase in Q. This makes sense since the internal loss limited Q for membrane modes of this device should be on the order of 2×10^6, meaning that the (1,1) mode experiences large amounts of radiation loss both before and after deposition. A similar story is present for the (1,3) - (3,1) membrane mode and to a lesser extent the (3,3) mode, which did experience a statistically significant drop in Q.

Of the modes measured in this work, the (2,2) and S_2 did not experience a reduction in the measured mean Q upon addition of the absorber up to the statistical error of the measurement 5.5. In most cases, 100 ringdowns were performed to get 100 independent measurements of Q. The standard error of this ensemble average is plotted as the error bars on 5.5. A consequence of this error is that it allows for a bound to be placed on Q_{abs} in Eq. 5.6. We can assume a worst-case scenario in which the error in the measurement of Q (ΔQ) can be attributed to the addition of the absorber. Under this assumption, it follows that $Q_{\text{abs}} = Q^2_{\text{before}}/\Delta Q$. As an example, the (2,2) mode has a lower bound of $Q_{\text{abs}} \approx 10^8$ from the error of bound of Q being $\pm\ 10^4$.

After deposition, the quality factor of the MD mode can be used to calibrate the mechanical loss tangent, or Q_{int}, of the absorber. We note here that the quality factor of this mode was expected to be quite low due to a relatively high participation of the lossy epoxy used as the absorber. This made the mode difficult to optically drive, and thus the Q was estimated from linewidth measurements. A technical difficulty associated with these measurements involves the potential for power from the probe beam heating the absorber, leading to anomalous heating-induced line broadening. To mitigate this effect, measurements were performed with a wide range of probe beam locations. The linewidth was constant regardless of the probe beam location, indicating that

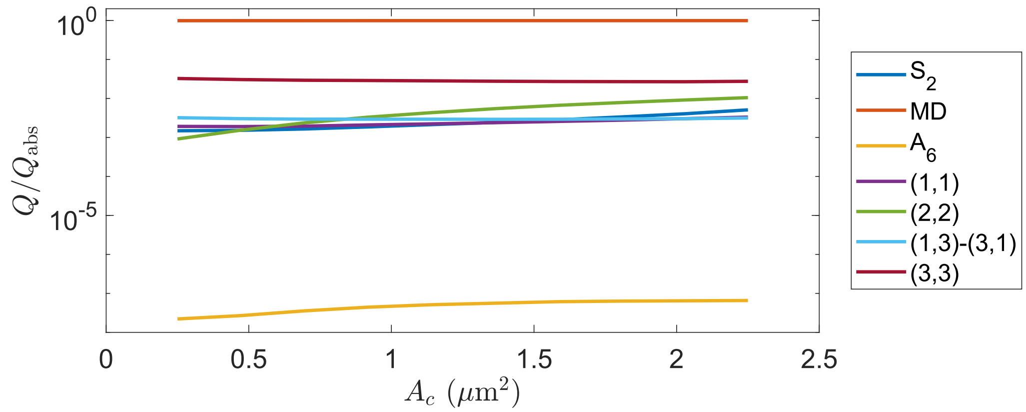

Figure 5.6: Results from FEA simulations of the relative dissipation of certain modes while sweeping over the contact area of the absorber sphere.

the linewidth measured corresponded to the energetic decay of the mechanics.

Using this calibrated value of the Q, one is able to make predictions about the effect that the addition of the absorber has on the dissipation of each mode. One way to quantify this would be to calculate the dissipation fraction of the absorber, given as $Q/Q_{\rm ab}$. As stated before, the exact geometry and composition of the glue are unknown because of the heterogeneous nature of the absorbing material at the micron scale. Simulating all possible geometries of the absorber thus would be computationally intensive. Therefore, to capture qualitative effects, in this work the absorber is assumed to be spherical and homogeneous for all FEA simulations, including the one described here. In order to probe some effect of the geometry, the contact area of the sphere with the device tether was swept while the density of the absorber was adjusted in order to maintain a constant MD frequency of ≈ 2.45 MHz. For all of these geometries, setting the $Q_{\rm int,abs} \approx 800$ yields a simulated value of $Q_{\rm MD}$ to be in close agreement with the observed value of 12,500. In this study, $Q_{\rm abs}$ is taken to be the loss that is inside the absorber itself. In principle, there is additional loss in the silicon nitride near the absorber. However, this was found to be negligible in the case of all modes studied. Fig. 5.6 displays the effect of contact area on the relative absorber participation for many of the modes studied in this work. One sees that there are three main predicted behaviors. The MD mode has a dissipation participation factor close to unity as expected. The membrane modes, along with the S_2 mode, are predicted to have participation between 0.001 and 0.01. Notably, the (3,3) mode should have relatively high absorber participation since the absorber is located at an anti-node of motion for this mode. Finally, the A_6 is predicted to have extremely low glue participation, due to its symmetry and high mechanical isolation from the location of the absorber. There is a trend among almost all modes that an increase in contact area results in higher fractional participation of the absorber, most likely attributed to a higher direct coupling. However, this effect is rather small, indicating that for all modes studied in this work, save the MD, one does not expect there to be appreciable dissipation participation of the absorber.

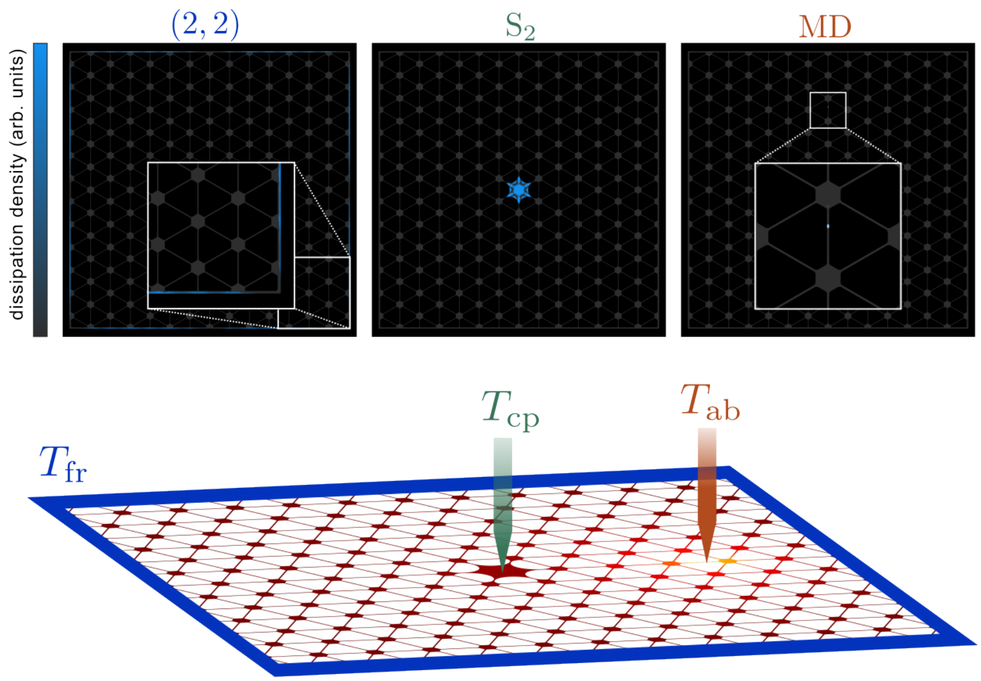

Figure 5.7: Spatial map of α for the (2,2), S_2 and MD modes. (Top) The (2,2) has a loss map akin to all bending loss limited membrane modes where the loss is concentrated to a small region at the membrane edge. The S_2 mode has its dissipation localized at the center of the device, well isolated from the thermal environment of the substrate. Due to the dissipative nature of the absorber, the MD mode has α that is concentrated solely in the added mass. (Bottom) Temperature map (color scale has yellow indicating hot regions, red indicates ambient conditions) of the device due to local heating. Effective probe locations of each mode are schematically indicated, and the colors are matched to their corresponding mode labels above the temperature maps. One sees that the (2,2) mode samples the temperature of the whole frame (T_{fr}), while the S_2 and MD modes sample the temperature of the center pad T_{cp} and absorber T_{ab} respectively.

Through this modeling, one is able to construct the map of α for each mechanical mode. Fig. 5.7. Outlined here are the qualitatively different dissipation maps studied in this work. Notably, the (2,2) mode has a dissipation that is limited by the bending of the membrane itself, but due to the clamped boundary condition, this loss is limited to a small region around the membrane edge. This means that the (2,2) mode should experience a thermal bath that is well-thermalized to the substrate temperature. Although not denoted here, radiation loss limited modes are qualitatively different since their dissipation maps have contributions within the substrate itself. For the purpose of this experiment, one does not expect there to be a measurable difference in behavior between radiation loss limited and bending loss limited membrane modes, since the edge of the membrane structure should be well thermalized to the substrate itself. However, one could distinguish between the two cases in principle by measuring the device with a temperature gradient within the substrate itself. The dissipation map of the S_2 mode is concentrated to the geometric defect at the center of the device (unaffected by the addition of the absorber) and thus one expects that the modal temperature of this mode to sample the temperature of this center defect. One can calculate a modal temperature from Eq. 5.3 and find that the modal temperature should be approximately the average temperature of the geometric defect in the limit of small thermal gradients across the pad. We note that this behavior holds for all geometrically defined defect modes of this device, such as the A_6. Finally, the MD mode has almost all of its dissipation contribution contained within the absorber. Therefore, its modal temperature should coincide with the average temperature of the absorber. Conceptually, having this wide class of modes with different spatial temperature profiles allows for spatial temperature probing across the device structure, as indicated in Fig 5.7.

5.4 Experimental control and procedure

To measure Brownian motion in a well-calibrated manner, both the probe beamline and heating beamline needed to be well controlled in order to reduce technical noise. We will first discuss the control of the probe beamline. A diagram of the experiment-specific section of the optical system is displayed in Fig. 5.4. The probing system is composed of a Michelson interferometer, much akin to what was discussed in Ch. 2. The unique parts of this system begin with the control of the intensity of the power incident on the Michelson interferometer, which is monitored by the ATS9462 DAQ card prior to each experiment. Although the power drifts due to temperature fluctuations in the lab of this system were determined to be minimal – less than five percent – stability and accuracy of the displacement readout necessitated coarse control over the power entering the Michelson interferometer. Hence, the power exiting the probe beam fiber was adjusted to a desired setpoint by an AOM prior to the fiber (not pictured in Fig. 5.4. After this adjustment was made, each experiment was operated in an open-loop manner with respect to the power of the probe beam.

The 950 nm wavelength heating beam resulting from a QPhotonics QFBGLD-950-5 laser diode was similarly monitored and controlled. Before combining the probe and heating beams on a dichroic mirror, the heating beam power was monitored on a photodiode. This signal was directed towards a Red Pitaya 125-14 FPGA which served as a programmable PID controller in order to servo the intensity of this beam. The set point of this intensity servo was adjusted digitally by changing the lock parameters of the FPGA. To avoid adding either electrical or optical shot noise onto the heating beam, the bandwidth of this intensity servo was limited to 100 Hz. Due to thermal instabilities in the heating laser current controller, 60 seconds of settle time elapsed prior to taking data when the set point was adjusted. These instabilities typically occurred at relatively high output laser powers around 2 mW.

Another source of technical noise in this experiment resulted from beam pointing of both the probe beam and heating beam. For the probe beam, beam pointing has two effects. Firstly, beam pointing can change the Michelson calibration factor of optical power to motion, thus giving inaccurate results for the calibrated motion of the device. Secondly, beam pointing can change the probe location of the Gaussian beam, resulting in a noisy value for the effective mass. These two effects can be differentiated by looking at differential effects between the measured mechanical motion of mechanical modes of differing geometries. Notably, mechanical modes with small mode volumes, such as the S_2 would be much more susceptible to the second effect when compared to the (1,1) membrane mode. Long-term measurements – taken over the course of a few hours – showed that there was a long-term drift of the observed thermal motion of the S_2, while the (1,1) membrane mode showed no discernible time correlation in the measurement of its thermal motion. This indicates our apparatus is indeed susceptible to beam pointing resulting in a change in effective mass. However, this measurement also shows that this noise occurs on the order of 10s of minutes, and therefore for measurements that occur within seconds of one another this effect is weak. Therefore, the effect of beam pointing can be mitigated in measurements of the Brownian motion by taking the data in an interleaved fashion, alternating between measuring the device under a heated versus ambient temperature profile. Taking the ratio of these two data sets should result in a cancellation of this beam-pointing effect with enough statistics. Under these conditions, we can define an estimator for the temperature in the following way:

$$\tilde{T}_{\mathrm{eff}}^{(i)} = \frac{\langle x_i^2 \rangle \omega_i^2}{\langle \langle x_{i,0}^2 \rangle \omega_{i,0}^2 \rangle_{\mathrm{all}}} T_{\mathrm{lab}}. \tag{5.7}$$

Here, $\langle \cdot \rangle$ denotes an average over a single-shot 0.3 s time interval, and $\langle \cdot \rangle_{\mathrm{all}}$ denotes a full average over all the no-heating data, which was taken with large statistics and is assumed to have negligible variance. $\langle x_{i,0}^2 \rangle$ and $\omega_{i,0}$ are the measured displacement power and angular frequency of the mode with no absorber heating, respectively, and T_{lab} is the lab temperature measured with a thermometer to be 293 K. The ratio of $\omega_i^2/\omega_{i,0}^2$ is present in order to account for the fact that the frequency of each mechanical mode changes when the device is heated.

5.5 Experimental results

Here I will present the results of the experiment described above. For this experimental run, the heating power set point was swept over a set of quantized values, each averaged many times in order to accumulate strong statistics. Fig. 5.8 displays the effective modal temperature inferred from the observed Brownian motion in accordance with Eq. 5.7. From the heating data, it is apparent that there are strong differences between the heating curves of each mode. This corresponds to the different effective thermal probe locations of each mode in accordance with Fig. 5.7. Notably, the (2,2) mode does not heat in a statistically significant manner, as expected since its dissipation map is concentrated to the membrane frame. Meanwhile, the MD mode was observed to heat to over 1000 K. We note here that since the observed modes were spatially separated, each heating curve corresponds to a different experimental run. Therefore, although the MD mode was observed to have a maximal modal temperature of around 1250 K, one can infer that the local temperature of the absorber exceeded 1500 K on the other experimental runs of the experiment from the observed value of $|\Delta f_{(1,1)}|$ (see the extrapolated fit line for the MD heating data on Fig. 5.8a). This maximum achieved temperature is consistent with the fact that the device survived with experiment without damage to the resonator structure since the melting point of silicon nitride is around 2200 K. Different behavior is observed for both the S_2 and A_2 modes, as indicated on Fig. 5.8b. Here, both modes heat at an intermediate level, which probes the effect of the local heating of the absorber over a long range. Notably, these two modes heat to a similar level. This indicates two things: (1) that the modes have dissipation density profiles that are localized to a similar region of the device and (2) that these two modes most likely do not possess large amounts of absorber participation. This second point can be argued by comparing the symmetry of these two modes, notably that the S_2 is a symmetric mode and the A_2 is an antisymmetric mode. Antisymmetric modes of the geometric defect should have a nodal line at the location of the absorber. Therefore, one would predict that they should have quite different modal participation at the absorber location, regardless of the exact geometry or nature of the absorber.

By measuring the modal temperatures of these modes, we have probed the local temperature of the phononic crystal membrane structure at two locations – the geometric center pad and the absorber – as well as a proxy for the average temperature of the frame of the device. We can also inspect the behavior of other modes under these conditions, namely the rest of the membrane modes. As can be seen in Fig. 5.9, none of the membrane modes, both bending loss and radiation loss limited, experience an increase in Brownian motion. This is perhaps rather surprising given that one can infer that the maximal temperature of the absorber reached in excess of 1500 K in

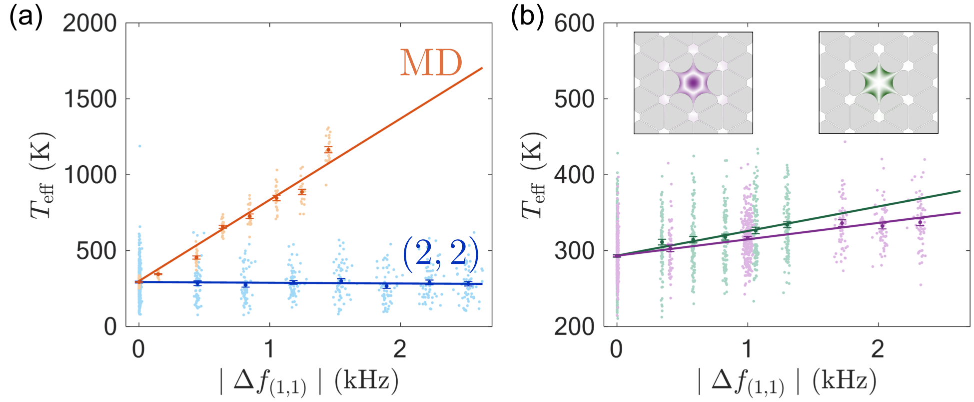

Figure 5.8: T_{eff} inferred from Brownian motion for mechanical modes of a phononic crystal device subject to a spatially varying thermal bath. A measurement of the frequency shift of the (1,1) membrane mode ($\Delta f_{(1,1)}$) serves as a proxy for the heating power for each iteration of the experiment. (Left) Brownian motion for the MD and (2,2) modes. The light orange (light blue) points correspond to the raw integrated Brownian motion for each run of the experiment for the MD ((2,2)) modes respectively. The orange (blue) data corresponds to the average of the raw data binned around the desired heating values. Orange (blue) lines are linear fits to the data. (Right) The similar data set and presentation for the S_2 and A_6 modes (insets of defect motion are color-matched to their respective data). One sees that the S_2 and A_6 modes experience very similar heating curves, indicating that they possess very similar spatial dissipation profiles.

some of these measurements. These no-heating results can therefore bound the values of Q_{abs} for all of the modes in which a "no heating" result was measured. Such a bound can be seen theoretically in Fig. 5.10. For the absorber temperatures achieved in this work, one can roughly calculate that the dissipation fraction of the (2,2) mode (quantified as Q/Q_{abs}) can be bound above by around 10^{-2}, thereby bounding Q_{abs} to 2×10^8 for the (2,2) mode. A similar bound can be established for all modes in which "no heating" was observed. This calculation highlights the dual nature of this experiment. For modes in which heating is observed, the dissipation can be used to probe the temperature profile of the device in a direct spatially resolving manner. However, we can also use the heating data (or "no heating" data) to spatially probe and quantify the dissipation of certain modes. This is of interest when studying the effects of functionalizing micro-mechanical resonators. Notably, one could in principle use this measure dissipative properties of certain materials, or to search for geometric dependence of dissipation in functionalized resonators.

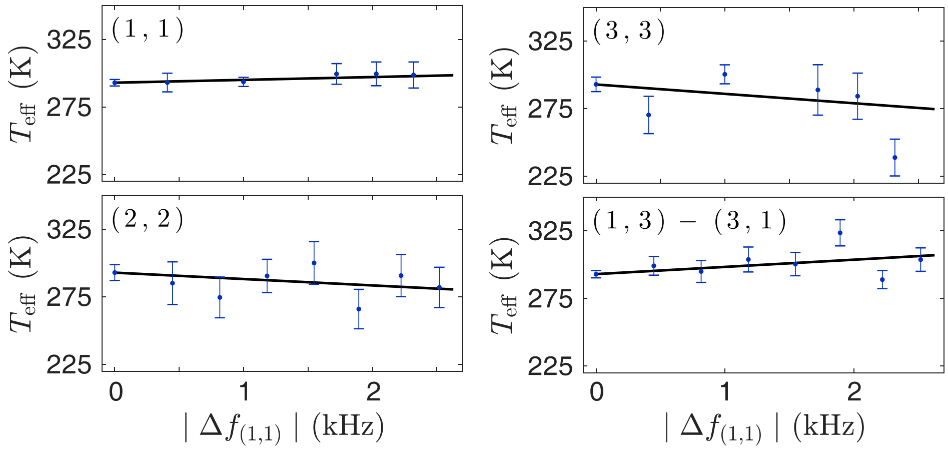

Figure 5.9: Effective temperature of membrane-like modes. $\Delta f_{1,1}$- binned (full blue circles with error bars) $\tilde{T}_{\mathrm{eff}}^{(\mathrm{i})}$ for $i = (1,1)\,,\,(2,2)\,,\,(3,3)$ and $(1,3) - (3,1)$ modes.

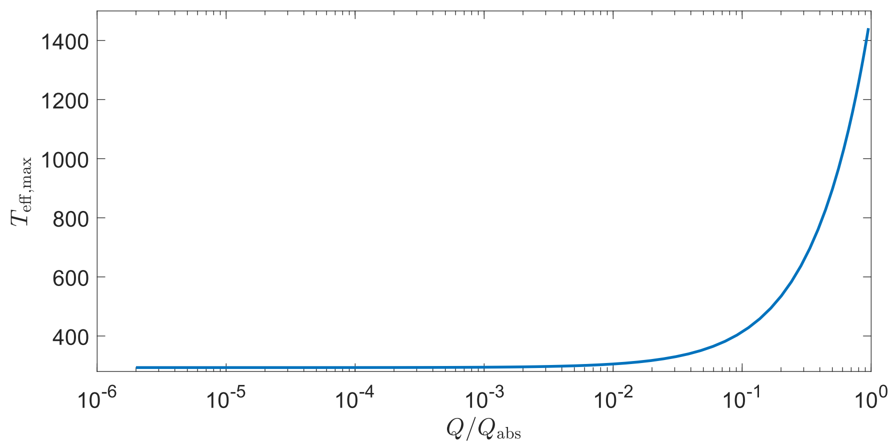

Figure 5.10: Theoretical maximally achieved temperature for a membrane mode that has glue participation. The participation fraction Q/Q_{abs} quantifies what fraction of the loss is contained in the absorber itself.

5.6 Calibration of temperature maps

The previous measurements probed the temperature map resulting for a local heating of the phononic crystal suspension in a few select places. Here we use the results of this measurement, as well as some additional measurements, to produce a calibrated map of temperature over the entire structure. In this section, we will outline the procedure for this calibration.

The temperature profile will be determined by the heat equation:

$$\rho C_p \frac{\partial T}{\partial t} + \nabla \cdot \mathbf{q} = \dot{\mathcal{Q}}(x, y, z) \tag{5.8}$$

Here ρ is the material density, C_p is the specific heat capacity at constant pressure, $\mathbf{q}$ is the heat flux and $\dot{\mathcal{Q}}(x, y, z)$ is the heat source due to laser light absorption. When considering effects of radiative cooling (or heating), then $\mathbf{q}$ is:

$$\mathbf{q} = -k_c \nabla T - \mathbf{n}\sigma\varepsilon(x, y, z)(T_{\text{env}}^4 - T^4) \tag{5.9}$$

where k_c is the coefficient of thermal conductivity, $\mathbf{n}$ is the surface normal vector, $\varepsilon(x, y, z)$ is the surface emissivity, σ is the Stefan Boltzmann constant and T_{env} is the temperature of the blackbody environment. In principle, if all parameters in Eq. 5.8 and Eq. 5.9 are known, then the temperature profile can be calculated for an arbitrary geometry and arbitrary heat source. However, prior to this work, not all material parameters were known for the particular device used in this work. Additionally, nanoscale effects of thermal transport also can come into effect in such devices, and therefore the use of the bulk values of many parameters can lead to incorrect predictions.

One example of this is the thermal conductivity of silicon nitride k_c. This parameter has been shown to have geometry-dependent values. A reduction in thermal conductivity is typically attributed to geometries where the mean free path of phonons becomes less than a key geometrical dimension, such as the membrane thickness. Notably, it has been calculated and observed that long-wavelength phonons (between 1 and 10 microns) dominate heat transport in amorphous materials such as silicon nitride [150]. However, when comparing the conductive properties of silicon nitride nanostructures made from thin silicon nitride (around 200 nm) it has been found that there are further discrepancies between membrane-like and string-like structures [145]. Therefore care must be taken in order to properly measure the value of k_c when predicting the temperature profiles of our devices.

There are also nanoscale effects that contribute to the effect of radiative cooling. One effect in question arises from optical effects associated with treating a suspended thin film of silicon nitride as an etalon. Infrared radiation arising from the material inside the thin film has the possibility of reflecting off of either surface, changing the effective emissivity of the structure. This effect is also directional since the reflection and transmission coefficients of the etalon depend on the angle of incidence [146]. This may have applications for radiative sensing using micro-mechanical resonators, allowing for sensitivity to radiation. Taking into account these effects, it can be shown that for 100 nm nitride films, the effective emissivity should be much reduced to 0.1, down from the bulk value of 0.6 [151]. For our work, we cannot assume that the predictions from a membrane should hold since the structure in question is much more complex. In principle, one could calculate the effects of radiative heat transfer by via extensions of optical thin film calculations. This was not done for this work. Rather, the emissivity was considered to be spatially uniform, but unknown. This value for emissivity can be considered an effective value for this geometry, and therefore would not be necessarily the correct value for an arbitrary geometry. However, the purpose of this discussion is to outline how to extract this effective emissivity – and in the same vein, k_c – for an arbitrary silicon nitride nanostructure. With this established procedure, a systematic study of the geometric effects on these parameters could in principle be performed, which would be a germane study to perform when considering these structures as the basis for thermal or radiative sensors.

An inspection of Eq. 5.8 and Eq. 5.9 reveals that in principle 4 parameters are unknown for a given temperature map, $\dot{\mathcal{Q}}, k_c, \varepsilon$ and C_p. For this study, we will assume that the C_p is known and does not vary from its bulk value. Therefore, there are 3 unknown parameters. For a given Brownian motion measurement, we reveal two previously unknown values of the temperature map, the temperature of the central pad T_{cp} and the temperature of the absorber T_{ab}. Note that a measurement of "no heating" at the frame does not provide additional information, save for the correct boundary condition to use when solving the heat equation. Therefore, a single measurement Brownian motion measurement does not reveal enough information to uniquely determine a temperature map. In principle, it would be possible if there were other modes that had large contributions towards α that were not colocalized to either the central pad or the absorber. However, such a mode was not found to exist in this device. Future studies could be performed with different resonators that are engineered to give more information – such as a device with two spatially separated defect pads – that would allow for a unique determination from a single measurement.

This deficiency in information can be circumvented by performing a different class of measurement, namely one that takes into account the time dynamics of the heating. Such AC heating measurements are routinely performed to study the effects of nanoscale heating on calorimeters [145]. For this work, it was decided to subject the device to a step heat load. Qualitatively, the sudden change in heat load establishes a new steady-state solution for the temperature map, which the system will slowly approach in time on a timescale (τ_{th}). Although not purely exponential in character, we will fit all simulations for the time-dependent temperature profile to an approximate exponential fit. Measuring this τ_{th} can give information about the material parameters of the device. For example, it can be shown that a string resonator of length L with a heat load at the center will thermalize on a timescale given by $\tau_{\mathrm{th}} = \rho C_p L / k_c$ when effects of radiative cooling are neglected. It is apparent here that with knowledge of geometry, it would be possible to extract k_c from such a measurement on the current device. However, the effects of radiative cooling have an effect on the thermal transport for highly thermally isolated structures, even in the presence of negligible temperature gradients. Therefore, it is difficult to extract k_c from a single measurement of τ_{th}. In this work, we instead use this as just another measure of the material properties to be used in conjunction with the spatial Brownian motion measurements.

When performing a step-response heating measurement, there are in principle two observables of the system that one could extract to learn about the time-dependent temperature profile. The most direct would be readout the Brownian motion of each mode as a function of time, much like the DC measurement protocol. However, this measurement has a complication given that the modes used in this work have values of $2\pi/\gamma$ comparable to τ_{th}, complicating this measurement protocol. We first draw attention to the simplest case, where $\tau_{\mathrm{th}} \gg 2\pi/\gamma$. In this case, one can consider that the mechanical mode in question is subject to a stochastic force whose power changes at a timescale equal to τ_{th}. Solving the equation of motion for this scenario reveals that the Brownian motion of the oscillator will adiabatically follow the thermal steady state established by this stochastic force since the energetic decay timescale of the oscillator is much faster than the change of the thermal profile. The behavior is quite different in the opposite case, where $\tau_{\text{th}} \ll 2\pi/\gamma$. Here, the state of the oscillator greatly lags behind the change in its thermal environment, since it takes an appreciable amount of time for the memory of its initial condition to decay. Therefore, the record of the Brownian motion would change on a timescale solely determined by $2\pi/\gamma$. As a consequence of this, it follows that a readout of the time-dependent Brownian motion is not a viable protocol for every mode of the device.

Here we present an alternative method. Rather than reading out the Brownian motion of a mode, one can instead read out the frequency when subject to a step heat load. In this case, there is only one timescale of the mechanics that matters, which is the timescale at which the stress in the structure redistributes. This will happen at a rate defined by the speed of sound c, as well as the overall device size L. For the device used in this work, this is found to be around $L/c \approx 1\ \mu$s, and therefore so long as $\tau_{\text{th}} \gg L/c$, then the instantaneous frequency of any mechanical mode will serve as a measure of τ_{th}.

Fig. 5.11 shows the results of such a measurement in the form of a spectrogram. One sees that the thermal-mechanical noise peak lags behind the monitor of the heat load, approximately exponentially decaying to the new frequency of the system at a rate $1/\tau_{\text{th}} = 12.5$ Hz. This same behavior was seen for all modes studied in this work, and therefore only data for the S_2 mode is presented here. Note that for this data set, a relatively modest heating power was used, one that produced a frequency shift of ≈ 250 Hz on the (1,1) mode. This corresponds to an elevation in temperature for the absorber of around 150 degrees K above ambient lab conditions. It is important to not perform this calibration when operating at high temperatures of the absorber, since the effect of radiative cooling is non-linear, thus having an effect that the thermalization time constant would change as a function of temperature. One sees that for a lumped sum model of the system, the rate of radiative cooling is much less than that of conductive cooling for absorber temperatures much less than 1000 K 5.12.

With this added information, we are now able to accurately model the temperature maps

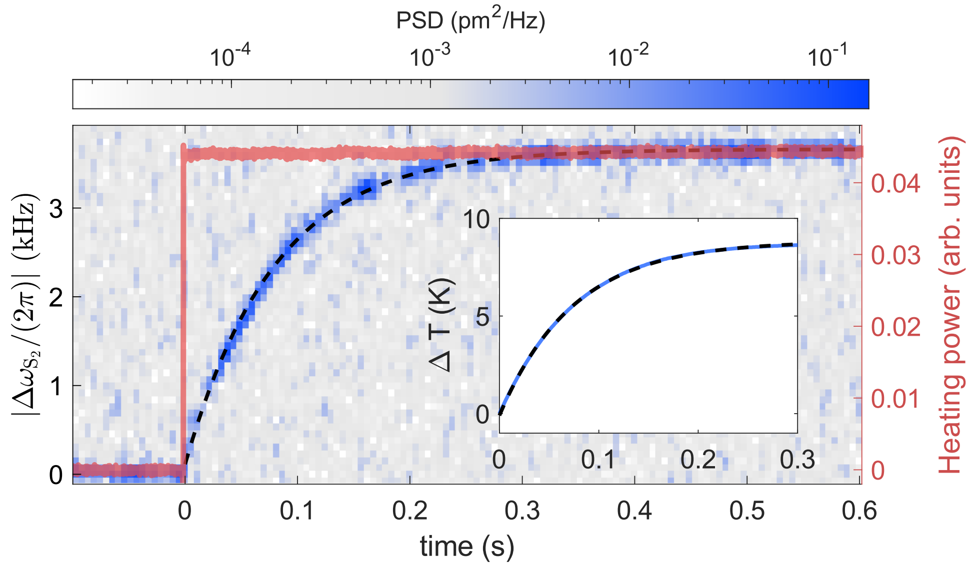

Figure 5.11: Determination of thermalization time scale τ_{th} from step function response of $\Delta\omega_{\mathrm{S}_2}$. Left axis: Spectrogram of thermomechanical motion. The dashed black line shows an exponential fit to the peak power of each time bin of the spectrogram. The fitted rate of the frequency shift $1/\tau_{\mathrm{th}}$ is 12.5 Hz. Right axis: monitor of the heating laser power during this experiment. Inset: The simulated time dependence of the temperature increase at the defect pad center (blue line). Example exponential fit to this curve (black dashed line).

generated from the local heat source in this experiment. The first step will be to perform a sweep over k_c and ε while holding the heating power to a constant, but low value of 1 μW in order to match the conditions of the experiment when performing the step-response frequency shift measurements. In order to reduce computational complexity, a relatively coarse parameter grid was used for FEA simulations. Assuming that the simulated value of $\tau_{\mathrm{th}}(k_c, \varepsilon)$ is a smooth function, one can readily perform a 3D spline interpolation in order to estimate the results over a finer parameter sweep. We can then use the spline interpolation function to find a manifold where $\tau_{\mathrm{th}}(k_c, \varepsilon) = 12.5$Hz. One sees in Fig. 5.13 that the FEA results do indeed appear to change smoothly with the swept parameters, meaning that there is high confidence in the consistent parameter manifold calculated from the condition $\tau_{\mathrm{th}}(k_c, \varepsilon) = 12.5$ Hz. One can see that this manifold indicates an inverse relation between the consistent values of k_c and ε.

To continue, we perform FEA simulations of the static temperature map while changing the

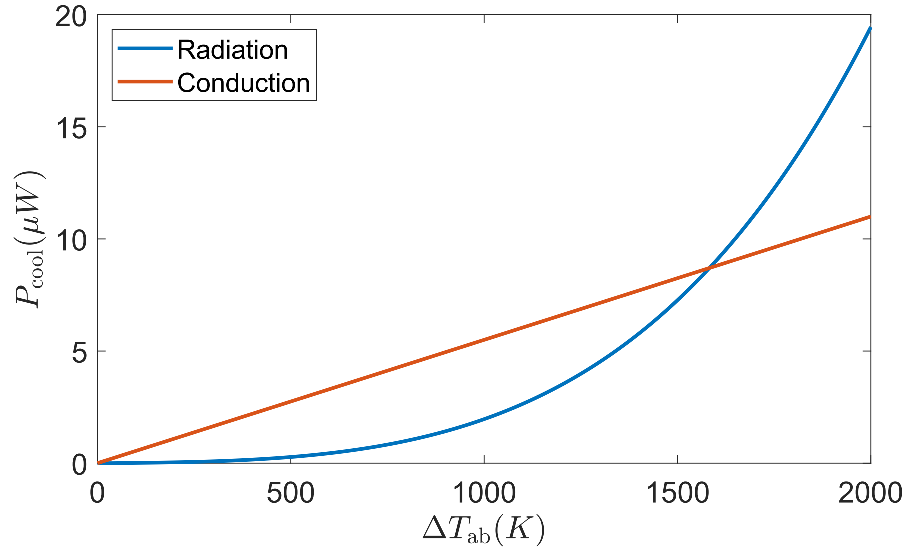

Figure 5.12: Comparing the rate of conductive cooling and radiative cooling of the absorbed in a 1D lumped sum model. The conductive cooling rate was estimated assuming that a single 200-micron tether with a cross-sectional area equal to those found in the device forms a conductive link between the absorber and the environment, and thus is an underestimate of the conductive cooling rate compared to the device. The radiative cooling rate assumes that the absorber is a perfect blackbody.

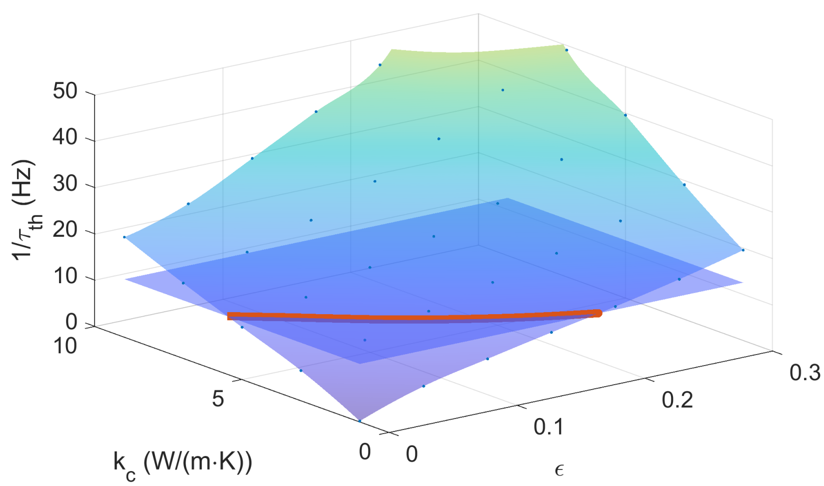

Figure 5.13: Results from FEA simulation of time-dependent heat equation using a step-function heat source. A coarse parameter grid of ε and k_c was used (blue dots), from which a 3D spline interpolation was calculated. The red line indicates a 1D manifold of parameters consistent with the observed value of $\tau_{\rm th}$

material parameters. In particular, we sweep over (ε,k_c) pairs, while also adjusting the heat load $\dot{\mathcal{Q}}$ applied to the system. Since our experiment only probes $T_{\rm cp}$ and $T_{\rm ab}$, we extract the functional dependence $T_{\rm cp}(T_{\rm ab})$ from the temperature map for all parameter triplets studied. The results are shown in Fig. 5.14, where the rise in temperature above ambient conditions for the absorber is plotted as a function of the rise above ambient temperature for the pad. There is clearly a strong trend present when the effects of radiative cooling are increased (increasing ε). Notably, the presence of more radiative cooling allows for stronger gradients of temperature across the device. We note here these FEA results are for relatively low heating powers ($\approx 1\mu W$). In this regime, there is a linear relationship between both studied temperature increases and heating power. For higher heating powers, nonlinear effects of radiative cooling begin to dominate the behavior, much as was seen in the toy model of the system considered in Fig. 5.12.

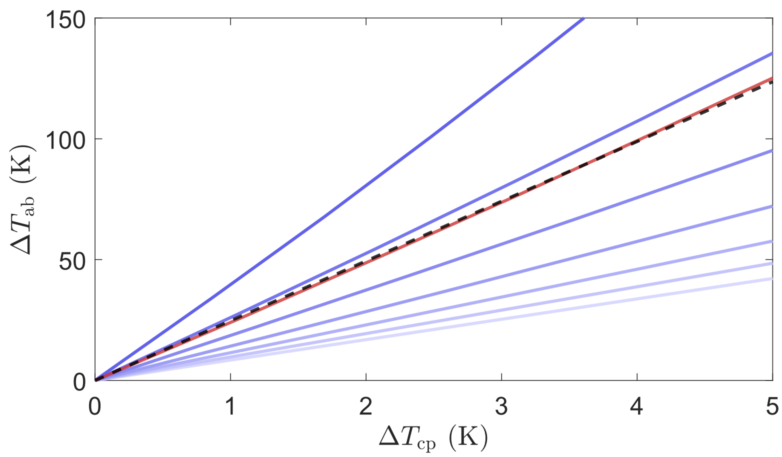

Figure 5.14: Temperature increase of the absorber versus the temperature increase of the central pad for increasing heating power. Purple lines correspond to finite element analysis (FEA) simulations where the values of ε and k_c were consistent with the observed $\tau_{\rm th}$. Light to dark purple indicate the trend when varying ε from 0 to 0.15. The black dashed shows the inferred local temperature increase from the measured modal temperatures, while the red line shows the best fit FEA simulation.

We can compare the results of these FEA simulations with our observed data. Namely, fitting both the observed values of $T_{\rm cp}$ and $T_{\rm ab}$, we can extract an observed functional dependence for $T_{\rm ab}(T_{\rm cp})$ to compare to the simulation results. From this comparison, we can perform an interpolation in order to estimate the values for ε and k_c, which match the observed dependence with high accuracy (see the comparison between the black dotted line and the red line in Fig. 5.14. We note that this correspondence only occurs at relatively low-temperature increases. At larger temperature increases, we begin to see deviations (beyond the bounds of Fig. 5.14). This can be explained by multiple phenomena. One explanation could be the temperature dependence of material properties. Notably, if the thermal properties of the device change at the highly elevated temperatures observed in this experiment, one might expect that the FEA simulation would become inaccurate since these simulations were performed under the assumption of temperature-independent values of all material parameters.

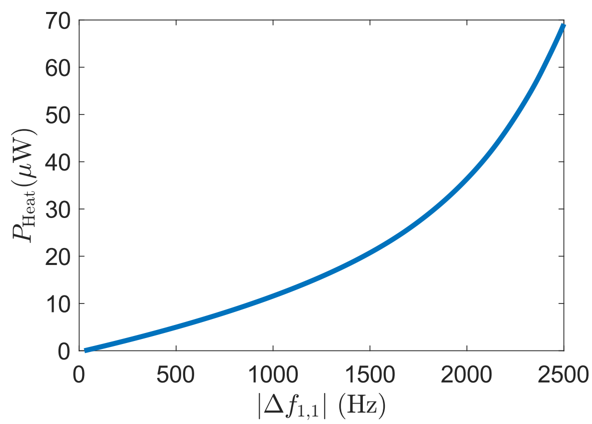

Figure 5.15: Simulated heating power P_{Heat} with respect to the simulated frequency shift of the (1,1) mode $\Delta f_{1,1}$. This dependence can be used as a calibration for heating power as a function of observed frequency shift. The change in the functional form at larger frequency shifts is due to the transition between the heat transfer being conduction-dominated to radiative cooling-dominated.

Another explanation might be in how the observed fits to data was performed. Under the effects of radiative cooling, one expects that there to be a nonlinear relationship between the temperature increase and the frequency shift of the (1,1) mode. Therefore, our model of a linear fit is only valid at low-temperature increases (low heating power). To attempt to quantify this relationship, we can also fit the observed value of the $\Delta f_{(1,1)}$ to the simulated value. Note that since the temperature maps are fully determined at this point, the only free parameter needed to perform this fit is the coefficient of thermal expansion of silicon nitride α_{th}. Not only does this allow for direct calibration of the heating power with respect to the observed frequency shift, but also provides a measure of $\alpha_{\rm th}$ for this particular sample of silicon nitride. One can see the nonlinear relationship between heating power and frequency shift in Fig. 5.15. This can be explained by the nature of the temperature maps, where at high heating powers the ratio of temperature between the absorber and the central pad is larger than what is seen at lower cooling powers. $\Delta f_{(1,1)}$ is mostly determined by the average temperature of the device. Radiative cooling effectively acts as a stronger thermal link to the environment as the temperature increases, meaning that more power is required to raise the average temperature of the device, and thus shift the (1,1) frequency, at higher heating powers. From a lumped sum model of heating, the average temperature of the device would exhibit two different power-law dependencies between heating power and temperature depending on whether or not the system is dominated by conductive cooling or radiative cooling. In our system, the crossover from conductive to radiative cooling can thus be seen to be around heating powers around 20 μW as seen in both Fig. 5.15, which qualitatively matches the behavior predicted from the lumped sum model results shown in Fig. 5.4. Overall, we argue that in order to calibrate material parameters, it is sufficient to match the low heating power data given the complications associated with radiative cooling on such a complicated geometry. Given all of this, the calibrated device parameters are tabulated in Tab. 5.1. We draw attention to the fact that these values match closely other values observed in the literature on other device geometries [99, 146]. This correspondence increases our confidence in the local geometry-independent values of the material properties used in our FEA simulations to explain the data, although one might expect that if additional studies were performed on equally complicated but distinct device geometries there might be deviations from our observed values.

5.7 Thermal motion of hybridized mechanical modes

The above experiment studied the effects of a spatially varying thermal bath on the Brownian motion of a wide range of mechanical modes. In this experiment, the temperature profile was changed by virtue of a changing heating power. Another possible experiment to change the observed Brownian motion would be to change the mode shape, and thus the dissipation map, of

thermal parameter	value
k_c	2.2 W/(m·K)
$\varepsilon_{\mathrm{Si_3N_4}}$	0.12
$C_{p,\mathrm{Si_3N_4}}$	700 J/(kg · K)
α_{th}	1.9×10^{-6} (K^{-1})
mechanical parameter	**value**
$\rho_{\mathrm{Si_3N_4}}$	3100 kg/(m^3)
$E_{\mathrm{Si_3N_4}}$	250 GPa
$\sigma_{\mathrm{Si_3N_4}}$	1.05 GPa
$\nu_{\mathrm{Si_3N_4}}$	0.23

Table 5.1: Thermal and mechanical parameters of Si_3N_4 used to produce temperature maps used in this work. k_c is the thermal conductivity, $\varepsilon_{\mathrm{Si_3N_4}}$ is the emissivity, $C_{p,\mathrm{Si_3N_4}}$ is the heat capacity at constant pressure and α_{th} is the coefficient of thermal expansion. $\rho_{\mathrm{Si_3N_4}}$ is the bulk density, $E_{\mathrm{Si_3N_4}}$ is the Young's modulus, $\sigma_{\mathrm{Si_3N_4}}$ is the tensile stress and $\nu_{\mathrm{Si_3N_4}}$ is the Poisson ratio of the stoichiometric LPCVD silicon nitride used in this work.

the mechanical modes themselves. One avenue towards such a control over mechanical mode shape is through a controlled hybridization of two mechanical modes. By tuning the hybridization of two modes, the relative mechanical dissipation between different regions of the mechanical device can be adjusted *in situ*. For this device, this hybridization can be engineered between the S_2 and MD modes due to their naturally low difference frequency of 40 kHz, and their different responses to local heating-induced frequency shifts. In studies of thermally induced mechanical frequency shifts – one such instance is micromechanical bolometers – it is useful to define the relative responsivity of a mechanical mode to a heat source:

$$R_f = \frac{1}{f}\frac{df}{dP}. \tag{5.10}$$

For the case of this particular device, it is observed and predicted that $R_f^{(\mathrm{MD})} \approx 13R_f^{(\mathrm{S_2})}$, which allows the two modes to be degenerate in frequency for the heating powers achievable on this device. We note that this property of mechanical modes is only realizable for local heat sources; global heating of the device, for instance by heating the entire apparatus or substrate, gives rise to all out-of-plane mechanical modes of the device having identical values of R_f. In this case, all mechanical modes will always be nondegenerate in frequency.

To begin this discussion, it is useful to first establish a theoretical basis for such a situation. To clarify terminology, we will refer to the eigenmodes of the system as mechanical normal modes. We imagine that the normal modes of the system with no heating power to be completely uncoupled, and will hereafter refer to these mechanical modes as local modes. We expect that the observed Brownian motion of the normal modes of the system to be nontrivial since the hybridization of the MD and S_2 modes is achievable via heating of the device. We expect that the hybridization will occur when each of the unhybridized local modes is exposed to relatively localized thermal baths with distinct temperatures.

To begin our discussion, we will begin with a discussion of the coupling of continuum local modes of a micromechanical resonator. This coupling has been considered in the context of PnC devices with two distinct geometric defect locations [77]. In this work, one can reduce the complexity of the problem via the Galerkin discretization method. Here, one can reduce the dynamics of the system to a subset of local modes, allowing for a description of the continuum model as an effective set of coupled degrees of freedom. The parameters of the degrees of freedom, as well as their coupling, can then be derived from the properties of the continuum modes. As a result of this discretization, one can derive an effective equation of motion:

$$\begin{aligned} K_{11}u_1 + K_{12}u_2 &= M_{11}\ddot{u}_1 + M_{12}\ddot{u}_2 \\ K_{21}u_1 + K_{22}u_2 &= M_{21}\ddot{u}_1 + M_{22}\ddot{u}_2 \end{aligned} \tag{5.11}$$

where the entries for the modal mass matrix M_{ij} and the modal stiffness matrix K_{ij} are given as:

$$M_{nm} = \rho\langle\phi_n|\phi_m\rangle \tag{5.12}$$

$$K_{nm} = \sigma\langle\nabla\phi_n|\nabla\phi_m\rangle \tag{5.13}$$

where the $\langle\cdot|\cdot\rangle$ corresponds to the volumetric overlap integral of the quantities in question. u_1 and u_2 represent the mechanical amplitude of each degree of freedom, while ϕ_n is the normalized mode shape as defined in Ch. 1

Eq. 5.11 can be rearranged to the more familiar form:

$$\mathcal{M}\ddot{u} + \mathcal{K}u = 0 \tag{5.14}$$

where $\mathcal{M}$ is given as:

$$\begin{pmatrix} M_{11} - \frac{M_{12}M_{21}}{M_{22}} & 0 \\ 0 & M_{22} - \frac{M_{12}M_{21}}{M_{11}} \end{pmatrix} \tag{5.15}$$

and $\mathcal{K}$ is:

$$\begin{pmatrix} K_{11} - \frac{K_{21}M_{12}}{M_{22}} & K_{12} - \frac{K_{22}M_{12}}{M_{22}} \\ K_{21} - \frac{K_{11}M_{21}}{M_{11}} & K_{22} - \frac{K_{12}M_{21}}{M_{11}} \end{pmatrix} \tag{5.16}$$

u is a column vector with components u_1 and u_2. For modes that are well localized and spatially separated, the overlap integrals are small: $M_{11}, M_{22} \gg M_{12} = M_{21}, K_{11}, K_{22} \gg K_{12} = K_{21}$. Also, since we are interested in the behavior where hybridization may occur – and thus the frequencies of the two modes are nearly degenerate – it follows that $K_{11}/M_{11} \approx K_{22}/M_{22}$.

Taking the leading order terms in the coupling, it follows that we can write $\mathcal{M}$ and $\mathcal{K}$ as:

$$\mathcal{M} = \begin{pmatrix} M_{11} & 0 \\ 0 & M_{22} \end{pmatrix} \equiv \begin{pmatrix} m_1 & 0 \\ 0 & m_2 \end{pmatrix} \tag{5.17}$$

$$\mathcal{K} = \begin{pmatrix} K_{11} & K_{12} - \frac{K_{22}M_{12}}{M_{22}} \\ K_{21} - \frac{K_{11}M_{21}}{M_{11}} & K_{22} \end{pmatrix} \equiv \begin{pmatrix} k_1 & -\kappa \\ -\kappa & k_2 \end{pmatrix} \tag{5.18}$$

An inspection of Eqs. 5.17 and 5.18 shows that two coupled continuum mechanical modes with small overlap can be reduced to two coupled simple harmonic oscillators.

To continue this discussion, we consider the effects of damping on the hybridization of two-point mass-coupled oscillators. To model this system, the equations of motion are defined as:

$$\mathcal{M}\ddot{u} + \mathcal{C}\dot{u} + \mathcal{K}u = 0. \tag{5.19}$$

Here we define the mass matrix M, the damping matrix C and the spring matrix K as:

$$\mathcal{M} = \begin{pmatrix} m_1 & 0 \\ 0 & m_2 \end{pmatrix}$$
$$\mathcal{C} = \begin{pmatrix} m_1\gamma_1 & 0 \\ 0 & m_2\gamma_2 \end{pmatrix} \tag{5.20}$$
$$\mathcal{K} = \begin{pmatrix} m_1\omega_1^2 & -\sqrt{m_1 m_2}\, g^2 \\ -\sqrt{m_1 m_2}\, g^2 & m_2\omega_2^2 \end{pmatrix}$$

Note that the convention for coupling terms in K is selected such that the normal mode splitting at zero detuning is g^2/ω_0 for all values of m_1 and m_2 in the undamped case.

To calculate the normal modes, one can assume that $u(t) = u_0 e^{\lambda t}$. With this assumption, we have effectively elected to solve the problem via a Laplace transformation. In this case, the equations of motion can be rephrased as a polynomial in λ with matrix coefficients:

$$(\mathcal{M}\lambda^2 + \mathcal{C}\lambda + \mathcal{K})u_0 = 0. \tag{5.21}$$

Much like an eigenvalue problem, this equation has nontrivial solutions for both λ and u_0 if λ is a root of the following polynomial:

$$A(\lambda) = \det(\mathcal{M}\lambda^2 + \mathcal{C}\lambda + \mathcal{K}) = 0 \tag{5.22}$$

In general, there are four solutions for λ for the above equation, coming in two complex conjugate pairs. Physically, the imaginary part of λ corresponds to the frequency of each mode, while the real part corresponds to the energy decay rate of the mode in question. Although there is an analytical expression for each λ, its form is rather involved and will not be presented in this work, as the general solution can be generated by the quartic formula. Once the roots of Eq. 5.22 are known, then inserting each root into Eq. 5.21 produces a system of linear equations whose null space contains the normal mode corresponding to the eigenvalue in question. The two complex conjugate pair solutions for λ produce a complex conjugate pair of normal modes up to a scale factor that without loss of generality can be neglected.

Although the forms of the equation are rather complicated, one can still investigate the properties of the solutions analytically. One such investigation would be to identify critical parameters of the system where changes in qualitative behavior occur. For this section of the work, we seek to identify in which parameter regime one can observe a hybridization of the two modes. This might be a surprising question to ask if one is only familiar with the undamped case of this problem, where hybridization will always occur. However, it can be shown that there is a critical value of the coupling – when compared to the dissipation present in the system – below which full hybridization ceases to occur, even the natural frequency of the two local mechanical oscillators is fully degenerate. Incomplete hybridization coincides with the property that two of the roots of Eq. 5.22 have equal imaginary parts, meaning that the system does not exhibit an avoided crossing. A common tool to study the properties of roots of polynomials is to study the discriminant of the polynomial:

$$\mathrm{Disc}_x(A) = a_n^{2n-2} \prod_{i<j} (r_i - r_j)^2. \tag{5.23}$$

Here $A(x)$ is a polynomial of the form:

$$A(x) = a_n x^n + a_{n-1} x^{n-1} + \cdots + a_1 x + a_0 \tag{5.24}$$

with roots r_i.

An inspection of Eq. 5.23 obviates the property that a polynomial with discriminant 0 is indicative of repeated roots of the polynomial. In our case, Eq. 5.22 defines the characteristic polynomial of our problem. The discriminant with respect to λ of Eq. 5.22, can be considered to be a polynomial of some parameter in its own right. For the case of searching for the lack of avoided crossing, one can consider $\mathrm{Disc}_\lambda(A(\lambda))$ as a polynomial in the detuning δ between the two modes in question, which we can define as $B(\delta)$. By setting $\mathrm{Disc}_\delta(B(\delta)) = 0$, one can search for parameters where the roots $A(\lambda)$ change their behavior, notably where the system can or cannot exhibit degenerate imaginary parts of their roots. This condition, although analytical, produces rather high-order polynomials that are difficult to manipulate in the most general cases. A more simplified case of the problem is when $m_1 = m_2$, $\gamma_1 = 0$, $\omega_1 = \omega_0$ and $\omega_2 = \omega_0 + \delta$. In this case, one can verify that by setting $\mathrm{Disc}_\delta(B(\delta)) = 0$, the condition that $g^2 = \gamma_1\omega_0$ is revealed.

For the more general case, Eq. 5.22 can be numerically solved. Since we are most concerned with the degree of hybridization in this model, we define a parameter μ_i hereafter referred to as the mixing factor:

$$\mu_i \equiv \min\left(||u_1^{(i)}(\delta)|^2 - |u_2^{(i)}(\delta)|^2|\right). \tag{5.25}$$

μ_i ranges between 0 and 1, and $u_j^{(i)}$ is the normalized motional amplitude of mass j in normal mode i. When $\mu_i = 0$, this means that there is a detuning at which the mode is fully hybridized (equal participation of masses m_1 and m_2), while when $\mu_i = 1$, this means that the mode has the participation of only a single mass.

In Fig. 5.16 one can see the effects of dissipation on the mixing factor. For values of g^2 below the critical value, the $\mu_i > 0$ indicating incomplete hybridization. For values of g^2 much larger than the critical value, the behavior of the system matches that of the undamped system. We can evaluate which regime our system is in by considering the dissipation of both the MD and S_2 modes. The hybridization of two modes is dominated by the more dissipative mode, in this case, the MD mode. By extracting γ from experimental results, and the simulated undamped splitting $\delta\omega_m$ from FEA simulations targetting the MD - S_2 hybridization, we can compare the coupling strength to the dissipation present in the system. This comparison is denoted by the black dotted line in Fig. 5.16, indicating that our system should exhibit behavior closely matching that of the undamped system, and thus one should expect full hybridization to occur in theory.

We again continue our analysis by studying the properties of the normal modes calculated from Eq. 5.22. At the outset, the masses, damping rates, and temperatures (expressed as m_i, γ_i, and T_i respectively) of the local modes are known. The goal will be to derive the analogous

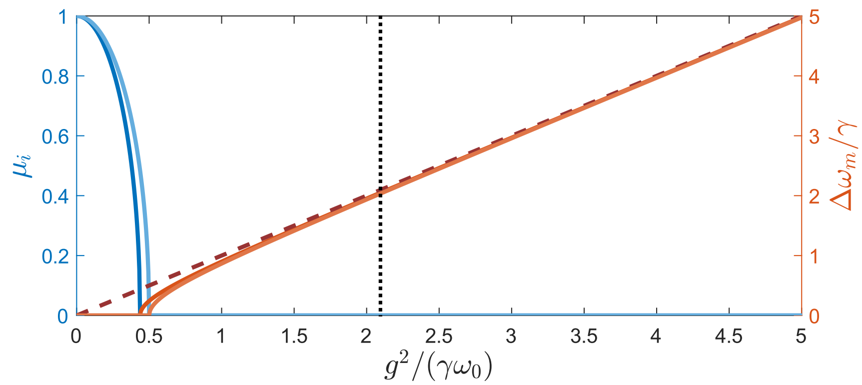

Figure 5.16: Left axis: mixing factor μ_i as a function of coupling strength g. Right axis: normal mode splitting $\Delta\omega_m$ as a function of coupling g in the case when $\gamma_2 = \gamma \gg \gamma_1$. Dark (light) lines correspond to the behavior in the case when $\gamma_1 = 0$ ($\gamma_1 = \gamma_2/8$). The dotted red line indicates the asymptotic value of the splitting expected when $\gamma_1 = \gamma_2 = 0$. The latter case corresponds to the parameters explored experimentally. In both cases, there is a critical value of g, below which an avoided crossing does not occur. In the case of no avoided crossing, it is evident that the degree of hybridization also decreases since $\mu_i > 0$ in this regime. The vertical dotted line corresponds to the value of g between the S_2 mode and the mass-defined defect mode (MD) explored experimentally in this work.

properties (M_i, Γ_i and $T_{\text{eff}}^{(i)}$) of the normal modes.

The damping rates of the normal modes can be calculated from energetic arguments. Notably, it can be interpreted as the energy lost per oscillation times the oscillation rate:

$$\Gamma = \omega_m \frac{\Delta W}{2\pi W} \tag{5.26}$$

where ΔW is the energy lost per oscillation, and W is the energy stored in the oscillator. In this coupled mode model, ΔW can be calculated as the sum of the work done by damping forces on each point mass per cycle. For harmonic motion, W can be calculated to be twice the average kinetic energy over a single oscillation period. Therefore in the case of two coupled point masses, the expression for the damping rate of mode i is then:

$$\Gamma_i = \gamma_1 m_1 \frac{|u_1^{(i)}|^2}{(|u_1^{(i)}|^2 m_1 + |u_2^{(i)}|^2 m_2)} + \gamma_2 m_2 \frac{|u_2^{(i)}|^2}{(|u_1^{(i)}|^2 m_1 + |u_2^{(i)}|^2 m_2)} \tag{5.27}$$

To calculate the effective temperature of the mode in this model, we begin with the general case of a continuous oscillator subject to a spatially varying thermal bath:

$$T_{\text{eff}} = \frac{\int \alpha T dV}{\int \alpha dV} = \frac{\int \alpha T dV}{\Gamma} \tag{5.28}$$

where T is the local physical temperature of the mechanical structure, and α is the dissipation density of the mode. The analogous formula for the coupled point oscillator model would replace integrals over volume with summations over the contributions from each mass:

$$T_{\text{eff}} = \frac{\int \alpha T dV}{\Gamma} \rightarrow \frac{\sum_{i=1}^{2} \tilde{\alpha}_i T_i}{\Gamma} \tag{5.29}$$

Here we have neglected the mode indices on T_{eff} and α for clarity. An inspection of Eq. 5.27 readily identifies an expression for $\tilde{\alpha}_i$:

$$\tilde{\alpha}_i = \frac{\gamma_i m_i |u_i|^2}{|u_1|^2 m_1 + |u_2|^2 m_2} \tag{5.30}$$

Therefore, the effective temperature for normal mode i is:

$$T_{\text{eff}}^{(i)} = \frac{T_1 \gamma_1 m_1 |u_1^{(i)}|^2 + T_2 \gamma_2 m_2 |u_2^{(i)}|^2}{\gamma_1 m_1 |u_1^{(i)}|^2 + \gamma_2 m_2 |u_2^{(i)}|^2} \tag{5.31}$$

Note that in this calculation, normalization conventions for the mode shape vector components $u_{i,j}$ have no effect on the result. Furthermore, this result relies only on the hybridized mode shape and thus is valid for all regimes of the hybridization process.

To infer the Brownian motion from the effective temperature, the effective mass of each mode must be considered. We note that the effective mass depends not only on the mode being probed but also on the probe location. In the point mass case, there are two probe locations — one for each mass — and thus we can define the effective mass of mode i observed at mass j to be:

$$M_{eff,j}^{(i)} = m_1 \frac{|u_1^{(i)}|^2}{|u_j^{(i)}|^2} + m_2 \frac{|u_2^{(i)}|^2}{|u_j^{(i)}|^2} \tag{5.32}$$

Finally, the observed Brownian motion can be expressed from the equipartition theorem:

$$\langle (x_j^{(i)})^2 \rangle = \frac{k_B T_{\text{eff}}^{(i)}}{M_{eff,j}^{(i)} \Omega_i^2} \tag{5.33}$$

When experimentally probing the effects of hybridization on the modal temperatures, a salient quantity to consider is y_i:

$$\langle y_i^2 \rangle = \langle (x_i^{(1)})^2 \rangle + \langle (x_i^{(2)})^2 \rangle \tag{5.34}$$

From the above formalism, it can be shown that if the normal modes are computed in the undamped limit:

$$\begin{aligned} \langle y_i^2 \rangle &= \frac{k_B \mathcal{T}_{\text{eff}}^{(i)}}{m_i \omega_i^2} \\ \mathcal{T}_{\text{eff}}^{(i)} &= T_i \frac{(\frac{T_j}{T_i} - 1)\frac{\omega_i^2}{\omega_j^2} + \frac{\gamma_j T_j}{\gamma_i T_i} + 2 + \frac{\gamma_i}{\gamma_j} + (\frac{\omega_i^2 - \omega_j^2}{g^2})^2}{\left(1 - \frac{g^4}{\omega_i^2 \omega_j^2}\right)\left((\frac{\gamma_i}{\gamma_j} + 2 + \frac{\gamma_j}{\gamma_i}) + (\frac{\omega_i^2 - \omega_j^2}{g^2})^2\right)} \end{aligned} \tag{5.35}$$

This expression for $\langle y_i^2 \rangle$ has the property that it depends only on m_i, the mass of the non-hybridized mode i. Another notable property is revealed when considering the case that $T_i = T_j = T$:

$$\begin{aligned} \langle y_i^2 \rangle &= \frac{k_B T}{m_i \omega_i^2} \left(1 - \frac{g^4}{\omega_i^2 \omega_j^2}\right)^{-1} \\ &= \frac{k_B T}{m_i \omega_i^2} \left(1 + \mathcal{O}(\frac{g^4}{\omega_i^2 \omega_j^2})\right) \end{aligned} \tag{5.36}$$

For this work, the simulated minimal normal mode splitting is 500 Hz, therefore $\frac{g^4}{\omega_i^2 \omega_j^2} \approx 10^{-8}$. Hence, a measurement of $\langle y_i^2 \rangle$ has no discernible dependence on detuning when bath temperatures are equal, regardless of any other parameter mismatch between the modes in question. Therefore, any change in $\langle y_i^2 \rangle$ necessarily arises from a mismatch in thermal bath temperatures. When the two oscillators are degenerate ($\omega_i = \omega_j$), the expression for $\langle y_i^2 \rangle$ reduces to the simple form:

$$\langle y_i^2 \rangle = \frac{k_B}{m_i \omega_i^2} \left(\frac{T_i \gamma_i + T_j \gamma_j}{\gamma_i + \gamma_j} + \mathcal{O}(\frac{g^4}{\omega_i^4}) \right) \tag{5.37}$$

This expression of the quantity $\langle y_i^2 \rangle$ corresponds to a single local oscillator subject to two different baths. The inferred temperature of this local oscillator would be:

$$\mathcal{T}_{\text{eff}}^{(i)} \approx \frac{T_i\gamma_i + T_j\gamma_j}{\gamma_i + \gamma_j} \tag{5.38}$$

Here we will present the results of the hybridization of the MD and S_2 modes. As stated previously, we found it experimentally useful to study the quantity $\langle y_i^2 \rangle$ However, in principle, one could measure the thermomechanical noise spectrum S_{xx} as a function of heating power while probing at either the defect pad or near the absorber in order to probe the effects of the hybridization. However, this was difficult due to the instability of the heating of the device. Although the intensity of the heating laser was locked, there was appreciable frequency instability of the MD mode while the heating laser was operated, as seen in Fig. 5.17. We attribute this added noise to mechanical instabilities of the optical system giving rise to beam pointing, and thus intensity noise of the absorbed light. Such instability complicates the quantitative analysis of the thermomechanical noise spectrum. However, frequency noise does not change the energy of the system in question, and thus one can in principle study the integrated motion of each mode across a bandwidth that is wider than the size of the frequency fluctuations. This is difficult when the modes are close to resonance, precluding the ability to distinguish the energetic contribution from each normal mode of the system. Thus we found it useful to integrate the power across both modes, meaning that we will probe the quantity $\langle y_i^2 \rangle$.

The results of the hybridization experiment are shown in Fig. 5.18. Firstly, one can observe the mechanical frequency of the S_2 and MD modes as they are brought close to hybridization. Note that at the heating poweres needed for hybridization, one expects a linear relationship between the frequency shift of the two modes and the (1,1) frequency shift. However, an additional mechanical mode was also observed close to the MD natural frequency. The presence causes the frequency shift of the MD modes to be slightly nonlinear due to effects of an avoided crossing. The presence of this mode is negligible near the hybridization of the S_2 and MD modes.

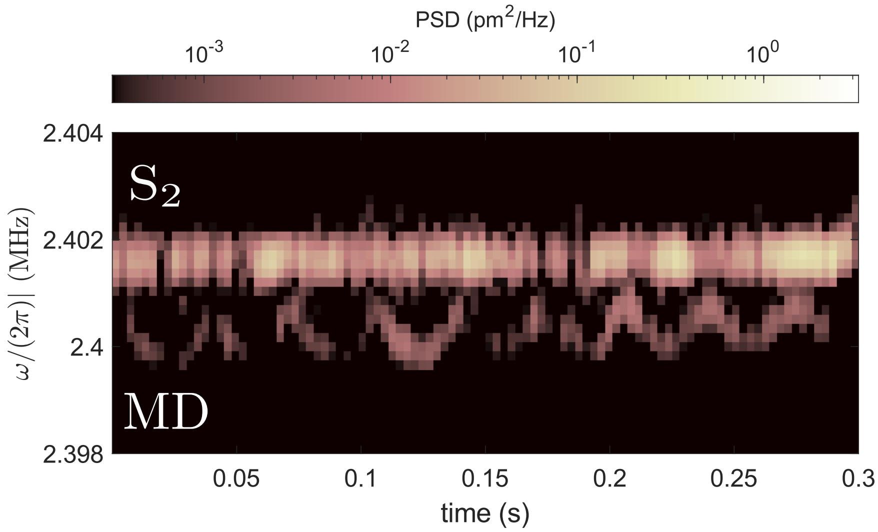

Figure 5.17: Spectrogram of thermomechanical motion acquired while probing on the central defect pad while heating such that the S_2 and MD modes are closely hybridized. The MD mode has relatively large frequency fluctuations due to its relatively large fractional frequency shift.

As discussed above, one can define an additional parameter related to $\langle y_i^2 \rangle$:

$$\tilde{\mathcal{T}}_{\text{eff}}^{(\text{S}_2,\text{MD})} \equiv \frac{\langle y^2_{(\text{S}_2,\text{MD})} \rangle \omega^2_{\text{S}_2}}{\langle \langle y^2_{(\text{S}_2,\text{MD}),0} \rangle \omega^2_{\text{S}_2,0} \rangle_{\text{all}}} T_{\text{lab}}. \tag{5.39}$$

Here, ω_{S_2} is the extrapolated angular frequency of the S_2 mode without hybridization. As stated before, this "temperature" does not depend on the effective mass changes due to the mode coupling, yet can still carry information about the local temperatures of the two non-hybridized modes. As seen in Eq. 5.35, the form of $\tilde{\mathcal{T}}_{\text{eff}}^{(\text{S}_2,\text{MD})}$ depends on the dissipation, the effective mass, the frequency, and the coupling between the two modes, as well as the local bath temperature of each mode, namely T_{cp} and T_{ab}. It is, however, constructive to write the expected value for $\tilde{\mathcal{T}}_{\text{eff}}^{(\text{S}_2,\text{MD})}$ in two specific limits:

$$\tilde{\mathcal{T}}_{\text{eff}}^{(\text{S}_2,\text{MD})} = \begin{cases} T & T_{\text{cp}} = T_{\text{ab}} = T \\ \frac{T_{\text{cp}}\gamma_{\text{S}_2} + T_{\text{ab}}\gamma_{\text{MD}}}{\gamma_{\text{S}_2} + \gamma_{\text{MD}}} & \omega_{\text{S}_2} = \omega_{\text{MD}} \end{cases}. \tag{5.40}$$

The first limit shows that for a spatially uniform bath, the temperature associated with the motional observable $\langle y_i^2 \rangle$ is just the physical temperature of the oscillator. We find this notable because it shows that any increase of $\langle y_i^2 \rangle$ can be attributed to a spatially varying thermal bath. To quantify this change in temperature, one can inspect the second case, which predicts what happens when the two oscillators are brought into resonance. Here, the value of $\tilde{\mathcal{T}}_{\text{eff}}^{(\mathrm{S}_2,\mathrm{MD})}$ takes the form of Eq. 5.4 for a single oscillator in the presence of two different loss channels, and thus two different baths.

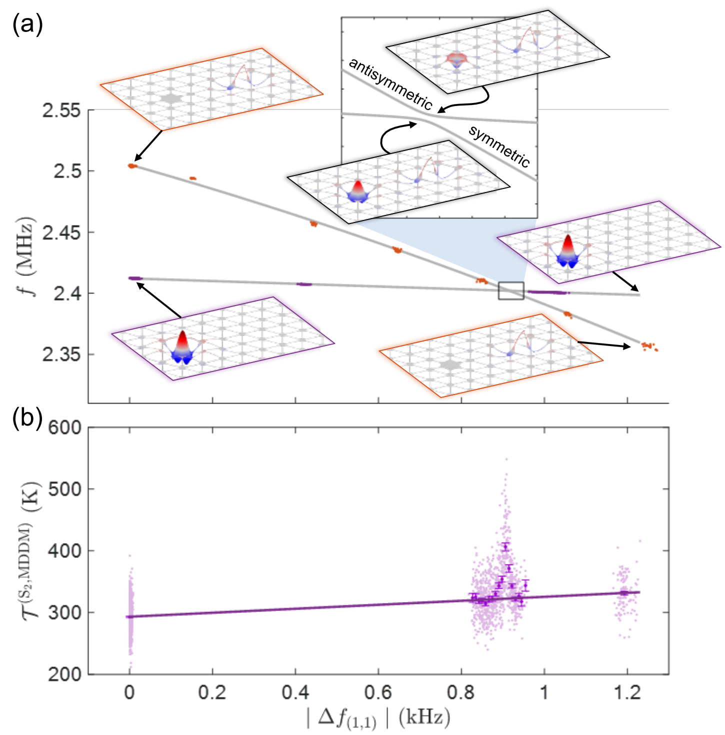

Figure 5.18: Hybridization of S_2 and MD modes. (a) Measured frequencies of S_2 and MD modes with respect to $\Delta f_{1,1}$ (orange and purple points). Gray lines mark the theoretical hybridization frequency curves obtained from fits to the measured modes' frequencies and FEA prediction for their coupling strength. The mode-hybridization shape determined from FEA is shown along the frequency curves. The inset shows a zoomed-in plot around the full hybridization point. (b) $\tilde{\mathcal{T}}_{\text{eff}}^{(\mathrm{S}_2,\mathrm{MD})}$ as a function of $\Delta f_{1,1}$, Measured (purple points) and $\Delta f_{1,1}$-binned (purple full circles with error bars). The line is a single parameter fit, disregarding all points around $\delta f_{1,1} \approx 0.9\,\text{kHz}$. (a) and (b) share the horizontal axis.

The heating results are shown in Fig. 5.18b. Here, one sees that there is a noticeable increase in $\tilde{\mathcal{T}}_{\text{eff}}^{(\mathrm{S}_2,\mathrm{MD})}$ when the two modes are brought into resonance. This is expected when considering the results of the first heating experience, where the temperature of the absorber should exceed the central pad temperature by approximately 500 K (Fig. 5.8). We note that the increase in $\tilde{\mathcal{T}}_{\mathrm{eff}}^{(\mathrm{S}_2,\mathrm{MD})}$ is considerably less than the expected value of 750 K predicted from Eq. 5.40. We attribute this to the aforementioned heating-induced frequency noise of the MD. The size of the noise was on the order of 1 kHz, exceeding the predicted frequency splitting from FEA simulation. Fluctuations with the observed size and time correlation lead to rather complicated dynamical effects. Firstly, one would expect that much of the experimental time was spent where the instantaneous state of the oscillators was not fully hybridization. Furthermore, since the fluctuations occurred on a time scale of around 10 ms, the normal modes of the system changed at a rate faster than the predicted values of Γ in the steady state, and thus could never fully thermalize to the spatially varying thermal bath. We acknowledge that these effects most likely led to the reduced value of $\tilde{\mathcal{T}}_{\mathrm{eff}}^{(\mathrm{S}_2,\mathrm{MD})}$ observed in the experiment, but did not seek to perform further analysis to relate the observed frequency noise to this reduced value of motion.

Chapter 6

Micromechanical bolometer based on silicon nitride membrane resonators

In this section, we will discuss a recent effort in our group to expand the range of sensing applications for low-dissipation mechanical resonators based on tensioned silicon nitride membranes. The thermal physics explored in Ch. 5 is a coupling between the nature of the mechanical motion of the resonators we study and their thermal environment. We propose a mechanical sensor that leverages this coupling to probe the thermal environment of the resonator, namely the thermal radiation impinging on the device. Such a device is called a bolometer, or a sensor of radiant heat. In this section, we will overview the design principles and considerations associated with making a micromechanical bolometer.

Conventional bolometers have many applications, ranging from thermal imaging to instrumental astrophysics. Typically, the readout is achieved by measuring a change in the resistance of some electronic circuit element [152–155]. The nature of this readout, although simple, is typically limited by Johnson noise in the readout circuitry. Thus a common approach to improve bolometric sensitivity is to cool down the detector, often to cryogenic conditions. The current state-of-the-art bolometers in fact rely on a superconducting phase transition, where a thermal photon can locally break superconductivity, giving rise to a sharp increase in the observed resistance of the circuit. The state-of-the-art in this sensing paradigm currently achieves sensitivities on the order of $10\ \mathrm{zW}/\sqrt{\mathrm{Hz}}$ [156]. This technology has led to superconducting nanowire single-photon detectors, which leverage this effect to detect single photons over a wide range of frequencies [157]. However, despite the exemplary sensitivities of these methods, they are highly reliant on the cooling of the device. Therefore, there is a large interest in improving the sensitivities of ambient condition bolometers. These have advantages in many fields, one of which is astrophysics, where achieving cryogenic conditions on satellites presents a considerable engineering challenge.

Current state-of-the-art uncooled resistive bolometers reach sensitivities around 10 pW/$\sqrt{\text{Hz}}$, so any improvements beyond this scale will advance our current technological capabilities [158]. These sensitivities are limited by Johnson noise associated with the resistive readout of the bolometric signal. Therefore, potential improvements could arise from alternative readout methods. For instance, a pW/$\sqrt{\text{Hz}}$ bolometer has been realized based on a graphene mechanical resonator, while silicon nitride trampoline resonators have exhibited 10 pW/$\sqrt{\text{Hz}}$ have been demonstrated on silicon nitride trampoline resonators [149, 159]. For silicon nitride devices, a goal of micromechanical bolometer design would be for the noise floor to be defined not by the Brownian motion of the device, but rather by the intrinsic fluctuations of the surrounding blackbody environment. These fluctuations arise from both thermal photons associated with material absorption, and through thermal phonons associated with a thermally conductive link to the environment. As discussed in this chapter, the level of these fluctuations depends on the specific geometry in question but will be on the order of 100 fW/$\sqrt{\text{Hz}}$ for the scale of tensioned silicon nitride mechanical resonators typically implemented. To achieve higher bandwidth detection, the geometry can be modified to be more thermally conductive, allowing for a faster response to incoming signal radiation, albeit at the cost of sensitivity. In this chapter, we will work towards this goal by modifying the mechanical resonator geometry that is typically used for these types of measurements. In doing so, we will leverage a unique aspect of frequency-shift-based mechanical sensors, where the functionalizing agent, the absorber in this case, can be spatially separated from the mechanical motion. This is because both temperature and stress perturbations have long-range influences on the device. Our proposed design utilizes this in full, allowing for flexibility in the choice of absorber since the lack of mechanical motion at the absorbing point minimizes the additional loss associated with the added material.

6.1 Bolometer fundamental noise sources

The operating principle of any bolometer relies on the absorption of incoming thermal radiation leading to a change in a physical quantity. Bolometers are typically conceptualized as a thermal mass with a heat capacity $\mathcal{C}$ linked to a thermal bath with a conductance G. A fundamental source of noise concerns the random exchange of thermal quanta with the environment through this conductance. In the systems studied in this work, G has two main contributions. The first is from the conductive link to the environment. This can be modeled through a bridge of length L and cross-sectional area A_c connecting the thermal mass to the environment. In this situation, the thermal quanta being exchanged with the environment are phonons. Hence, we will call this noise phonon noise [160]. Therefore, the conductance associated with the conductive pathway G_c is given as:

$$G_{\text{phonon}} = k_c A_c / L \tag{6.1}$$

where k_c is the coefficient of thermal conductivity for the bridge material.

The other link in question is the radiative link. Here, we want to know the effect of incoming thermal photons on the device. We can call this photon noise [160]. This can be given as:

$$G_{\text{photon}} = 4 A_{rad} \sigma \epsilon (T^3) \tag{6.2}$$

where ϵ_{env} is the emissivity of thermal mass, σ is the Stefan-Boltzmann constant, T is the device temperature, and A_{rad} is the radiational cross section of the thermal mass. For uncooled bolometers, the radiative conductance can be strong given the T^3 scaling. The total conductance of the system will be $G = G_{\text{phonon}} + G_{\text{photon}}$. Therefore, the noise equivalent power associated with these two pathways can be given as:

$$\eta_{th} = \sqrt{4 k_B G T^2} \tag{6.3}$$

where we have used the subscript th to indicate that this noise is from the thermal background of the detector.

Any practical implementation of a bolometer will also have additional noise associated with the readout of the physical quantity of interest. Therefore, the total noise of a bolometric measurement will be:

$$\eta = \sqrt{\eta_{th}^2 + \eta_{ro}^2} \tag{6.4}$$

where η_{ro} is the readout noise associated with the bolometer archetype in question. For many resistive bolometers, this readout noise will typically limited by Johnson noise in the readout circuitry [161]. In principle, micromechanical bolometers afford a different readout scheme, in principle limited by the thermomechanical noise of a single degree of freedom of the system.

6.2 Micromechanical bolometer operating principle

It is not obvious at the outset how one should utilize a micromechanical resonator as a bolometer. In Ch. 5, we demonstrated two effects arising from the heating of the device: an increase in Brownian motion, and a mechanical frequency shift. We assert that for the desired sensitivities of uncooled bolometers (< 1 pW/$\sqrt{\text{Hz}}$), observing a change in the Brownian motion due to such a small amount of absorbed power would require long averaging times. However, we note that some mechanical modes, namely the MD mode, experienced frequency shifts in great excess of the intrinsic linewidth of the resonator. Therefore, we identify a detection of a mechanical frequency shift due to stress changes — as seen in Ch. 5 — as the proposed method of transducing the amount of absorbed power [99, 149, 162].

Here, we will discuss a theory of how to best detect mechanical frequency shifts. A naive measurement of a frequency shift would be to observe the change in the thermal motion. If the frequency shift δf is greater than the linewidth of the mechanical resonance, then the shift is observable. However, it would take a measurement time τ equal to $1/\gamma$ in order to resolve the two peaks. Therefore, the sensitivity can be expressed as:

$$\eta = \sqrt{\frac{1}{Q\omega_0 R_f^2}} \tag{6.5}$$

where the quantity η will be referred to hereafter as the noise-equivalent power of the sensor. The above analysis is rather crude and does not take into account aspects of this measurement such as random sampling of S_{xx} in a finite measurement time.

This number can be improved by introducing a mechanical drive. The reason for this improvement can be seen from the equation of motion, where the contribution of the mechanical frequency scales as the mechanical motion $x(t)$. In more concrete terms, we can imagine a situation where the mechanical resonator is maintained at a constant amplitude A through an external resonant drive. We can then encode the information about the resonator's motion in quadratures of motion:

$$dx(t) = X(t)\cos(\omega_0)t + Y(t)\sin(\omega_0 t) = A\cos(\omega t) + Y(t)\sin(\omega_0 t) \tag{6.6}$$

where we have assumed that the resonant drive results in motion in only the X quadrature of motion, which can be defined as the amplitude quadrature. To linear order, any information about a frequency change of the oscillator will be present in $Y(t)$, the phase quadrature. Under this scheme, the phase of the oscillator can be calculated as:

$$\phi \approx Y(t)/A. \tag{6.7}$$

For a micromechanical oscillator, this measurement will be inherently limited by the thermal noise of the oscillator. Therefore, we can define an rms phase noise resulting from thermal motion as:

$$\delta\phi_{\text{th}} \approx \sqrt{\frac{k_B T}{m_{\text{eff}}\omega_0^2 A^2}} \tag{6.8}$$

Here we observe that the amount of phase fluctuations, which are directly related to frequency fluctuations, caused by the thermal motion of the oscillator are diminished by a factor of $1/A$.

Therefore, any scheme that wishes to read the frequency shift of a mechanical oscillator benefits from a mechanical drive. Typically, we are interested in the spectrum of the measurement noise. Here we are interested in the phase noise spectrum $S_{\phi\phi}$ in relation to the motional spectrum produced from Brownian motion S_{xx}. They can be related as:

$$S_{\phi\phi} = \frac{S_{xx}}{A^2}. \tag{6.9}$$

The frequency and phase noise spectra are related as:

$$S_{\Omega\Omega} = \omega^2 S_{\phi\phi} \tag{6.10}$$

where $S_{\Omega\Omega}$ here we have adopted a notation where Ω is the instantaneous frequency of the oscillator. In essence, what $S_{\Omega\Omega}$ encodes is the frequency stability of the oscillator. Oftentimes it is useful to relate this to another quantity, the Allan variance of the resonance σ_f. The definition of the Allan variance of a quantity y is expressed as:

$$(\sigma_y^{(\mathrm{A})}(\tau))^2 = \frac{1}{2}\frac{1}{N-1}\sum_{k=2}^{N}(\bar{y}_k - \bar{y}_{k-1})^2. \tag{6.11}$$

Here, $\bar{y}_k$ is an averaged value of y over the kth measurement bin with time length τ, and N is the number of bins for a given τ [1]. For the case of frequency noise, the Allan variance can be related to the frequency noise spectrum as:

$$(\sigma_\Omega^{(\mathrm{A})}(\tau))^2 = \frac{16}{\pi\tau^2}\int_0^\infty d\omega S_{\Omega\Omega}(\omega)\frac{\sin^4(\omega\tau/2)}{\omega^2} = \frac{16}{\pi\tau^2}\int_0^\infty d\omega S_{xx}(\omega)\frac{\sin^4(\omega\tau/2)}{A^2} \tag{6.12}$$

Assuming a classical thermal noise spectrum, this yields an Allan variance of the form:

$$\left(\sigma_\Omega^{(\mathrm{A})}(\tau)\right)^2 = \frac{k_B T}{m_{\mathrm{eff}}\omega_0 A^2 Q\tau}\frac{(\tau\gamma)^2}{1+(\tau\gamma)^2}. \tag{6.13}$$

Eq. 6.13 gives the Allan variance in the ideal case where the oscillator is only subject to Brownian motion. We emphasize that this is the fundamental noise that dictates the frequency stability. In general, there can be other sources of frequency noise for mechanical oscillators. Ambient temperature drifts of the laboratory, or packaging environment, can give rise to corresponding long-term frequency drifts of the device. There is some evidence that silicon nitride mechanical resonators can experience excess frequency noise, which would increase the Allan variance [163]. We draw attention here to there is little evidence of excess frequency noise observed on tensioned silicon nitride micromechanical resonators, outside of ambient temperature fluctuations of the environment [33, 37]. This is in contrast to other material platforms that exhibit frequency jitter or instability [70, 164]. Depending on the vacuum environment, there have also been observations of unidirectional long-term frequency drifts, indicative of slow deposition of contaminants on the device [1]. All of these drifts should be taken into account. It has been shown that many sources of frequency noise are common-mode between mechanical modes, and therefore it is possible to stabilize the frequency of a target mechanical mode with respect to another mode of the device [71].

The Allan variance can be related to the noise-equivalent-power in the following relation:

$$\eta_{ro} = \frac{\sigma^{(\mathrm{A})}_{\delta\Omega/\Omega}\sqrt{\tau}}{R_f} \tag{6.14}$$

where we have used the fractional Allan variance ($\sigma^{(\mathrm{A})}_{\delta\Omega/\Omega}$) and the relative responsivity of the mode in question. The subscript "*ro*" refers to readout in this case.

The performance of bolometers is not strictly determined by the sensitivity. Notably, a sensor with a larger bandwidth (short response times) is desired. As explored in Ch. 5, the response time of a mechanical frequency shift is dictated by a host of factors but is overall determined by the thermal isolation of the structure. Another aspect of bolometer design is the overall sensor size. Many applications for these sensors seek to create arrays of these sensors, and therefore miniaturization of the device is a thrust in order to reduce the pixel size.

6.3 Mechanical frequency tracking schemes

We have established that the effects of Brownian motion on the Allan variance of a mechanical mode can be diminished via the application of a large mechanical drive amplitude. These large oscillation amplitudes are typically achieved by applying a drive resonant with the instantaneous frequency of the oscillator. If the signal of interest is a frequency shift, there should be a scheme in place to allow the resonant drive to follow this frequency. There is currently a lot of interest in investigating various schemes to achieve frequency tracking, which we will summarize in this section [5].

We identify three schemes that one can pursue for frequency tracking, feedback-free, phase-locked-loop, and self-sustained oscillation, some of which I have pursued in the lab in preliminary analysis of membrane frequency shift, and phase noise measurements. Although all three can reach similar performance in principle, each possesses technical advantages which we discuss here. First, we will discuss the most straightforward scheme, feedback-free. Here, no frequency tracking is necessary. It is assumed that the oscillator will maintain a nearly constant frequency and that the frequency shifts one wishes to detect are smaller than the resonant linewidth of the mechanical oscillator. Under a near-resonant drive, the motion of the oscillator will be a sum of two terms, which can be thought of as the fast and slow response of the oscillator. The slow term results from the accumulation of driven motion resulting from the near-resonant drive. If there is a sudden change in oscillator frequency, it will take a timescale $\tau_r = 1/\gamma$ in order to establish the new steady state response. At the same time as this solution to the equation of motion develops, there is also a fast response that can be extracted by simply calculating the instantaneous phase of the oscillator and differentiating in order to extract an instantaneous frequency. Combining these two responses, the inferred frequency can be calculated as:

$$\Delta\omega(t) = \frac{\Delta\theta(t)}{\tau_r} + \frac{d\Delta\theta(t)}{dt} \tag{6.15}$$

where $\Delta\theta(t)$ is the phase difference from the reference drive signal. As stated before, the assumption in this scheme is that one will always drive near resonance, and therefore the readout of these phases will be associated with relatively small amounts of thermal noise.

For a more robust detection scheme, feedback can be implemented in order to maintain a resonant drive even for large frequency deviations of the resonator. This is of practical importance since ambient temperature fluctuations of the resonator housing can lead to slow, long-term drifts of the resonator frequency. The first scheme we will discuss is the self-sustained oscillation (SSO) scheme. This scheme can be understood as an application of an anti-damping force of the form $\gamma\dot{x}(t)$, meaning that the oscillator will maintain constant energy. To achieve this, a feedback loop is implemented as shown in Fig. 6.1a. Here, the oscillator motion is phase-shifted by $+\ \pi/2$ and then passed through a saturating amplifier. The phase shifter converts the motion signal $x(t)$ to $\dot{x}(t)$, while the saturating amplifier defines the level of desired force one wants to apply for an operating mechanical amplitude. In a frequency-locked system, this amounts to a perfectly anti-damped force.

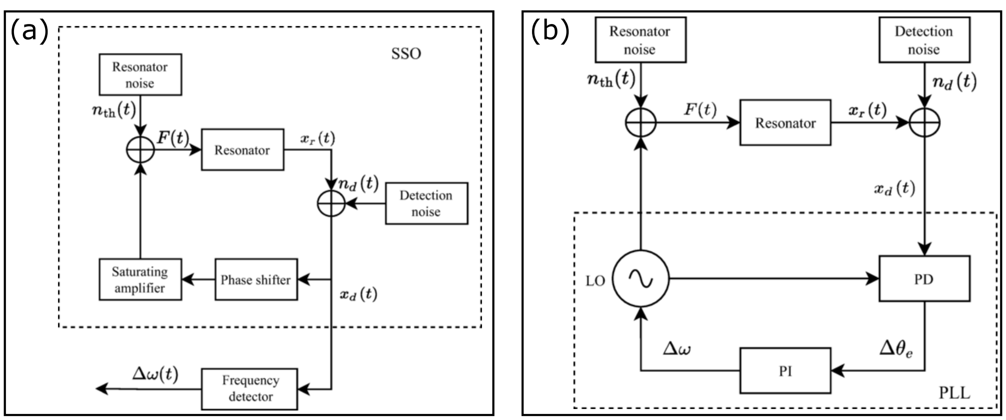

Figure 6.1: Adapted with permission from APS. Both (a) and (b) are taken from [5], where these frequency tracking schemes are described in depth. In (a), the SSO scheme is diagrammed. In this particular implementation, the frequency deviation is measured out-of-loop with a frequency counter. In principle, this could also be measured in post-processing as well. (b) Diagram of a PLL-based scheme. This particular diagram would use an in-loop measurement in order to determine the frequency deviation.

Two elements of interest in the SSO loop are the phase shifter and the saturating amplifier. We envision the phase shifter could be implemented with a variety of components, such as digital programmable phase shifting integrated circuits, analog adjustable phase shifters, or a delay line. All of these solutions should have enough frequency bandwidth in order to achieve the proper frequency shift over the frequency excursions experienced in a typical measurement. The saturating amplifier could be implemented with a variety of nonlinear circuits. Both the phase shifter and saturating amplifier could also be achieved with a properly programmed FFPA. The SSO method would also require an out-of-loop measurement of the oscillator frequency, which could be achieved with the shelf components such as a frequency counter (Fig. 6.1a), or with post-processing of the raw mechanical signal. We also point out that this scheme of measurement would require some form of bandpass filtering in order to address a single mechanical mode.

For a PLL-based scheme, the oscillator is driven with a local oscillator. The relative phase of the oscillator response and the drive is then used to adjust the local oscillator frequency in order to maintain a resonant drive. This is typically achieved via a PI filter which integrates the phase difference in order to infer the frequency difference. Readout of the frequency deviation can be achieved either through a readout of the in-loop control voltage fed to the local oscillator or through an out-of-loop measurement as used in the SSO scheme. We note that for high-Q mechanical oscillators, the PLL has a drawback where the bandwidth of the oscillator response limits how quickly the PLL can follow the mechanical frequency, while in the SSO scheme, the feedback force frequency changes immediately since it is derived from the oscillator motion directly. However, as indicated in more thorough examinations of frequency tracking schemes, the stability and added noise of all schemes discussed amounts to the same performance for integration times longer than the oscillator bandwidth [5].

6.4 Micromechanical bolometer design with stressed silicon nitride resonators

Here we will discuss the basic design goals of the construction of a micromechanical bolometer out of a tensioned silicon nitride resonator. As seen in the form of Eq. 6.13 and Eq. 6.14, the sensitivity of a micromechanical bolometer relies on a host of factors. Generally, sensing modes benefit from being low-dissipation (high Q), and low-thermal motion (high frequency and high mass). At the same time, we also desire that the relative change in frequency is maximized when subject to a flux of incident radiation. Finally, maximizing the mechanical drive A can also improve sensitivity. We will discuss all of these optimization problems, as well as the coupling between them in this section.

In regards to the pure mechanical properties of modes, we note that a general bolometer requires some mechanism in order to absorb the target radiation. In general, this can be achieved either by using an absorbing mechanical material or by functionalizing the resonator with an additional absorber, as explored in Ch. 5. We will explore the latter option, as it has the advantage of providing a more flexible sensor, allowing the device to be tailored to the choice application. As noted earlier in Ch. 3, functionalizing mechanical resonators change all properties of the mode, notably the dissipative properties. For the previously explored case of force sensors, this presented a large challenge, since the motion of the added mass was necessary in order to couple to the external field. We assert that for a micromechanical bolometer, or any sensor that relies on a parametric change to achieve transduction, this is not necessarily the case. This is because the frequency of a mechanical mode in a tensioned device is dependent on the static stress distribution. Most of the time, we discuss this as resulting from geometry. However, in the case of heat, thermal expansion can also result in a stress redistribution. Notably, a *local* stress perturbation can result in a *global* change in the stress of the structure, resulting in a frequency shift. This has large ramifications for device design, where now the functionalizing agent can be spatially separated from the mechanical mode.

With this added freedom in the placement of the absorber, we propose a conceptual device construction. Since the thermal expansion of the device should scale with how much temperature change is induced per unit of absorbed power, the absorber should be placed at the most thermally isolated location on the device. This means different things for different device archetypes. For a PnC device, this means that the absorber should be placed at the center of the device, while for a trampoline device, this means that the absorber should be placed on the optical detection pad. For both cases, a new type of mechanical mode is needed, where the mechanical motion is located at the region surrounding the absorber. Although not intentionally designed for this purpose, device E studied in Ch. 4 exhibits a promising mode that fits this archetype. This mode, pictured in Fig. 6.2a, consists largely of tether motion. Such a mode has been recently discovered in the field of micromechanical resonators and has been called a perimeter mode [1]. These modes boast many advantageous properties, notably their low dissipation through a new type of soft clamping. Rather than exponentially decaying into a support structure, the mode wraps itself along the edges of a polygon. Thus a sinusoidal, clamping-free mode profile is achieved.

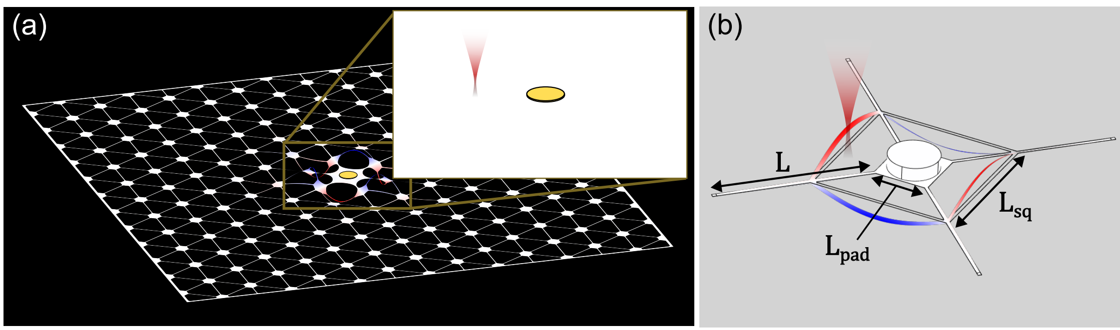

Figure 6.2: (a) Perimeter mode in a high-contrast PnC device. The absorber (in yellow) can be placed on a large pad. The narrow tethers near the large pad exhibit a sinusoidal profile along a hexagonal path encircling the pad. (b) A perimeter mode in a trampoline device. The large cylindrical object represents a generic absorbing element. Included are labels of commonly referenced dimensions of the device. The support length L indicates the distance from the corner of the pad to where the tether meets the substrate.

The instantiation of a perimeter mode found for device E, although not ideal, provides inspiration for a promising micromechanical bolometer archetype, where a large central pad supporting the absorbing element is surrounded by a polygon of narrow tethers. We can apply the same idea to a simpler device like a trampoline resonator. This concept is presented in Fig. 6.2b. Between these two designs, we see trade-offs. For perimeter modes housed in PnCs, we note that PnC structures have a minimum size requirement — or number of unit cells — in order for there to be a well-defined acoustic band gap. Therefore, PnC devices will have a larger footprint than trampoline devices, meaning that pixel sizes will be larger. One way to avoid this would be to design devices with many such defects in an array. Ideally, these defects would be localized to allow for spatial information about the impinging radiation to be preserved. This could be achieved by introducing slight geometric differences between each defect, which would detune them spectrally, preventing mode hybridization. Another issue with PnC perimeter mode devices is that the necessitated of a pad-tether geometry in the PnC is sub-optimal compared to the ideal perimeter mode, and therefore will not have the best dissipative properties. For these reasons, we will discuss perimeter modes on trampoline devices primarily in this chapter, although we do not necessarily rule out the use of multiplexed perimeter modes housed in PnCs for future-generation devices.

6.5 Micromechanical perimeter-mode bolometer design: thermal properties

In this section, we will present an exploration of optimizing the design of perimeter-mode-based micromechanical bolometers. The design will mainly center around the optimization of both mechanical and thermal properties, as well as understanding the trade-offs between the two. We will begin with a discussion of the thermal properties. Due to the rather simplistic geometry of this structure, we can derive a lumped-sum model for the thermal properties of the system. The model will consist of a central pad supporting a large absorbing region. This pad will then be connected to the environment with 4 narrow tethers. For the lumped sum model, we will disregard thermal transport effects arising from the perimeter mode tethers themselves, as these will only provide higher-order effects to the conductive cooling rates. In the lumped sum model, we will be interested in small temperature increases of the device, which will be valid in the small-signal limit, which is the regime of interest for precision sensing applications. Therefore, we can derive the following expressions for the radiative and conductive cooling rates:

$$P_{rad} = 4\epsilon\sigma A_{\text{pad}} T_{\text{env}}^3 \Delta T = G_{rad}\Delta T \tag{6.16}$$

$$P_c = \frac{4k_c w_t h}{L}\Delta T = G_c \Delta T \tag{6.17}$$

where $A_{\text{pad}} = L_{\text{pad}}^2$ is the pad area, w_t is the tether width, h is the membrane thickness, and

L is the support tether lengths. We note that the factor of 4 appearing in the expression for G_c is because there are 4 support tethers. One can therefore solve for the temperature difference ΔT as a function of the absorbed heating power:

$$\Delta T = (G_c + G_{rad})P_{\text{heat}}. \tag{6.18}$$

We claim that even without calculating the frequency shift directly, maximizing $\Delta T/P_{\text{heat}}$ is equivalent to maximizing R_f for a given geometry. To maximize ΔT, we see that this is achieved by smaller values of A_{pad} and larger values of L, assuming all other parameters are fixed. We focus on these two parameters as these will scale with the overall device size. Therefore, as the device size scales, there are two competing effects, one where the larger pad yields larger rates of radiative cooling, while longer support tethers make the effective conductive links weaker. We can study these two effects for increasing device size for a set geometric relation between A_{pad} and L of $A_{pad} = L^2/16$. The results can be seen in Fig. 6.3a. One sees that in the small-device limit, the cooling is dominated by conductive cooling and relatively low temperature increases are achieved. Increasing from here, the temperature reaches a maximum as the radiative cooling starts to increase as the pad size increases, peaking around 150 microns of tether support length. This happens to be around where the fraction of radiative cooling is close to 0.5. The details of the dependencies should change as the relative pad size in relation to the overall device size changes, but the concept stays the same.

In terms of device design, this dictates a strategy for creating more sensitive devices. Naively, one would think that simply scaling the device to larger sizes would yield higher sensitivity. However, for a set amount of incoming heating power, this is not the case, due to the added effects of radiative cooling. Here, we will claim that this scaling holds if one is interested in the quantity $\Delta T/P_{\text{heat}}$. In many cases, we are more interested in measuring the effects due to incoming flux Φ_{heat}. In this case, the absorbed power will scale as the pad size. In this regime, we recover a different functional form:

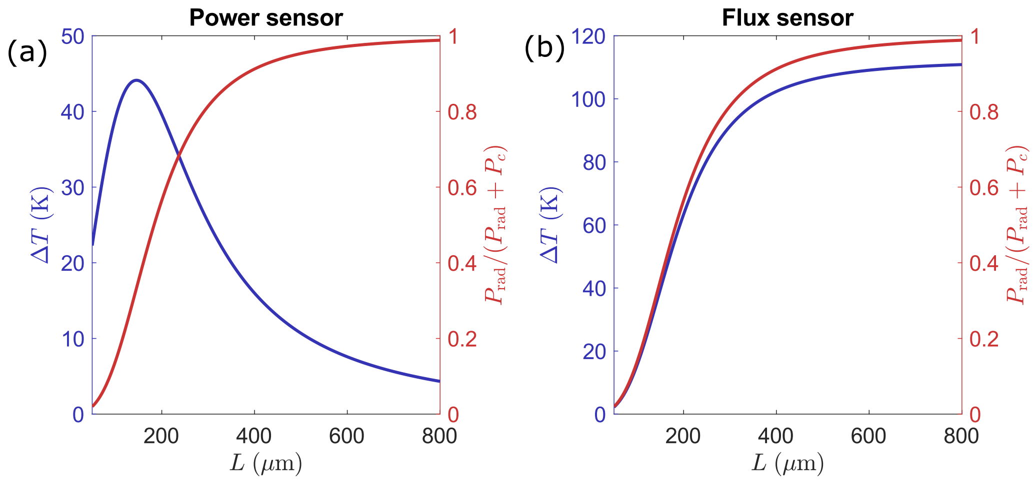

Figure 6.3: (a) Left axis: Temperature increase as a function of L for 1 μW of incident heating power in the lumped-sum model. Right axis: Fraction of cooling through the radiative cooling channel. We observe a peak of increased ΔT around where the cooling fraction is 0.5. (b) Same quantities, but here now the device measures the incoming flux, and thus the heating power scales as the size of the central pad. Here, larger devices will always yield more sensitivity, albeit with diminishing returns.

$$\Delta T = (4\epsilon\sigma A_{\mathrm{pad}} T_{\mathrm{env}}^3 + \frac{4k_c w_t h}{L})^{-1} A_{\mathrm{pad}} \Phi_{\mathrm{heat}}. \tag{6.19}$$

One can see the results of this behavior in Fig. 6.3b. Here, we see that there is no maximum value for ΔT, and rather the behavior asymptotes in the limit of larger devices. Therefore larger devices yield the highest sensitivities, albeit with diminishing returns. Thus a device wishing to probe an incoming flux will probably have a size that wishes to balance pixel size versus sensitivity. We note here that to this point, the flux sensor treatment of the lumped-sum model seems the most applicable to a general bolometer. However, there are other device applications where measuring with respect to a heating power is a more accurate figure of merit. Notably, absorption IR spectroscopy is one potential application for these devices [162]. Here, a sample is placed on the central pad, while a rather small laser beam locally heats the sample. In this case, the experimenter dictates the amount of incoming power, and in general, it will be quite localized, meaning that $\Delta T/P_{\mathrm{heat}}$ is the correct quantity to optimize. We can also investigate the effects of the temperature increase on other geometric parameters. Fig. 6.4 shows this dependence on the tether width. We see that in general, narrower tethers yield higher values of ΔT for both a flux sensor and a power sensor. This is because we are holding the pad size constant for these simulations. We note that here, there is a direct trade-off between sensitivity (higher ΔT) and bandwidth. We propose that tuning the tether widths allows for tuning between more sensitive and slower sensors, to fast sensors with less sensitivity.

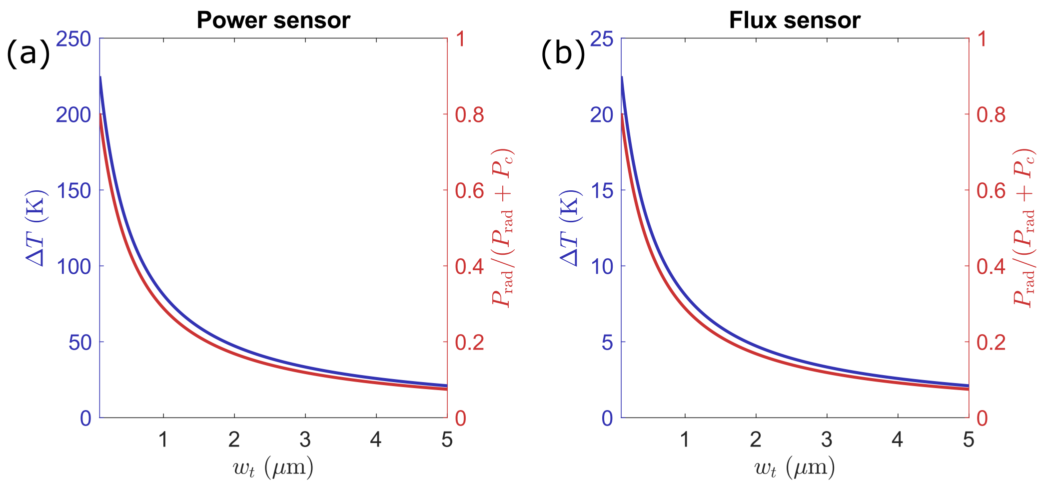

Figure 6.4: (a) Left axis: Temperature increase as a function of tether width for 1 μW of incident heating power in the lumped-sum model for a device with 100-micron support tethers, and 25-micron pad length. Right axis: Fraction of cooling through the radiative cooling channel. We see that in general the temperature increase is diminished with wider tethers. (b) The same overall trends hold for the flux sensor.

6.6 Micromechanical perimeter-mode bolometer design: mechanical properties

We can now discuss the mechanical properties of the device, where the goal is to maximize the Q of the resonator mode in order to reduce thermal coupling and achieve the readout needed to achieve the radiative noise limit discussed previously. As a baseline, the device can be understood as having two separate components, a polygonal (in this case we will only talk about a square) frame, as well as a central pad. Between these two elements are thin support tethers as well as support tethers to the surrounding substrate. The mechanics of the frame have been studied extensively in other work and depend mainly on the width of the frame and support tethers, as well as the frame and support length [1]. In that work, the case of equal stress was studied. That is, the tether widths of the supports and frame were adjusted so as to have constant stress throughout the device. This was performed in order to maximize the stress in the device, thus ensuring maximal dissipation dilution. For our work, the problem is more complicated, as not only do the mechanical properties matter but also the thermal properties. Since this study is in its early stages, we will begin by considering designs where all tethers have the same widths. We imagine that future designs could iterate on the devices presented in this work by modulating the relevant tether widths in order to maximize a trade-off of the mechanical and thermal properties of the device.

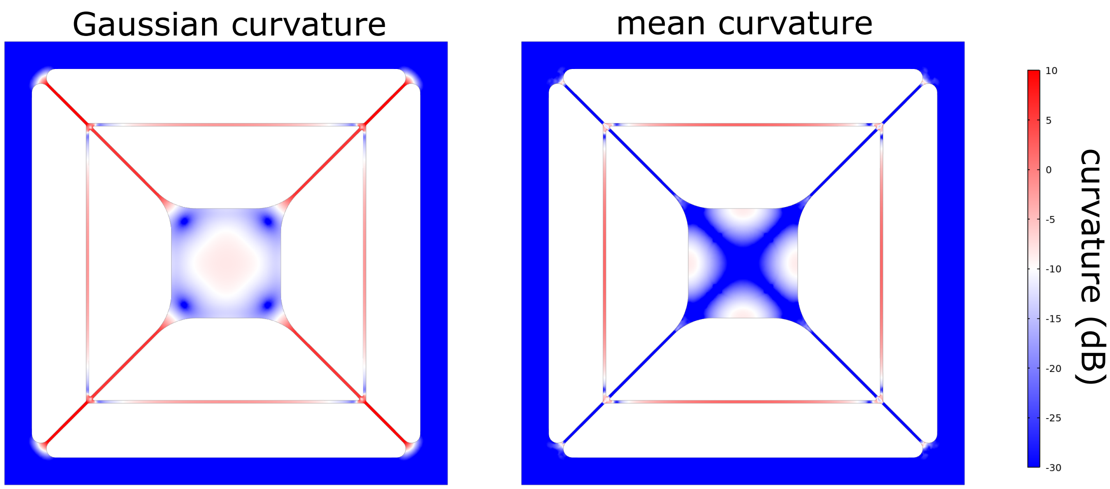

Figure 6.5: Comparison between the Gaussian (left) and mean (right) curvature profiles for a device with 500 nm tethers with a 100-micron perimeter mode frame length. We see that the Gaussian curvature is concentrated strongly in the support tethers since they must necessarily torque in order to comply with the perimeter mode profile.

In the previous study of perimeter modes [1], it was found that it was insufficient to model the loss of the mode by evaluating the mean curvature, as has been customary in this work and the field in general. Therefore, in this section, we will include the effects of the Gaussian curvature. It was found that this term can become large for these perimeter mode devices, where the torquing of the tether becomes large. A torquing tether will in general have nonzero values of the cross derivative $\frac{\partial^2 w}{\partial x \partial y}$ along its length and across its width. Therefore, an inspection of Eq. 1.44 indicates that the Gaussian curvature term need not be zero, and in fact, might be dominated by the Gaussian curvature. This behavior can be seen in Fig. 6.5. Here, we see that the Gaussian curvature is heavily concentrated in the device support tethers, as they must torque in order to allow for the perimeter mode motion. Notably, the magnitude of the curvature in the tethers is larger than what is observed in the perimeter mode itself, meaning that we expect that the perimeter mode Q will be limited by the torquing of the tethers. Another attribute of these devices highlighted in Fig. 6.5 is the curvature distribution on the pad. This curvature distribution, or the dissipation density, is at least 2 orders of magnitude attenuated from the loss experienced in the torquing of the support tethers. Therefore, we expect that these devices can be readily loaded with an arbitrary absorber or sample on this pad while maintaining the dissipative properties desired.

We can investigate this effect over a range of geometries. First, we will study the effect of tether width. In this study, we will study the same perimeter mode device with the same square frame size of 300 microns, but with a variable tether width. The results of this study can be seen in Fig. 6.6. Here, the overall trend is that thinner tethers yield higher values of Q since the torque of the perimeter mode tethers themselves is minimized for this geometry. However, we see that we eventually saturate to a constant value in the thin-tether limit. This is because there will be a constant torque in the support tethers, regardless of the support tether widths. We note that this study focused on keeping the support tether length constant such that the distance between the pad center and the edge of the device was equal to the perimeter mode frame length. In order to maximize Q, this length can be adjusted. It has been seen previously that a sweep of this tether length will increase the Q for low support tether lengths since this increases the length scale at which the support tethers torque [1]. However, if the natural frequencies of the torque modes of the support tethers become close to the perimeter mode frequency, the perimeter mode begins to hybridize with the tether widths of the other modes, leading to a reduction in Q. For our problem, we also have the connection tether between the absorbing pad and perimeter mode frame to take into account. In general, this adds to the dissipation due to the added torquing material and also introduces another hybridization mechanism.

Yet another hybridization mechanism can occur in the same way, except that a perimeter mode can hybridize with the torque modes of the perimeter mode tethers themselves, or the central pad. An example of the former can be seen in Fig. 6.7. We emphasize that the behavior observed in this particular device is not universal. That is, in general, it is not the 5th perimeter mode that hybridizes with the torque modes of the perimeter mode tethers. In general, this depends greatly on the particular geometry of the device. One general statement we can make is that the higher-order perimeter modes are more susceptible to these effects, especially hybridization with pad modes. This can be explained by the relatively large density of states at higher mechanical frequencies, which increases the probability that a spectator mechanical mode will be near the ideal perimeter mode frequency, making hybridization more likely to occur. In order to minimize and avoid these effects in general, extensive modeling of the system should be carried out in order to maximize the mechanical quality factor of the device. We also acknowledge that although the Q is maximized for thinner tethers, efficient optical readout at these tether widths presents a technical problem since it is near or beyond the diffraction limit for most optical systems. This can be addressed by introducing relatively small detection pads to the tethers themselves. It has been shown that this addition only reduces Q by around a factor of 2 [1]. Thus thin-tether devices can be used near their potential while still maintaining stable optical readout.

To continue the discussion of perimeter modes, we can begin to inspect the properties of higher-order perimeter modes. In general, so long as they do not hybridize with other polarizations of motion of the device, they will maintain the exemplary dissipation properties of the other modes in the device. This can be seen in the overall trend of the unhybridized perimeter modes in Fig. 6.7. The first 4 perimeter modes exhibit a $1/n$ dependence on the Q, where n is the perimeter mode number. This means that the first few perimeter modes will have decent sensing properties. For the purpose of a bolometer, this can be leveraged in order to minimize the fractional Allan deviation. An inspection of Eq. 6.13 shows that $\sigma^{(\mathrm{A})}_{\delta\Omega/\Omega}$ has a $\omega^{-3/2}Q^{-1/2}$ scaling, thus implying a n^{-1} scaling. Thus the frequency noise floor will be lower for higher order perimeter modes. Working with these higher-order modes introduces a drawback of potential nearby spectator modes, but we have observed that working with the 3rd order — and thus improving the frequency stability by a factor

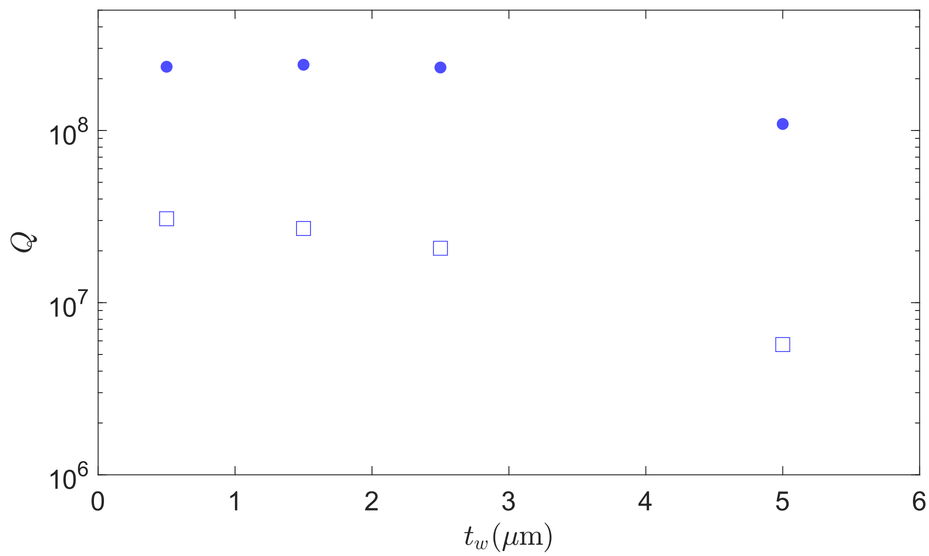

Figure 6.6: Comparison of Q calculated from only the mean curvature (circles) compared to Q calculated with the inclusion of Gaussian curvature as a function of tether width for the first perimeter mode of a 300-micron perimeter frame length device. We see a few trends. At low tether widths, the true Q is lower than the Q calculated from the mean curvature, with the Q increasing for thinner tethers. There is a large drop-off in Q for tether widths approaching 5 microns, even for the mean curvature Q.

of 3 — typically avoids the effects of hybridization. To understand how this increased frequency stability can be used for a bolometer, we need to also understand how R_f scales for a perimeter mode device. This can be easily modeled through an understanding of the ideal perimeter mode frequency:

$$\omega_{n,\mathrm{perim}} = \sqrt{\frac{\sigma_t}{\rho}}\frac{n}{L} \tag{6.20}$$

where σ_t is the stress inside the perimeter mode tethers. Therefore:

$$\frac{\delta\omega_{n,\mathrm{perim}}}{\omega_{n,\mathrm{perim}}} = -\frac{\delta\sigma_t}{2\sigma_t}. \tag{6.21}$$

We thus observe that regardless of the mechanism through which the stress changes, all perimeter modes will experience the same fractional frequency shift, and thus will all have the same value of R_f. Therefore, higher-order perimeter modes will in general be more sensitive.

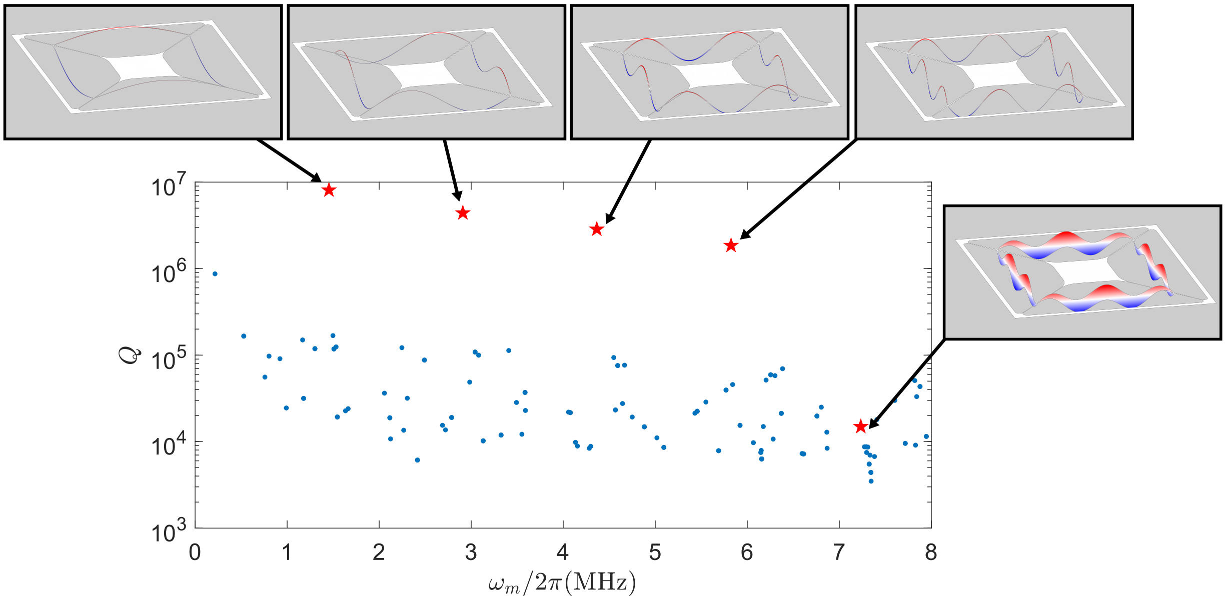

Figure 6.7: Calculated Q for a perimeter mode device with 500 nm tether widths, and a frame length of 150 microns. The first 5 perimeter modes are labeled with red stars on the plot. All other modes are labeled as blue circles. An FEA simulation of each perimeter mode is also displayed with an arrow pointing towards to corresponding Q on the spectrum plot. We see that the first 4 perimeter modes have vastly elevated Q than the rest of the device. The 5th perimeter mode has a greatly diminished Q. This can be understood from the mode geometry which has a large torque contribution in the perimeter mode tethers themselves.

To see the interplay of all of these effects, we will calculate the performance of a 100-micron frame-size bolometer as a function of tether width. The results are displayed in Fig. 6.8. We have already discussed Q in detail, so we will now discuss the calculated η as a function of tether width, and perimeter mode order (Fig. 6.8b). We have also computed an estimation of η_{th} from both the photon (phonon) pathways — shown as the dashed (dotted) line in Fig. 6.8b — for these devices, assuming that an absorber is deposited onto the central pad. We observe that the thin-tether devices have better Brownian motion-defined noise equivalent powers (η_{Brownian}). We also note that increasing the perimeter mode order also improves the η_{Brownian}, so long as the Q is maintained to be relatively high. This particular realization shows that the 3rd perimeter mode exhibits mode hybridization for some tether widths, limiting performance. We envision that a deployed device might specifically engineer this higher-order mode in order to optimize the operation of the device. With this in mind, we see that all modes of all geometries explored will be ultimately limited by the phonon noise. The increase in η_{Brownian} as a function of tether width can be explained by both a reduction in Q and R_f. We note that R_f is the same for each perimeter mode order, as expected from the analysis presented in Eq. 6.21. The decrease of R_f with increasing tether width can be explained by an increased conductive link to the environment as tether width increases. This observation also indicates that this particular geometry has a significant fraction of thermalization resulting from conductive cooling. We would expect that increasing the support tethers would yield devices that would become radiative cooling dominated, and thus we would have a saturation of R_f at higher values of t_w. This increased conductive link also plays a role in the thermalization rate, shown in Fig. 6.8d. Here, as the tether width increases, the thermalization rate (or the detection bandwidth) also increases. It is thus apparent that this family of devices allows for tuning of sensitivity versus bandwidth by increasing or decreasing the tether width, a strategy seen elsewhere in the field of micromechanical bolometers [149].

For this particular geometry, we can ask what are the absolute values of the thermal conductance G. The simulated values for G, as well as the contribution from the radiative (photon) and conductive (phonon) channels, are plotted in Fig. 6.9. We see that in this particular geometric configuration, these devices have a thermal conductance anywhere in the range of 10 nW/K to 100 nW/K depending on the tether width. Narrower tethers will cause the structure to be limited by the radiative conduction channel, setting the lower bound for G. These values are similar to what is observed in conventional electrical readout bolometers, for instance in this work by Varpula *et al* [161]. However, when comparing these particular structures, we observe that our noise-equivalent-power is lower by an order of magnitude or more in some cases while having longer response times by a factor of 10 or greater. This difference in response times can be attributed to the relative difference in heat capacities of the two devices. What is notable, is that even though the devices studied in this work are more sensitive, the limiting sensitivity will be η_{th}, owing to the low-noise mechanical frequency shift readout. This is in contrast to what is observed for electrical readout, where the Johnson noise is found to be the limiting noise contribution [161]. Therefore,

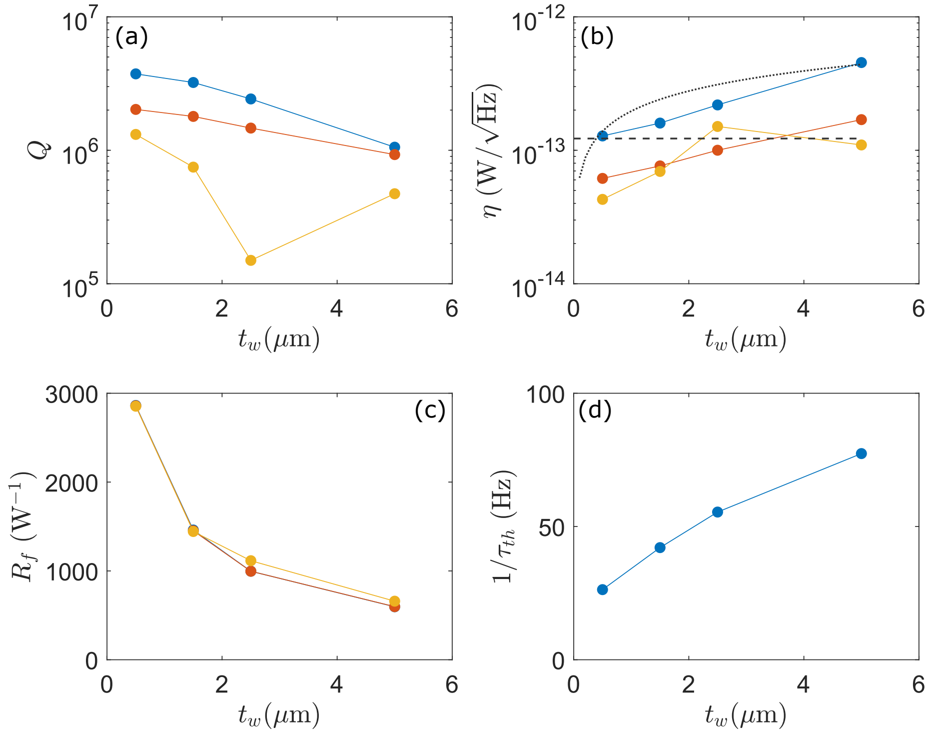

Figure 6.8: Summary of performance of a 100-micron perimeter mode-frame length perimeter mode bolometer. In all panels, the blue, red, and yellow points correspond to the 1st, 2nd, and 3rd perimeter modes respectively. (a) Q versus tether width. The drop in Q for the 3rd perimeter mode at a tether width fo 2.5 microns is caused by hybridization with a lower-Q mode. (b) Noise equivalent power from multiple sources. The dashed line indicates the contribution to η_{th} from thermal photons for this device assuming an ideal absorber. The dotted line corresponds to the contribution to η_{th} from phonons. The points correspond to the inferred η_{ro} (Brownian motion-defined readout noise) for each mode. We see that all geometries explored in this set of simulations will be limited by the phonon noise. (c) R_f as a function of tether width. We see that for wider tethers, the R_f decreases due to the increased conductive link with the environment. (d) Thermalization rate versus tether width. The thermalization rate should be the same for each order perimeter mode. We see that as the conductive link becomes stronger, the thermalization rate, and thus the bandwidth of the device, increases.

we see this particular study as an example of the benefits of micromechanical bolometers, and in particular, the use of low-dissipation perimeter modes in these devices. Conceptually, we can understand this advantage in readout as arising from the transduction being achieved through a single degree of freedom of the system. Notably, we can tune the dissipative properties of this mechanical degree of freedom through the methods discussed in this work. In contrast, resistive bolometers limited by Johnson noise are limited by all degrees of freedom of the electronic system and therefore do not benefit from the tunability afforded by mechanical resonators.

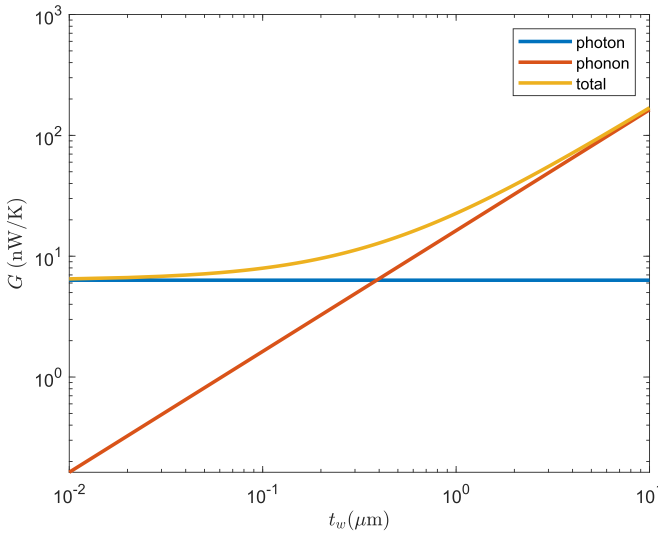

Figure 6.9: Contributions to the thermal conductance through both the phonon and photon channels. For a 100-micron frame length perimeter mode device. The nitride thickness was assumed to be 100 nm for all simulated values. We observe that in the narrow tether regime, the conductance is dominated by the photon contribution, while in the wider tether regime, the total conductance increases as the phonon contribution begins to dominate

Now that we have established potential performance metrics for these devices, we should discuss avenues for improvement. Given this work's focus on the mechanical properties of devices, we will devote most of our attention to improving the mechanical readout of these devices. One such avenue has already been pointed out by others in the field, reducing the stress of the device [165]. In this work, it is noted that the relative responsivity of their device is inversely proportional to the prestress of the membrane. This can be understood by inspecting Eq. 6.21, where it appears that the fractional frequency change is inversely proportional to the stress of the perimeter mode tether. The factor in the numerator, $\delta\sigma$, can be derived by understanding the operating principle of these devices. By heating the central pad, the entire structure should expand, or experience in change in the static strain. We note that this change in the static strain does not depend on the prestress, rather it generates a change in the stress depending on Young's modulus of the material:

$E\delta\epsilon \propto \delta\sigma$.

It should be noted that the dependence on the prestress of the device affects other parameters, notably the mechanical frequency and the quality factor. For our perimeter mode devices, we can derive the scalings of these two parameters for those of soft-clamped mechanical modes [51]. Notably, the quality factor should scale as σ, since prestressing the device gives rise to dissipation dilution. We can seek to derive a general scaling argument for a mechanical device with an arbitrary $Q(\sigma) \propto \sigma^b$, which would depend on the dominant loss mechanism of the mechanical mode in question, notably whether it is soft-clamped (σ^1) or clamping-loss limited ($\sigma^{1/2}$), or radiation-loss limited (σ^0). Taking into account all of these factors, we can derive the following scalings:

$$\begin{aligned} Q &\propto \sigma^b \\ \omega_m &\propto \sqrt{\sigma} \\ \sigma^{(\mathrm{A})}_{\delta\Omega/\Omega} &\propto \omega_0^{-3/2} Q^{-1/2} \propto \sigma^{-(3/4+b/2)} \\ R_f &\propto \sigma^{-1} \\ \eta &\propto \sigma^{-b/2+1/4} \end{aligned} \tag{6.22}$$

With the above scaling arguments, one can see that there is a weak, albeit appreciable advantage ($\sigma^{-1/4}$) to working with higher-stress devices when working with soft-clamped mechanical modes. This is in contrast to approaches suggested by other groups pursuing micromechanical bolometers, which typically utilize less-engineered mechanical membrane devices [162]. Such devices will have scaling with $b = 1/2$, meaning that the NEP will be independent of σ, meaning that to first order there is no advantage to working with low-stress devices. However, we do identify a few advantages associated with working with these lower-frequency, lower-stress devices. Notably, operating at a lower frequency presents an easier task when it comes to employing frequency tracking schemes, as the feedback needs to be performed on a slower timescale. In regards to utilizing high-stress membranes, we anticipate benefits beyond just a lower NEP. We also anticipate advantages when it comes to the dynamic range of the device. This will arise from a phenomenon associated with a large amount of incident power, leading to a large relaxation of the stress. In principle, there is a scale of absorbed power at which the modal properties of the device change appreciably, thus rendering the mode unusable as a transducer of absorbed power. Due to the higher values of R_f in low-stress devices, we anticipate that such devices will have a lower maximal absorbed power. Anecdotally, we have performed simulations in which 1 MPa perimeter mode devices experience a cross-over from tensile to compressive stresses for even 1 uW of absorbed power. Thus such devices might need to be handled with care, so as to not cause damage to the device prior to deployment, or even during operation. Meanwhile, high-stress devices can handle much higher levels of absorbed power and are more likely to be limited by thermally induced physical damage due to extreme temperatures.

Another potential avenue for improvement might be to consider changing the thickness of the membrane. The inspiration for this approach arises from the $Q \propto 1/h$ scaling for soft-clamped mechanical modes. However, it has been observed that linear operation of mechanical devices is typically achieved with oscillation amplitudes on the order of the membrane thickness, and therefore the allowed mechanical driving amplitude $A \propto h$, while the effective mass will also scale as h. This yields a scaling for the fractional Allan deviation as $\sigma^{(\mathrm{A})}_{\delta\Omega/\Omega} \propto 1/h$. At the same time, a device that thermalizes due to conduction will experience a thermal link, and thus an R_f, that scales as $1/h$ as well. Therefore, changing the thickness of the membrane will not change the noise-equivalent power of the device. However, we just remarked that increasing the thickness increases the thermal link, and thus the thermalization time. Therefore, despite not improving the sensitivity of the device, increasing the thickness should also increase the bandwidth. This approach can be safely pursued until the bulk losses of the silicon nitride begin to dominate, meaning that one could in principle work with a device with a thickness of 500 nm, resulting in bandwidths approaching 1 kHz [80].

6.7 Absorber characterization and selection

In this section, we will overview a brief study of the compatibility between a vertically aligned carbon nanotube (VACNT) absorber and a SiN PnC device. VACNT-based absorbers are of interest to the bolometer field, owing to their high absorption (near 100 percent) over a broad range of frequencies [166]. There have also been attempts at the creation of a metamaterial absorber, where a geometrically patterned VACNT forest would have frequency selective absorbption [166]. Similar approaches using patterned semi-conductor arrays have also been shown to exhibit narrowband absorption, which can reduce the background radiation levels [167].

The VACNT deposition was carried out Nathan Tomlin and Chris Yung from the Sources and Detectors group at NIST. To grow the VACNT forest on a device, first, a 10-20 nm aluminum oxide layer is deposited on the released silicon nitride membrane, followed by a 1-2 nm layer of iron. We anticipate that future devices will utilize a shadow mask during these deposition steps so as to selectively deposit the absorber onto the central pad of the device while leaving the surrounding structure pristine. The growth is achieved in an 800-degree C oven in order to grow a 50 μm tall VACNT forest. Given the adverse conditions of this process, it is prudent to test whether or not the released SiN PnC will survive such a process. Also, we could expect that the silicon nitride membrane could become more or less stressed, given differential coefficients of thermal expansion of the aluminum oxide layer and the silicon nitride membrane itself. This stress will contribute to the mechanical properties of the final device.

Fig. 6.10 shows a SiN PnC device with a deposited VACNT. We can see from these images that the device survived the deposition process. An inspection from the backside also determines that the tethers did not experience mechanical phenomena such as buckling, which might arise from excess compressive stresses on the device. We note that although Fig. 6.10 displays a single device, this deposition process was carried out for 4 different SiN PnC devices with similar results. We anticipate that less intricate devices will also survive the process.

In order to characterize the mechanical properties arising from the VACNT, we decided to measure a SiN PnC with a square PnC lattice. In order to carry out the measurement, we need to probe the membrane from the backside, where we will harness the prompt reflection from the vacuum-silicon nitride interface for our interferometric readout of the resonator motion.

Fig. 6.11 displays the thermomechanical noise spectrum of such a device. The first aspect of the spectrum is the observation of the (1,1) membrane mode. We find that this mode has a greatly

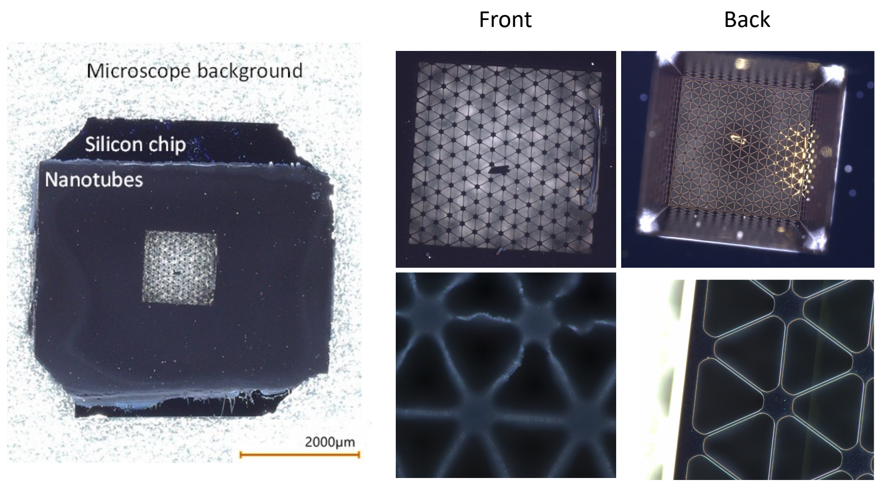

Figure 6.10: Microscope images of a VACNT forest deposited onto a SiN PnC device. Left column: complete chip. The VACNT forest covers most of the chip save for the top and bottom. The PnC device is located at the center of the image. Middle column: Front side of the chip. The bottom image is a zoom-in of the PnC. Here we see that the tops of the CNT appear wavy. Right column: Back side of the chip. The zoomed-in image on the bottom indicates that the silicon nitride tethers survived the CNT deposition.

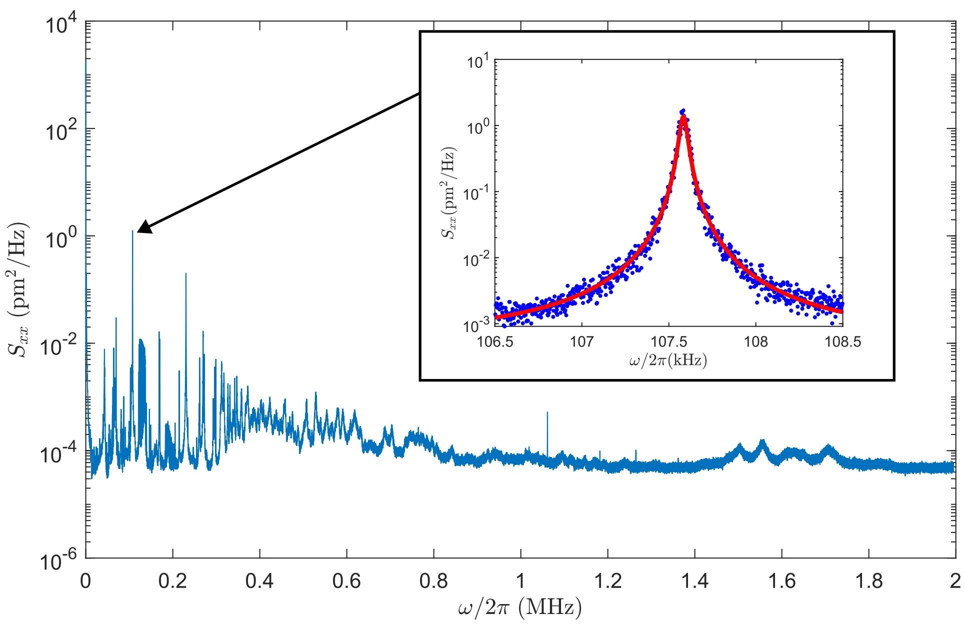

Figure 6.11: Thermal motion spectral density of a SiN PnC device with a deposited VACNT. The inset shows the Brownian motion (blue points) of the (1,1) mode of the device. A Lorentizan fit (red line) to this resonance reveals that the Q of this mode is 2200, meaning that the VACNT introduces appreciable mechanical loss.

reduced quality factor of 2200. For reference, we often observe that the (1,1) membrane mode of SiN PnC devices is typically around 100,000 due to radiative losses associated with the mounting of the device. This indicates — not surprisingly — that the VACNT introduces appreciable dissipation to the mode. We attribute this to the complex characteristics of the VACNT structure, where the interweaving of individual CNT may lead to the introduction of friction within the VACNT itself, creating dissipation. Also, since the VACNT is not tensioned, we will expect that the introduction of non-tensioned material to the system will reduce the effects of dissipation dilution. Other notable aspects of the observed (1,1) resonance are the resonant frequency and magnitude of the mechanical motion. The frequency is around 0.5 of the expected value, while the thermal motion is 8 times less than expected. The latter is readily explained by the introduction of mass to the resonator, thus increasing the effective mass of the (1,1) mode, and reducing its motion. This increase in mass and dissipation explains our second observation, being that we do not readily observe a bandgap for this device. We attribute this to the increased mass and dissipation of the higher-order modes, which will obviate our ability to readout the Brownian motion of these modes with the imprecision of the interferometer used. We also hypothesize that the combination of increased density of states and increased dissipation could have effects on the mode spectrum itself for the higher-order modes.

The decrease in resonant frequency is a more complicated story. Firstly, we expect that the silicon nitride film stress will change from the pre-deposition value. Also, there will be bi-layer film effects from the addition of the aluminum oxide. More complications arise when considering how to model the VACNT. We might think of modeling the addition of the nanotubes through the addition of a non-tensioned layer of another material. However, the mechanical properties of VACNT are not readily known. Furthermore, we would expect them to be anisotropic, given that the composition of a VACNT is linearly aligned CNT. Although the mechanical properties of individual carbon nanotubes have been studied, to our knowledge, mechanical studies of VACNT have not been pursued to this date [168]. Therefore, we encourage future studies of the mechanical properties of VACNT for the incorporation of VACNT into micromechanical bolometers. These studies should focus strongly on the dissipative properties of VACNT, as to discern whether or not the addition of the absorber to a perimeter mode bolometer will hamper the sensing performance of the device.

Despite performing this test, we also point out that there are other absorbers other than VACNT. VACNT is useful mainly for its near-perfect absorbance over a wide bandwidth. However, given the sensitivities of our devices, a slightly sub-optimal absorber with better and more tractable mechanical properties might be preferable. Notably, thin films of Pt and Au have been used in similar micromechanical bolometers, demonstrating the mechanical compatibility of these materials with silicon nitride membranes [99, 159].

Bibliography

[1] Mohammad J Bereyhi, Amirali Arabmoheghi, Alberto Beccari, Sergey A Fedorov, Guanhao Huang, Tobias J Kippenberg, and Nils J Engelsen. Perimeter modes of nanomechanical resonators exhibit quality factors exceeding 10^9 at room temperature. Physical Review X, 12(2):021036, 2022.

[2] RP Photonics. Rp photonics encyclopedia. http://www. rp-photonics. com/chirp. html, 2018.

[3] Daniel Rugar, Raffi Budakian, HJ Mamin, and BW Chui. Single spin detection by magnetic resonance force microscopy. Nature, 430(6997):329–332, 2004.

[4] Ran Fischer, Dylan P McNally, Chris Reetz, Gabriel GT Assumpcao, T Knief, Yiheng Lin, and Cindy A Regal. Spin detection with a micromechanical trampoline: towards magnetic resonance microscopy harnessing cavity optomechanics. New Journal of Physics, 21(4):043049, 2019.

[5] Hajrudin Bešić, Alper Demir, Johannes Steurer, Niklas Luhmann, and Silvan Schmid. Schemes for tracking resonance frequency for micro-and nanomechanical resonators. Physical Review Applied, 20(2):024023, 2023.

[6] CA Regal, JD Teufel, and KW Lehnert. Measuring nanomechanical motion with a microwave cavity interferometer. Nature Physics, 4(7):555–560, 2008.

[7] A. D. O'Connell, M. Hofheinz, M. Ansmann, Radoslaw C. Bialczak, M. Lenander, Erik Lucero, M. Neeley, D. Sank, H. Wang, M. Weides, J. Wenner, John M. Martinis, and A. N. Cleland. Quantum ground state and single-phonon control of a mechanical resonator. Nature, 464(7289):697–703, 2010.

[8] Yiwen Chu, Prashanta Kharel, Taekwan Yoon, Luigi Frunzio, Peter T Rakich, and Robert J Schoelkopf. Creation and control of multi-phonon fock states in a bulk acoustic-wave resonator. Nature, 563(7733):666–670, 2018.

[9] Yiwen Chu, Prashanta Kharel, William H Renninger, Luke D Burkhart, Luigi Frunzio, Peter T Rakich, and Robert J Schoelkopf. Quantum acoustics with superconducting qubits. Science, page eaao1511, 2017.

[10] Benjamin Lassagne, Yury Tarakanov, Jari Kinaret, Daniel Garcia-Sanchez, and Adrian Bachtold. Coupling mechanics to charge transport in carbon nanotube mechanical resonators. Science, 325(5944):1107–1110, 2009.

[11] Antoine Reigue, Francesco Fogliano, Philip Heringlake, Laure Mercier de Lépinay, Benjamin Besga, Jakob Reichel, Benjamin Pigeau, and Olivier Arcizet. Cavity nano-optomechanics with suspended subwavelength-sized nanowires. Physical Review Applied, 20(1):014025, 2023.

[12] DeLamar T Bell and Robert CM Li. Surface-acoustic-wave resonators. Proceedings of the IEEE, 64(5):711–721, 1976.

[13] Georg Anetsberger, Olivier Arcizet, Quirin P Unterreithmeier, Rémi Rivière, Albert Schliesser, Eva Maria Weig, Jörg Peter Kotthaus, and Tobias J Kippenberg. Near-field cavity optomechanics with nanomechanical oscillators. Nature Physics, 5(12):909–914, 2009.

[14] Nikolai Kiesel, Florian Blaser, Uroš Delić, David Grass, Rainer Kaltenbaek, and Markus Aspelmeyer. Cavity cooling of an optically levitated submicron particle. Proceedings of the National Academy of Sciences, 110(35):14180–14185, 2013.

[15] Uroš Delić, Manuel Reisenbauer, Kahan Dare, David Grass, Vladan Vuletić, Nikolai Kiesel, and Markus Aspelmeyer. Cooling of a levitated nanoparticle to the motional quantum ground state. Science, 367(6480):892–895, 2020.

[16] Uroš Delić, Manuel Reisenbauer, David Grass, Nikolai Kiesel, Vladan Vuletić, and Markus Aspelmeyer. Cavity cooling of a levitated nanosphere by coherent scattering. Physical review letters, 122(12):123602, 2019.

[17] P. Ovartchaiyapong, K. W. Lee, B. A. Myers, and A. C. Bleszynski Jayich. Dynamic strain-mediated coupling of a single diamond spin to a mechanical resonator. Nature Commun., 5:4429, 2014.

[18] Kenneth W Lee, Donghun Lee, Preeti Ovartchaiyapong, Joaquin Minguzzi, Jero R Maze, and Ania C Bleszynski Jayich. Strain coupling of a mechanical resonator to a single quantum emitter in diamond. Physical Review Applied, 6(3):034005, 2016.

[19] Katrin Gajo, Simon Schüz, and Eva M Weig. Strong 4-mode coupling of nanomechanical string resonators. Applied Physics Letters, 111(13), 2017.

[20] Tobias Westphal, Hans Hepach, Jeremias Pfaff, and Markus Aspelmeyer. Measurement of gravitational coupling between millimetre-sized masses. Nature, 591(7849):225–228, 2021.

[21] AB Shkarin, AD Kashkanova, CD Brown, S Garcia, K Ott, J Reichel, and JGE Harris. Quantum optomechanics in a liquid. Physical review letters, 122(15):153601, 2019.

[22] JGE Harris, AD Kashkanova, AB Shkarin, CD Brown, S Garcia, K Ott, and J Reichel. Quantum optomechanics experiments in superfluid helium. In Conference on Coherence and Quantum Optics, pages Tu2B–1. Optica Publishing Group, 2019.

[23] Kyu Hyun Kim, Gaurav Bahl, Wonsuk Lee, Jing Liu, Matthew Tomes, Xudong Fan, and Tal Carmon. Cavity optomechanics on a microfluidic resonator with water and viscous liquids. Light: Science & Applications, 2(11):e110–e110, 2013.

[24] Mario F Gely, Marios Kounalakis, Christian Dickel, Jacob Dalle, Rémy Vatré, Brian Baker, Mark D Jenkins, and Gary A Steele. Observation and stabilization of photonic fock states in a hot radio-frequency resonator. Science, 363(6431):1072–1075, 2019.

[25] Nancy Aggarwal, Torrey J Cullen, Jonathan Cripe, Garrett D Cole, Robert Lanza, Adam Libson, David Follman, Paula Heu, Thomas Corbitt, and Nergis Mavalvala. Room-temperature optomechanical squeezing. Nature Physics, 16(7):784–788, 2020.

[26] AG Kuhn, M Bahriz, O Ducloux, Claude Chartier, O Le Traon, T Briant, P-F Cohadon, A Heidmann, Christine Michel, L Pinard, et al. A micropillar for cavity optomechanics. Applied Physics Letters, 99(12), 2011.

[27] Nicolas Spethmann, Jonathan Kohler, Sydney Schreppler, Lukas Buchmann, and Dan M Stamper-Kurn. Cavity-mediated coupling of mechanical oscillators limited by quantum back-action. Nature Physics, 12(1):27–31, 2016.

[28] D Zoepfl, ML Juan, CMF Schneider, and G Kirchmair. Single-photon cooling in microwave magnetomechanics. Physical Review Letters, 125(2):023601, 2020.

[29] Jacob M Pate, Maxim Goryachev, Raymond Y Chiao, Jay E Sharping, and Michael Edmund Tobar. Casimir spring and dilution in macroscopic cavity optomechanics. Nature Physics, 16(11):1117–1122, 2020.

[30] Albert Schliesser and Tobias J Kippenberg. Cavity optomechanics with whispering-gallery mode optical micro-resonators. In Advances In Atomic, Molecular, and Optical Physics, volume 58, pages 207–323. Elsevier, 2010.

[31] T. A. Palomaki, J. D. Teufel, R. W. Simmonds, and K. W. Lehnert. Entangling Mechanical Motion with Microwave Fields. Science, 342(6159):710–713, 2013.

[32] BM Zwickl, WE Shanks, AM Jayich, C Yang, AC Bleszynski Jayich, JD Thompson, and JGE Harris. High quality mechanical and optical properties of commercial silicon nitride membranes. Applied Physics Letters, 92(10):103125, 2008.

[33] Mingyun Yuan, Martijn A Cohen, and Gary A Steele. Silicon nitride membrane resonators at millikelvin temperatures with quality factors exceeding 108. Applied Physics Letters, 107(26):263501, 2015.

[34] AM Jayich, JC Sankey, BM Zwickl, C Yang, JD Thompson, SM Girvin, AA Clerk, F Marquardt, and JGE Harris. Dispersive optomechanics: a membrane inside a cavity. New Journal of Physics, 10(9):095008, 2008.

[35] RW Peterson, TP Purdy, NS Kampel, RW Andrews, P-L Yu, KW Lehnert, and CA Regal. Laser cooling of a micromechanical membrane to the quantum backaction limit. Physical review letters, 116(6):063601, 2016.

[36] N. S. Kampel, R. W. Peterson, R. Fischer, P.-L. Yu, K. Cicak, R. W. Simmonds, K. W. Lehnert, and C. A. Regal. Improving Broadband Displacement Detection with Quantum Correlations. Phys. Rev. X, 7(2):021008, April 2017.

[37] Massimiliano Rossi, David Mason, Junxin Chen, Yeghishe Tsaturyan, and Albert Schliesser. Measurement-based quantum control of mechanical motion. Nature, 563(7729):53, 2018.

[38] Stefan Weis, Rémi Rivière, Samuel Deléglise, Emanuel Gavartin, Olivier Arcizet, Albert Schliesser, and Tobias J Kippenberg. Optomechanically induced transparency. Science, 330(6010):1520–1523, 2010.

[39] E. Verhagen, S. Deleglise, S. Weis, A. Schliesser, and T. J. Kippenberg. Quantum-coherent coupling of a mechanical oscillator to an optical cavity mode. Nature, 482(7383):63–67, 2012.

[40] A. Schliesser, Riviére R, G. Anetsberger, O. Arcizet, and T. J. Kippenberg. Resolved-sideband cooling of a micromechanical oscillator. Nature Physics, 4:415–419, April 2008.

[41] Reed W Andrews, Robert W Peterson, Tom P Purdy, Katarina Cicak, Raymond W Simmonds, Cindy A Regal, and Konrad W Lehnert. Bidirectional and efficient conversion between microwave and optical light. Nature Physics, 10(4):321–326, 2014.

[42] T. P. Purdy, R. W. Peterson, and C. A. Regal. Observation of Radiation Pressure Shot Noise on a Macroscopic Object. Science, 339(6121):801–804, 2013.

[43] Maryse Ernzer, Manel Bosch Aguilera, Matteo Brunelli, Gian-Luca Schmid, Thomas M Karg, Christoph Bruder, Patrick P Potts, and Philipp Treutlein. Optical coherent feedback control of a mechanical oscillator. Physical Review X, 13(2):021023, 2023.

[44] A P Higginbotham, P S Burns, M D Urmey, R W Peterson, N S Kampel, B M Brubaker, G Smith, K W Lehnert, and C A Regal. Harnessing electro-optic correlations in an efficient mechanical converter. Nature Physics, 14(10):1038, 2018.

[45] Christoffer B Møller, Rodrigo A Thomas, Georgios Vasilakis, Emil Zeuthen, Yeghishe Tsaturyan, Mikhail Balabas, Kasper Jensen, Albert Schliesser, Klemens Hammerer, and Eugene S Polzik. Quantum back-action-evading measurement of motion in a negative mass reference frame. Nature, 547(7662):191–195, 2017.

[46] R. Rivière, S. Deléglise, S. Weis, E. Gavartin, O. Arcizet, A. Schliesser, and T. J. Kippenberg. Optomechanical sideband cooling of a micromechanical oscillator close to the quantum ground state. Phys. Rev. A, 83(6):063835, June 2011.

[47] Gabriela I González and Peter R Saulson. Brownian motion of a mass suspended by an anelastic wire. The Journal of the Acoustical Society of America, 96(1):207–212, 1994.

[48] P-L Yu, TP Purdy, and CA Regal. Control of material damping in high-q membrane microresonators. Physical Review Letters, 108(8):083603, 2012.

[49] Yeghishe Tsaturyan, Andreas Barg, Eugene S Polzik, and Albert Schliesser. Ultracoherent nanomechanical resonators via soft clamping and dissipation dilution. Nature nanotechnology, 12(8):776–783, 2017.

[50] Amir Hossein Ghadimi, Dalziel Joseph Wilson, and Tobias J Kippenberg. Radiation and internal loss engineering of high-stress silicon nitride nanobeams. Nano Letters, 17(6):3501–3505, 2017.

[51] Amir H Ghadimi, Sergey A Fedorov, Nils J Engelsen, Mohammad J Bereyhi, Ryan Schilling, Dalziel J Wilson, and Tobias J Kippenberg. Elastic strain engineering for ultralow mechanical dissipation. Science, 360(6390):764–768, 2018.

[52] Mohammad J Bereyhi, Alberto Beccari, Sergey A Fedorov, Amir H Ghadimi, Ryan Schilling, Dalziel J Wilson, Nils J Engelsen, and Tobias J Kippenberg. Clamp-tapering increases the quality factor of stressed nanobeams. Nano Letters, 19(4):2329–2333, 2019.

[53] Mohammad J Bereyhi, Alberto Beccari, Robin Groth, Sergey A Fedorov, Amirali Arabmoheghi, Tobias J Kippenberg, and Nils J Engelsen. Hierarchical tensile structures with ultralow mechanical dissipation. Nature Communications, 13(1):1–9, 2022.

[54] Dennis Høj, Ulrich Busk Hoff, and Ulrik Lund Andersen. Ultra-coherent nanomechanical resonators based on density phononic crystal engineering. arXiv preprint arXiv:2207.06703, 2022.

[55] Dennis Høj, Fengwen Wang, Wenjun Gao, Ulrich Busk Hoff, Ole Sigmund, and Ulrik Lund Andersen. Ultra-coherent nanomechanical resonators based on inverse design. Nature communications, 12(1):5766, 2021.

[56] Christoph Reinhardt, Tina Müller, Alexandre Bourassa, and Jack C Sankey. Ultralow-noise sin trampoline resonators for sensing and optomechanics. Physical Review X, 6(2):021001, 2016.

[57] Jon R Pratt, Aman R Agrawal, Charles A Condos, Christian M Pluchar, Stephan Schlamminger, and Dalziel J Wilson. Nanoscale torsional dissipation dilution for quantum experiments and precision measurement. Physical Review X, 13(1):011018, 2023.

[58] Sushanth Kini Manjeshwar, Anastasiia Ciers, Fia Hellman, Jurgen Blasing, André Strittmatter, and Witlef Wieczorek. High-q trampoline resonators from strained crystalline ingap for integrated free-space optomechanics. Nano Letters, 2023.

[59] Garrett D Cole, Pen-Li Yu, Claus Gärtner, Karoline Siquans, Ramon Moghadas Nia, Jonas Schmöle, Jason Hoelscher-Obermaier, Thomas P Purdy, Witlef Wieczorek, Cindy A Regal, et al. Tensile-strained inxga1- xp membranes for cavity optomechanics. Applied Physics Letters, 104(20):201908, 2014.

[60] Junuthula Narasimha Reddy. Theory and analysis of elastic plates and shells. CRC press, 2006.

[61] AW Leissa. Nasa sp-160. Vibration of plates, pages 59–60, 1969.

[62] Pen-Li Yu. Quantum Optomechanics with Engineered Membrane Resonators. PhD thesis, University of Colorado, 2016.

[63] Silvan Schmid, Luis Guillermo Villanueva, and Michael Lee Roukes. Fundamentals of nanomechanical resonators, volume 49. Springer, Berlin, 2016.

[64] SA Fedorov, Vivishek Sudhir, R Schilling, Hendrik Schütz, Dalziel Joseph Wilson, and TJ Kippenberg. Evidence for structural damping in a high-stress silicon nitride nanobeam and its implications for quantum optomechanics. Physics Letters A, 382(33):2251–2255, 2018.

[65] Gabriela I González and Peter R Saulson. Brownian motion of a torsion pendulum with internal friction. Physics Letters A, 201(1):12–18, 1995.

[66] Herbert B Callen and Theodore A Welton. Irreversibility and generalized noise. Physical Review, 83(1):34, 1951.

[67] Markus Aspelmeyer, Tobias J Kippenberg, and Florian Marquardt. Cavity optomechanics. Reviews of Modern Physics, 86(4):1391, 2014.

[68] Aashish A Clerk, Michel H Devoret, Steven M Girvin, Florian Marquardt, and Robert J Schoelkopf. Introduction to quantum noise, measurement, and amplification. Reviews of Modern Physics, 82(2):1155, 2010.

[69] Chris Reetz, Ran Fischer, Gabriel GT Assumpcao, Dylan P McNally, Peter S Burns, Jack C Sankey, and Cindy A Regal. Analysis of membrane phononic crystals with wide band gaps and low-mass defects. Physical Review Applied, 12(4):044027, 2019.

[70] Andreas Wallucks, Igor Marinković, Bas Hensen, Robert Stockill, and Simon Gröblacher. A quantum memory at telecom wavelengths. Nature Physics, 16(7):772–777, 2020.

[71] Emanuel Gavartin, Pierre Verlot, and Tobias J Kippenberg. Stabilization of a linear nanomechanical oscillator to its thermodynamic limit. Nature communications, 4(1):2860, 2013.

[72] Dalziel J Wilson, Vivishek Sudhir, Nicolas Piro, Ryan Schilling, Amir Ghadimi, and Tobias J Kippenberg. Measurement-based control of a mechanical oscillator at its thermal decoherence rate. Nature, 524(7565):325–329, 2015.

[73] Sergey A Fedorov, Nils J Engelsen, Amir H Ghadimi, Mohammad J Bereyhi, Ryan Schilling, Dalziel J Wilson, and Tobias J Kippenberg. Generalized dissipation dilution in strained mechanical resonators. Physical Review B, 99(5):054107, 2019.

[74] Nils J Engelsen, Aman R Agrawal, and Dalziel J Wilson. Ultra-high-q nanomechanics through dissipation dilution: Trends and perspectives. In 2021 21st International Conference on Solid-State Sensors, Actuators and Microsystems (Transducers), pages 201–205. IEEE, 2021.

[75] Clarence M Zener and Sidney Siegel. Elasticity and anelasticity of metals. The Journal of Physical Chemistry, 53(9):1468–1468, 1949.

[76] Quirin P Unterreithmeier, Thomas Faust, and Jörg P Kotthaus. Damping of nanomechanical resonators. Phys. Rev. Lett., 105(2):027205, 2010.

[77] Letizia Catalini, Yeghishe Tsaturyan, and Albert Schliesser. Soft-clamped phononic dimers for mechanical sensing and transduction. Physical Review Applied, 14(1):014041, 2020.

[78] Yeghishe Tsaturyan. Ultracoherent soft-clamped mechanical resonators for quantum cavity optomechanics. PhD thesis, University of Copenhagen, Faculty of Science, Niels Bohr Institute, Danish . . . , 2019.

[79] Ron Lifshitz and Michael L Roukes. Thermoelastic damping in micro-and nanomechanical systems. Physical review B, 61(8):5600, 2000.

[80] Luis Guillermo Villanueva and Silvan Schmid. Evidence of surface loss as ubiquitous limiting damping mechanism in sin micro-and nanomechanical resonators. Physical Review Letters, 113(22):227201, 2014.

[81] Niklas Luhmann, Artur Jachimowicz, Johannes Schalko, Pedram Sadeghi, Markus Sauer, Annette Foelske-Schmitz, and Silvan Schmid. Effect of oxygen plasma on nanomechanical silicon nitride resonators. Applied Physics Letters, 111(6), 2017.

[82] Minhang Bao, Heng Yang, Hao Yin, and Yuancheng Sun. Energy transfer model for squeeze-film air damping in low vacuum. Journal of Micromechanics and Microengineering, 12(3):341, 2002.

[83] I Wilson-Rae, RA Barton, SS Verbridge, DR Southworth, B Ilic, Harold G Craighead, and JM Parpia. High-q nanomechanics via destructive interference of elastic waves. Physical review letters, 106(4):047205, 2011.

[84] Matthew J Weaver, Brian Pepper, Fernando Luna, Frank M Buters, Hedwig J Eerkens, Gesa Welker, Blaise Perock, Kier Heeck, Sven de Man, and Dirk Bouwmeester. Nested trampoline resonators for optomechanics. Applied Physics Letters, 108(3):033501, 2016.

[85] Y. Tsaturyan, A. Barg, A. Simonsen, L. G. Villanueva, S. Schmid, A. Schliesser, and E. S. Polzik. Demonstration of suppressed phonon tunneling losses in phononic bandgap shielded membrane resonators for high-Q optomechanics. Opt. Express, 22(6):6810–6821, March 2014.

[86] P-L Yu, K Cicak, NS Kampel, Y Tsaturyan, TP Purdy, RW Simmonds, and CA Regal. A phononic bandgap shield for high-q membrane microresonators. Applied Physics Letters, 104(2):023510, 2014.

[87] Albert A Michelson. Art. xxi.–the relative motion of the earth and the luminiferous ether. American Journal of Science (1880-1910), 22(128):120, 1881.

[88] Benjamin P Abbott, Richard Abbott, TDe Abbott, MR Abernathy, Fausto Acernese, Kendall Ackley, Carl Adams, Thomas Adams, Paolo Addesso, RX Adhikari, et al. Observation of gravitational waves from a binary black hole merger. Physical review letters, 116(6):061102, 2016.

[89] Carlton M. Caves. Quantum-Mechanical Radiation-Pressure Fluctuations in an Interferometer. Phys. Rev. Lett., 45(2):75–79, July 1980.

[90] MJ Collett, R Loudon, and CW Gardiner. Quantum theory of optical homodyne and heterodyne detection. Journal of Modern Optics, 34(6-7):881–902, 1987.

[91] Arthur L Schawlow and Charles H Townes. Infrared and optical masers. Physical review, 112(6):1940, 1958.

[92] Melvin Lax. Classical noise. v. noise in self-sustained oscillators. Physical Review, 160(2):290, 1967.

[93] Michał Parniak, Ivan Galinskiy, Timo Zwettler, and Eugene S Polzik. High-frequency broadband laser phase noise cancellation using a delay line. Optics Express, 29(5):6935–6946, 2021.

[94] R. W. P. Drever, J. L. Hall, F. V. Kowalski, J. Hough, G. M. Ford, A. J. Munley, and H. Ward. Laser phase and frequency stabilization using an optical resonator. Applied Physics B, 31(2):97–105, 1983.

[95] Eric D. Black. An introduction to Pound-Drever-Hall laser frequency stabilization. American Journal of Physics, 69(1):79–87, 2001.

[96] Walt Kester. Understand sinad, enob, snr, thd, thd+ n, and sfdr so you don't get lost in the noise floor. MT-003 Tutorial, www. analog. com/static/importedfiles/tutorials/MT-003. pdf, 2009.

[97] Christian M Pluchar, Aman R Agrawal, Edward Schenk, and Dalziel J Wilson. Towards cavity-free ground-state cooling of an acoustic-frequency silicon nitride membrane. Applied Optics, 59(22):G107–G111, 2020.

[98] D Rugar, O Züger, S Hoen, CS Yannoni, H-M Vieth, and RD Kendrick. Force detection of nuclear magnetic resonance. Science, 264(5165):1560–1563, 1994.

[99] Leonardo Vicarelli, Alessandro Tredicucci, and Alessandro Pitanti. Micromechanical bolometers for subterahertz detection at room temperature. ACS photonics, 9(2):360–367, 2022.

[100] Georg Enzian, Zihua Wang, Anders Simonsen, Jonas Mathiassen, Toke Vibel, Yeghishe Tsaturyan, Alexander Tagantsev, Albert Schliesser, and Eugene S Polzik. Phononically shielded photonic-crystal mirror membranes for cavity quantum optomechanics. Optics Express, 31(8):13040–13052, 2023.

[101] Ravid Shaniv, S Kumar Keshava, Chris Reetz, and Cindy A Regal. Understanding the quality factor of mass-loaded tensioned resonators. Physical Review Applied, 19(3):L031006, 2023.

[102] JA Sidles. Folded stern-gerlach experiment as a means for detecting nuclear magnetic resonance in individual nuclei. Physical Review Letters, 68(8):1124, 1992.

[103] JOHN A Sidles, JOSEPH L Garbini, KJ Bruland, D Rugar, O Züger, S Hoen, and CS Yannoni. Magnetic resonance force microscopy. Rev. Mod. Phys., 67(1):249, 1995.

[104] Thomas R Albrecht, Peter Grütter, David Horne, and Daniel Rugar. Frequency modulation detection using high-q cantilevers for enhanced force microscope sensitivity. Journal of applied physics, 69(2):668–673, 1991.

[105] CL Degen, M Poggio, HJ Mamin, CT Rettner, and D Rugar. Nanoscale magnetic resonance imaging. Proceedings of the National Academy of Sciences, 106(5):1313–1317, 2009.

[106] HJ Mamin and D Rugar. Sub-attonewton force detection at millikelvin temperatures. Applied Physics Letters, 79(20):3358–3360, 2001.

[107] TD Stowe, K Yasumura, TW Kenny, D Botkin, K Wago, and D Rugar. Attonewton force detection using ultrathin silicon cantilevers. Applied Physics Letters, 71(2):288–290, 1997.

[108] D. Rugar, C. S. Yannoni, and J. A. Sidles. Mechanical detection of magnetic resonance. Nature, 360:563, 1992.

[109] A. O. Sushkov, I. Lovchinsky, N. Chisholm, R. L. Walsworth, H. Park, and M. D. Lukin. Magnetic resonance detection of individual proton spins using quantum reporters. Phys. Rev. Lett., 113:197601, Nov 2014.

[110] Ashok Ajoy, Ulf Bissbort, Mikhail D Lukin, Ronald Lee Walsworth, and Paola Cappellaro. Atomic-scale nuclear spin imaging using quantum-assisted sensors in diamond. Physical Review X, 5(1):011001, 2015.

[111] Igor Lovchinsky, AO Sushkov, E Urbach, NP de Leon, Soonwon Choi, Kristiaan De Greve, R Evans, R Gertner, E Bersin, C Müller, et al. Nuclear magnetic resonance detection and spectroscopy of single proteins using quantum logic. Science, 351(6275):836–841, 2016.

[112] HJ Mamin, M Poggio, CL Degen, and D Rugar. Nuclear magnetic resonance imaging with 90-nm resolution. Nature Nanotechnology, 2(5):301–306, 2007.

[113] Urs Grob, Marc-Dominik Krass, M Héritier, Raphael Pachlatko, Jan Rhensius, Jan Kosata, BA Moores, H Takahashi, Alexander Eichler, and Christian L Degen. Magnetic resonance force microscopy with a one-dimensional resolution of 0.9 nanometers. Nano letters, 19(11):7935–7940, 2019.

[114] Francesco Casola, Toeno Van Der Sar, and Amir Yacoby. Probing condensed matter physics with magnetometry based on nitrogen-vacancy centres in diamond. Nature Reviews Materials, 3(1):1–13, 2018.

[115] Thomas Gisler, Mohamed Helal, Deividas Sabonis, Urs Grob, Martin Héritier, Christian L Degen, Amir H Ghadimi, and Alexander Eichler. Soft-clamped silicon nitride string resonators at millikelvin temperatures. Physical Review Letters, 129(10):104301, 2022.

[116] Alexander Eichler. Ultra-high-q nanomechanical resonators for force sensing. Materials for Quantum Technology, 2(4):043001, 2022.

[117] David Hälg, Thomas Gisler, Yeghishe Tsaturyan, Letizia Catalini, Urs Grob, Marc-Dominik Krass, Martin Héritier, Hinrich Mattiat, Ann-Katrin Thamm, Romana Schirhagl, et al. Membrane-based scanning force microscopy. Physical Review Applied, 15(2):L021001, 2021.

[118] A Vinante, GHCJ Wijts, O Usenko, L Schinkelshoek, and TH Oosterkamp. Magnetic resonance force microscopy of paramagnetic electron spins at millikelvin temperatures. Nature communications, 2(1):572, 2011.

[119] Eric W Moore, SangGap Lee, Steven A Hickman, Lee E Harrell, and John A Marohn. Evading surface and detector frequency noise in harmonic oscillator measurements of force gradients. Applied physics letters, 97(4), 2010.

[120] Martino Poggio and Benedikt E Herzog. Force-detected nuclear magnetic resonance. Micro and Nano Scale NMR: Technologies and Systems, page 381, 2018.

[121] Nicolas Scozzaro, William Ruchotzke, Amanda Belding, Jeremy Cardellino, Erick C Blomberg, Brendan A McCullian, Vidya P Bhallamudi, Denis V Pelekhov, and P Chris Hammel. Magnetic resonance force detection using a membrane resonator. Journal of Magnetic Resonance, 271:15–20, 2016.

[122] H Jonathon Mamin, Raffi Budakian, Ben W Chui, and Daniel Rugar. Detection and manipulation of statistical polarization in small spin ensembles. Physical Review Letters, 91(20):207604, 2003.

[123] John M Nichol, Tyler R Naibert, Eric R Hemesath, Lincoln J Lauhon, and Raffi Budakian. Nanoscale fourier-transform magnetic resonance imaging. Physical Review X, 3(3):031016, 2013.

[124] William Rose, Holger Haas, Angela Q Chen, Nari Jeon, Lincoln J Lauhon, David G Cory, and Raffi Budakian. High-resolution nanoscale solid-state nuclear magnetic resonance spectroscopy. Physical Review X, 8(1):011030, 2018.

[125] John M Nichol, Eric R Hemesath, Lincoln J Lauhon, and Raffi Budakian. Nanomechanical detection of nuclear magnetic resonance using a silicon nanowire oscillator. Phys. Rev. B, 85(5):054414, 2012.

[126] Holger Haas, Sahand Tabatabaei, William Rose, Pardis Sahafi, Michèle Piscitelli, Andrew Jordan, Pritam Priyadarsi, Namanish Singh, Ben Yager, Philip J Poole, et al. Nuclear magnetic resonance diffraction with subangstrom precision. Proceedings of the National Academy of Sciences, 119(40):e2209213119, 2022.

[127] Jan Košata, Oded Zilberberg, Christian L Degen, Ramasubramanian Chitra, and Alexander Eichler. Spin detection via parametric frequency conversion in a membrane resonator. Physical Review Applied, 14(1):014042, 2020.

[128] K. Wago, O. Züger, J. Wegener, R. Kendrick, C. S. Yannoni, and D. Rugar. Magnetic resonance force detection and spectroscopy of electron spins in phosphorus-doped silicon. Review of Scientific Instruments, 68(4):1823–1826, 1997.

[129] D Rugar and P Grutter. Mechanical parametric amplification and thermomechanical noise squeezing. Phys. Rev. Lett., 67:699, August 1991.

[130] Sanjay Kumar Keshava. Mass Loaded Tensioned Mechanical Resonators. PhD thesis, 2023.

[131] Aman R Agrawal, Charles Condos, Christian Pluchar, Jon Pratt, Stephan Schlamminger, and Dalziel Wilson. Ultra-high-q torsional nanomechanics for quantum experiments and precision measurement. In CLEO: QELS_Fundamental Science, pages FW4D–3. Optica Publishing Group, 2022.

[132] Yulong Liu, Jay Mummery, Jingwei Zhou, and Mika A Sillanpää. Gravitational forces between nonclassical mechanical oscillators. Physical Review Applied, 15(3):034004, 2021.

[133] JD Teufel, Tobias Donner, Dale Li, JW Harlow, MS Allman, Katarina Cicak, AJ Sirois, Jed D Whittaker, KW Lehnert, and Raymond W Simmonds. Sideband cooling of micromechanical motion to the quantum ground state. Nature, 475(7356):359–363, 2011.

[134] Jingkun Guo, Richard Norte, and Simon Gröblacher. Feedback cooling of a room temperature mechanical oscillator close to its motional ground state. Physical Review Letters, 123(22):223602, 2019.

[135] Dustin Kleckner and Dirk Bouwmeester. Sub-kelvin optical cooling of a micromechanical resonator. Nature, 444(7115):75–78, 2006.

[136] Matt Eichenfield, Jasper Chan, Ryan M Camacho, Kerry J Vahala, and Oskar Painter. Optomechanical crystals. Nature, 462(7269):78–82, 2009.

[137] Suxia Yang, John H Page, Zhengyou Liu, Michael L Cowan, Che Ting Chan, and Ping Sheng. Focusing of sound in a 3d phononic crystal. Physical review letters, 93(2):024301, 2004.

[138] Yan Pennec and Bahram Djafari-Rouhani. Fundamental properties of phononic crystal. Phononic crystals: Fundamentals and applications, pages 23–50, 2016.

[139] Rosa Martínez-Sala, J Sancho, Juan V Sánchez, Vicente Gómez, Jaime Llinares, and Francisco Meseguer. Sound attenuation by sculpture. Nature, 378(6554):241–241, 1995.

[140] Gregory S MacCabe, Hengjiang Ren, Jie Luo, Justin D Cohen, Hengyun Zhou, Alp Sipahigil, Mohammad Mirhosseini, and Oskar Painter. Nano-acoustic resonator with ultralong phonon lifetime. Science, 370(6518):840–843, 2020.

[141] Jordi Gomis-Bresco, Daniel Navarro-Urrios, Mourad Oudich, Said El-Jallal, Amadeu Griol, Daniel Puerto, Emiglio Chavez, Yan Pennec, Bahram Djafari-Rouhani, Franscesca Alzina, et al. A one-dimensional optomechanical crystal with a complete phononic band gap. Nature communications, 5(1):4452, 2014.

[142] J. Chan, A. H. Safavi-Naeini, J. T. Hill, S. Meenehan, and O. Painter). Optimized optomechanical crystal cavity with acoustic radiation shield. Appl. Phys. Lett., 101:081115, 2012.

[143] Kentaro Komori, Yutaro Enomoto, Hiroki Takeda, Yuta Michimura, Kentaro Somiya, Masaki Ando, and Stefan W Ballmer. Direct approach for the fluctuation-dissipation theorem under nonequilibrium steady-state conditions. Physical Review D, 97(10):102001, 2018.

[144] Melvin Lax. Fluctuations from the nonequilibrium steady state. Reviews of modern physics, 32(1):25, 1960.

[145] MM Leivo and JP Pekola. Thermal characteristics of silicon nitride membranes at sub-kelvin temperatures. Applied Physics Letters, 72(11):1305–1307, 1998.

[146] Chang Zhang, Mathieu Giroux, Thea Abdul Nour, and Raphael St-Gelais. Radiative heat transfer in freestanding silicon nitride membranes. Physical Review Applied, 14(2):024072, 2020.

[147] Markus Piller, Pedram Sadeghi, Robert G West, Niklas Luhmann, Paolo Martini, Ole Hansen, and Silvan Schmid. Thermal radiation dominated heat transfer in nanomechanical silicon nitride drum resonators. Applied Physics Letters, 117(3):034101, 2020.

[148] Ravid Shaniv, Chris Reetz, and Cindy A. Regal. Direct measurement of a spatially varying thermal bath using brownian motion. Physical Review Research, 5(4), 2023.

[149] Andrew Blaikie, David Miller, and Benjamín J Alemán. A fast and sensitive room-temperature graphene nanomechanical bolometer. Nature Communications, 10(1):4726, 2019.

[150] Rubina Sultan, AD Avery, JM Underwood, SJ Mason, D Bassett, and BL Zink. Heat transport by long mean free path vibrations in amorphous silicon nitride near room temperature. Physical Review B, 87(21):214305, 2013.

[151] XC Zhang, EB Myers, JE Sader, and ML Roukes. Nanomechanical torsional resonators for frequency-shift infrared thermal sensing. Nano letters, 13(4):1528–1534, 2013.

[152] Dongcheol Seo, BJ Peterson, and Seung Hun Lee. First results of the resistive bolometers on kstar. Review of Scientific Instruments, 81(10), 2010.

[153] Samuel Pierpont Langley. The bolometer and radiant energy. In Proceedings of the American Academy of Arts and Sciences, volume 16, pages 342–358. JSTOR, 1880.

[154] K F Mast, JC Vallet, C Andelfinger, P Betzler, H Kraus, and G Schramm. A low noise highly integrated bolometer array for absolute measurement of vuv and soft x radiation. Review of Scientific Instruments, 62(3):744–750, 1991.

[155] YM Duan, LQ Hu, ST Mao, KY Chen, SY Lin, and EAST Diagnostics Team. The resistive bolometer for radiated power measurement on east. Review of Scientific Instruments, 83(9), 2012.

[156] Roope Kokkoniemi, Joonas Govenius, Visa Vesterinen, Russell E Lake, András M Gunyhó, Kuan Y Tan, Slawomir Simbierowicz, Leif Grönberg, Janne Lehtinen, Mika Prunnila, et al. Nanobolometer with ultralow noise equivalent power. Communications Physics, 2(1):124, 2019.

[157] Francesco Marsili, Varun B Verma, Jeffrey A Stern, Susanmarie Harrington, Adriana E Lita, Thomas Gerrits, Igor Vayshenker, Burm Baek, Matthew D Shaw, Richard P Mirin, et al. Detecting single infrared photons with 93% system efficiency. Nature Photonics, 7(3):210–214, 2013.

[158] PV Karthik Yadav, Isha Yadav, B Ajitha, Abraham Rajasekar, Sudha Gupta, and Y Ashok Kumar Reddy. Advancements of uncooled infrared microbolometer materials: A review. Sensors and Actuators A: Physical, 342:113611, 2022.

[159] Markus Piller, Johannes Hiesberger, Elisabeth Wistrela, Paolo Martini, Niklas Luhmann, and Silvan Schmid. Thermal ir detection with nanoelectromechanical silicon nitride trampoline resonators. IEEE Sensors Journal, 2022.

[160] John C Mather. Bolometer noise: nonequilibrium theory. Applied optics, 21(6):1125–1129, 1982.

[161] Aapo Varpula, Kirsi Tappura, Jonna Tiira, Kestutis Grigoras, Olli-Pekka Kilpi, Kuura Sovanto, Jouni Ahopelto, and Mika Prunnila. Nano-thermoelectric infrared bolometers. APL Photonics, 6(3), 2021.

[162] Miao-Hsuan Chien, Mario Brameshuber, Benedikt K Rossboth, Gerhard J Schütz, and Silvan Schmid. Single-molecule optical absorption imaging by nanomechanical photothermal sensing. Proceedings of the National Academy of Sciences, 115(44):11150–11155, 2018.

[163] King Y Fong, Wolfram HP Pernice, and Hong X Tang. Frequency and phase noise of ultrahigh Q silicon nitride nanomechanical resonators. Phys. Rev. B, 85(16):161410, 2012.

[164] Gregory S MacCabe, Hengjiang Ren, Jie Luo, Justin D Cohen, Hengyun Zhou, Alp Sipahigil, Mohammad Mirhosseini, and Oskar Painter. Phononic bandgap nano-acoustic cavity with ultralong phonon lifetime. arXiv preprint arXiv:1901.04129, 2019.

[165] Markus Piller, Niklas Luhmann, Miao-Hsuan Chien, and Silvan Schmid. Nanoelectromechanical infrared detector. In Optical Sensing, Imaging, and Photon Counting: From X-Rays to THz 2019, volume 11088, pages 9–15. SPIE, 2019.

[166] Anna Vaskuri, Michelle S Stephens, Nathan A Tomlin, Christopher S Yung, Andrew J Walowitz, Cameron Straatsma, David Harber, and John H Lehman. Microfabricated bolometer based on a vertically aligned carbon nanotube absorber. In Synthesis and Photonics of Nanoscale Materials XVII, volume 11269, pages 41–52. SPIE, 2020.

[167] Dan Hu, Tianhua Meng, Hongyan Wang, Yongkang Ma, and Qiaofen Zhu. Ultra-narrow-band terahertz perfect metamaterial absorber for refractive index sensing application. Results in Physics, 19:103567, 2020.

[168] MM JEBBESSEN Treacy, Thomas W Ebbesen, and John M Gibson. Exceptionally high young's modulus observed for individual carbon nanotubes. Nature, 381(6584):678–680, 1996.